Los Alamos
NATIONAL LABORATORY
EST.1943

LA-UR-15-23856
Approved for public release; distribution is unlimited.

Title:	Dissertation: Precompound Emission of Energetic Light Fragments in Spallation Reactions
Author(s):	Kerby, Leslie Marie
Intended for:	Dissertation
Issued:	2015-08-04 (rev.1)

Disclaimer:
Los Alamos National Laboratory, an affirmative action/equal opportunity employer,is operated by the Los Alamos National Security, LLC for the National NuclearSecurity Administration of the U.S. Department of Energy under contract DE-AC52-06NA25396. By approving this article, the publisher recognizes that the U.S. Government retains nonexclusive, royalty-free license to publish or reproduce the published form of this contribution, or to allow others to do so, for U.S. Government purposes. Los Alamos National Laboratory requests that the publisher identify this article as work performed under the auspices of the U.S. Departmentof Energy. Los Alamos National Laboratory strongly supports academic freedom and a researcher's right to publish; as an institution, however, the Laboratory does not endorse the viewpoint of a publication or guarantee its technical correctness.

Precompound Emission of Energetic Light Fragments in Spallation Reactions

Presented in Partial Fulfillment of
the Requirements for the Degree of

Doctor of Philosophy

with a Major in

Nuclear Engineering

in the

College of Graduate Studies

University of Idaho

by

Leslie Marie Kerby

july 2015

Major Professor
Akira Tokuhiro, Ph.D.

Los Alamos National Laboratory Mentor
Stepan Mashnik, Ph.D.

Committee
Forrest Brown, Ph.D.
Ruprecht Machleidt, Ph.D.
Francesca Sammarruca, Ph.D.

Authorization to Submit Dissertation

This dissertation of Leslie Marie Kerby, submitted for the degree of Doctor of Philosophy with a Major in Nuclear Engineering and titled "Precompound Emission of Energetic Light Fragments in Spallation Reactions," has been reviewed in final form. Permission, as indicated by the signatures and dates below, is now granted to submit final copies to the College of Graduate Studies for approval.

Major Professor:	Akira Tokuhiro, Ph. D.	Date
Committee Members:	Stepan Mashnik, Ph. D.	Date
	Forrest Brown, Ph. D.	Date
	Ruprecht Machleidt, Ph. D.	Date
	Francesca Sammarruca, Ph. D.	Date
Department Administrator:	Lee Ostrom, Ph. D.	Date

Abstract

Emission of light fragments (LF) from nuclear reactions is an open question. Different reaction mechanisms contribute to their production; the relative roles of each, and how they change with incident energy, mass number of the target, and the type and emission energy of the fragments is not completely understood.

None of the available models are able to accurately predict emission of LF from arbitrary reactions. However, the ability to describe production of LF (especially at energies $\gtrsim$ 30 MeV) from many reactions is important for different applications, such as cosmic-ray-induced Single Event Upsets (SEUs), radiation protection, and cancer therapy with proton and heavy-ion beams, to name just a few. The Cascade-Exciton Model (CEM) version 03.03 and the Los Alamos version of the Quark-Gluon String Model (LAQGSM) version 03.03 event generators in Monte Carlo N-Particle Transport Code version 6 (MCNP6) describe quite well the spectra of fragments with sizes up to ^{4}He across a broad range of target masses and incident energies (up to $\sim$ 5 GeV for CEM and up to $\sim$ 1 TeV/A for LAQGSM). However, they do not predict the high-energy tails of LF spectra heavier than ^{4}He well. Most LF with energies above several tens of MeV are emitted during the precompound stage of a reaction. The current versions of the CEM and LAQGSM event generators do not account for precompound emission of LF larger than ^{4}He.

The aim of our work is to extend the precompound model in them to include such processes, leading to an increase of predictive power of LF-production in MCNP6. This entails upgrading the Modified Exciton Model currently used at the preequilibrium stage in CEM and LAQGSM. It also includes expansion and examination of the coalescence and Fermi break-up models used in the precompound stages of spallation reactions within CEM and LAQGSM. Extending our models to include emission of fragments heavier than ^{4}He at the precompound stage has indeed provided results that have much better agreement with experimental data.

Table of Contents

List of Tables

List of Figures

Acknowledgements

I first met Dr. Stepan Mashnik in June of 2012. I was a brand new intern at Los Alamos National Laboratory and definitely felt a bit over my head. I also was not the typical graduate intern. I had taken a break from my science career to stay home with my kids, and then over a decade later went back to school to support myself and my children. So there I was: in my mid-30s, with a houseful of children, recently back in science, hailing from my relatively small regional school, and very thrilled—and a little nervous—to be at LANL. Stepan was patient, kind, and an excellent teacher. I got along well with his non-conforming personality, and he took me under his wing. He asked about how my children were doing. And he brought me peaches and other fruit from his own fruit trees.

In January 2014, Stepan was diagnosed with lung cancer again. He had beaten it the first time seven years prior and lived far longer and better than the doctors had expected. The cancer continued to spread that spring, and in the summer he began chemotherapy. Despite all these personal challenges, Stepan has continued to be an incredible mentor. He continues to teach me about life and about physics. He is always available and happy to answer my questions.

I cannot think of a better mentor for me than Stepan Mashnik. He probably does not realize how much I have appreciated his tutelage, as he is not a man of many words and doesn't like mushiness. But he has taught me what is important in life, he has made me feel welcome at LANL, and he has made me a better physicist and scientist.

I first met Dr. Akira Tokuhiro the end of 2010 when I was eight months pregnant with my fifth child, recently divorced, recently having "come out" as lesbian in my predominantly conservative community, having completed my previous science degree (a BS in Physics) over 12 years earlier, and inquiring about the Ph.D. program in Nuclear Engineering at the University of Idaho. Even though I was smart and determined, I knew there was significant probability I would not be taken seriously. Akira, however, as a self-avowed feminist, never batted an eye at my personal difficulties.

Akira believed in me and supported me. He did not give me a free pass, but he gave me a chance to prove myself. He suggested I enroll in Advanced Nuclear Reactor Engineering (the introductory course would bore me, he said). My youngest child was born the first week of the class. I was over my head in both the engineering principles (I had never had an engineering course before) and the plethora of acronyms that is nuclear engineering. Engineers apparently like acronyms. Nevertheless, I did well in the class. And I was admitted into the Ph.D. program.

Throughout my tenure as a student, Akira has "taught me the ropes" about government contracts, graduate school bureaucracy, industry practice, as well as encouraging me professionally and personally. I owe several of my honors and awards to his recommendation as well, because had he not been watching for new awards for me to apply for I would have missed the opportunities.

I first met Dr. Forrest Brown the fall of 2011 at an MCNP week-long training course, the first semester of my full-time graduate study at the University of Idaho. As a single mom, I saw my kids off to school in the morning, and then commuted, and so was consistently late for class. I also repeatedly fell asleep during class, despite Forrest being known—for good reason—as a great lecturer (infants are very tiring; sorry Forrest). He was not offended by any of this, and at the end of the week when I talked with him about my interest in quantum physics, he offered me an internship at LANL the next summer. This opened the door to what would become my dissertation research and was also a tremendous boost to my career.

Forrest played another role in my professional and personal development as well. I am a stutterer. With friends and family it is not very noticeable, but with public speaking it was unpredictable. During my preliminary exam and proposal, I stuttered badly. I felt deeply humiliated. It is difficult to explain to people the frustration and embarrassment of feeling like you cannot speak, especially when everyone is looking at and waiting for you. I talked with Forrest later about my "poor performance" during my proposal, and he immediately disagreed with my assessment and said that I had done well.

Furthermore, several months later, after my presentation at the 2014 ANS Annual Meeting, I met with Forrest. He told me that he knew I had a speech impediment, and

that I had done well in my presentation and my impediment did not interfere with my ability to communicate. I don't recall ever feeling both such acknowledgement of my stutter and at the same time such acceptance. It had a tremendous impact on me. I have recently begun speech therapy. But whether or not I stutter, the messages of acceptance I received from Forrest (and others) play a significant role in my ability to speak without fear or shame.

These three men have had a profound impact on me professionally and personally, but of course, there are many others who have shaped my journey. Dr. Ruprecht Machleidt has been my "nuclear physics" professor. From him I learned particle physics, and graduate quantum physics. He was an excellent teacher, and I loved how he never used PowerPoint slides. I, myself, also feel much more at home teaching at a chalkboard. Dr. Francesca Sammarruca, another nuclear physicist, has been available to answer my questions and supports my progress as a female scientist. Dr. Tim Goorley, the XCP-3 group leader when I first came to LANL, supported my development as a scientist and funded this research and my schooling. Dr. Avneet Sood, current XCP-3 group leader, and Drs. Larry Cox and Chris Werner, past and present Eolus Project Leaders, respectively, have continued to support me professionally and have continued collaboration and financial support of this research. I have also felt tremendous support and understanding from these leaders for my situation, both in living remotely and being a single parent. I thank them for their support. I have, furthermore, learned much from Drs. Arnold Sierk and Konstantin Gudima, renowned experts in the field of spallation reactions. In addition, Drs. Jeff Bull and Mike James provided invaluable support when I began modifying MCNP6. There are many other colleagues and mentors at LANL who have made my work more enjoyable, as it is invigorating to work in a place with so many brilliant, dedicated, and kind people.

I would like to thank my children: Alison, Emily, Rachel, Philip, and Daniel. They are my #1 fans, always cheering me on and always believing in me. I am also their #1 fan, always cheering them on and believing in them. They bring depth, color, and brilliance to my life and it is a privilege to be their mother and help them and watch them grow and develop.

I would also like to thank the staff and faculty at the University of Idaho. I will mention only two by name. Alice Allen has been indispensable as a guide through the bureaucracy of Ph.D. requirements, as well as being personally supportive. Sara Moore has managed expertly the tangle of financial bureaucracy and contracts that I have brought to the school.

I would like to end by thanking all those people and organizations who have funded me, my schooling, and this research. The lion's share has been paid by Los Alamos National Laboratory, under Contract No. DE-AC52-06NA25396. A significant portion has been provided by the American Physical Society M. Hildred Blewett Fellowship (www.aps.org). I am deeply grateful to these two institutions, as without their generosity this dissertation would not have been possible. I also wish to express thanks to the University of Idaho and Dr. Bob Hiromoto, with whom I gained valuable experience working as a research assistant my first year at UI. Finally, I wish thank the National Organization of Gay and Lesbian Scientists and Technical Professionals for their Motorola Out-to-Innovate Graduate Scholarship, the American Nuclear Society for their John and Muriel Landis Scholarship, and the Roy G. Post Foundation for their Graduate Scholarship.

Dedication

This dissertation is dedicated to my children:
Alison, Emily, Rachel, Philip, and Daniel.
They bring countless joys to my life.

CHAPTER 1

Introduction

Below are relevant publications that result from the author's work pertaining to this chapter.

- L.M. Kerby, S.G. Mashnik, and A.J. Sierk, Preliminary Results of Investigating Precompound Emission of Light Fragments in Spallation Reactions, Summer 2012, LANL Report, LA-UR-12-24190 (August 2012);
- L.M. Kerby, S.G. Mashnik, and A.J. Sierk, Comparison of Expanded Preequilibrium CEM Model with CEM03.03 and Experimental Data, FY2013, LANL Report, LA-UR-13-21828 (November 2013);
- L.M. Kerby and S.G. Mashnik, Fiscal Year 2014 Report, LANL Report, LA-UR-14-27533 (November 2014);
- S.G. Mashnik and L.M. Kerby, MCNP6 Fragmentation of Light Nuclei at Intermediate Energies, Nuclear Instruments and Methods in Physics Research A **764** (2014) 59; arXiv:1404.7820.

Emission of light fragments (LF) from nuclear reactions is an open question. Different reaction mechanisms contribute to their production; the relative roles of each, and how they change with incident energy, mass number of the target, and the type and emission energy of the fragments is not completely understood.

None of the available models are able to accurately predict emission of LF from arbitrary reactions. However, the ability to describe production of LF (especially at energies $\gtrsim$ 30 MeV) from many reactions is important for different applications, such as cosmic-ray-induced Single Event Upsets (SEUs), radiation protection, and cancer therapy with proton and heavy-ion beams, to name just a few. The Cascade-Exciton Model (CEM) version 03.03 [1, 2] and the Los Alamos version of the Quark-Gluon String Model (LAQGSM) version 03.03 [2, 3] event generators in Monte Carlo N-Particle Transport Code version 6 (MCNP6) [4] describe quite well the spectra of

fragments with sizes up to ^{4}He across a broad range of target masses and incident energies (up to $\sim$ 5 GeV for CEM and up to $\sim$ 1 TeV/A for LAQGSM). However, they do not predict the high-energy tails of LF spectra heavier than ^{4}He well. Most LF with energies above several tens of MeV are emitted during the precompound stage of a reaction. The current versions of the CEM and LAQGSM event generators do not account for precompound emission of LF larger than ^{4}He.

The aim of our work is to extend the precompound model in them to include such processes, leading to an increase of predictive power of LF-production in MCNP6. This entails upgrading the Modified Exciton Model currently used at the preequilibrium stage in CEM and LAQGSM. It also includes expansion and examination of the coalescence and Fermi break-up models used in the precompound stages of spallation reactions within CEM and LAQGSM. Extending our models to include emission of fragments heavier than ^{4}He at the precompound stage has indeed provided results that have much better agreement with experimental data.

1.1 WHY THIS RESEARCH IS NEEDED

In October 2008 an Airbus plane was struck by a cosmic ray en route from Perth to Singapore, one of its inertial reference computer units failed, and it sharply lost altitude [5]. It did land safely, but as seen in Figure 1.1, it caused significant injury to both the occupants and the plane.

FIGURE 1.1: Photographs of the damaged Airbus after the SEU [5].

These SEUs are not rare, and can wreak significant havoc. For example, in a typical 14-day space mission the shuttles' 5 computers typically receive 400-500 SEUs [6]. In addition, even though the plane accident was serious, much more serious incidents can occur: during the Cold War, U. S. satellites hit by a cosmic rays malfunctioned and caused false alarms of nuclear attacks [7]. Understanding how high-energy fragments interact with matter is critical to preventing these malfunctions.

Accurate simulation of LF spectra is also important in the fields of radiation shielding, especially for applications in space. Modern computers cannot be used in space because the electronics are too small and delicate and cannot, at present, be shielded well enough. An even larger problem is radiation shielding for the human astronauts exposed to Galactic Cosmic Rays (GCRs) [6].

This research is also important to several medical fields, such as cancer treatment with proton or heavy-ion beams. Proton and heavy-ion therapy has been shown to be more effective than x-ray therapy, and have much fewer side effects [8].

Another indication of the importance of this research is the recommendation of an international evaluation and comparison, the 2008-2010 IAEA (International Atomic Energy Agency) Benchmark of Spallation Models, that we make this change in our code [9, 10]. While no other spallation model can generally predict high-energy light fragment emission from arbitrary reactions, it is an accomplishment several model development groups are working to achieve.

Furthermore, MCNP6's GENXS option at present does not produce tallies of spectra for particles larger than ^{4}He. This limitation is serious for some of our interest groups. For example, NASA recently contacted us to inquire if our codes could produce LF spectra in the intermediate- and high-energy regimes. At present they cannot.

Last, but not least, this research helps us understand better the mechanisms of nuclear reactions.

1.1.1 *Comparison with Experimental Data*

Figure 1.2 shows the double-differential cross section of the reaction 200 MeV p + ^{27}Al $\rightarrow$ ^{6}Li, comparing Machner et al. [11] experimental data (open symbols) and unmodified CEM03.03 (solid red lines).

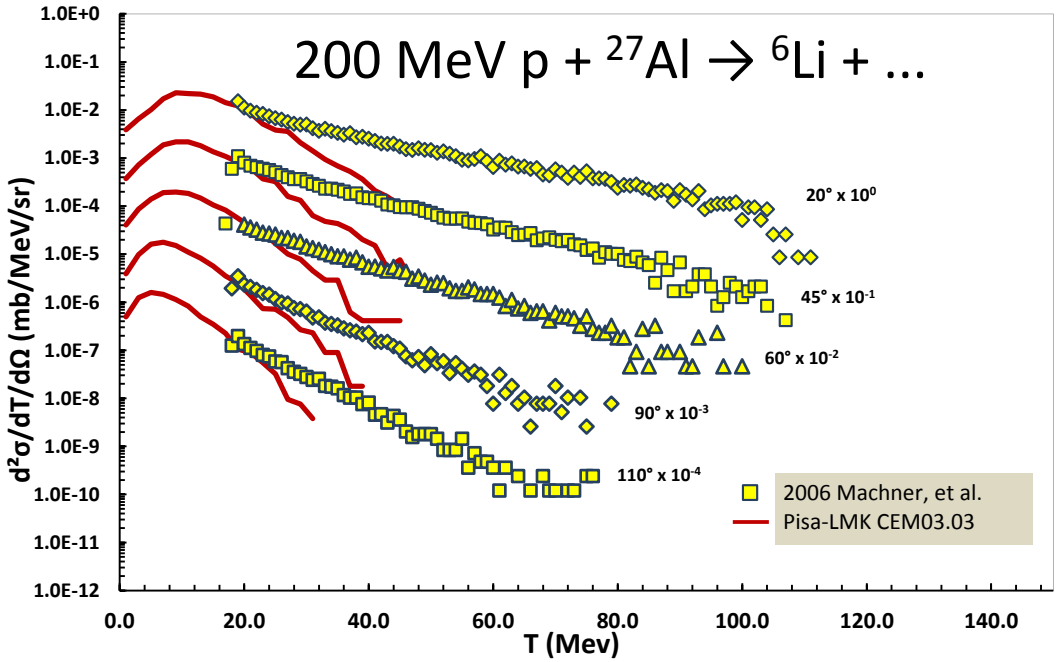

FIGURE 1.2: Comparison of CEM03.03 (solid red lines) and experimental data by Machner et al. [11] (open symbols).

The vertical axis presents the double differential cross sections. The horizontal axis shows the kinetic energy of the emitted particles (^{6}Li in this case) in MeV. The different data bands represent ^{6}Li detected (or simulated) at different angles, and are separated out by multiplying each band by a different factor of 10. As can be seen, the current version of CEM does not predict the high-energy tails of ^{6}Li well. This is true across other reaction energies and target mass numbers for all fragments heavier than ^{4}He, for higher energies. At lower energies ($\lesssim$ 25 MeV) CEM matches well, but as we enter intermediate energies ($\gtrsim$ 25 MeV) CEM falls off sharply. This is because the peak which occurs at lower energy is a result of the evaporation stage, which does consider emission of LF (up to ^{28}Mg) [12]. At higher energies ($\gtrsim$ 25 MeV), the fragment spectra is largely produced by the Modified Exciton Model (MEM) within the preequilibrium stage, with a secondary, but significant, contribution from the coalescence model, also

a precompound stage. Neither the MEM nor the coalescence model presently consider emission of light fragments heavier than ^{4}He.

1.2 CEM AND LAQGSM PHYSICS

Details, examples of results, and useful references to different versions of CEM and LAQGSM may be found in a recent lecture [2].

The Cascade-Exciton Model (CEM) of nuclear reactions was proposed more than 30 years ago at the Laboratory of Theoretical Physics, JINR, Dubna, USSR by Gudima, Mashnik, and Toneev [1]. It is based on the standard (non time-dependent) Dubna IntraNuclear Cascade (INC) [13, 14] and the Modified Exciton Model (MEM) [15, 16]. The code LAQGSM03.03 is the latest modification [17] of LAQGSM [3], which in its turn is an improvement of the Quark-Gluon String Model (QGSM) [18]. It describes reactions induced by both particles and nuclei at incident energies up to about 1 TeV/nucleon.

The basic version of both the CEM and LAQGSM event generators is the so-called "03.03" version, namely CEM03.03 [19, 2, 20] and LAQGSM03.03 [2, 17, 21]. The CEM code calculates nuclear reactions induced by nucleons, pions, and photons. It assumes that the reactions occur generally in three stages (see Fig. 1.3). The first stage is the INC, in which primary particles can be re-scattered and produce secondary particles several times prior to absorption by, or escape from, the nucleus. When the cascade stage of a reaction is completed, CEM uses the coalescence model to "create" high-energy d, t, ^{3}He, and ^{4}He by final-state interactions among emitted cascade nucleons outside of the target. The emission of the cascade particles determines the particle-hole configuration, Z, A, and the excitation energy that is the starting point for the second, preequilibrium stage of the reaction. The subsequent relaxation of the nuclear excitation is treated in terms of an improved version of the modified exciton model of preequilibrium decay followed by the equilibrium evaporation/fission stage.

Generally, all three components may contribute to experimentally measured particle spectra and other distributions. But if the residual nuclei after the INC have atomic numbers with $A \leq A_{Fermi} = 12$, CEM uses the Fermi breakup model to calcu-

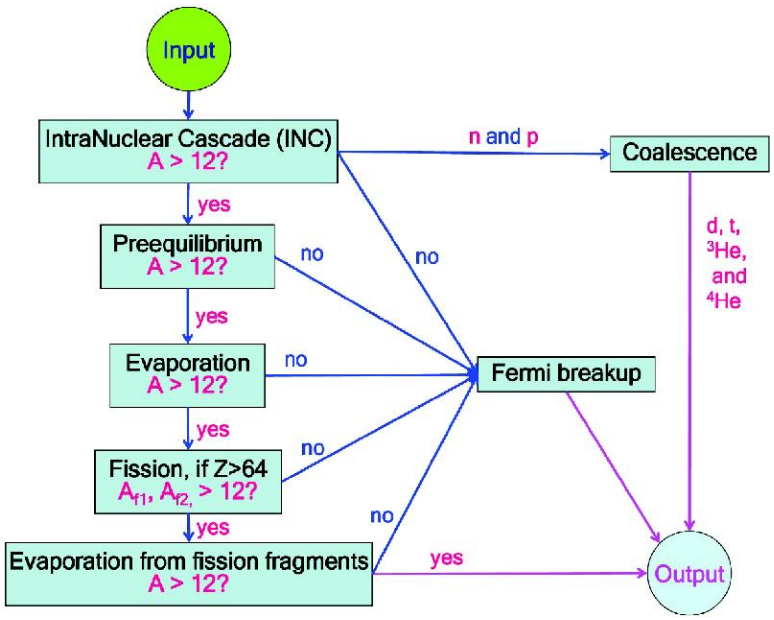

FIGURE 1.3: Flow chart of nuclear-reaction calculations by CEM03.03 and LAQGSM03.03.

late their further disintegration instead of using the preequilibrium and evaporation models. Fermi breakup is much faster to calculate and gives results very similar to the continuation of the more detailed models to much lighter nuclei. LAQGSM also describes nuclear reactions, generally, as a three-stage process: INC, followed by preequilibrium emission of particles during the equilibration of the excited residual nuclei formed after the INC, followed by evaporation of particles from or fission of the compound nuclei. LAQGSM was developed with a primary focus on describing reactions induced by nuclei, as well as induced by most elementary particles, at high energies, up to about 1 TeV/nucleon. The INC of LAQGSM is completely different from the one in CEM. LAQGSM also considers Fermi breakup of nuclei with $A \leq 12$ produced after the cascade, and the coalescence model to "produce" high-energy d, t, ^{3}He, and ^{4}He from nucleons emitted during the INC.

Many people participated in the CEM and LAQGSM code development over their more than 40-year history. Contributors to their "03.03" versions are S. G. Mashnik, K. K. Gudima, A. J. Sierk, R. E. Prael, M. I. Baznat, and N. V. Mokhov. The author of this dissertation (L.M.K.) has joined these efforts recently to extend the precompound

models of CEM and LAQGSM by accounting for possible emission of light fragments (LF) heavier than ^{4}He, up to ^{28}Mg.

1.2.1 *The Intranuclear Cascade Mechanism*

The INC approach is based on the ideas of Heisenberg and Serber, who regarded intranuclear cascades as a series of successive quasi-free collisions of the fast primary particle with the individual nucleons of the nucleus. Basic assumptions of and conditions for INC applicability may be found in [2]. Comprehensive details and useful references are published in [13, 14].

1.2.2 *The INC of CEM03.03*

The intranuclear cascade model in CEM03.03 is based on the standard (non-time-dependent) version of the Dubna cascade model [13, 14]. All the cascade calculations are carried out in a three-dimensional geometry. The nuclear matter density $\rho(r)$ is described by a Fermi distribution with two parameters taken from the analysis of electron-nucleus scattering. For simplicity, the target nucleus is divided by concentric spheres into seven zones in which the nuclear density is considered to be constant. The energy spectrum of the target nucleons is estimated in the perfect Fermi-gas approximation. The influence of intranuclear nucleons on the incoming projectile is taken into account by adding to its laboratory kinetic energy an effective real potential, as well as by considering the Pauli principle which forbids a number of intranuclear collisions and effectively increases the mean free path of cascade particles inside the target. The interaction of the incident particle with the nucleus is approximated as a series of successive quasi-free collisions of the fast cascade particles (N, π, or γ) with intranuclear nucleons.

The integral cross sections for the free NN, πN, and γN interactions are approximated in the Dubna INC model [13, 14] using a special algorithm of interpolation/extrapolation through a number of picked points, mapping as well as possible the experimental data. This was done very accurately by Prof. Barashenkov's group using all experimental data available at that time, more than 45 years ago [22]. Cur-

rently the experimental data on cross sections is much more complete than at that time; therefore the approximations of all the integral elementary cross sections used in CEM have recently been revised.

The kinematics of two-body elementary interactions and absorption of photons and pions by a pair of nucleons is completely defined by a given direction of emission of one of the secondary particles. The cosine of the angle of emission of secondary particles in the c.m. system is calculated by the Dubna INC with approximations based on available experimental data. For elementary interactions with more than two particles in the final state, the Dubna INC uses the statistical model to simulate the angles and energies of products (see details in [13]).

For the improved version of the INC in CEM03.03, we use currently available experimental data and recently published systematics proposed by other authors and have developed new approximations for angular and energy distributions of particles produced in nucleon-nucleon and photon-proton interactions. In addition, newer versions of CEM incorporate a possibility to normalize the final results to systematics based on available experimental reaction cross sections. The condition for the transition from the INC stage of a reaction to preequilibrium was changed for CEM03.03; on the whole, the INC stage in CEM03.03 is longer while the preequilibrium stage is shorter in comparison with previous versions. Real binding energies have been incorporated for nucleons in the cascade instead of the approximation of a constant separation energy of 7 MeV used in the initial versions of the CEM and momentum-energy conservation us imposed for each simulated event (conservation was only "on the average" in earlier versions). Details, examples of results, and references to this portion of the work may be found in [2].

1.2.3 *The INC of LAQGSM03.03*

The INC of LAQGSM03.03 is described with a recently improved version [17, 21, 23] of the time-dependent intranuclear cascade model developed initially at JINR in Dubna, often referred to in the literature as the Dubna intranuclear Cascade Model, DCM (see [24] and references therein). The DCM models interactions of fast cascade particles ("participants") with nucleon spectators of both the target and projectile

nuclei and includes as well interactions of two participants (cascade particles). It uses experimental cross sections at energies below 4.5 GeV/nucleon, and those calculated by the Quark-Gluon String Model [18, 25] at higher energies to simulate angular and energy distributions of cascade particles, and also considers the Pauli Exclusion Principle.

In contrast to the CEM version of the INC described above, DCM uses a continuous nuclear density distribution; therefore, it does not need to consider refraction and reflection of cascade particles inside or on the border of a nucleus. It also keeps track of the time of an intranuclear collision and of the depletion of the nuclear density during the development of the cascade (the so-called "trawling effect") and takes into account the hadron formation time.

All the new approximations developed recently for the INC of CEM to describe total cross sections and elementary energy and angular distributions of secondary particles from hadron-hadron interactions were previously incorporated also into the INC of LAQGSM [21]. In addition, a new high-energy photonuclear reaction model based on the event generators for γp and γn reactions from the Moscow INC [26] (kindly provided to us by Dr. Igor Pshenichnov) and on the latest photonuclear version of CEM [27] was developed and incorporated into the INC of LAQGSM; this allows the user to calculate reactions induced by photons with energies of up to tens of GeV. In the latest version of LAQGSM [17], the INC was modified for a better description of nuclear reactions at very high energies (above 20 GeV/nucleon). Details, examples of results, and references to this portion of work may be found in [2].

1.2.4 *The Coalescence Model*

When the cascade stage of a reaction is completed, CEM and LAQGSM use the coalescence model described in Ref. [24] to "create" high-energy d, t, ^{3}He, and ^{4}He by final-state interactions among emitted cascade nucleons outside of the target nucleus. In contrast to most other coalescence models for heavy-ion-induced reactions, where complex-particle spectra are estimated simply by convolving the measured or calculated inclusive spectra of nucleons with corresponding fitted coefficients, CEM03.03

and LAQGSM03.03 use in their simulations of particle coalescence real information about all emitted cascade nucleons and do not use integrated spectra. We assume that all the cascade nucleons having differences in their momenta smaller than p_c and the correct isotopic content form an appropriate composite particle. The coalescence parameters p_c were fit for each composite particle in Ref. [24] to describe available data for the reaction Ne+U at 1.04 GeV/nucleon, but the fitted values turned out to be quite universal and were subsequently found to describe high-energy complex-particle production satisfactorily for a variety of reactions induced both by particles and nuclei at incident energies up to about 200 GeV/nucleon, when describing nuclear reactions with different versions of LAQGSM [2] or with its predecessor, the Quark-Gluon String Model (QGSM) [18]. These parameters are:

$$\begin{aligned} p_c(d) &= 90 \text{ MeV/c} ; \\ p_c(t) &= p_c(^3\text{H}e) = 108 \text{ MeV/c} ; \\ p_c(^4\text{H}e) &= 115 \text{ MeV/c} . \end{aligned} \tag{1.1}$$

As the INC of CEM is different from those of LAQGSM or QGSM, it is natural to expect different best values for p_c as well. Recent studies show that the values of parameters p_c defined by Eq. (1) are also good for CEM for projectile particles with kinetic energies T_0 lower than 300 MeV and equal to or above 1 GeV. For incident energies in the interval 300 MeV $\leq T_0 <$ 1 GeV, a better overall agreement with the available experimental data is obtained by using values of p_c equal to 150, 175, and 175 MeV/c for d, t (^{3}He), and ^{4}He, respectively. These values of p_c are fixed as defaults in CEM03.03. If several cascade nucleons are chosen to coalesce into composite particles, they are removed from the distributions of nucleons and do not contribute further to such nucleon characteristics as spectra, multiplicities, *etc*.

1.2.5 *Preequilibrium Reactions*

The subsequent preequilibrium interaction stage of nuclear reactions is considered by the current CEM and LAQGSM in the framework of the latest version of the Modified Exciton Model (MEM) [15, 16] as described in Ref. [20]. At the preequilibrium stage of

a reaction, we take into account all possible nuclear transitions changing the number of excitons n with $\Delta_n = +2$, -2, and 0, as well as all possible multiple subsequent emissions of n, p, d, t, ^{3}He, and ^{4}He. The corresponding system of master equations describing the behavior of a nucleus at the preequilibrium stage is solved by the Monte-Carlo technique [1].

CEM considers the possibility of fast d, t, ^{3}He, and ^{4}He emission at the preequilibrium stage of a reaction in addition to the emission of nucleons. We assume that in the course of a reaction p_j excited nucleons (excitons) are able to condense with probability γ_j forming a complex particle which can be emitted during the preequilibrium state. The "condensation" probability γ_j is estimated as the overlap integral of the wave function of independent nucleons with that of the complex particle (see details in [1]):

$$\gamma_j \simeq p_j^3 (V_j/V)^{p_j-1} = p_j^3 (p_j/A)^{p_j-1} \; . \tag{1.2}$$

This is a rather crude estimate. As is frequently done, the values γ_j are taken from fitting the theoretical preequilibrium spectra to the experimental ones. In CEM, to improve the description of preequilibrium complex-particle emission, we estimate γ_j by multiplying the estimate provided by Eq. (2) by an empirical coefficient $F_j(A, Z, T_0)$ whose values are fitted to available nucleon-induced experimental complex-particle spectra.

CEM and LAQGSM predict forward-peaked (in the laboratory system) angular distributions for preequilibrium particles. For instance, CEM assumes that a nuclear state with a given excitation energy E^* should be specified not only by the exciton number n but also by the momentum direction $\mathbf{\Omega}$. This calculation scheme is easily realized by the Monte-Carlo technique [1]. It provides a good description of double differential spectra of preequilibrium nucleons and a not-so-good but still satisfactory description of complex-particle spectra from different types of nuclear reactions at incident energies from tens of MeV to several GeV. For incident energies below about 200 MeV, Kalbach [28] has developed a phenomenological systematics for preequilibrium-particle angular distributions by fitting available measured spectra of

nucleons and complex particles. As the Kalbach systematics are based on measured spectra, they describe very well the double-differential spectra of preequilibrium particles and generally provide a better agreement of calculated preequilibrium complex-particle spectra with data than does the CEM approach [1]. This is why the Kalbach systematics [28] were incorporated into CEM03.03 and LAQGSM03.03 to describe angular distributions of both preequilibrium nucleons and complex particles at incident energies up to 210 MeV. At higher energies, the CEM approach [1] is used.

The standard version of the CEM [1] provides an overestimation of preequilibrium particle emission from different reactions that have been analyzed (see more details in [29]). One way to solve this problem, suggested in Ref. [29], is to change the criterion for the transition from the cascade stage to the preequilibrium one. Another easy way, suggested in Ref. [29], to shorten the preequilibrium stage of a reaction is to arbitrarily allow only transitions that increase the number of excitons, $\Delta n = +2$, *i.e.*, only allow the evolution of a nucleus toward the compound nucleus. In this case, the time of the equilibration will be shorter and fewer preequilibrium particles will be emitted, leaving more excitation energy for the evaporation. This approach was used in the CEM2k [29] version of the CEM and it allowed much better descriptions of the p+A reactions measured at GSI in inverse kinematics at energies around 1 GeV/nucleon. Nevertheless, the "never-come-back" approach seems unphysical; therefore it is no longer used. The problem of emitting fewer preequilibrium particles in the CEM is addressed by following Veselsky [30]. We assume that the ratio of the number of quasi-particles (excitons) n at each preequilibrium reaction stage to the number of excitons in the equilibrium configuration n_{eq}, corresponding to the same excitation energy, to be a crucial parameter for determining the probability of preequilibrium emission P_{pre} (see details in [2, 20, 30]).

1.2.6 *Evaporation*

CEM and LAQGSM use an extension of the Generalized Evaporation Model (GEM) code GEM2 by Furihata [31] after the preequilibrium stage of reactions to describe evaporation of nucleons, complex particles, and light fragments heavier than ^{4}He (up

to ^{28}Mg) from excited compound nuclei and to describe fission, if the compound nuclei are heavy enough to fission ($Z \geq 65$).

When including evaporation of up to 66 types of particles in GEM2, running times increase significantly compared to the case when evaporating only 6 types of particles, up to ^{4}He. The major particles emitted from an excited nucleus are n, p, d, t, ^{3}He, and ^{4}He. For most cases, the total emission probability of particles heavier than α is negligible compared to those for the emission of light ejectiles. A detailed investigation of different reactions shows that if we study only nucleon and complex-particle spectra or only spallation and fission products and are not interested in light fragments, we can consider evaporation of only 6 types of particles in GEM2 and save much time, getting results very close to the ones calculated with the more time consuming "66" option. In the current code versions, the number of types of evaporated particles may be selected in advance. A detailed description of GEM2, as incorporated into CEM and LAQGSM, may be found in [2, 20].

1.2.7 *Fission*

The fission model used in GEM2 is based on Atchison's model [32], often referred in the literature as the Rutherford Appleton Laboratory (RAL) fission model, which is where Atchison developed it. The mass-, charge-, and kinetic energy-distribution of fission fragments are simulated by RAL using approximations based on available experimental data (see details in [2, 20, 31, 32]). For CEM03.03 and LAQGSM03.03, GEM2 was modified slightly [33]. We will not discuss further the fission model; interested readers may find details and further references in [2, 20, 33, 34].

1.2.8 *The Fermi Breakup Model*

After calculating the coalescence stage of a reaction, CEM and LAQGSM move to the description of the last slower stages of the interaction, namely to preequilibrium decay and evaporation, with a possible competition of fission. But at any stage, if the residual nuclei have atomic numbers with $A \leq A_{Fermi} = 12$, CEM and LAQGSM use the Fermi breakup model [35] to calculate their further disintegration instead of

using the preequilibrium and evaporation models. All formulas and details of the algorithms used in the version of the Fermi breakup model developed in the group of the Late Prof. Barashenkov at JINR, Dubna, may be found in [36]; this model is used in CEM03.03 and LAQGSM03.03, with several recent improvements and corrections, as described in Ref. [2].

The original version of the model contained a few features which very occasionally could lead to unphysical fragments; these could cause problems in a transport model. All these issues have been dealt with in the current version, which no longer encounters such problems (see details in Ref. [2]).

1.2.9 *Comments on the Emission of Energetic LF*

The goal of this research is to enable MCNP6 to produce high-energy light fragments. Energetic light fragments can only be emitted through precompound processes, because by the time the reaction reaches compound stage processes (evaporation and fission), there is not enough energy left in the system to emit a high-energy light fragment. Therefore, energetic light fragments may be emitted through three processes:

- Fermi breakup
- Coalescence
- Preequilibrium

This research explores the emission of light fragments through each of these channels.

1.3 EMISSION OF HIGH-ENERGY LF IN OTHER MODELS

The bulk of our research focuses on the emission of high-energy LF at the preequilibrium stage of nuclear reactions, as considered by our models. However, high-energy LF can be produced at other precompound stages of reactions. Cugnon *et al.* have modified their Liège IntraNuclear Cascade (INCL) code to consider emission of light fragments heavier than ^{4}He during the cascade stage of reactions via coalescence of several nucleons at the nuclear periphery [37]. These modifications have not yet

been generalized across all types of reactions. In addition, the INCL+ABLA model is limited to relatively light incident projectiles (particles and light ions, typically, up to oxygen) [38]. Several previous papers by the same group discuss the production of light fragments up to $A = 10$ (see, e.g., [39, 40]). A recent 2013 paper by the same authors presents satisfactory results for emission spectra of ^{6}He, ^{6}Li, ^{7}Li, and ^{7}Be in the reaction $p +^{197} Au \rightarrow$ ... and discusses emission of clusters up to $A = 12$ [41].

Emission of ^{7}Be at the preequilibrium stage (described by a hybrid exciton model and coalescence pick-up model) was studied by A. Yu. Konobeyev and Yu. A. Korovin more than a decade ago [42]. Additionally, preequilibrium emission of helium and lithium ions and the necessary adjustments to the Kalbach systematics was discussed in Ref. [43]. Preequilibrium emission of light fragments was also studied within the CEM in 2002 [44], but that project was never completed.

Finally, energetic fragments can be produced via Fermi break-up [35] and multifragmentation processes, as described, e.g., by the Statistical Multifragmentation Model (SMM) [45]; (see a comparison of the Fermi break-up model with SMM in the recent paper by Souza *et al.* [46]).

Light fragments can also be emitted during the compound stage of reactions. GEM2, the evaporation model used in CEM, emits light fragments up to ^{28}Mg [12]. In addition, light fragments can be produced via very asymmetric binary fission, as described, e.g., by the fission-like binary decay code GEMINI by Charity et al. [47], and also via ternary fission. For more information, see the recent Ref. [48] wherein Y. Ronen discusses the physics of how light fragments are products seen in ternary fission. However, neither evaporation nor fission processes can produce high-energy fragments, of interest to our current study.

Finally, let us mention that, as a rule, the authors of most of the recent measurements of LF spectra analyze their experimental data using a variety of simplified approaches assuming emission of LF from different "moving sources" (see, e.g., [11, 49, 50, 51]). True, such simplified "moving source prescriptions" are fitted to describe as well as possible only their own measured LF spectra, and are never developed further to become universal models with predictive powers for spectra of LF from arbitrary reactions. In addition, such approaches cannot describe at all many other

characteristics of nuclear reactions, like the yields and energies of spallation products, fission fragments productions, etc., and therefore cannot be used as event-generators in transport codes.

Lastly, for detailed information on spallation reactions and research, see the book *Handbook of Spallation Research*, by D. Filges and F. Goldenbaum [52]. A useful summary paper, by J.-C. David, on spallation models is also available in Ref. [53].

CHAPTER 2

Fermi Breakup

Below are relevant publications that result from the author's work pertaining to this chapter.

- L.M. Kerby, S.G. Mashnik, and A.T. Tokuhiro, Production of Energetic Light Fragments with Expanded Cascade Exciton Model (CEM), Transactions of the American Nuclear Society **110** (2014) 465;
- S.G. Mashnik, L.M. Kerby, K.K. Gudima, and A.J. Sierk, Extension of the CEM and LAQGSM Models to Describe Production of Energetic Light Fragments in Spallation Reactions, European Physical Journal Web of Conferences **66** (2014) 03059; arXiV:1306.6547;
- L.M. Kerby, S.G. Mashnik, and A.J. Sierk, Preliminary Results of Investigating Precompound Emission of Light Fragments in Spallation Reactions, Summer 2012, LANL Report, LA-UR-12-24190 (August 2012);
- S.G. Mashnik and L.M. Kerby, MCNP6 Fragmentation of Light Nuclei at Intermediate Energies, Nuclear Instruments and Methods in Physics Research A **764** (2014) 59; arXiv:1404.7820.

The Fermi Breakup model is used in CEM and LAQGSM for residual nuclei with atomic number $A \leq 12$, making it particularly important in reactions with light target nuclei. Fragmentation reactions induced by protons and light nuclei of energies around 1 GeV/nucleon and below on light target nuclei are involved in different applications, like cosmic-ray-induced single event upsets (SEUs), radiation protection, and cancer therapy with proton and ion beams, among others. It is impossible to measure all nuclear data needed for such applications; therefore, Monte Carlo transport codes are usually used to simulate impacts associated with fragmentation reactions. It is important that available transport codes simulate such reactions as well as possible. For this reason, during the past several years, efforts have been done to

investigate the validity and performance of, and to improve where possible, nuclear reaction models simulating fragmentation of light nuclei in GEANT4 [54], SHIELD-HIT [55, 56, 57], and PHITS [58, 59].

The Los Alamos Monte Carlo transport code MCNP6 [4] uses the latest version of the cascade-exciton model (CEM) as incorporated in its event generator CEM03.03 [19, 2] to simulate fragmentation of light nuclei at intermediate energies for reactions induced by nucleons, pions, and photons, and the Los Alamos version of the quark-gluon string model (LAQGSM) as implemented in the code LAQGSM03.03 [2, 17] to simulate fragmentation reactions induced by nuclei and by particles at higher energies, up to about 1 TeV/nucleon.

In recent years, MCNP6, with its CEM and LAQGSM event generators, has been extensively validated and verified (V&V) against a large variety of nuclear reactions on both thin and thick targets (see, e.g. Refs. [60, 61, 62, 63] and references therein), but was never tested specifically on fragmentation of light nuclei at intermediate energies. To address this, we investigate the performance of MCNP6, CEM, and LAQGSM in simulating fragmentation reactions at intermediate energies and discuss possible ways of further improving these codes. See our recent publication in Nuclear Instruments and Methods A for further details [64].

2.1 INVESTIGATION OF FERMI BREAKUP CUT-OFF

De-excitation of light nuclei with $A \leq A_{Fermi}$ produced after the INC is described by CEM and LAQGSM only with the Fermi break-up model, where A_{Fermi} is a "cut-off value" fixed in our models. The value of A_{Fermi} is a model dependent parameter, not a physics characteristic of nuclear reactions. Actually, the initial version of the Fermi breakup model we incorporated in CEM and LAQGSM [20, 21] was used when $A \leq A_{Fermi} = 16$, just as $A_{Fermi} = 16$ is used currently in GEANT4 (see [54]) and in SHIELD-HIT (see [55, 56, 57]). But as mentioned in Section 1.2.8, that initial version of the Fermi breakup model had some problems and crashed our codes in some cases. To avoid unphysical results and code crashes, we chose the expedient of using $A_{Fermi} = 12$ in both CEM and LAQGSM. Later, we fixed the problems in the

Fermi break-up model, but did not at that time change the value of A_{Fermi}, and never studied how its value affects the final results calculated in these codes. We address this here, calculating spectra of emitted particles and light fragments, and yields of all possible products from various reactions using different values for A_{Fermi}. We discuss below separately product cross sections (Section 2.2) and spectra of particles and light fragments (Section 2.3).

2.2 FRAGMENT PRODUCTION CROSS SECTIONS

One of the most difficult tasks for any theoretical model is to predict cross sections of arbitrary products as functions of the incident energy of the projectiles initiating the reactions, *i.e.*, excitation functions. Therefore, we chose to start our study with comparing the available experimental data on excitation functions of products from several proton-induced reactions on light nuclei at intermediate energies with predictions by MCNP6 using its default event generator for such reactions, CEM03.03, as well as with results calculated by CEM03.03 used as a stand-alone code.

Figs. 2.1–2.14 present examples of excitation functions for all products we found at least several measured values for proton-induced reactions on ^{14}N, ^{16}O, ^{27}Al, and ^{28}Si. To understand better the reasons of agreements or disagreements of calculated values with the measured excitation functions, we present in our figures also the total reaction cross sections, experimental and theoretical.

Figs. 2.1–2.4 show our results for the p + ^{14}N reaction. The first thing to note is that the total reaction cross sections simulated with MCNP6 and shown in the upper-left plot in Fig. 2.1 with small solid circles agree well with the available experimental data (symbols) and with calculations by CEM03.03 used as a stand-alone code (solid line). There is a difference between the models, especially in the regions of incident proton energies $T_p = 50 - 100$ MeV and $T_p \geq 2$ GeV. To be expected, since MCNP6 and CEM03.03 use very similar, but slightly different approximations for the total proton-nucleus reaction cross sections (see details and references in [4, 19]). These little differences in the total reaction cross sections will produce, respectively, similar differences in all excitation functions simulated with MCNP6 and CEM03.03.

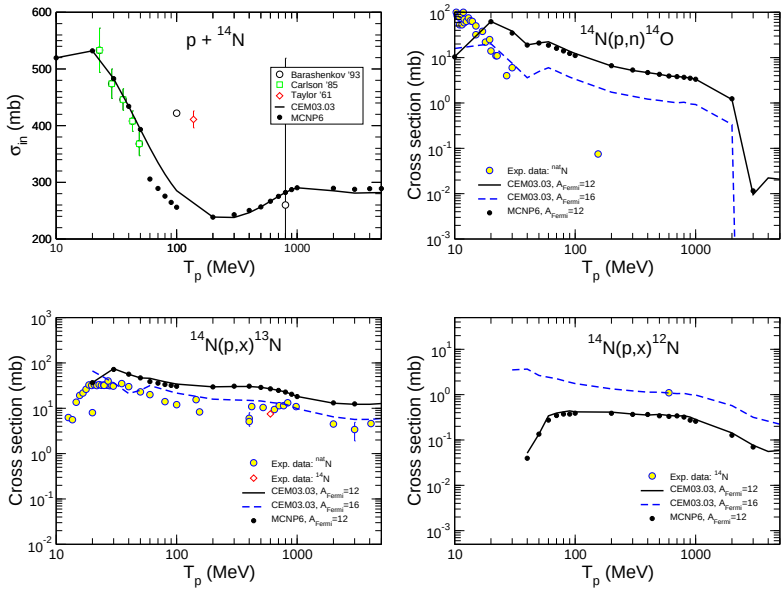

FIGURE 2.1: Total inelastic cross section and excitation functions for the production of ^{14}O, ^{13}N, and ^{12}N from p + ^{14}N calculated with CEM03.03 using the "standard" version of the Fermi breakup model ($A_{Fermi} = 12$) and with a cut-off value of 16 for A_{Fermi}, as well as with MCNP6 using CEM03.03 ($A_{Fermi} = 12$) compared with experimental data, as indicated. Experimental data for inelastic cross sections are from Refs. [65, 66, 67], while the data for excitation functions are from the T16 Lib compilation [68].

The total reaction cross sections are based on systematics (see details and references in [4, 19]), therefore they do not depend on the value of A_{Fermi} we use in our calculations. However, we performed calculations of all excitation functions shown in Figs. 2.1–2.4 with CEM03.03 used as a stand-alone code with its "default value" $A_{Fermi} = 12$, as well as with a modification of the code using $A_{Fermi} = 16$, which in case of these p + ^{14}N reactions, actually corresponds to $A_{Fermi} = 14$. We cannot get a mass number A = 16 from p + ^{14}N interactions, and even a nucleus with $A = 15$ would not be produced by the INC of CEM03.03 at these intermediate energies.

First, from the results presented in Figs. 2.1–2.4, we see a very good agreement between the excitation functions simulated by MCNP6 using CEM03.03 and calculations by CEM03.03 used as a stand-alone code, and a reasonable agreement with most of available experimental data. This fact serves as a validation and verification (V&V) of MCNP6 and shows no problems with the implementation of CEM03.03 in MCNP6 or with the simulations of these reactions by either code.

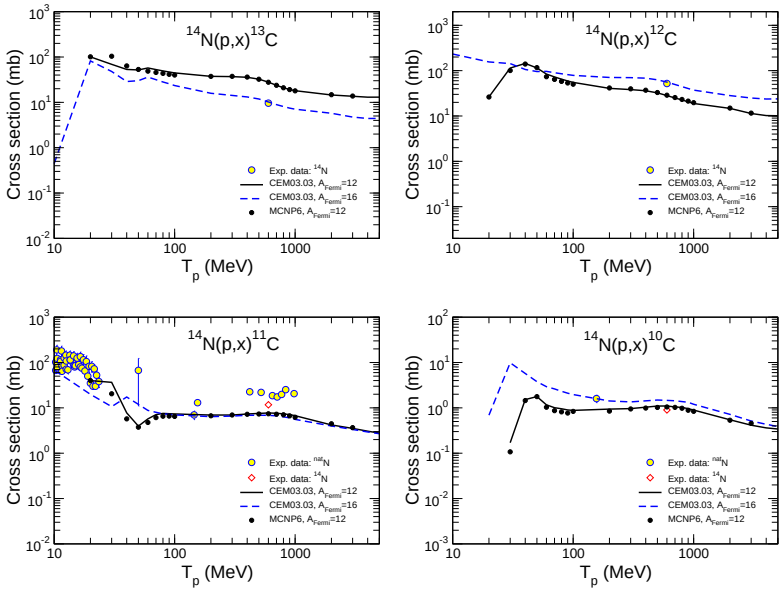

FIGURE 2.2: Excitation functions for the production of ^{13}C, ^{12}C, ^{11}C, and ^{10}C from p + ^{14}N calculated with CEM03.03 using the "standard" version of the Fermi breakup model ($A_{Fermi} = 12$) and with a cut-off value of 16 for A_{Fermi}, as well as with MCNP6 using CEM03.03 ($A_{Fermi} = 12$) compared with experimental data, as indicated. Experimental data are from the T16 Lib compilation [68].

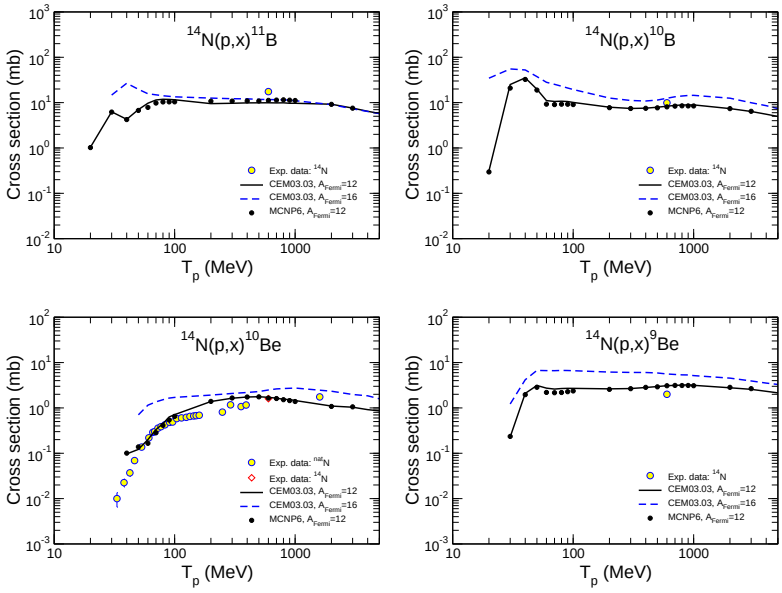

FIGURE 2.3: The same as in Fig. 2.2, but for the production of ^{11}B, ^{10}B, ^{10}Be, and ^{9}Be.

Second, we'd like to explicitly inform the readers that we do not worry too much about some observed discrepancies between some calculated excitation functions and

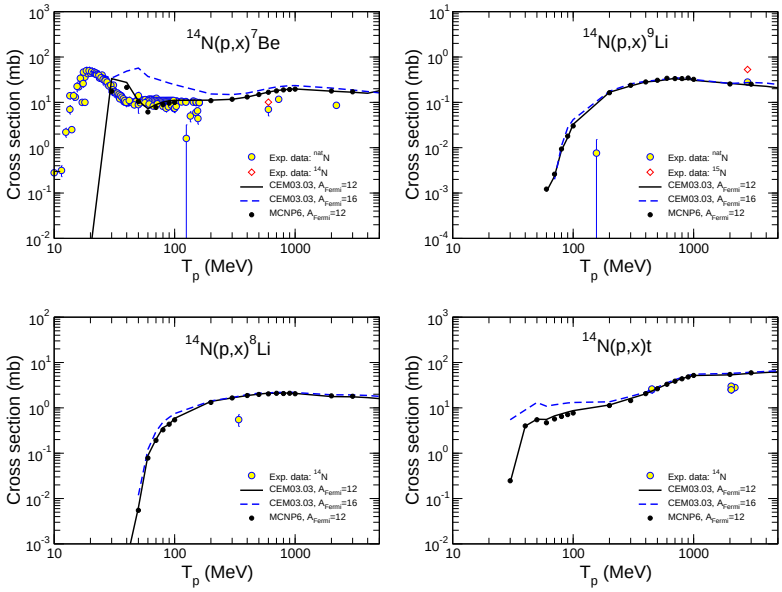

FIGURE 2.4: The same as in Fig. 2.2, but for the production of ^{7}Be, ^{9}Li, ^{8}Li, and t.

measured data at low energies, below 20 MeV. As the default, MCNP6 uses data libraries at such low energies and never uses CEM03.03 or its other event generators, if data libraries are available (MCNP6 has proton-induced data libraries for the reactions studied here). By contrast, CEM uses its INC to simulate the first stage of nuclear reactions, and the INC is not supposed to work properly at such low energies (see details in [19, 2]).

Third, results calculated both with $A_{Fermi} = 12$ and 16 agree reasonably well with available data, taking into account that all calculations, at all energies and for all reactions were done with the fixed version of our codes, without any tuning or changing of any parameters. However, in some cases, we can observe significant differences between excitation functions calculated with $A_{Fermi} = 12$ and 16.

For this particular reaction, the excitation functions for the production of ^{14}O, ^{13}N, ^{12}N, ^{13}C, ^{12}C, and ^{10}C calculated with $A_{Fermi} = 16$ (that for our p + ^{14}N reaction is the same as $A_{Fermi} = 14$, which from a physical point of view means that we use only Fermi breakup after INC and never use preequilibrium and/or evaporation models to calculate this reaction) agree better with available experimental data than results obtained with $A_{Fermi} = 12$. On the other hand, excitation functions for the production of ^{9}Be and ^{7}Be are reproduced better with $A_{Fermi} = 12$.

Figs. 2.5–2.8 present results similar to the ones shown in Figs. 2.1–2.4, but for the reaction p + ^{16}O. Most of the experimental data for these reactions were measured on ^{nat}O, with only a few data points obtained for ^{16}O; all our calculations were performed for ^{16}O. For these reactions, we performed three sets of calculations, using $A_{Fermi} = 12$, 14, and 16 in CEM03.03. The general agreement/disagreement of our results with available measured data for oxygen is very similar to what we showed above for p + ^{14}N, with the major difference that almost all products from oxygen are better predicted with $A_{Fermi} = 14$; production of ^{11}B is described a little better with $A_{Fermi} = 16$, while ^{9}Be and ^{7}Be are reproduced better with $A_{Fermi} = 12$, just as for nitrogen (see Figs. 2.3 and 2.4).

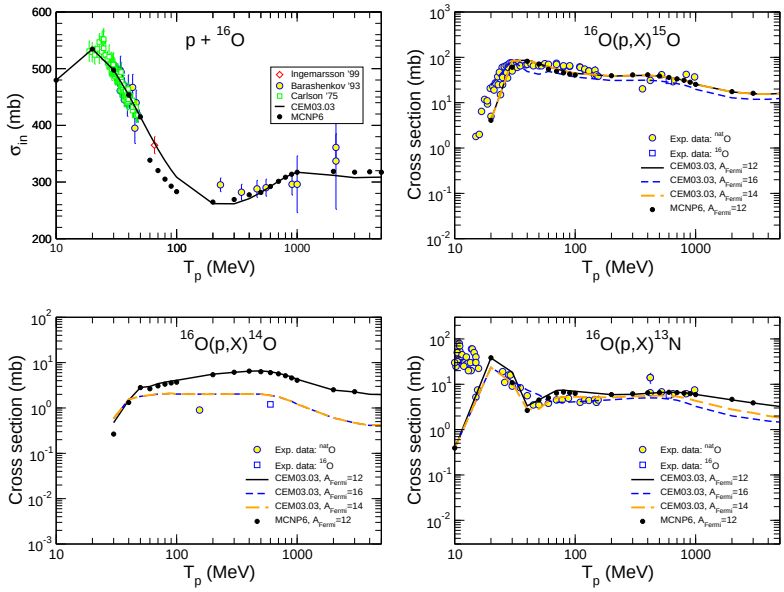

FIGURE 2.5: Total inelastic cross section and excitation functions for the production of ^{15}O, ^{14}O, and ^{13}N from p + ^{16}O calculated with CEM03.03 using the "standard" version of the Fermi breakup model ($A_{Fermi} = 12$) and with cut-off values for A_{Fermi} of 16 and 14, as well as with MCNP6 using CEM03.03 ($A_{Fermi} = 12$) compared with experimental data, as indicated. Experimental data for inelastic cross sections are from Refs. [65, 69, 70], while the data for excitation functions are from the T16 Lib compilation [68].

Figs. 2.9–2.14 show results similar to those in Figs. 2.1–2.8, but for proton interactions with ^{27}Al and ^{28}Si. All reactions on silicon were calculated for ^{28}Si, while most of the data were measured from ^{nat}Si (see details in legends of Fig. 2.13). Aluminum and silicon are interesting because they are used in many applications. From a

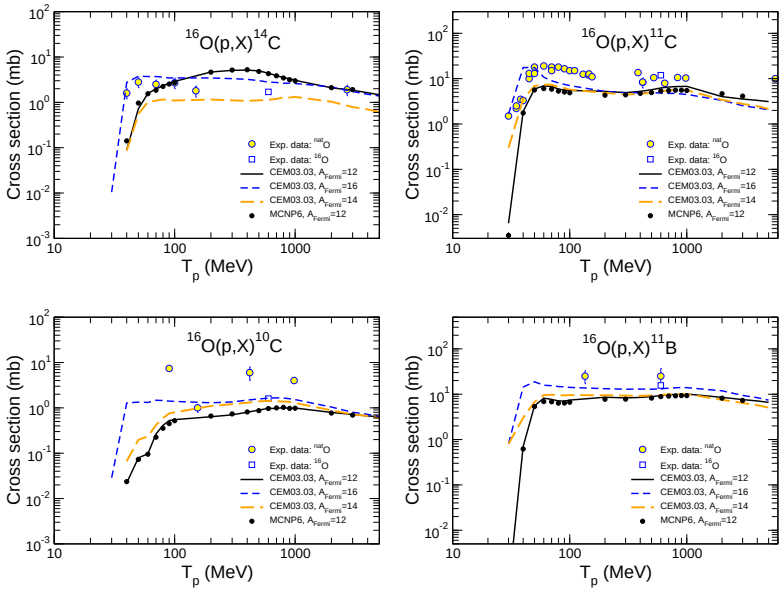

FIGURE 2.6: Excitation functions for the production of ^{14}C, ^{11}C, ^{10}C, and ^{11}B from p + ^{16}O calculated with CEM03.03 using the "standard" version of the Fermi breakup model ($A_{Fermi} = 12$) and with cut-off values for A_{Fermi} of 16 and 14, as well as with MCNP6 using CEM03.03 ($A_{Fermi} = 12$) compared with experimental data, as indicated. Experimental data are from the T16 Lib compilation [68].

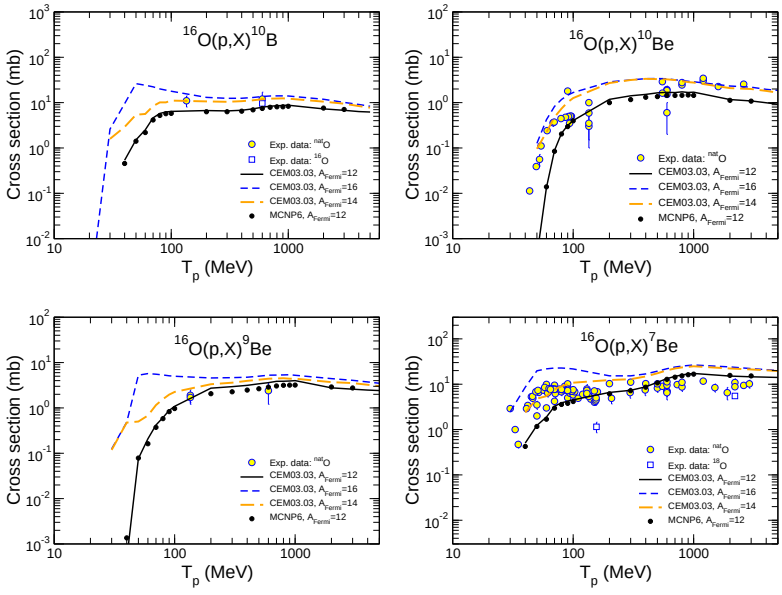

FIGURE 2.7: The same as in Fig. 2.6, but for the production of ^{10}B, ^{10}Be, ^{9}Be, and ^{7}Be.

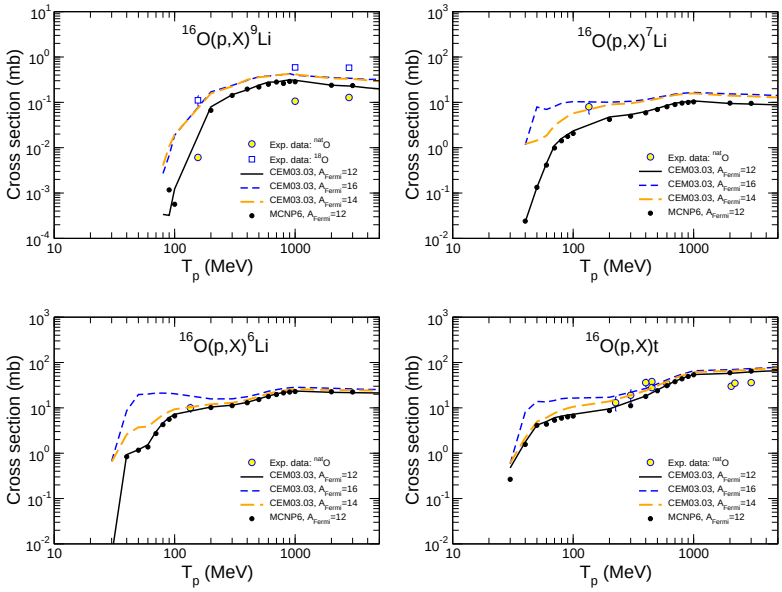

FIGURE 2.8: The same as in Fig. 2.6, but for the production of ^{9}Li, ^{7}Li, ^{6}Li, and t.

theoretical point of view, p + ^{27}Al and ^{28}Si reactions are challenging because Al and Si are relatively light, with significant contributions from the Fermi breakup models in our simulations. At the same time Al and Si have mass numbers higher than the discussed above, allowing some significant contribution to the calculated values from preequilibrium and evaporation processes. On the whole, the agreement of the results with available measured data for Al and Si is very similar to what we find for N and O.

In many cases, we get a better description of the heavy fragments when we use $A_{Fermi} = 16$ or 14, and usually we predict a little better the light fragments using $A_{Fermi} = 12$. For comparison, for Al and Si, we show also excitation functions for the production of all complex particles from d to ^{4}He, as well as of secondary protons, as we found experimental data available for them. Because the absolute values of the yields of light fragment production is much lower compared to the yields of complex particles, and especially of protons, the production cross sections of d, t, ^{3}He, ^{4}He, and especially of p calculated with different values of A_{Fermi} are very close to each other. This is true also for the production of neutrons; although we do not have experimental data for neutron production for these reactions. Generally, emission of nucleons and complex particles are the most determinative in the calculation of

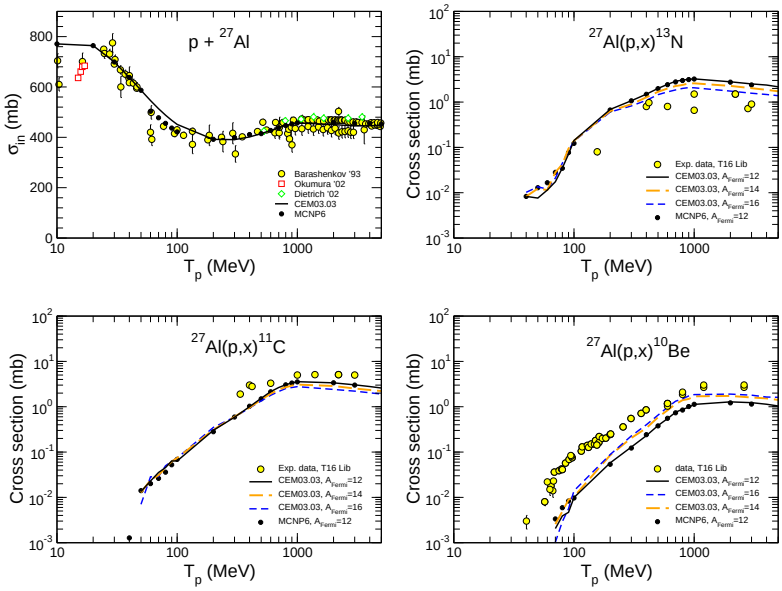

FIGURE 2.9: Total inelastic cross section and excitation functions for the production of ^{13}N, ^{11}C, and ^{10}Be, from p + ^{27}Al calculated with CEM03.03 using the "standard" version of the Fermi breakup model ($A_{Fermi} = 12$) and with cut-off values for A_{Fermi} of 16 and 14, as well as with MCNP6 using CEM03.03 ($A_{Fermi} = 12$) compared with experimental data, as indicated. Experimental data for inelastic cross sections are from Refs. [65, 71, 72], while the data for excitation functions are from the T16 Lib compilation [68].

spallation products (heavier residuals) from reactions on medium-mass nuclei, while LF yields are generally low, and their calculation does not affect significantly the final cross sections for these heavier products.

Figs. 2.15 and 2.16 show mass-number dependences of the yield of H, He, Li, Be, B, C, N, and O isotopes produced in 600 MeV p + ^{16}O, with a comparison of our CEM results calculated with $A_{Fermi} = 12$ and 16 with measured data from Ref. [73]. There is a relatively good agreement of both values of A_{Fermi}, which does not allow us to choose a preferred value. The yields of ^{11}B, ^{12}B, and ^{14}O with $A_{Fermi} = 16$ agree better with the data, while that of ^{12}N is predicted better using $A_{Fermi} = 12$.

Fig. 2.17 shows an example of one more type of nuclear reaction characteristic: Atomic-number dependence of the fragment-production cross sections from the interactions of ^{20}Ne (600 MeV/nucleon) with H. For this reaction, besides experimental data from Ref. [74, 75], we compare to results calculated with CEM03.03 used as a stand-alone code with $A_{Fermi} = 12$ and 16, results by MCNP6 using the CEM03.03

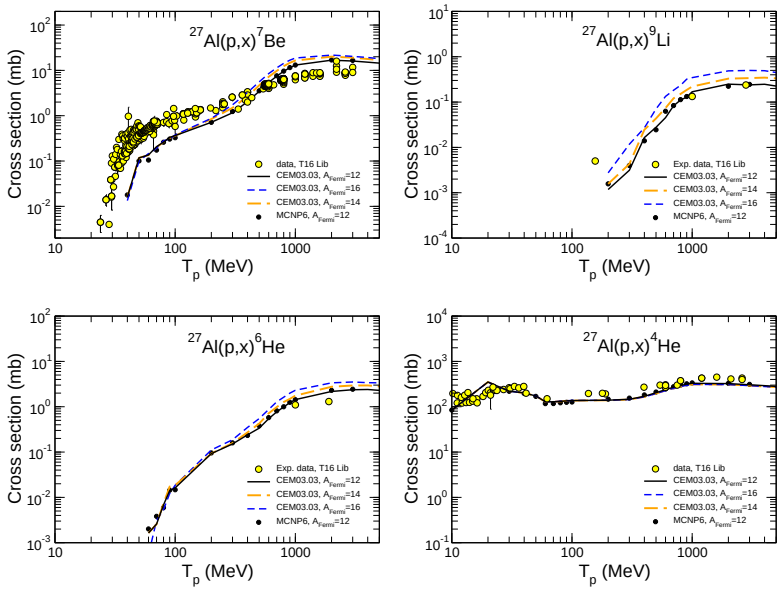

FIGURE 2.10: Excitation functions for the production of ^{7}Be, ^{9}Li, ^{6}He, and ^{4}He from p + ^{27}Al calculated with CEM03.03 using the "standard" version of the Fermi breakup model ($A_{Fermi} = 12$) and with cut-off values for A_{Fermi} of 16 and 14, as well as with MCNP6 using CEM03.03 ($A_{Fermi} = 12$) compared with experimental data, as indicated. Experimental data are from the T16 Lib compilation [68].

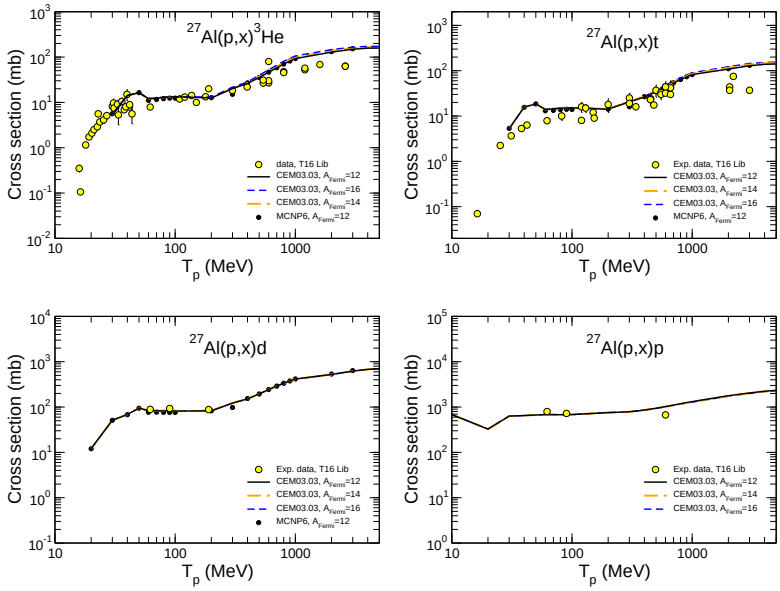

FIGURE 2.11: The same as in Fig. 2.10, but for the production of ^{3}He, t, d, and p.

event generator with $A_{Fermi} = 12$, as well as results by the NASA semi-empirical nuclear fragmentation code NUCFRG2 [76], and by a parameterization by Nilsen et al. [77] taken from Tab. III of Ref. [75].

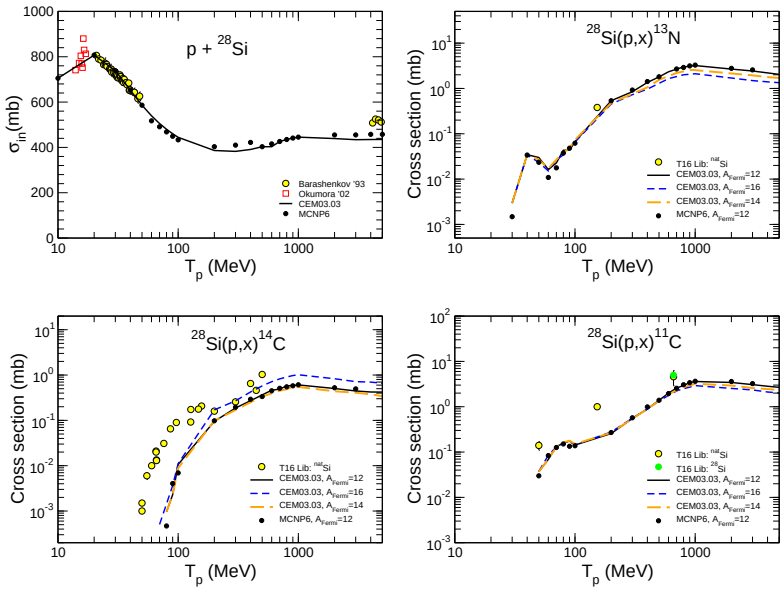

FIGURE 2.12: Total inelastic cross section and excitation functions for the production of ^{13}N, ^{14}C, and ^{11}C, from p + ^{28}Si calculated with CEM03.03 using the "standard" version of the Fermi breakup model ($A_{Fermi} = 12$) and with cut-off values for A_{Fermi} of 16 and 14, as well as with MCNP6 using CEM03.03 ($A_{Fermi} = 12$) compared with experimental data, as indicated. Experimental data for inelastic cross sections are from Refs. [65, 71], while the data for excitation functions are from the T16 Lib compilation [68].

We see that all models agree quite well with the measured data, especially for LF with $Z > 4$. For LF with $Z > 4$, it is difficult to determine from which version of CEM03.03 results agree better with the data: the one using $A_{Fermi} = 12$ or the one with $A_{Fermi} = 16$. Light fragments with $Z = 3$ and 4 are described a little better with the $A_{Fermi} = 12$ version. As we discuss at the end of the next Section, preequilibrium emission described with an extended version of the MEM (not accounted for in our calculations shown in Fig. 18), can be important and may change the final CEM results for this reaction; therefore we are not ready to make a final decision about which version of the Fermi breakup model works better for this system.

All the examples in Figs. 2.1 to 2.17 are for reactions induced by protons, which at such relatively low incident energies are simulated by default in MCNP6 with CEM03.03. Figs. 2.18 and 2.19 show examples of nucleus-nucleus reactions with light nuclei, *i.e.*, involving the Fermi breakup model, but simulated in MCNP6 with LAQGSM03.03. The figures compare experimental [74, 75] Z-dependences of prod-

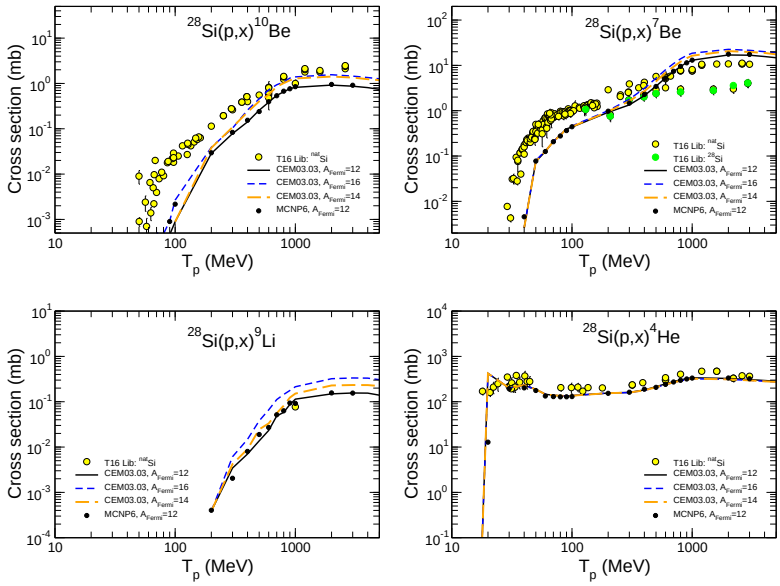

FIGURE 2.13: Excitation functions for the production of ^{10}Be, ^{7}Be, ^{9}Li, and ^{4}He from p + ^{28}Si calculated with CEM03.03 using the "standard" version of the Fermi breakup model ($A_{Fermi} = 12$) and with cut-off values for A_{Fermi} of 16 and 14, as well as with MCNP6 using CEM03.03 ($A_{Fermi} = 12$) compared with experimental data, as indicated. Experimental data are from the T16 Lib compilation [68].

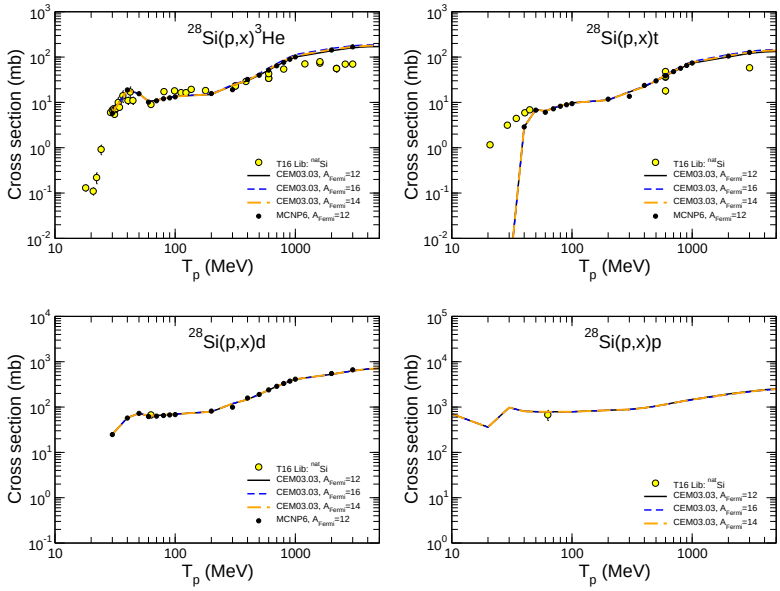

FIGURE 2.14: The same as in Fig. 2.13, but for the production of ^{3}He, t, d, and p.

ucts from interactions of 290 MeV/nucleon ^{14}Ne and ^{16}O with C and Al; 600 MeV/nucleon ^{20}Ne with C and Al; and 400 MeV/nucleon ^{24}Mg with C and Al with LAQGSM03.03 results using $A_{Fermi} = 12$ and 16, as well as with results of calculations using models of Refs. [76, 77, 78], in the case of 600 MeV/nucleon ^{20}Ne + C and Al.

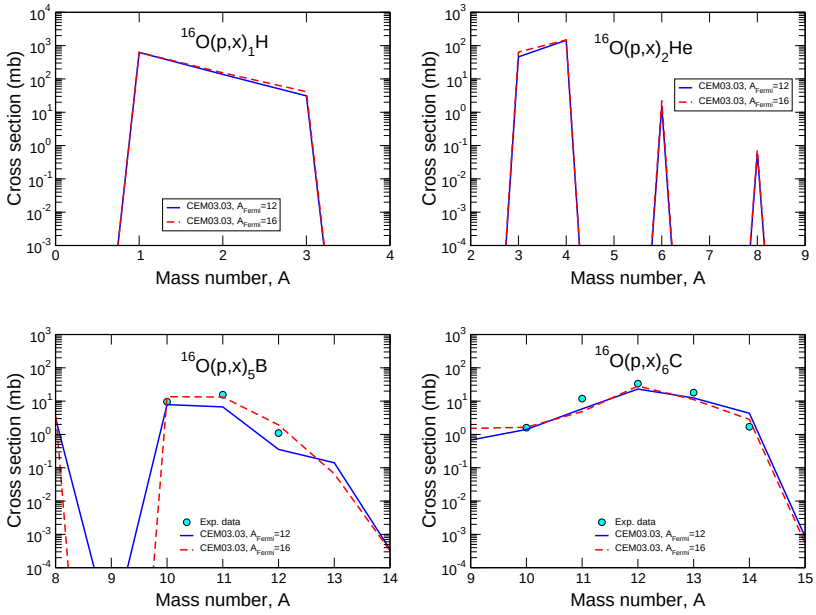

FIGURE 2.15: Examples of measured particle and LF production cross sections from p + ^{16}O at 600 MeV [73] (symbols) compared with our CEM results for a Fermi breakup cut-off of $A \leq 16$ and $A \leq 12$, as indicated. All the LF from these reactions are calculated by CEM either as final products (residual nuclei) after all possible stages of reaction or via Fermi breakup after INC (Fermi breakup is used for nuclei with $A < 13$ or $A < 17$ instead of using preequilibrium emission and/or evaporation of particles).

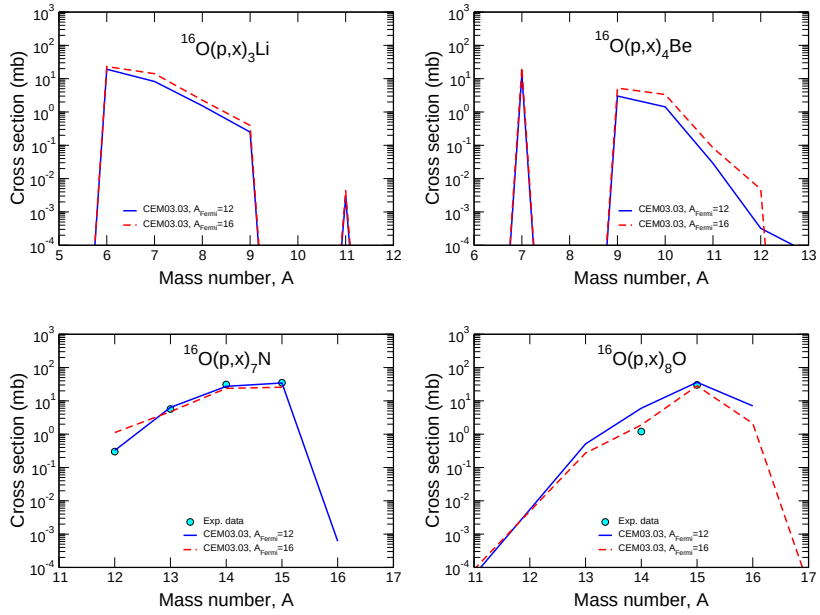

FIGURE 2.16: The same as in Fig. 2.15, but for the production of Li, Be, N, and O isotopes.

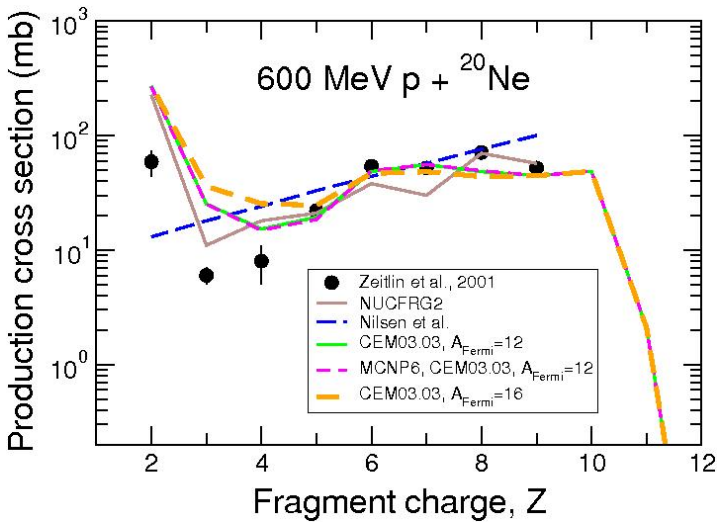

FIGURE 2.17: Atomic-number dependence of the fragment-production cross sections from the interactions of ^{20}Ne of 600 MeV/nucleon with H. Experimental data (circles) are by Zeitlin et al. [75]. For comparison, results by the NASA semi-empirical nuclear fragmentation code NUCFRG2 [76], and from a parameterization by Nilsen et al. [77] taken from Tab. III of Ref. [75] are shown as well, as indicated. Our results by CEM03.03 using the "standard" version of the Fermi breakup model ($A_{Fermi} = 12$) and $A_{Fermi} = 16$, as well as MCNP6 calculations using CEM03.03 ($A_{Fermi} = 12$) are plotted with different lines, as indicated.

The cross sections shown in Figs. 2.18 and 2.19 are only for the fragmentation of the projectile-nuclei ^{14}N, ^{16}O, ^{20}Ne, and ^{24}Mg; they do not contain contributions from the fragmentation of the C and Al target-nuclei. For all calculations using all models general agreement to the experimental data is quite good. On the whole, for these particular reactions, the products with $Z = 3$ and 4 are described a little better with the $A_{Fermi} = 12$ version of LAQGSM, while heavier fragments are often predicted better with $A_{Fermi} = 16$.

2.3 FRAGMENT SPECTRA

This Section presents several examples of particle and LF spectra from various proton- and nucleus-induced reactions, chosen so that although all of them are fragmentation of light nuclei at intermediate energies, they address different reaction mechanisms of fragment production, sometimes involving several mechanisms in the production of the same LF in a given reaction.

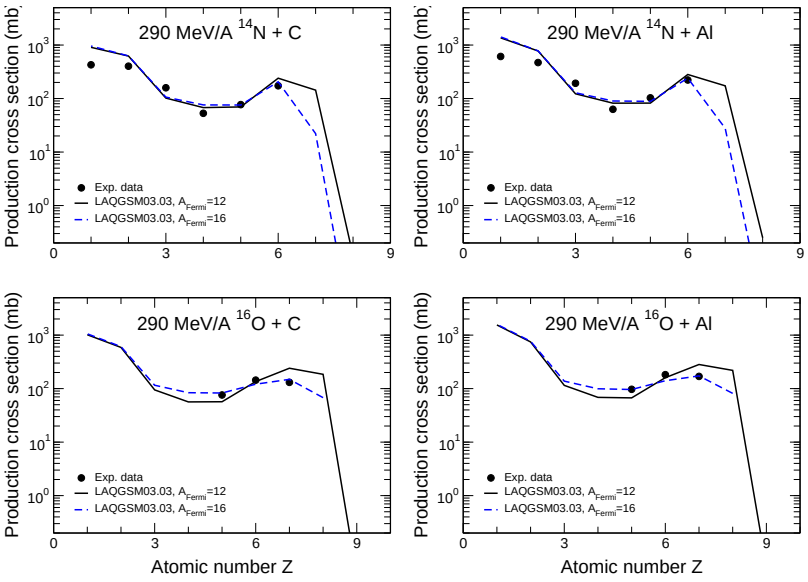

FIGURE 2.18: Atomic-number dependence of the fragment-production cross sections from the interactions of 290 MeV/nucleon ^{14}Ne and ^{16}O with C and Al. Experimental data (circles) are by Zeitlin et al. [74]. Our results by LAQGS03.03 using the "standard" version of the Fermi breakup model ($A_{Fermi} = 12$) are shown with solid lines, and for a cut-off value for A_{Fermi} of 16, with dashed lines, as indicated.

Figs. 2.20 to 2.22 show examples of measured particle and LF double-differential spectra from p + ^{9}Be at 190 and 300 MeV [79], as well as at 392 MeV [43] (symbols) compared with our CEM results (histograms). Because ^{9}Be has a mass number $A < A_{Fermi} = 12$, all the LF from these reactions are calculated by CEM either as fragments from the Fermi breakup of the excited nuclei remaining after the initial INC stage of reactions, or as "residual nuclei" after emission during INC of several particles from the ^{9}Be target nucleus. No preequilibrium or/and evaporation mechanisms are considered for these reactions by CEM. There is quite a good agreement of the CEM predictions with the measured spectra from ^{9}Be for all products shown in this example: protons (300 MeV p + Be), complex particles (t from 300 MeV p + Be and ^{3}He and ^{4}He from 190 and 392 MeV p + Be), and heavier ^{6}He to ^{7}Be.

Fig. 2.23 shows examples of similar LF spectra from a carbon nucleus, where only INC and Fermi breakup reaction mechanisms are considered by our CEM. CEM produces He and Li from these reaction via Fermi breakup after INC, while Be and B are probably produced as residual nuclei after emitting several nucleons during INC from the carbon target nucleus. The general agreement of the CEM predictions

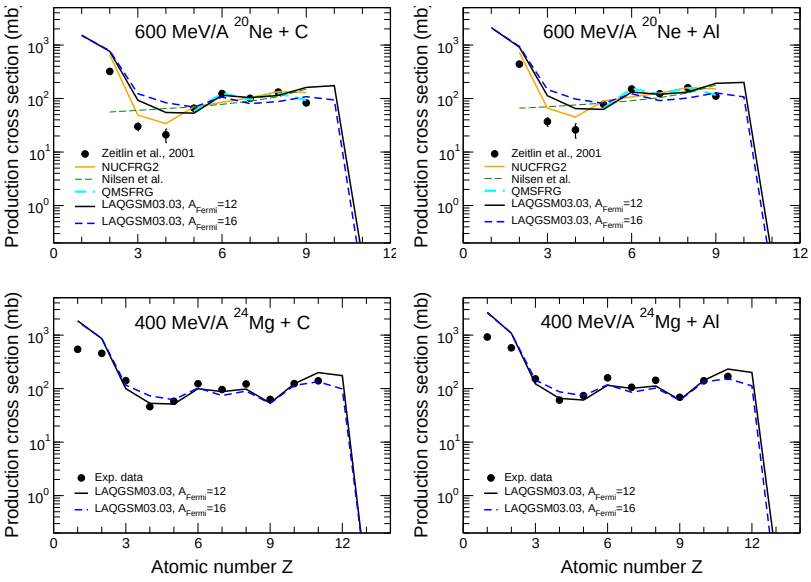

FIGURE 2.19: Atomic-number dependence of the fragment-production cross sections from the interactions of 600 MeV/nucleon ^{20}Ne with C and Al, and 400 MeV/nucleon ^{24}Mg with C and Al. Experimental data (circles) are by Zeitlin et al. [74, 75]. For comparison, at 600 MeV/A, results by the NASA semi-empirical nuclear fragmentation code NUCFRG2 [76] and the microscopic abrasion-ablation model QMSFRG [78], as well as from a parameterization by Nilsen et al. [77] taken from Tabs. III and IV of Ref. [75] are shown with different lines, as indicated. Our results by LAQGS03.03 using the "standard" version of the Fermi breakup model ($A_{Fermi} = 12$) are shown with solid lines, and for a cut-off value for A_{Fermi} of 16, with dashed lines, as indicated.

with these measured LF spectra is quite good, taking into account that no fitting or changing of any parameters in CEM was done; we used the fixed version of CEM03.03 as implemented in MCNP6.

Fig. 2.24 shows similar examples of LF spectra, namely, double-differential spectra at 45 degrees of Li, Be, B, and C from ^{14}N and ^{16}O nuclei bombarded with 70 MeV protons. With these higher mass numbers, we performed calculations with CEM03.03 using also $A_{Fermi} = 14$ and 16, to see how different values affect the final LF spectra. The general agreement of our CEM results with these LF spectra is reasonably good, but not quite as good as seen in Figs. 2.20 to 2.23. On the whole, for these particular reactions, CEM03.03 provides a better agreement with the measured LF spectra with $A_{Fermi} = 12$.

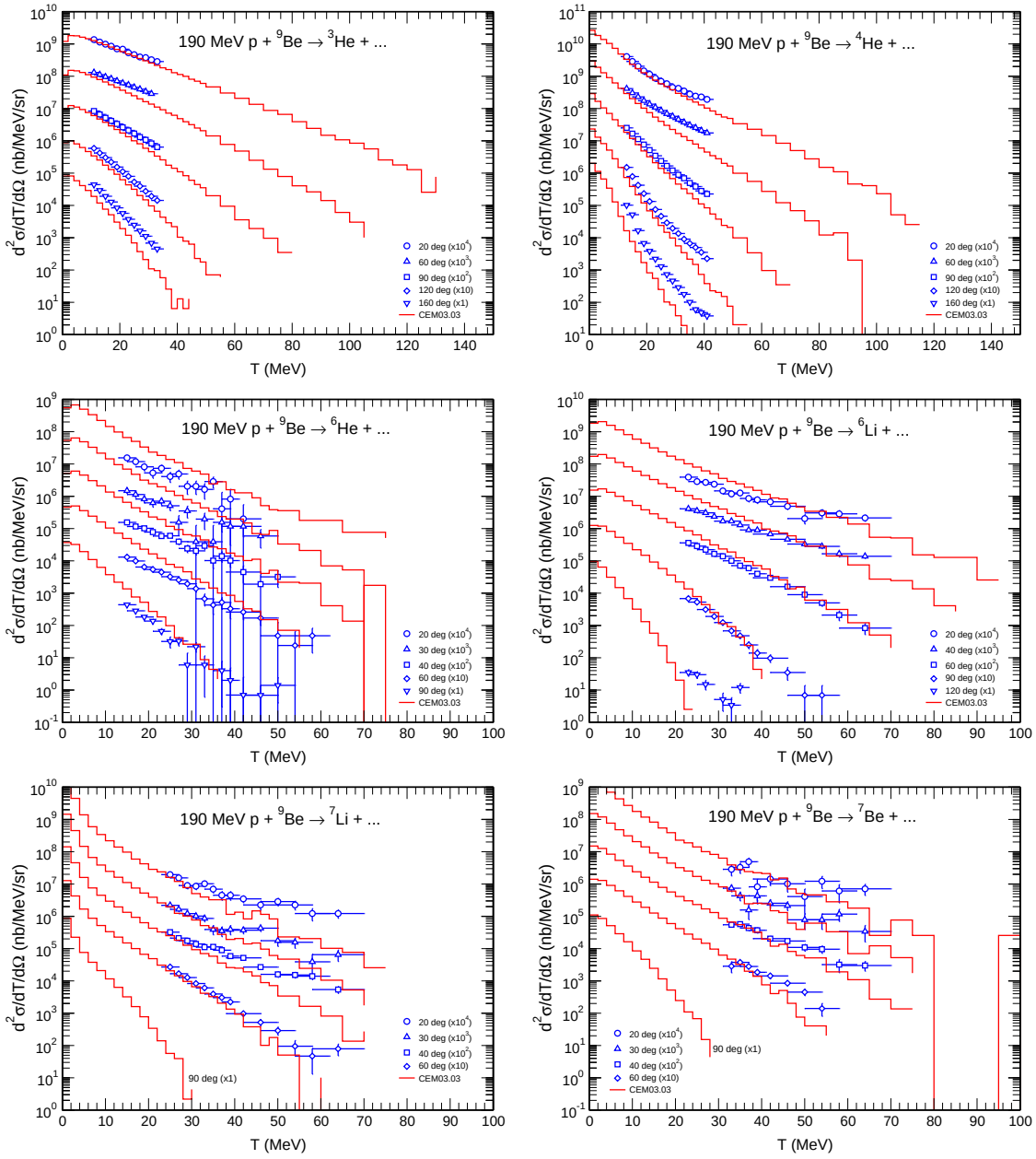

FIGURE 2.20: Examples of measured particle and LF double-differential spectra from p + ^{9}Be at 190 MeV [79], compared with our CEM results (histograms).

2.4 LIMITING FRAGMENTATION

The limiting fragmentation hypothesis, first proposed by Benecke, *et al.*, [82], suggests that fragmentation cross sections reach asymptotic values at sufficiently high incident-projectile energies. That is to say, that, above a given bombarding energy, both the

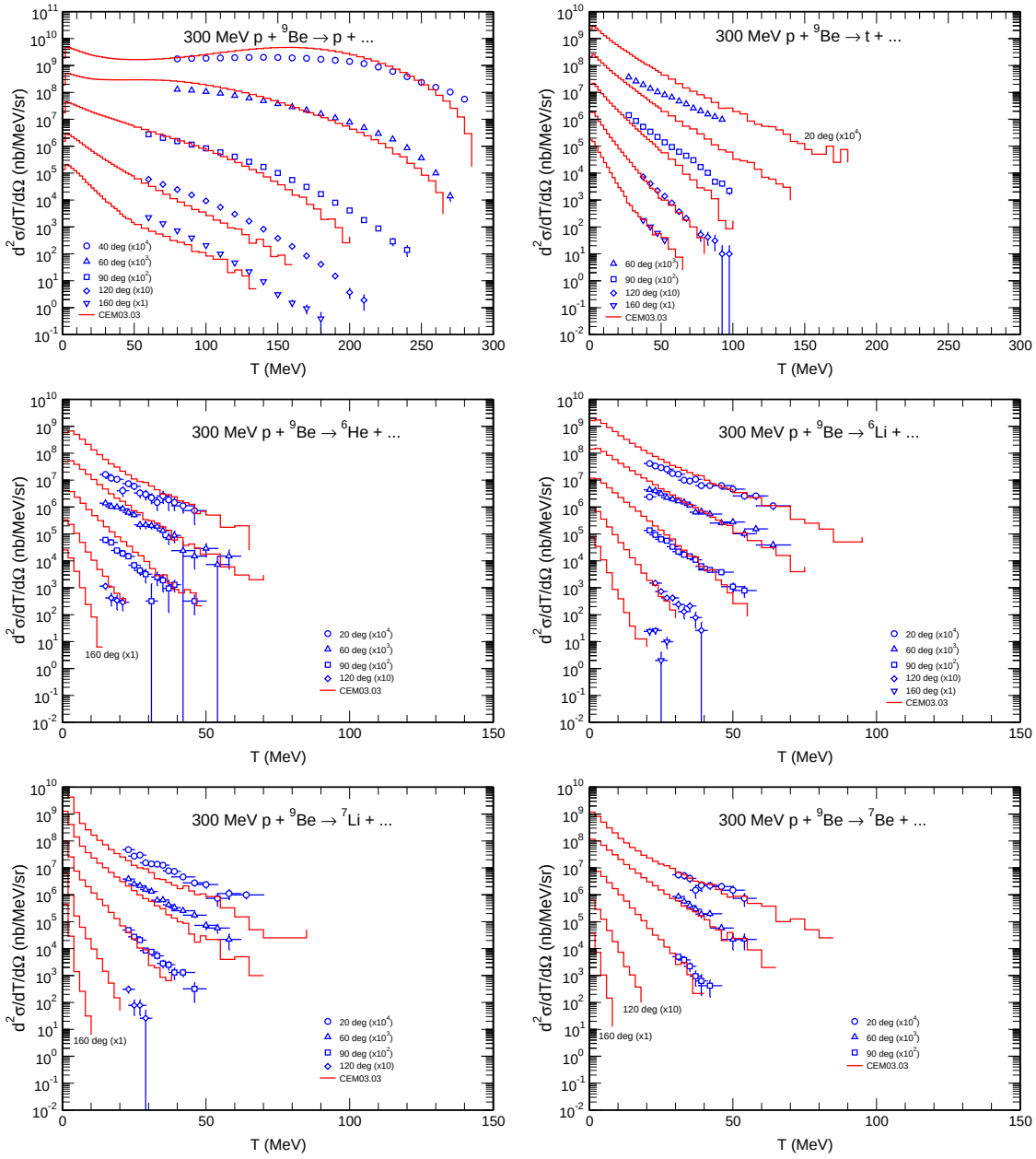

FIGURE 2.21: Examples of measured particle and LF double-differential spectra from p + ^{9}Be at 300 MeV [79], compared with our CEM results (histograms).

differential and total production cross sections remain constant. Figs. 2.25 and 2.26 validate the limiting fragmentation hypothesis.

Fig. 2.25 displays the double differential cross sections for the production of ^{4}He from the reaction 1.2/1.9/2.5 GeV p + ^{12}C. Fig. 2.26 shows the total production cross sections by isotope, from protons to ^{12}N, from the same reactions. We see that the

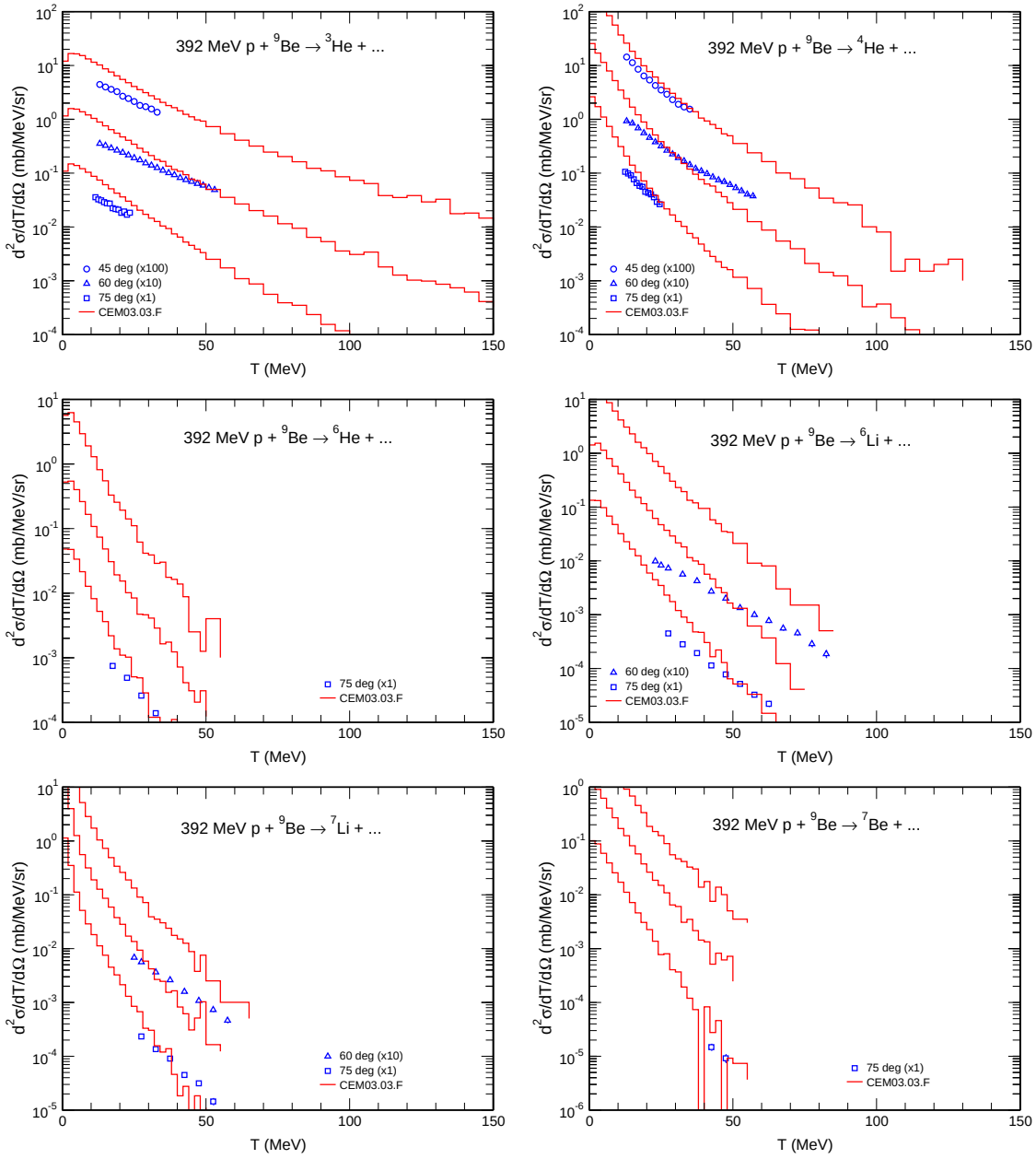

FIGURE 2.22: Examples of measured particle and LF double-differential spectra from p + ^{9}Be at 392 MeV [43], compared with our CEM results (histograms).

fragmentation differential cross sections for ^{4}He are approximately constant across the bombarding energies of 1.2, 1.9, and 2.5 GeV. Limiting fragmentation predicts this constancy. From Fig. 2.1 of M. Fidelus' Ph.D. thesis [83], we expect that, for the production of ^{7}Be, limiting fragmentation will begin at $\sim$ 200 MeV bombarding energy, for this case of protons incident on ^{12}C. ^{4}He is lighter than ^{7}Be, and our

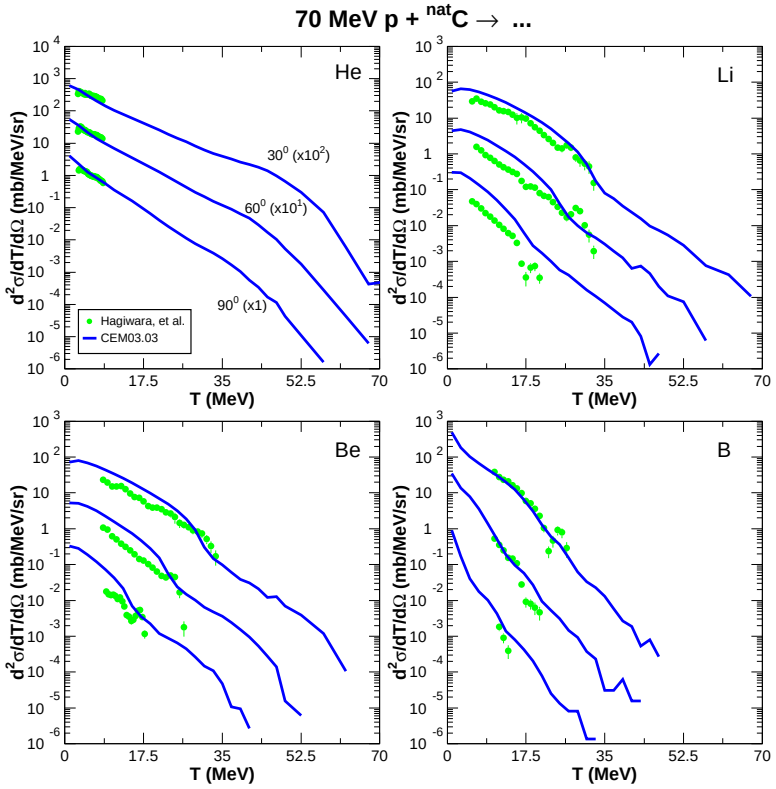

FIGURE 2.23: Comparison of CEM03.03 (solid lines) He, Li, Be, and B spectra from 70 MeV p + C with experimental data by Hagiwara et al. [80] (circles) for a natural carbon target. Our calculations were performed for ^{12}C.

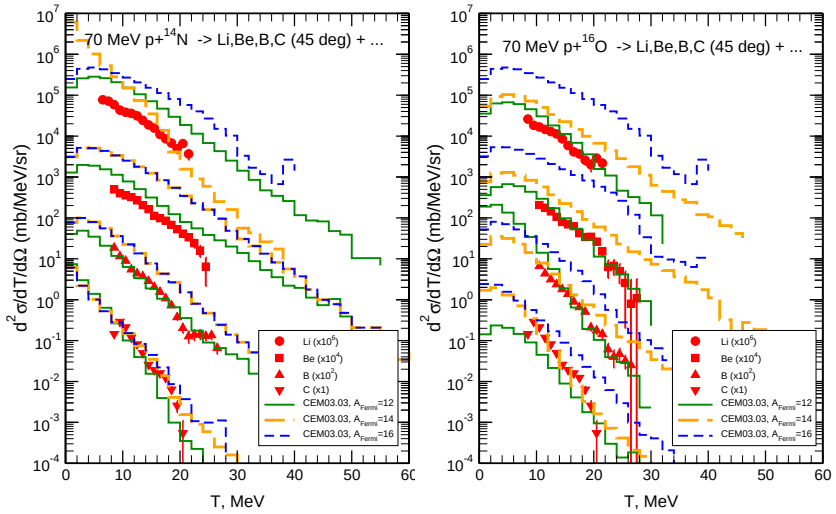

FIGURE 2.24: Comparison of Li, Be, B, and C spectra at 45 degrees from 70 MeV p + ^{14}N and ^{16}O measured by Sanami et al. [81] (symbols) with calculations by CEM03.03 using the "standard" version of the Fermi breakup model ($A_{Fermi} = 12$; solid histograms) and with cut-off values for A_{Fermi} of 16 (dashed histograms) and 14 (long-dashed histograms), as indicated.

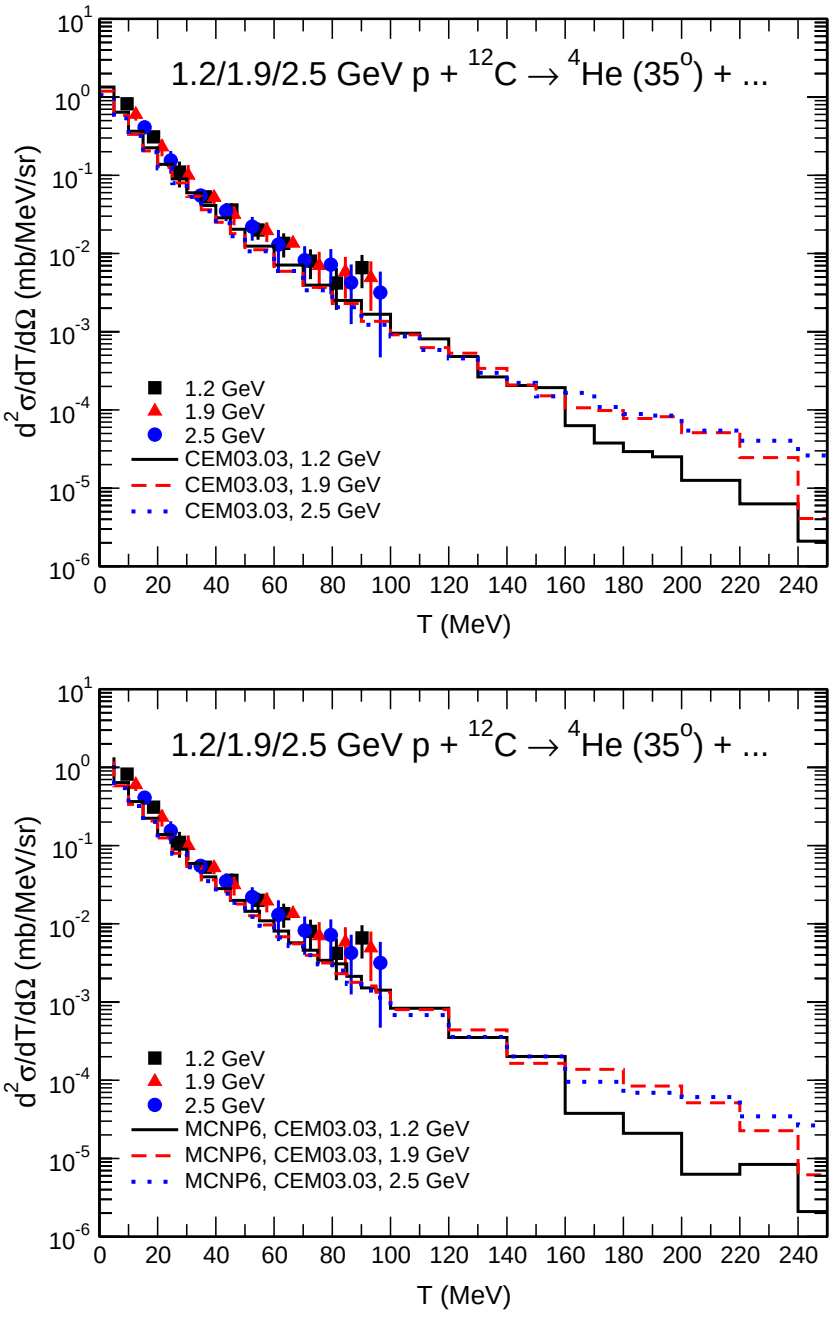

FIGURE 2.25: ^{4}He spectra (at 35°) from 1.2/1.9/2.5 GeV p + ^{12}C measured by M. Fidelus of the PISA collaboration [83] (symbols) with calculations by CEM03.03 (top) and MCNP6 (bottom).

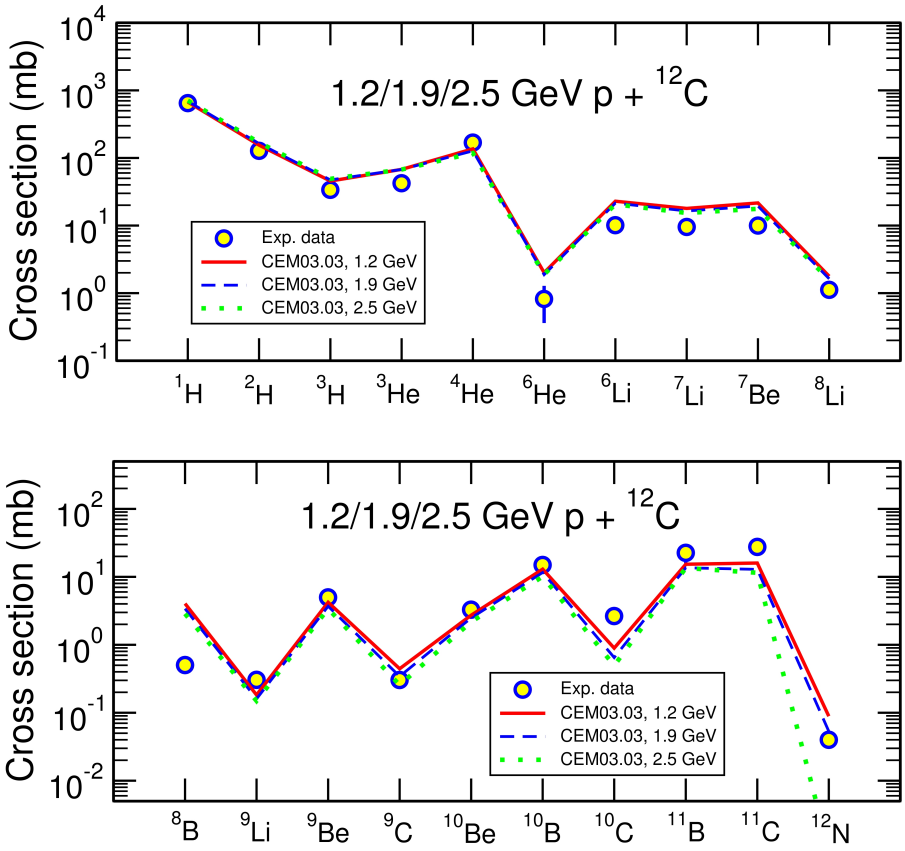

FIGURE 2.26: Total production cross sections by isotope, from protons to ^{12}N, from 1.2/1.9/2.5 GeV p + ^{12}C measured by M. Fidelus of the PISA collaboration [83] (symbols) with calculations by CEM03.03.

bombarding energies are all well above 200 MeV, therefore we expect constancy in differential and total production cross sections. Fig. 2.26 demonstrates constancy of total production cross sections. We see small differences in total production cross sections of the heavier clusters (*i.e.*, ^{10,11}C), which is also in agreement with the limiting fragmentation hypothesis, as heavier emitted fragments would have a higher bombarding energy at which limiting fragmentation occurs.

2.5 CONCLUSION

Various fragmentation reactions induced by protons and light nuclei of energies around 1 GeV/nucleon and below on light target nuclei are studied with the latest Los Alamos Monte Carlo transport code MCNP6 and with its cascade-exciton model (CEM) and Los Alamos version of the quark-gluon string model (LAQGSM) event generators, version 03.03, used as stand-alone codes. On the whole, MCNP6 and its CEM and LAQGSM event generators describe quite well all the reactions we tested here, providing good enough agreement with available experimental data. This is especially important for calculations of cross sections of arbitrary products as functions of incident projectile energies, *i.e.*, excitation functions, one of the most difficult tasks for any nuclear reaction model. Our current results show a good prediction by MCNP6 and CEM03.03, used as a stand-alone code, of a large variety of excitation functions for products from proton-induced reactions on N, O, Al, and Si. An older version of CEM, CEM95, was able to predict reasonably well most excitation functions for medium and heavy nuclei-targets, but had big problems in calculating some excitation functions for light nuclei [84].

CEM and LAQGSM assume that intermediate-energy fragmentation reactions on light nuclei occur generally in two stages. The first stage is the intranuclear cascade (INC), followed by the second, Fermi breakup disintegration of light excited residual nuclei produced after INC. Both CEM and LAQGSM also account for coalescence of light fragments (complex particles) up to ^{4}He from energetic nucleons emitted during INC.

We investigate the validity and performance of MCNP6, CEM, and LAQGSM in simulating fragmentation reactions at intermediate energies. We find that while the fixed "default" versions of CEM03.03 and LAQGSM03.03 in MCNP6 provide reasonably good predictions for all reactions tested here, a fine-tuning of the A_{Fermi} parameter in the Fermi breakup model (and of momentum cut-off parameters in the coalescence model; see next Chapter) may provide a better description of some experimental data.

At the end of this Chapter, let us mention that an independent testing of the Fermi Breakup model used by CEM03.03 and LAQGSM03.03 was performed recently by Konobeyev and Fischer [85] for the Fall 2014 Nuclear Data Week. The authors of Ref. [85] have calculated with MCNP6 using its Bertini [86], ISABEL [87], INCL+ABLA [88, 89], and CEM03.03 event generators [19], as well as with the known TALYS code [90], all the discussed above experimental spectra of ^{3}He and ^{4}He measured in Ref. [79] from the reaction 190 MeV p + ^{9}Be; all spectra of p, d, t, ^{3}He, and ^{4}He from the reaction of 300 MeV p + ^{9}Be [79], as well as all neutron spectra from interactions of 113 MeV protons with ^{9}Be [91] and from 256 MeV p + ^{8}Be [92]. As is often done in the literature, to get quantitative estimations of the agreement/disagreement of the calculated-by-different-models spectra with the measured ones, the authors of Ref. [85] performed a detailed statistical analysis using nine different "Deviation Factors," namely, H, R^{CE}, R^{EC}, $< F >$, S, L, $P_{2.0}$, $P_{10.0}$, and N_x. The definition of each is shown in Fig. 2.27, taken from Ref. [85].

As can be seen from Fig. 2.28, adopted from Ref. [85], the results by CEM03.03 for these particular reactions agree better with the experimental data than all other models tested in Ref. [85]. As ^{9}Be has a mass number of only 9, all these reactions are calculated by CEM03.03 using only the INC followed by the Fermi Breakup model. The best results provided by CEM03.03 in comparison with other models prove that the Fermi Breakup model used by CEM03.03 (and by LAQGSM03.03) in MCNP6 is reliable and can be used with confidence as a good predictive tool for various nuclear applications.

Deviation factors

$$H = \left(\frac{1}{N} \sum_{i=1}^{N} \left(\frac{\sigma_i^{exp} - \sigma_i^{calc}}{\Delta\sigma_i^{exp}} \right)^2 \right)^{1/2},$$

$$R^{CE} = \frac{1}{N} \sum_{i=1}^{N} \frac{\sigma_i^{calc}}{\sigma_i^{exp}}, \qquad R^{EC} = \frac{1}{N} \sum_{i=1}^{N} \frac{\sigma_i^{exp}}{\sigma_i^{calc}},$$

$$< F > = 10^{\left(\frac{1}{N} \sum_{i=1}^{N} \left[\log(\sigma_i^{exp}) - \log(\sigma_i^{calc}) \right]^2 \right)^{1/2}}, \quad \text{(Michel)}$$

$$S = 10^{\left\{ \left(\sum_{i=1}^{N} \left[\frac{\lg(\sigma_i^{exp}) - \lg(\sigma_i^{calc})}{(\Delta\sigma_i^{exp} / \sigma_i^{exp})} \right]^2 \right) \left(\sum_{i=1}^{N} \left[\frac{\sigma_i^{exp}}{(\Delta\sigma_i^{exp})} \right]^2 \right)^{-1} \right\}^{1/2}} \quad \text{(similar to <F> with experimental error)}$$

$$L = \left[\sum_{i=1}^{N} \left(\sigma_i^{calc} / \Delta\sigma_i^{exp} \right)^2 \left((\sigma_i^{calc} - \sigma_i^{exp}) / \sigma_i^{calc} \right)^2 \Big/ \sum_{i=1}^{N} \left(\sigma_i^{calc} / \Delta\sigma_i^{exp} \right)^2 \right]^{1/2}, \quad \text{(Leeb)}$$

$$P_x = N_x/N, \qquad N_x : \; 1/x < \sigma_i^{calc} / \sigma_i^{exp} < x$$

NEA Nuclear data week. November 24-28, 2014 21

FIGURE 2.27: Definitions of the nine different "Deviation Factors," namely, H, R^{CE}, R^{EC}, $< F >$, S, L, $P_{2.0}$, $P_{10.0}$, and N_x, used in the statistical analysis by Konobeyev, *et al.* [85].

All combinations x_i^{calc} / x_i^{exp}

Factor	Bertini	ISABEL	INCL4	CEM	TALYS
H	47.	49.	55.	40.	86.
R^{CE}	0.72	0.83	1.28	0.84	2.01
R^{EC}	74.	81.	39.	43.	45.
<F>	5.7	5.9	4.3	3.3	7.9
L	0.59	0.58	0.57	0.51	0.82
S	3.1	3.3	2.1	2.1	13.0
$P_{2.0}$	0.57	0.56	0.67	0.69	0.37
$P_{10.0}$	0.89	0.88	0.92	0.94	0.83
N	1216	1184	1251	1246	1254

CEM: best results

NEA Nuclear data week. November 24-28, 2014 22

$0.01 < x_i^{calc} / x_i^{exp} < 100$

Factor	Bertini	ISABEL	INCL4	CEM	TALYS
H	47.	49.	55.	40.	85.
R^{CE}	0.75	0.86	1.3	0.85	2.1
R^{EC}	4.2	4.2	2.9	3.1	4.7
<F>	3.5	3.5	2.8	2.7	4.6
L	0.59	0.58	0.57	0.51	0.79
S	2.8	2.8	1.9	2.0	6.5
$P_{2.0}$	0.59	0.58	0.68	0.69	0.40
$P_{10.0}$	0.92	0.91	0.95	0.95	0.88
N	1173	1141	1217	1234	1177

CEM: best results

NEA Nuclear data week. November 24-28, 2014 23

FIGURE 2.28: Results of the nine different "Deviation Factors" for the Bertini, ISABEL, INCL+ABLA, CEM03.03, and TALYS models, as reported by Konobeyev, *et al.* [85], for all combinations of x_i^{calc}/x_i^{exp} (top) and for $0.01 < x_i^{calc}/x_i^{exp} < 100$; CEM had the best results.

chapter 3

Coalescence

Below are relevant publications that result from the author's work pertaining to this chapter.

- L.M. Kerby and S.G. Mashnik, Production of Heavy Clusters with an Expanded Coalescence Model in CEM, Transactions of the American Nuclear Society **112** (2015) 577;
- L.M. Kerby and S.G. Mashnik, An Expanded Coalescence Model within the IntraNuclear Cascade of CEM, LANL Report, LA-UR-15-20322 (January 2015);
- S.G. Mashnik and L.M. Kerby, MCNP6 Fragmentation of Light Nuclei at Intermediate Energies, Nuclear Instruments and Methods in Physics Research A **764** (2014) 59; arXiv:1404.7820;
- S. G. Mashnik and L. M. Kerby, MCNP6 Simulation of Light and Medium Nuclei Fragmentation at Intermediate Energies, LA-UR-15-22811, Los Alamos (2015), talk presented at the 12th International Conference on Nucleus-Nucleus Collisions (NN2015), 2015-06-21/2015-06-26 (Catania, Italy);
- S. G. Mashnik, L. M. Kerby, and K. K. Gudima, Fragmentation of Light Nuclei at Intermediate Energies Simulated with MCNP6, LA-UR-15-20953, Los Alamos (2015), Invited to present at the Fifth International Conference on Nuclear Fragmentation "From Basic Research to Applications" (NUFRA2015), 2015-10-04/2015-10-11 (Antalya (Kemer), Turkey).

According to the Cascade Exciton Model (CEM) [1, 2], there are three ways high-energy heavy clusters can be produced. The first way is via coalescence of nucleons produced in the IntraNuclear Cascade (INC). The second way is via the preequilibrium model. The last way is via Fermi breakup. Previous work in CEM examines the impact of expansions of the preequilibrium model and Fermi breakup model on

heavy cluster production [93, 96, 97, 64, 94, 95]. This chapter studies the impact of expanding the coalescence model on heavy cluster emission. CEM03.03, the event generator in the MCNP6 [4] for intermediate-energy nuclear reactions, is capable of producing light fragments up to ^{4}He in its coalescence model. In this study, we have expanded the coalescence model to be able to produce up to ^{7}Be in CEM03.03F and up to ^{12}C in LAQGSM03.03F. Results are promising.

3.1 BACKGROUND

When the cascade stage of a reaction is completed, CEM uses the coalescence model described in Ref. [24, 98] to "create" high-energy d, t, ^{3}He, and ^{4}He by final-state interactions among emitted cascade nucleons outside of the target nucleus. The coalescence model used in CEM is similar to other coalescence models for heavy-ion-induced reactions. The main difference is that instead of complex-particle spectra being estimated simply by convolving the measured or calculated inclusive spectra of nucleons with corresponding fitted coefficients, CEM03.03 uses in its simulations of particle coalescence real information about all emitted cascade nucleons and does not use integrated spectra. (Note that the coalescence introduced recently in the Liège intranuclear cascade (INCL) [39, 41, 99, 38], is in a way similar to the coalescence considered by CEM as proposed in Ref. [24, 98], with the main contrast being that INCL considers coalescence of INC nucleons on the border of a nucleus, inside the target-nucleus, while CEM coalesces INC nucleons outside the nucleus.) We assume that all the cascade nucleons having differences in their momenta smaller than p_c and the correct isotopic content form an appropriate composite particle. The coalescence radii p_c as used in CEM03.03 are:
Incident energy, T, < 300 MeV or > 1000 MeV

$$\begin{aligned} p_c(d) &= 90 \text{ MeV/c} ; \\ p_c(t) &= p_c(^3\text{He}) = 108 \text{ MeV/c} ; \\ p_c(^4\text{He}) &= 115 \text{ MeV/c} . \end{aligned} \tag{3.1}$$

300 MeV $< T <$ 1000 MeV

$$\begin{aligned} p_c(d) &= 150 \text{ MeV/c} ; \\ p_c(t) &= p_c(^3He) = 175 \text{ MeV/c} ; \\ p_c(^4He) &= 175 \text{ MeV/c} . \end{aligned} \tag{3.2}$$

If several cascade nucleons are chosen to coalesce into composite particles, they are removed from the distributions of nucleons and do not contribute further to such nucleon characteristics as spectra, multiplicities, *etc*.

3.2 TEST CASE: 800 MEV/NUCLEON NE + NE

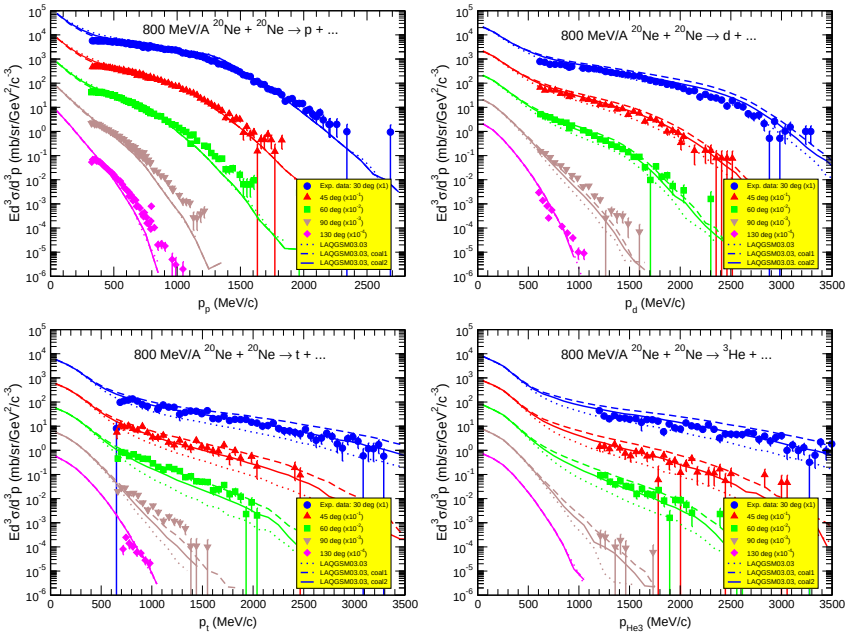

FIGURE 3.1: Comparison of p, d, t, and ^{3}He spectra at 45, 60, 90, and 130 degrees from 800 MeV/nucleon ^{20}Ne + NaF measured at the Bevatron/Bevalac at the Lawrence Berkeley Laboratory [100, 101] with calculations by LAQGS03.03 using its "standard" version of the coalescence model ($p_0 = 0.09$ GeV/c for d, 0.108 GeV/c for t and ^{3}He, and 0.115 GeV/c for ^{4}He; dotted lines) and with modified values of p_0 labeled in legend as "coal1" ($p_0 = 0.15$ GeV/c for d, and 0.175 GeV/c for t, ^{3}He, and ^{4}He; dashed lines), as well as with a second modification of p_0 labeled in legend as "coal2" ($p_0 = 0.12$ GeV/c for d, and 0.14 GeV/c for t and ^{3}He, and ^{4}He; solid lines), as indicated (for simplicity, all calculations were done on a ^{20}Ne target).

Here we will discuss the reaction 800 MeV/A Ne + Ne, which we analyzed in Ref. [64]. ^{20}Ne nuclei are light enough that LF can be produced by LAQGSM not only with the Fermi breakup model, when the residual excited nucleus after INC has a mass number $A < 13$, but also via preequilibrium emission and evaporation, as well as final residual nuclei after all stages of reactions.

Experimental data of the reaction 800 MeV/A Ne + Ne were collected at the Bevatron/Bevalac at the Lawrence Berkeley Laboratory [100, 101]. Only LF of high and very high energies were measured in these experiments, and only products from the fragmentation of the bombarding nuclei were detected. LAQGSM can reproduce such high-energy portions of spectra only with its coalescence model, as the Fermi breakup model would provide LF of lower energies, while the preequilibrium emission and evaporation would provide much lower LF energies; the energies of the LF produced as final "residual nuclei" after all other stages of reactions would be even much lower. In other words, the experimental data from Refs. [100, 101] are very convenient to test the coalescence model in LAQGSM.

As noted in Section I.B.4, LAQGSM uses fixed values for p_c as determined by Eq. (3.1). Results obtained with such "standard" values for p_c are shown in Fig. 3.1 with dotted lines: We see that these LAQGSM spectra underestimate the measured data, suggesting that we need to use higher values for p_c, at least for this particular reaction. As a second test of p_c values, we try to use for this reaction the values shown in Eq. (3.2), found to work the best in CEM03.03 in the 300 MeV $\leq T <$ 1 GeV region of incident energies. Results obtained with these values for p_c are shown in Fig. 3.1 with dashed lines: We see that values of p_c defined by Eq. (3.2) provide too many high energy LF, *i.e.*, these values are too big to provide the best results for LF spectra calculated by LAQGSM for this particular reaction. Finally, we try some intermediate p_c values:

$$\begin{aligned} p_c(d) &= 120 \text{ MeV/c} ; \\ p_c(t) &= p_c(^3\text{H}e) = \\ = p_c(^4\text{H}e) &= 140 \text{ MeV/c} . \end{aligned} \tag{3.3}$$

Results calculated with these values are shown with solid lines in Fig. 3.1: They agree much better with the measured spectra of d, t, and ^{3}He from this reaction than the previous two sets of results. Note that the aim of our work [64] was not to fine-tune the parameters used by the coalescence model in our CEM and LAQGSM event generators. We may consider such a fine-tuning at a later stage. Here, we just show that although the standard versions of our CEM and LAQGSM event generators for MCNP6 provide an overall good agreement of calculated spectra and yields of products from various reactions, a fine-tuning of some of their parameters would allow improving further the agreement of calculated results with available experimental data.

In addition, Fig. 3.1 demonstrates that coalescence plays a significant role in the emission of energetic light fragments. Therefore, extending coalescence to fragments heavier than ^{4}He should provide increased emission of these fragments in the high-energy region.

3.3 COALESCENCE EXPANSION IN CEM

The Coalescence Model in CEM03.03 allows for coalescence up to ^{4}He. We have expanded this to additionally allow for the coalescence of ^{6}He, ^{6}Li, ^{7}Li, and ^{7}Be.

CEM03.03 uses the simplest version of the coalescence model [24, 98] and checks only the momenta of nucleons emitted during the cascade stage of reactions, without checking their coordinates.

The momentum, p, of each nucleon is calculated relativistically from its kinetic energy, T (CEM03.03 provides in its output files the energy of particles, but not their momenta), as in Eq. 3.4:

$$p^2c^2 = KE(KE + 2m_0c^2), \tag{3.4}$$

where m_0 is the rest mass of the nucleon. Eq. 3.4 can be derived from the relativisitc energy relations

$$E^2 = p^2c^2 + m_0^2c^4 \tag{3.5}$$

and

$$E = KE + m_0c^2. \tag{3.6}$$

Coalescence occurs if each nucleon in the group has $|\Delta p| \leq p_c$, where Δp is defined as the difference between the nucleon momentum and the average momentum of all nucleons in the group.

The coalescence model of CEM03.03 first checks all nucleons to form 2-nucleon pairs, their momenta permitting. It then checks if an alpha particle can be formed from two 2-nucleon pairs (either from 2 n-p pairs or from a n-n and p-p pair). After this it checks to see if any of the 2-nucleon pairs left can combine with another nucleon to form either tritium or ^{3}He. And lastly, it checks to see if any of these 3-nucleon groups (tritium or ^{3}He) can coalesce with another nucleon to form ^{4}He.

The expanded coalescence model then takes these 2-nucleon pairs, 3-nucleon (tritium or ^{3}He only) groups, and ^{4}He to see if they can coalesce to form heavy clusters. ^{4}He can coalesce with a 3-nucleon group to form either ^{7}Be or ^{7}Li. Two 3-nucleon groups can coalesce to form either ^{6}Li or ^{6}He. And ^{4}He can coalesce with a 2-nucleon pair to form either ^{6}Li or ^{6}He. All coalesced nucleons are removed from the distributions of nucleons so that our coalescence model conserves both atomic- and mass-numbers.

For additional details of the Coalescence Model expansion, see Ref. [102].

3.3.1 *Coalescence Parameter p_c*

As mentioned in Section 3.1, p_c determines how dissimilar the momenta of nucleons can be and still coalesce. p_c was expanded to also include a value for heavy clusters, or light fragments (LF): $p_c(LF)$. Our new p_c's for incident energies, T, less than 300 MeV or greater than 1000 MeV are:

$$\begin{aligned} p_c(d) &= 90 \text{ MeV/c ;} \\ p_c(t) &= p_c(^3\text{He}) = 108 \text{ MeV/c ;} \\ p_c(^4\text{He}) &= 130 \text{ MeV/c .} \\ p_c(LF) &= 175 \text{ MeV/c .} \end{aligned} \tag{3.7}$$

And for 300 MeV $< T <$ 1000 MeV

$$\begin{aligned} p_c(d) &= 150 \text{ MeV/c ;} \\ p_c(t) &= p_c(^3\text{He}) = 175 \text{ MeV/c ;} \\ p_c(^4\text{He}) &= 205 \text{ MeV/c .} \\ p_c(LF) &= 250 \text{ MeV/c .} \end{aligned} \tag{3.8}$$

Note that the $p_c(^4\text{He})$ was also increased compared to the old p_c values. Too many alpha particles were lost (coalesced into heavy clusters), and therefore we compensated by increasing the coalescence of ^{4}He.

3.3.2 *Computation Time*

Expanding the coalescence model did not significantly impact computation times. Table 3.1 displays a sampling of computation times with and without the expanded coalescence model.

TABLE 3.1: Computation Times with and without the Expanded Coalescence Model

Reaction	# Events	Without Expansion	With Expansion	% Increase (Decrease)
p200Co	20 Million	83 min	90 min	+8.4%
p480Ag	99 Million	19.68 hr	19.60 hr	-0.4%
p1200Au	99 Million	72.87 hr	77.88 hr	+6.9%
p1900Ni	20 Million	395 min	361 min	-7.4%
p2500Au	20 Million	28.02 hr	27.19 hr	-3.0%

The increase in computation times appear to be statistically indistinguishable from the statistical variability of computational times on the LANL servers. The simple average increase was +0.9%, and the weighted average increase in computation time was +2.8%; neither are significant.

3.4 RESULTS AND ANALYSIS

Examples of results of our coalescence expansion are displayed in Figs. 3.2 and 3.3. The upgraded CEM03.03F **without** coalescence expansion (blue solid lines) and the

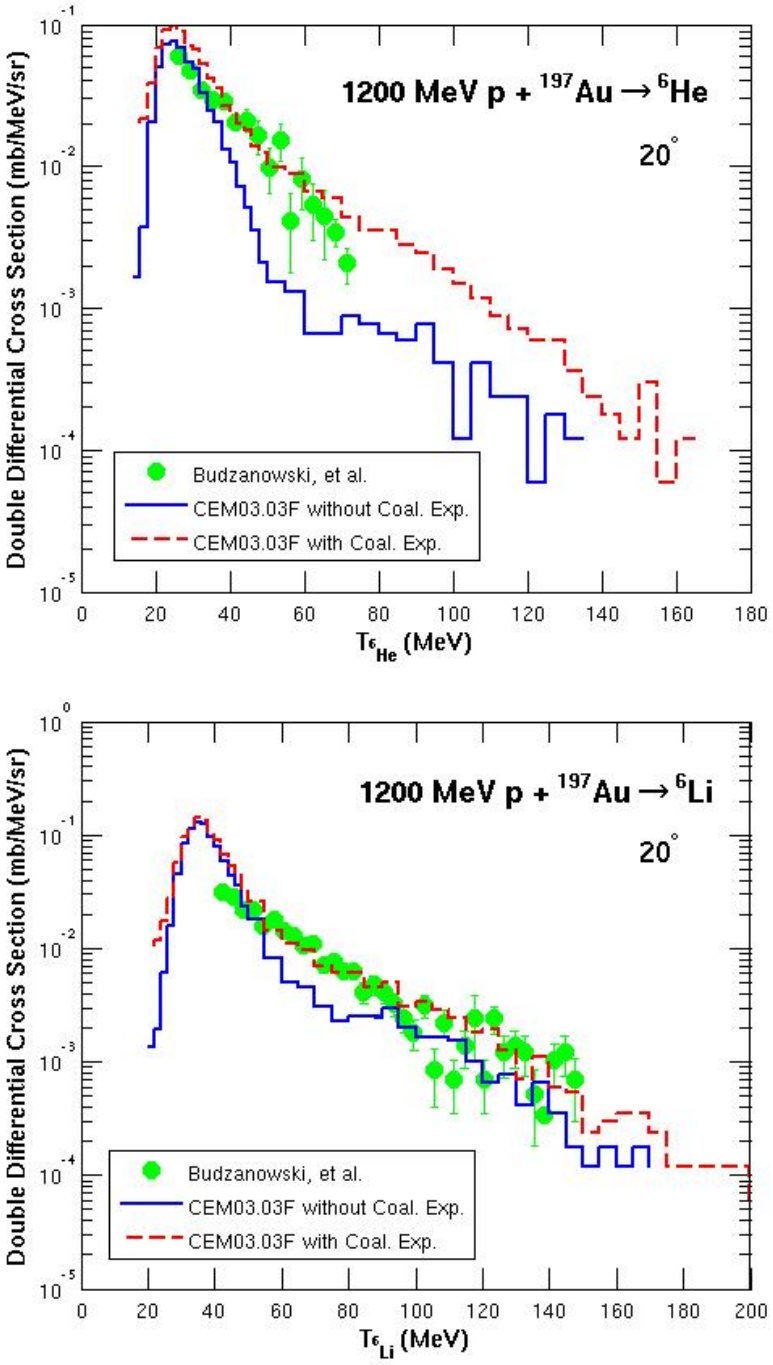

FIGURE 3.2: Comparison of experimental data by Budzanowski, *et al.* [49] (green circles) for the production of ^{6}He and ^{6}Li at an angle of 20° from the reaction 1200 MeV p + ^{197}Au, with results from CEM03.03F without coalescence expansion (blue solid lines) and CEM03.03F with coalescence expansion (red dashed lines).

upgraded CEM03.03F **with** coalescence expansion (red dashed lines) are compared with experimental data (green circles). CEM03.03F refers to the upgraded CEM03.03

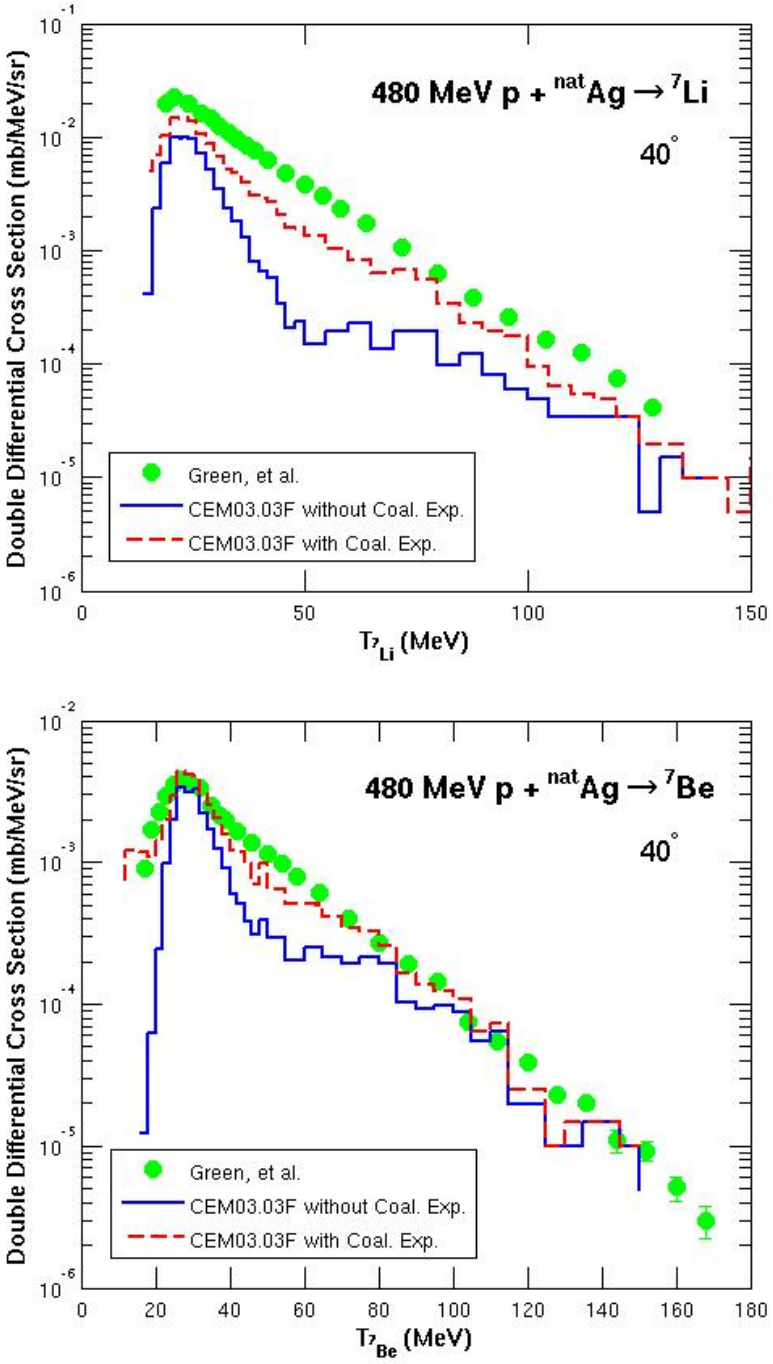

FIGURE 3.3: Comparison of experimental data by Green *et al.* [103] (green circles) for the production of ^{7}Li and ^{7}Be at an angle of 40° from the reaction 480 MeV p + ^{nat}Ag, with results from CEM03.03F without coalescence expansion (blue solid lines) and CEM03.03F with coalescence expansion (red dashed lines).

code, which has been upgraded with a Modified-Exciton-Model expansion and a total reaction cross section model improvement. The blue solid lines contain both of these

improvements over the original CEM03.03, and the red dashed lines contain both of these improvements plus the coalescence expansion.

Fig. 3.2 displays fragment production spectra of ^{6}He and ^{6}Li for the reaction 1200 MeV p + ^{197}Au. Experimental data by Budzanowski *et al.* [49] (green circles) are compared with results from CEM03.03F without coalescence expansion (blue solid lines) and CEM03.03F with coalescence expansion (red dashed lines). The coalescence expansion increases the production of high-energy ^{6}He and ^{6}Li, and improves agreement with experimental data.

Fig. 3.3 displays the fragment production spectra of ^{7}Li and ^{7}Be for the reaction 480 MeV p + ^{nat}Ag. Experimental data by Green *et al.* [103] (green circles) are compared with results from CEM03.03F without coalescence expansion (blue solid lines) and CEM03.03F with coalescence expansion (red dashed lines). Again, the coalescence expansion increases the production of heavy clusters, and improves agreement with experimental data.

These reactions also highlight how the coalescence can produce heavy clusters not just of high-energy, but also of low- and moderate-energy, thus improving agreement with experimental data in these energy regions as well.

Fig. 3.4 displays experimental results of the reaction 480 MeV p + ^{nat}Ag $\rightarrow$ ^{6}Li by Green *et al.* [103] (green circles), compared with simulations from results from CEM03.03F without coalescence expansion (blue solid lines), CEM03.03F with coalescence expansion (red dashed lines), and the original CEM03.03 (brown dashed-dotted lines). Even without the coalescence expansion, CEM03.03F (which contains a preequilibrium expansion and a total reaction cross section improvement) yields much better results than CEM03.03 without any of these improvements. Adding the coalescence expansion produces even better results.

Similar results for many other reactions induced by protons, neutrons, and heavy ions (the last are simulated with LAQGSM03.03, but with an extended coalescence model as described in Ref. [104]) and further discussions can be find in Refs. [102, 104, 105].

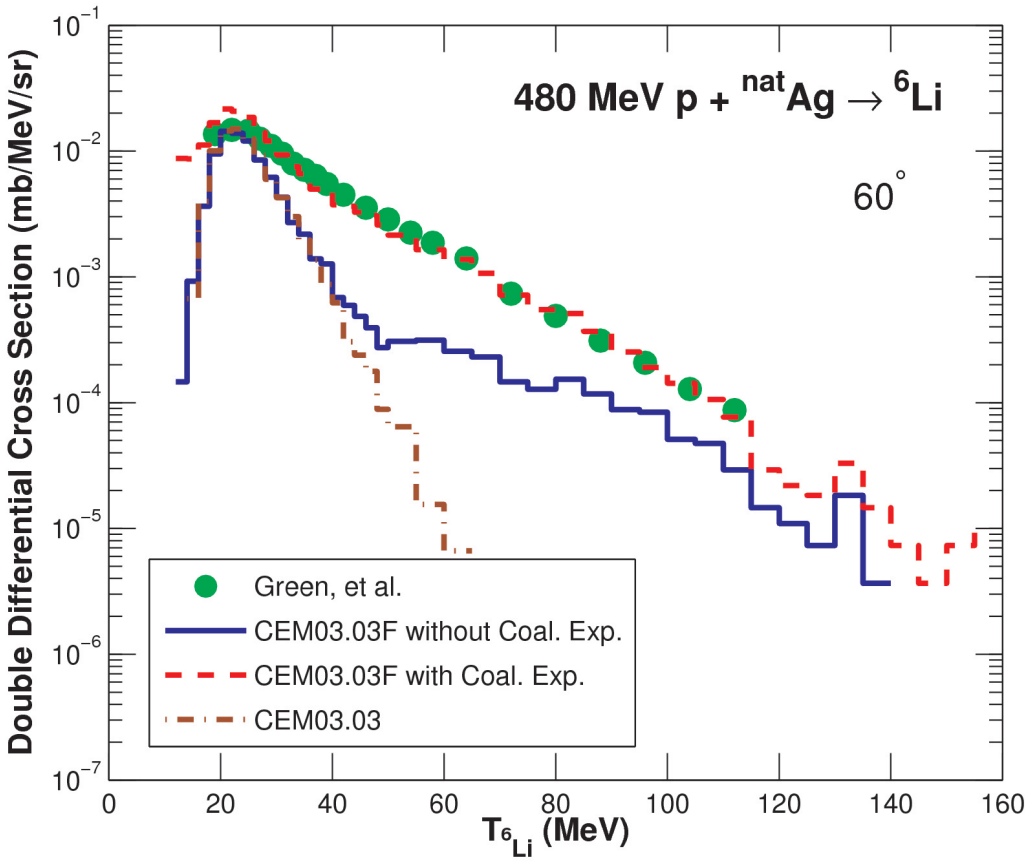

FIGURE 3.4: Comparison of experimental results of the reaction 480 MeV p + ^{nat}Ag → ^{6}Li at 60° by Green *et al.* [103] (green circles), with simulations from the original CEM03.03 (brown dashed-dotted lines), CEM03.03F without coalescence expansion (blue solid lines) and the CEM03.03F with coalescence expansion (red dashed lines).

3.5 CONCLUSION

Expanding the coalescence model within CEM yields increased production of heavy clusters in nuclear spallation reactions, particularly in the high-energy region, but also in the low- and moderate-energy regions. Preliminary results indicate this coalescence expansion yields improved agreement with experimental data. These upgrades were recently implemented into and tested in MCNP6 and will be described in detail in a future publication.

We further recommend a greater improvement of the coalescence model in the future, to include more heavy clusters, such as ^{8}Li and ^{9}Li, etc. The coalescence model favors the formation of neutron-rich heavy clusters for heavy targets (due to

the presence of more neutrons than protons produced during the cascade). We see that the predictions for the spectra for these neutron-rich heavy clusters could likely be improved by such a coalescence expansion. In this further improvement of the coalescence model we also recommend considering the Coulomb Barrier to limit low-energy production.

CHAPTER 4

Preequilibrium —Expansion

Below are relevant publications that result from the author's work pertaining to this chapter.

- L.M. Kerby, S.G. Mashnik, and A.J. Sierk, Preequilibrium Emission of Light Fragments in Spallation Reactions, Nuclear Data Sheets **118** (2014) 316;
- L.M. Kerby, S.G. Mashnik, and A.T. Tokuhiro, Production of Energetic Light Fragments with Expanded Cascade Exciton Model (CEM), Transactions of the American Nuclear Society **110** (2014) 465;
- S.G. Mashnik, L.M. Kerby, K.K. Gudima, and A.J. Sierk, Extension of the CEM and LAQGSM Models to Describe Production of Energetic Light Fragments in Spallation Reactions, European Physical Journal Web of Conferences **66** (2014) 03059; arXiV:1306.6547;
- L.M. Kerby, S.G. Mashnik, and A.J. Sierk, Comparison of Expanded Preequilibrium CEM Model with CEM03.03 and Experimental Data, FY2013, LANL Report, LA-UR-13-21828 (November 2013).

The preequilibrium interaction stage of nuclear reactions is considered by the current CEM and LAQGSM in the framework of the latest version of the Modified Exciton Model (MEM) [15, 16] as described in Ref. [20]. At the preequilibrium stage of a reaction, CEM03.03 and LAQGSM03.03 take into account all possible nuclear transitions changing the number of excitons n with $\Delta_n = +2$, -2, and 0, as well as all possible multiple subsequent emissions of n, p, d, t, ^{3}He, and ^{4}He. The corresponding system of master equations describing the behavior of a nucleus at the preequilibrium stage is solved by the Monte-Carlo technique [1]. This chapter investigates the impact of expanding our MEM to include the possibility of emitting heavy clusters, heavier than ^{4}He, up to ^{28}Mg.

4.1 THE MODIFIED EXCITON MODEL (MEM)

4.1.1 *MEM Physics*

The probability of finding the system at the time moment t in the $E\alpha$ state, $P(E,\alpha,t)$, is given by the following differential equation:

$$\frac{\delta P(E,\alpha,t)}{\delta t} = \sum_{\alpha\neq\alpha'} [\lambda(E\alpha, E\alpha')P(E,\alpha',t) - \lambda(E\alpha', E\alpha)P(E,\alpha,t)]. \tag{4.1}$$

Here $\lambda(E\alpha, E\alpha')$ is the energy-conserving probability rate, defined in the first order of the time-dependent perturbation theory as

$$\lambda(E\alpha, E\alpha') = \frac{2\pi}{h}| < E\alpha|V|E\alpha' > |^2\omega_\alpha(E). \tag{4.2}$$

The matrix element $< E\alpha|V|E\alpha' >$ is believed to be a smooth function in energy, and $\omega_\alpha(E)$ is the density of the final state of the system. One should note that Eq. (4.1) is derived provided that the "memory" time τ_{mem} of the system is small compared to the characteristic time for intranuclear transition $\hbar/\lambda(E\alpha, E\alpha')$ but, on the other hand, Eq. (4.1) itself is applicable for the time moments $t \gg \hbar/\lambda(E\alpha, E\alpha')$. Due to the condition $\tau_{mem} \gg \hbar/\lambda(E\alpha, E\alpha')$, being described by Eq. (4.1), the random process is the Markovian one.

The Modified Exciton Model (MEM) [1, 15, 16] utilized by CEM and LAQGSM uses effectively the relationship of the master equation (4.1) with the Markovian random processes. Indeed, an attainment of the statistical equilibration described by Eq. (4.1) is an example of the discontinuous Markovian process: the temporal variable changes continuously and at a random moment the state of the system changes by a discontinuous jump, the behavior of the system at the next moment being completely defined by its state at present. As long as the transition probabilities $\lambda(E\alpha, E\alpha')$ are time independent, the waiting time for the system in the $E\alpha$ state has the exponential distribution (the Poisson flow) with the average lifetime $\hbar/\Lambda(\alpha, E) = \hbar/\sum'_\alpha \lambda(E\alpha, E\alpha')$. This fact prompts a simple method of solving the related system of Eq. (4.1): simulation of the random process by the Monte Carlo technique. In this treatment it is possible to generalize the exciton model to all nuclear transitions with

$\Delta n = 0, \pm 2$, and the multiple emission of particles and to depletion of nuclear states due to the particle emission. In this case the system (4.1) is as follows: [106]

$$\begin{aligned}\frac{\delta P(E,\alpha,t)}{\delta t} =& -\Lambda(n,E)P(E,n,t) + \lambda_+(n-2,E)P(E,n-2,t)+ \\ &+\lambda_0(n,E)P(E,n,t) + \lambda_-(n+2,E)P(E,n+2,t)+ \\ &+\sum_j \int dT \int dE' \lambda_c^j(n,E,T)P(E',n+n_j,t)\delta(E'-E-B_j-T).\end{aligned} \tag{4.3}$$

Now we have our master equation Eq. (4.3) and can find the particle emission rates λ_c^j and the exciton transition rates λ_+, λ_0, and λ_-.

Particle Emission

According to the detailed balance principle, the emission width Γ_j, (or probability of emitting particle fragment j), is estimated as

$$\Gamma_j(p,h,E) = \int_{V_j^c}^{E-B_j} \lambda_c^j(p,h,E,T)dT, \tag{4.4}$$

where the partial transmission probabilities, λ_c^j, are equal to

$$\lambda_c^j(p,h,E,T) = \frac{2s_j+1}{\pi^2\hbar^3}\mu_j \Re(p,h)\frac{\omega(p-1,h,E-B_j-T)}{\omega(p,h,E)}T\sigma_{inv}(T). \tag{4.5}$$

p is number of particle excitons;

h is number of hole excitons;

E is internal energy of the excited nucleus (sometimes referred to as U);

s_j: spin of the emitted particle j;

μ_j: reduced mass of the emitted particle j;

ω: level density of the n-exciton state;

B_j: binding energy;

V_j^c: Coulomb barrier;

T: kinetic energy of the emitted particle j;

σ_{inv}: inverse cross section;

$\Re$: creates zero probability of emission if the number of particle excitons is less than the number nucleons of particle j.

Equation (4.5) describes the emission of neutrons and protons. For complex particles, the level density formula ω becomes more complicated and an extra factor γ_j must be introduced:

$$\gamma_j \approx p_j^3 (\frac{p_j}{A})^{p_j - 1}. \tag{4.6}$$

In reality Equation (4.6) for γ_j is a preliminary rough estimation that is refined by parameterizing over a mesh of residual nuclei energy and mass number [19]. As the MEM uses a Monte-Carlo technique to solve the master equations describing the behavior of the nucleus at the preequilibrium stage (see details in [1]), it is relatively easy to extend the number of types of possible LF that can be emitted during this stage. However, adding the possibility of LF emission alters the previous γ_j parameterization, effectively requiring new parameterization. This work of parameterizing γ_j is the focus of Chapter 6.

Assuming an equidistant level scheme with the single-particle density g, we have the level density of the n-exciton state as [107]

$$\omega(p, h, E) = \frac{g(gE)^{p+h-1}}{p!h!(p+h-1)!} \ . \tag{4.7}$$

This expression should be substituted into Eq. 4.5 to obtain the transmission rates λ_c^j.

Exciton Transitions

According to Equation (4.2), for a preequilibrium nucleus with excitation energy E and number of excitons $n = p + h$, the partial transition probabilities changing the exciton number by Δn are

$$\lambda_{\Delta n}(p, h, E) = \frac{2\pi}{\hbar} |M_{\Delta n}|^2 \omega_{\Delta n}(p, h, E) \ . \tag{4.8}$$

For these transition rates, one needs the number of states, ω, taking into account the selection rules for intranuclear exciton-exciton scattering. The appropriate formulae have been derived by Williams [108] and later corrected for the exclusion principle

and indistinguishability of identical excitons in Refs. [109, 110]:

$$\begin{aligned}
\omega_+(p,h,E) &= \frac{1}{2}g\frac{[gE-\mathcal{A}(p+1,h+1)]^2}{n+1}\left[\frac{gE-\mathcal{A}(p+1,h+1)}{gE-\mathcal{A}(p,h)}\right]^{n-1}, \\
\omega_0(p,h,E) &= \frac{1}{2}g\frac{[gE-\mathcal{A}(p,h)]}{n}[p(p-1)+4ph+h(h-1)], \\
\omega_-(p,h,E) &= \frac{1}{2}gph(n-2), \qquad (4.9)
\end{aligned}$$

where $\mathcal{A}(p,h) = (p^2+h^2+p-h)/4-h/2$. By neglecting the difference of matrix elements with different Δn, $M_+ = M_- = M_0 = M$, we estimate the value of M for a given nuclear state by associating the $\lambda_+(p,h,E)$ transition with the probability for quasi-free scattering of a nucleon above the Fermi level on a nucleon of the target nucleus. Therefore, we have

$$\frac{<\sigma(v_{rel})v_{rel}>}{V_{int}} = \frac{\pi}{\hbar}|M|^2\frac{g[gE-\mathcal{A}(p+1,h+1)]}{n+1}\left[\frac{gE-\mathcal{A}(p+1,h+1)}{gE-\mathcal{A}(p,h)}\right]^{n-1}. \quad (4.10)$$

Here, V_{int} is the interaction volume estimated as $V_{int} = \frac{4}{3}\pi(2r_c+\lambda/2\pi)^3$, with the de Broglie wave length $\lambda/2\pi$ corresponding to the relative velocity $v_{rel} = \sqrt{2T_{rel}/m_N}$. A value of the order of the nucleon radius is used for r_c in the CEM: $r_c = 0.6$ fm.

The averaging on the left-hand side of Eq. (4.10) is carried out over all excited states, taking into account the exclusion principle. Combining (4.8), (4.9), and (4.10) we finally get for the transition rates:

$$\begin{aligned}
\lambda_+(p,h,E) &= \frac{<\sigma(v_{rel})v_{rel}>}{V_{int}}, \\
\lambda_0(p,h,E) &= \frac{<\sigma(v_{rel})v_{rel}>}{V_{int}}\frac{n+1}{n}\left[\frac{gE-\mathcal{A}(p,h)}{gE-\mathcal{A}(p+1,h+1)}\right]^{n+1}\frac{p(p-1)+4ph+h(h-1)}{gE-\mathcal{A}(p,h)}, \\
\lambda_-(p,h,E) &= \frac{<\sigma(v_{rel})v_{rel}>}{V_{int}}\left[\frac{gE-\mathcal{A}(p,h)}{gE-\mathcal{A}(p+1,h+1)}\right]^{n+1}\frac{ph(n+1)(n-2)}{[gE-\mathcal{A}(p,h)]^2}. \qquad (4.11)
\end{aligned}$$

Angular Distributions

The CEM predicts forward peaked (in the laboratory system) angular distributions for preequilibrium particles. For instance, CEM03.03 assumes that a nuclear state with a given excitation energy E^* should be specified not only by the exciton number n

but also by the momentum direction Ω. Following Ref. [111], the master equation (Eq. (4.3)) can be generalized for this case provided that the angular dependence for the transition rates λ_+, λ_0, and λ_- (Eq. (4.11)) is factorized. In accordance with Eq. 4.10, in the CEM it is assumed that

$$< \sigma > \rightarrow < \sigma > F(\Omega) \ , \tag{4.12}$$

where

$$F(\Omega) = \frac{d\sigma^{free}/d\Omega}{\int d\Omega' d\sigma^{free}/d\Omega'} \ . \tag{4.13}$$

The scattering cross section $d\sigma^{free}/d\Omega$ is assumed to be isotropic in the reference frame of the interacting excitons, thus resulting in an asymmetry in both the nucleus center-of-mass and laboratory frames. The angular distributions of preequilibrium complex particles are assumed to be similar to those for the nucleons in each nuclear state [1].

This calculational scheme is easily realized by the Monte-Carlo technique. It provides a good description of double-differential spectra of preequilibrium nucleons and a not-so-good but still satisfactory description of complex-particle spectra from different types of nuclear reactions at incident energies from tens of MeV to several GeV. For incident energies below about 200 MeV, Kalbach [28] has developed a phenomenological systematics for preequilibrium-particle angular distributions by fitting available measured spectra of nucleons and complex particles. As the Kalbach systematics are based on measured spectra, they describe very well the double-differential spectra of preequilibrium particles and generally provide a better agreement of calculated preequilibrium complex particle spectra with data than does the CEM approach based on Eqs. (4.12, 4.13). Therefore, CEM03.03 incorporated the Kalbach systematics [28] to describe angular distributions of both preequilibrium nucleons and complex particles at incident energies up to 210 MeV. At higher energies, CEM03.03 uses the CEM approach based on Eqs. (4.12, 4.13).

TABLE 4.1: The emitted particles considered by the modified MEM.

Z_j	Ejectiles						
0	n						
1	p	d	t				
2	^{3}He	^{4}He	^{6}He	^{8}He			
3	^{6}Li	^{7}Li	^{8}Li	^{9}Li			
4	^{7}Be	^{9}Be	^{10}Be	^{11}Be	^{12}Be		
5	^{8}B	^{10}B	^{11}B	^{12}B	^{13}B		
6	^{10}C	^{11}C	^{12}C	^{13}C	^{14}C	^{15}C	^{16}C
7	^{12}N	^{13}N	^{14}N	^{15}N	^{16}N	^{17}N	
8	^{14}O	^{15}O	^{16}O	^{17}O	^{18}O	^{19}O	^{20}O
9	^{17}F	^{18}F	^{19}F	^{20}F	^{21}F		
10	^{18}Ne	^{19}Ne	^{20}Ne	^{21}Ne	^{22}Ne	^{23}Ne	^{24}Ne
11	^{21}Na	^{22}Na	^{23}Na	^{24}Na	^{25}Na		
12	^{22}Mg	^{23}Mg	^{24}Mg	^{25}Mg	^{26}Mg	^{27}Mg	^{28}Mg

4.1.2 *Precompound Particles Considered*

Table 4.1 displays the particles our expanded MEM can emit.

4.2 MEM EXPANSION

4.2.1 *Outputing Spectra for Light Fragments*

CEM03.03 does not have capability to output cross sections for fragments larger than ^{4}He. Therefore, the first task of this project was to add this capability. We also created the flexibility to output by isotope, Z number, or mass number. For more details of this work, see Ref. [112]

We next commenced an in-depth study of the code in MEM calculations. The flowchart in Fig. 4.1 describes the calculations and processes performed in the MEM.

4.2.2 *Distributions of Residual Nuclei After INC*

To understand the mechanisms of nuclear reactions better, we need to have information about various physical properties of our residual nuclei (such as momentum, angular momentum, energy, A and Z numbers, and exciton information) at various stages of the spallation reaction. We therefore built a module to calculate and output

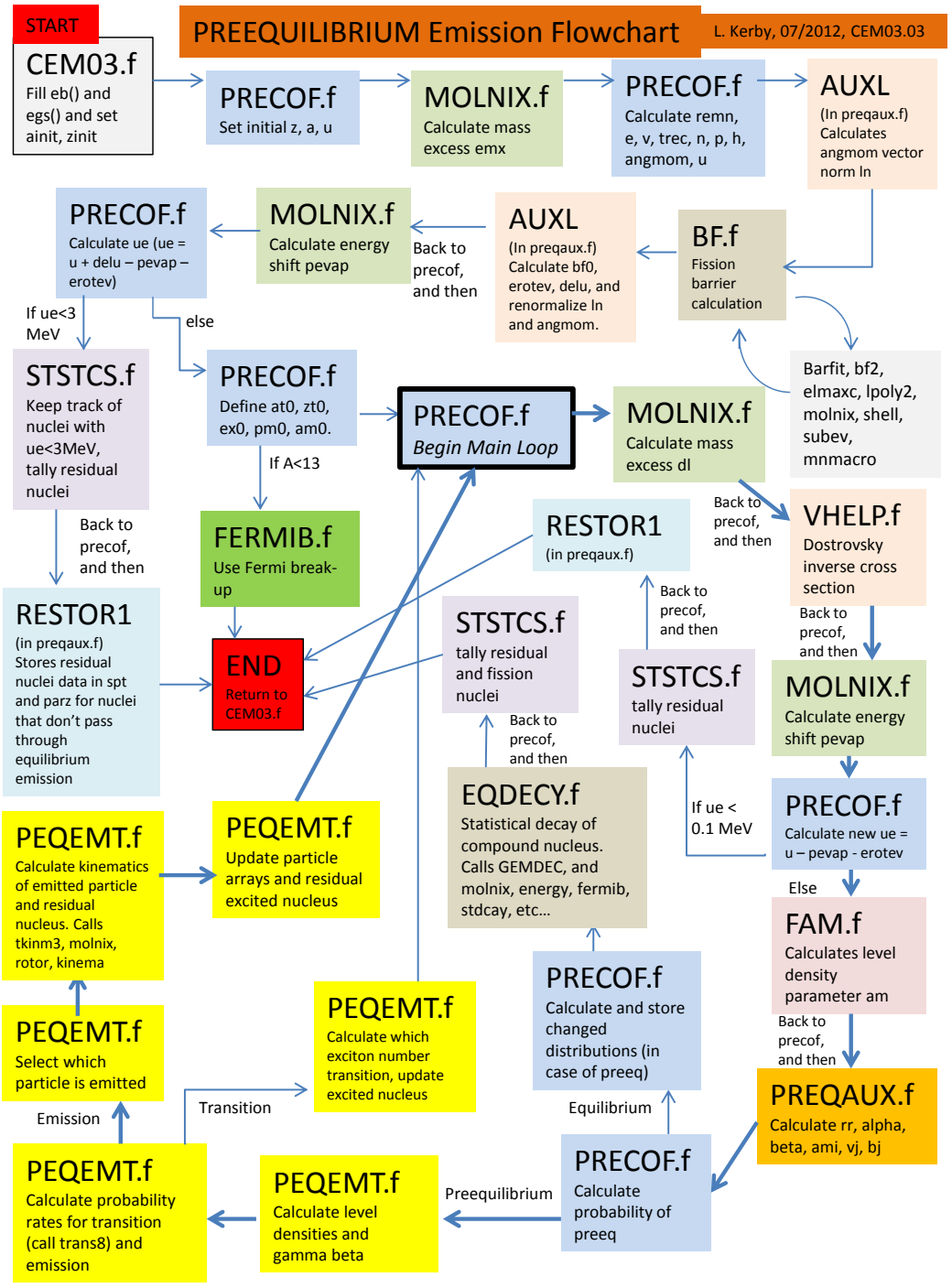

FIGURE 4.1: Flowchart for emission of light fragments in the MEM code.

these residual nuclei physical properties. The module can be inserted anywhere in the reaction process we want to investigate.

Figs. 4.2–4.4 show distributions of several properties of the residual nuclei after the INC, and right before the preequilibrium stage, for several reactions.

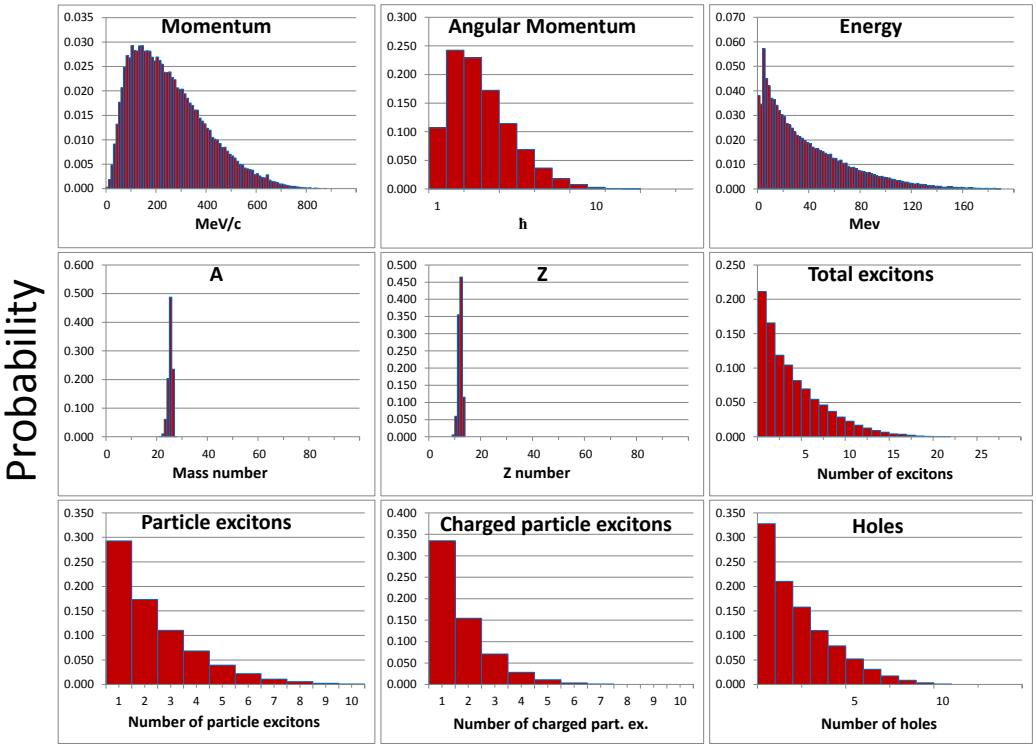

FIGURE 4.2: Momentum, angular momentum, energy, mass- and charge-numbers, number of excitons, particle excitons, charged particle excitons, and holes distributions of residual nuclei for the 200 MeV p + ^{27}Al → ... reaction directly after the INC, before the preequilibrium stage.

Observe how the number of charged particle excitons drops off sharply in Fig. 4.2. This demonstrates that we should expect the cross section to decrease dramatically as fragment size increases. We would also expect emission of LF from the MEM will be less of a factor in this reaction as it is in reactions with larger targets and/or higher incident energies.

Increasing the size of our target nucleus leads to a more gradual decline in our number of charged particle excitons in Fig. 4.3, and thus we would expect more emission from the MEM. Also notice the spikes in both the momentum and energy histograms. The momentum spike corresponds to the momentum of the incident

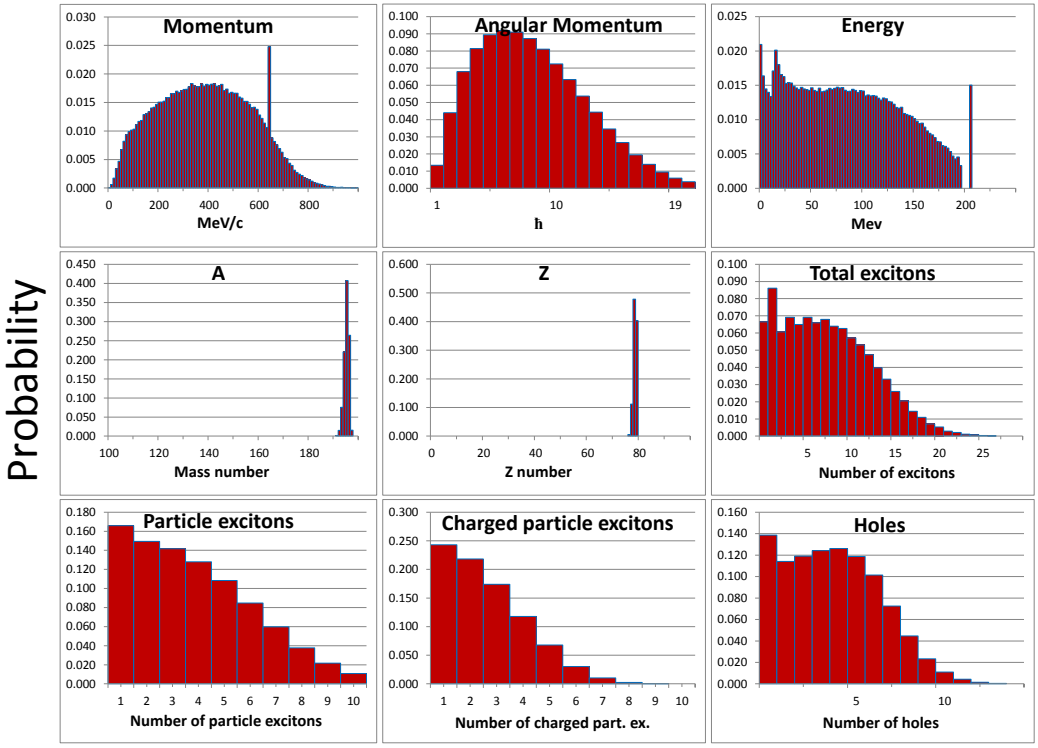

FIGURE 4.3: Momentum, angular momentum, energy, mass- and charge-numbers, number of excitons, particle excitons, charged particle excitons, and holes distributions of residual nuclei for the 200 MeV p + ^{197}Au $\rightarrow$ ... reaction directly after the INC, before the preequilibrium stage.

proton. The energy spike, which occurs at about 207 MeV, corresponds to the reaction in which the proton and its full 200 MeV of energy is absorbed within the gold nucleus. This provides 200 MeV from the incident proton plus approximately 7 MeV from the binding energy, for a total of 207 MeV. This is not a violation of energy conservation because we change reference frames–from the incident proton with 200 MeV in the laboratory system to the nucleus center-of-mass system which receives an extra 7 MeV from the binding energy of the proton. We did not see this spike in the aluminum target because the Al nucleus is too small and the incident proton (or a created scatter particle) escapes the nucleus.

In Fig. 4.4 the peaks disappear again, because the energy has significantly increased and either the incident proton or one of the created scatter particles escapes the gold nucleus. Notice that the number-of-charged-particle-excitons probability

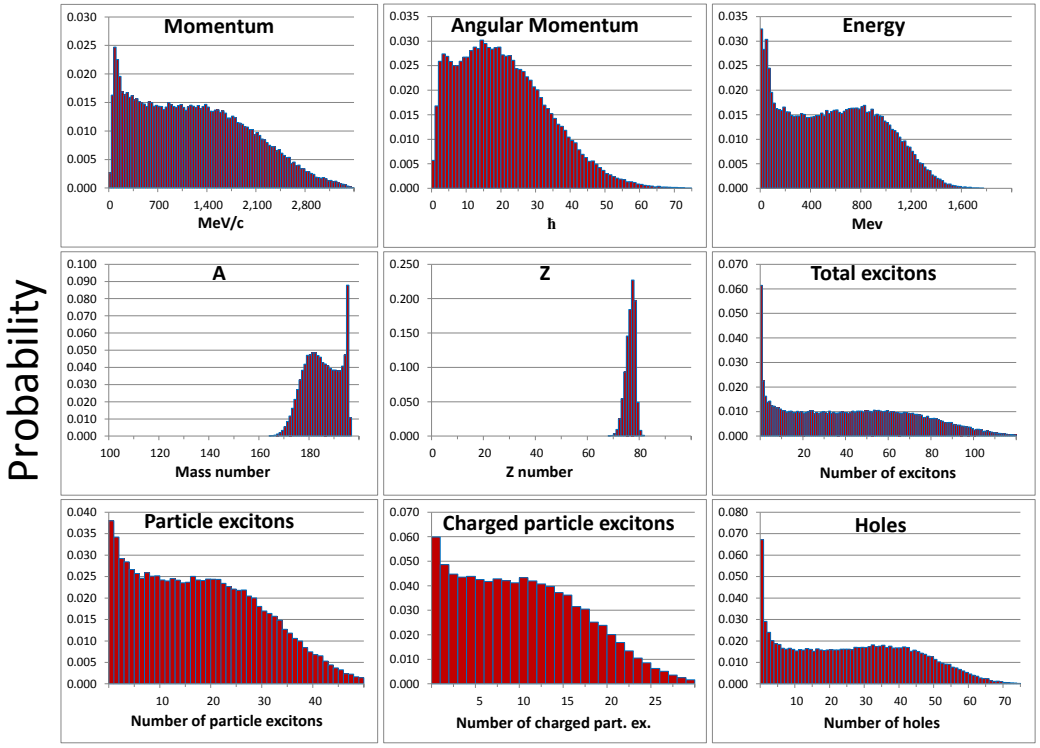

FIGURE 4.4: Momentum, angular momentum, energy, mass- and charge-numbers, number of excitons, particle excitons, charged particle excitons, and holes distributions of residual nuclei for the 2500 MeV p + ^{197}Au $\rightarrow$ ... reaction directly after the INC, before the preequilibrium stage.

does not begin to drop until after about 15. This means our MEM could emit a large fragment with high-energy from this high-energy reaction.

More physics can be extracted from Figs. 4.2–4.4. For example, the momentum influences the angular distribution of emitted fragments: the greater the momentum the more forward-peaked the emitted fragments will be. In addition, most multifragmentation models require an energy of at least $\geq$ 4 MeV per nucleon. Inspection reveals that we would expect multifragmentation to pertain to the reaction 2500 MeV p + ^{197}Au $\rightarrow$ ... only. Furthermore, the angular momentum effects the probability of fission, with greater angular momentum leading to more fissions. Thus we would expect more fissions in the 2500 MeV p + ^{197}Au $\rightarrow$ ... reaction than at the lower energy of 200 MeV presented in Fig. 4.3. Lastly, distributions of A and Z reveal the number of collisions that occurred in the target-nucleus, with larger distributions resulting from more collisions.

4.2.3 *Code Crash Protection*

Bugs used to be fixed on an as-encountered basis. However, after encountering one bug that could not feasibly be fixed in this manner, we decided to complete CEM-wide code crash protection. The entirety of the CEM code was modified to check, by if statements, for divide-by-zero errors and, if encountered, output error statements revealing where in the code such errors occurred (while fixing the divide-by-zero error to allow for completion of the simulations). Square root calculations were also protected to ensure no errors occurred. Logarithmic and inverse trigonometric functions were not universally error protected.

This was a large project as it involved slight modification of all the CEM code. However, as it will provide crash protection for future applications of CEM, including crash protection within future versions of MCNP, we determined it was worth it.

As this crash protection involved the addition of numerous if-statements into the code, we investigated the impact on computation time. The influence on CPU runtime was not significant and could not be detected above the normal variations in runtime that occur due to time-of-day CPU speed fluctuations, or having a month between runs (and LANL servers subsequently getting faster, perhaps). In addition, we validated the crash protected code by rerunning many reactions to ensure we got the same results as the non-protected code.

4.3 PRELIMINARY RESULTS

Preliminary results were very encouraging. Fig. 4.5 demonstrates the potential of the modified precompound code we built, for the same reaction and data as shown in Fig. 1.2: 200 MeV p + ^{27}Al $\rightarrow$ ^{6}Li. The blue dotted lines show double differential cross section results from the new precompound code we designed here; the red solid lines present calculations from the old code; and the yellow symbols are experimental data from Machner, *et al.* [11]. The upgraded MEM provides dramatically improved ability to describe the cross section at intermediate to high energies. Note that the bumpiness in the CEM results is due to statistical noise.

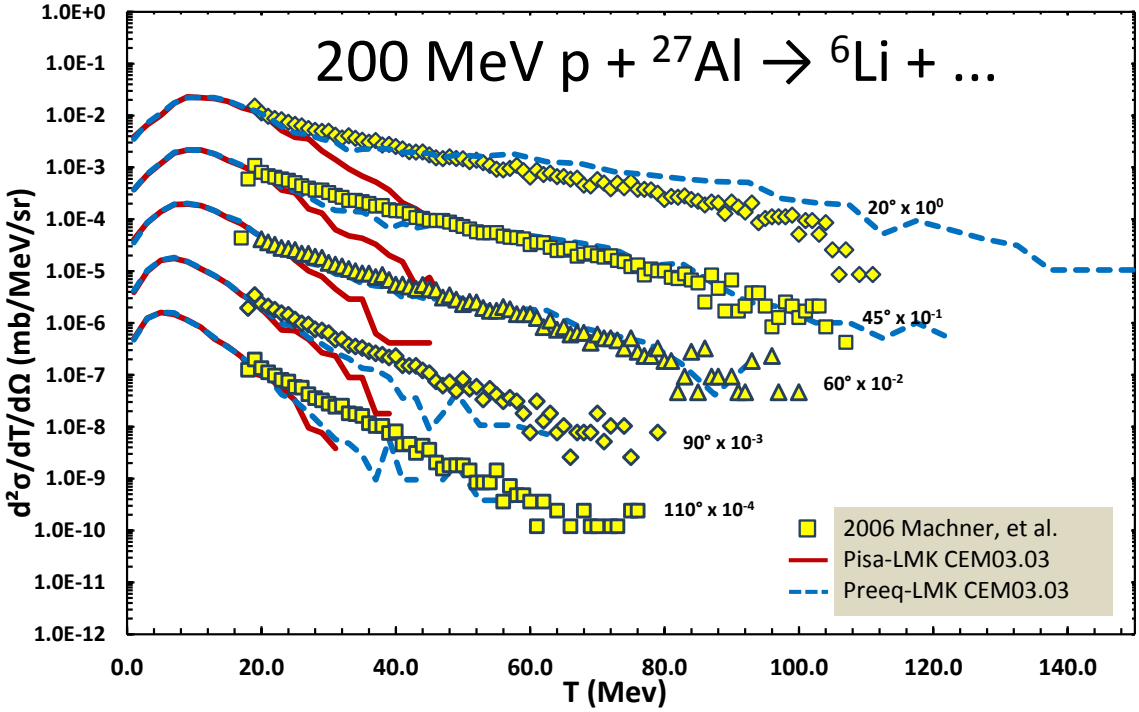

FIGURE 4.5: Comparison of double differential cross section experimental data by Machner, *et al.* [11] (open symbols) with results from the unmodified CEM03.03 (red solid lines) and the modified MEM CEM03.03 (blue dashed lines) for 200 MeV p + ^{27}Al $\rightarrow$ ^{6}Li.

Fig. 4.6 presents energy-spectra of nucleons, d, t, ^{3}He, and ^{4}He, as well as energy-spectra of heavier fragments ^{6}Li, ^{7}Be, ^{10}B, and ^{12}C. It demonstrates that the modified-MEM code predicts the high-energy tails of light fragment spectra, without destroying the spectra of established particles and fragments.

This was only the beginning of our work expanding the preequilibrium stage of CEM and LAQGSM. Chapters 5 and 6 detail upgrades to the inverse cross section model and the γ_j model used in our expanded MEM.

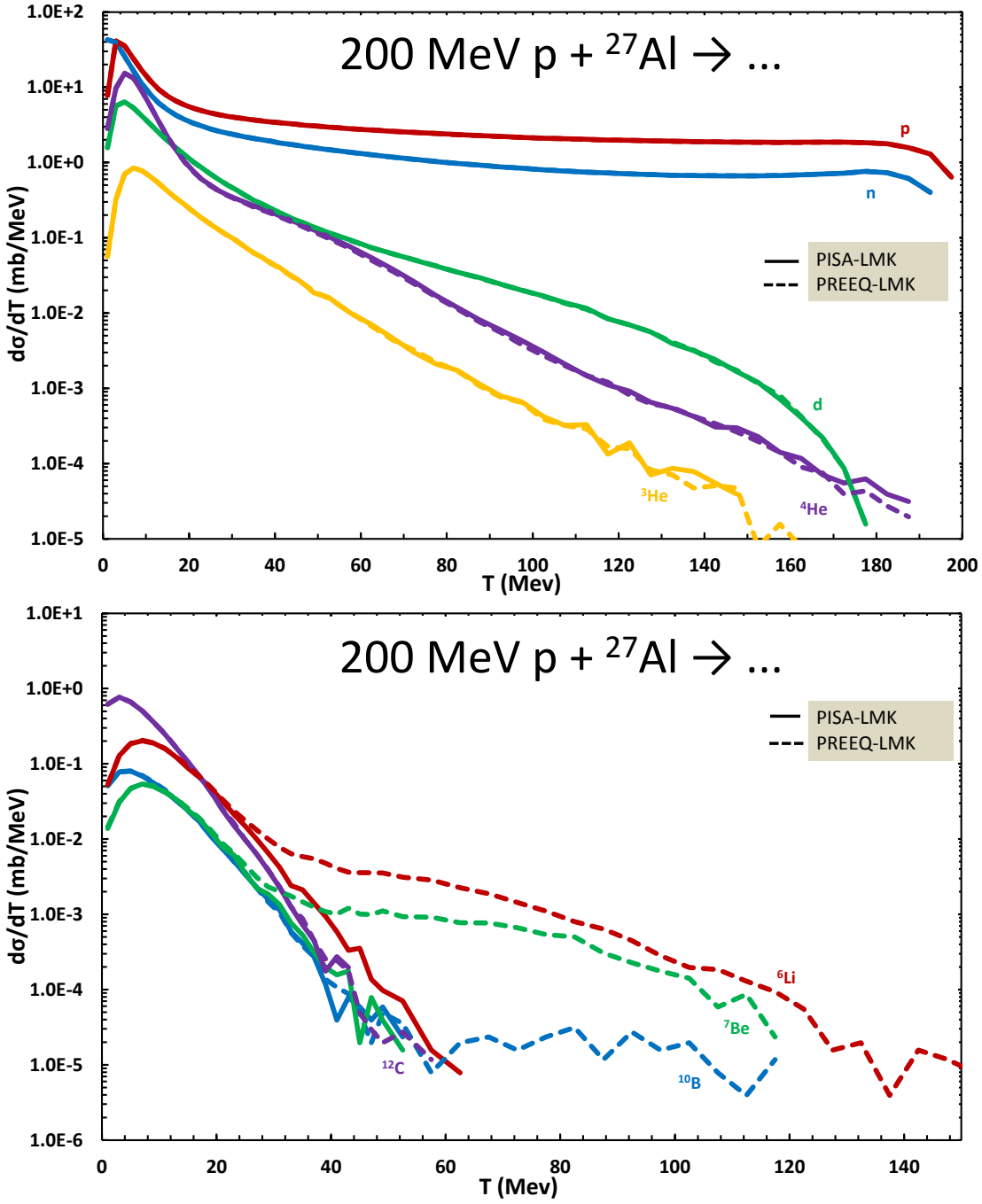

FIGURE 4.6: Comparison of angle integrated cross section results from the unmodified CEM03.03 (solid lines) and the modified MEM CEM03.03 (dashed lines) for emitted nucleons, d, t, ^{3}He, and ^{4}He (top), as well as heavier fragments ^{6}Li, ^{7}Be, ^{10}B, and ^{12}C, for the reaction 200 MeV p + ^{27}Al.

CHAPTER 5

Preequilibrium —Inverse Cross Sections

Below are relevant publications that result from the author's work pertaining to this chapter.

- L.M. Kerby and S. G. Mashnik, Total Reaction Cross Sections in CEM and MCNP6 at Intermediate Energies, Nuclear Instruments and Methods in Physics Research B **356-357** (2015) 135, arXiv:1505.00842;
- L.M. Kerby and S.G. Mashnik, Total Reaction Cross Section Models in CEM and MCNP6 in the Intermediate-Energy Range (>1 MeV), LANL Summer 2014 Internship Report, LANL Resport, LA-UR-14-26657 (August 2014);
- L.M. Kerby and S.G. Mashnik, Fiscal Year 2014 Report, LANL Report, LA-UR-14-27533 (November 2014).

Total reaction cross section models have a significant impact on the predictions and accuracy of spallation and transport codes. CEM03.03 and LAQGSM03.03, default event generators in MCNP6, each use such cross sections for different purposes. While total reaction cross sections are used throughout the transport and spallation models, there are two main utilizations. MCNP6 uses total reaction cross sections to determine where a reaction occurs (through the mean-free path length), then with what nucleus the projectile interacts with, and lastly what type of interaction it is (inelastic or elastic). CEM uses total reaction cross sections as *inverse* cross sections to predict what the excited nucleus emits. Phenomenological approximations of total reaction cross sections are also used by CEM03.03 as the default option for normalization of all results in the case of reactions induced by protons and neutrons, when CEM03.03 is used as a stand alone code, outside any transport codes; see details in Refs. [2, 19].

Having accurate total reaction cross section models in the intermediate energy region ($\sim$50 MeV to $\sim$5 GeV) is important for many different applications. Applications in space include astronaut radiation dosage, electronics malfunction analysis,

structural materials analysis, and Galactic Cosmic Rays (GCRs) shielding. Medical applications include hadron therapy for cancer [8], radiation shielding, medical isotope production, and high-radiation environment dosimetry. Other applications include accelerator design and simulation. In addition, implementing better inverse cross sections in CEM should provide more reliable predictions; that is, our current work should be useful also from an academic point of view, allowing us to better understand the mechanisms of nuclear reactions. Lastly, the 2008-2010 IAEA Benchmark of Spallation Models recommended an improvement to CEM's ability to predict the production of energetic light fragments [9, 10]. Our improvement of the inverse cross sections used by CEM03.03 addresses directly this point, both for a better description of light fragments, but also of nucleons.

The current inverse cross sections used in the preequilibrium and evaporation stages of CEM are based on the Dostrovsky *et al.* model, published in 1959 [113]. (For more information about the stages of CEM in its model of spallation reactions, see Ref. [2, 64, 19].) Better total reaction (*inverse*) cross section models are available now [114, 115, 116, 119, 120, 117, 118, 121, 122, 123, 124, 125].

MCNP6 uses an update of the Barashenkov and Polanski (B&P) cross section model [125] as described briefly in [126, 127] to calculate the mean-free path length for neutrons, protons, and light fragments up to ^{4}He. It uses a parameterization based on a geometric cross section for light fragments above ^{4}He. Implementing better cross section models in CEM and MCNP6 should yield improved results of particle spectra and total production cross sections, among other results. Our current results, upgrading the inverse cross section model in the preequilibrium stage of CEM, prove that this is, in fact, the case.

This cross section development work is part of a larger project aimed at enabling CEM to produce high-energy light fragments [64, 94, 95]. Figs. 5.1 and 5.2 illustrate two examples of results of that project: comparing results from CEM03.03 with an upgraded Modified Exciton Model (MEM) to results from CEM03.03 unmodified. For some reactions we obtained good results (see, e.g., Fig. 5.1), and for other reactions, while our results showed improvement, they could still be better (see, e.g., Fig. 5.2). We decided to upgrade the inverse cross section models used by CEM, in the preequi-

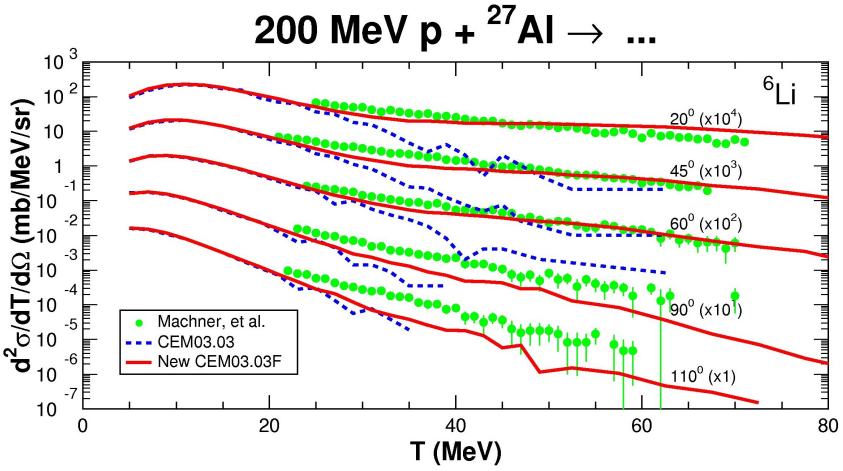

FIGURE 5.1: Comparison of experimental data by Machner *et al.* [11] (green circles) with results from the unmodified CEM03.03 (blue dotted lines) and the modified–MEM CEM03.03, we refer to here as CEM03.03F [94, 95] (red solid lines) for ^{27}Al(p,^{6}Li)X with incident proton energy of 200 MeV and for emission angles of 20°, 45°, 60°, 90°, and 110°.

librium stage, to improve such results further. As CEM is the default event generator in MCNP6 in the intermediate energy range, once these results were implemented into MCNP6, we see a corresponding improvement in MCNP6 as well.

5.1 BACKGROUND

As mentioned above, the current inverse cross sections in CEM are based on the Dostrovsky *et al.* model [113]. It is based on the strong absorption model and its general form is as shown in Eq. (5.1).

$$\sigma_{Dost.} = \pi r_0^2 A^{2/3} \alpha_j (1 - \frac{V_j}{T}). \tag{5.1}$$

The Dostrovsky *et al.* model was not intended for use above about 50 MeV/nucleon, and is not very suitable for emission of fragments heavier than ^{4}He. Better total reaction cross section models are available today, most notably the NASA model [114, 115, 116]. The NASA (or Tripathi *et al.*) model is also based on the strong absorption model and its general form is shown in Eq. (5.2). δ_T, X_m, and B_T are discussed more

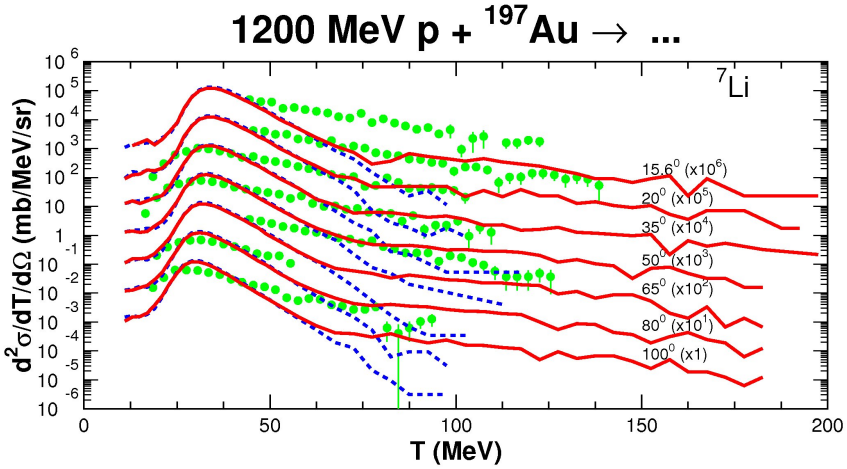

FIGURE 5.2: Comparison of experimental data by Budzanowski *et al.* [49] (green circles) with results from the unmodified CEM03.03 (blue dashed lines) and the modified-MEM CEM03.03, we refer to here as CEM03.03F [94, 95] (red solid lines) for ^{197}Au(p,^{7}Li)X with incident proton energy of 1200 MeV and for emission angles of 15.6°, 20°, 35°, 50°, 65°, 80°, and 100°. The 100°spectrum (the lower set) is shown unscaled, while the 80°, 65°, etc., down to 15.6°spectra are scaled up by successive factors of 10, respectively.

fully later, and defined in Eq. (5.7). The NASA cross section attempts to simulate several quantum-mechanical effects, such as the optical potential for neutrons (with X_m) and collective effects like Pauli blocking (through δ_T). (For more details, see Refs. [114, 115, 116].)

$$\sigma_{NASA} = \pi r_0^2 (A_P^{1/3} + A_T^{1/3} + \delta_T)^2 (1 - R_c \frac{B_T}{T_{cm}}) X_m \ , \tag{5.2}$$

where

r_0 is a constant related to the radius of a nucleus;

A_P is the mass number of the projectile nucleus;

A_T is the mass number of the target nucleus;

δ_T is an energy-dependent parameter;

R_c is a system-dependent Coulomb multiplier;

B_T is the energy-dependent Coulomb barrier;

T_{cm} is the colliding system center-of-momentum energy;

X_m is an optical model multiplier used for neutron-induced reactions.

There are other proposed total reaction cross section models, such as those by Shen, *et al.* [117], and Takechi, *et al.* [118], amongst others [125, 121, 122, 123, 124, 119, 120]. It should be noted that both the Shen model and the Kox model have projectile-target assymetry, as discussed in Ref. [128]. In Ref. [129], Sihver *et al*. explores a new total reaction cross section used in PHITS: the hybrid Kurotama model. This model is a combination of the Black Sphere model [121] and the NASA model [114, 115, 116]. Ref. [130] compares a number of different total reaction cross section models, most notably those in FLUKA, NASA, and several other recently developed models.

PHITS uses the NASA model as its default total reaction cross section model, but Shen can be specified as an option [130]. FLUKA uses a modified version of the NASA model as its total reaction cross section model [131]. GEANT4 has the option to use NASA, or a number of other total reaction cross section models such as Shen [117] or Sihver [132], or the Axen-Wellisch [133] total reaction cross section parameterizations for high-energy hadronic interactions. See Ref. [134, 135] for more details on the total reaction cross section models used in PHITS, FLUKA and GEANT4.

In the recent Ref. [136], Krylov et al., compares proton spectra as calculated by GEANT4, SHIELD, and MCNPX 2.6 for relativistic heavy-ion collisions. A newer (and better) version of MCNP is now available, but these results demonstrate the need for updated cross section models within CEM, LAQGSM, and MCNP6.

Stepan Mashnik with collaborators [137, 138] and Dick Prael with coauthors [127, 139] previously conducted at LANL an extensive comparison of the NASA [114, 115, 116], Tsang *et al.* [123], Dostrovsky *et al.* [113], Barashenkov and Polanski (using their code called CROSEC) [125], and Kalbach [124] systematics for total reaction (*inverse*) cross sections. Fig. 5.3 illustrates some results from the study [137]. Their results found that the NASA total reaction cross section model was superior, in general, to the other available models. See Ref. [127, 139, 137, 138, 97] for details of their findings.

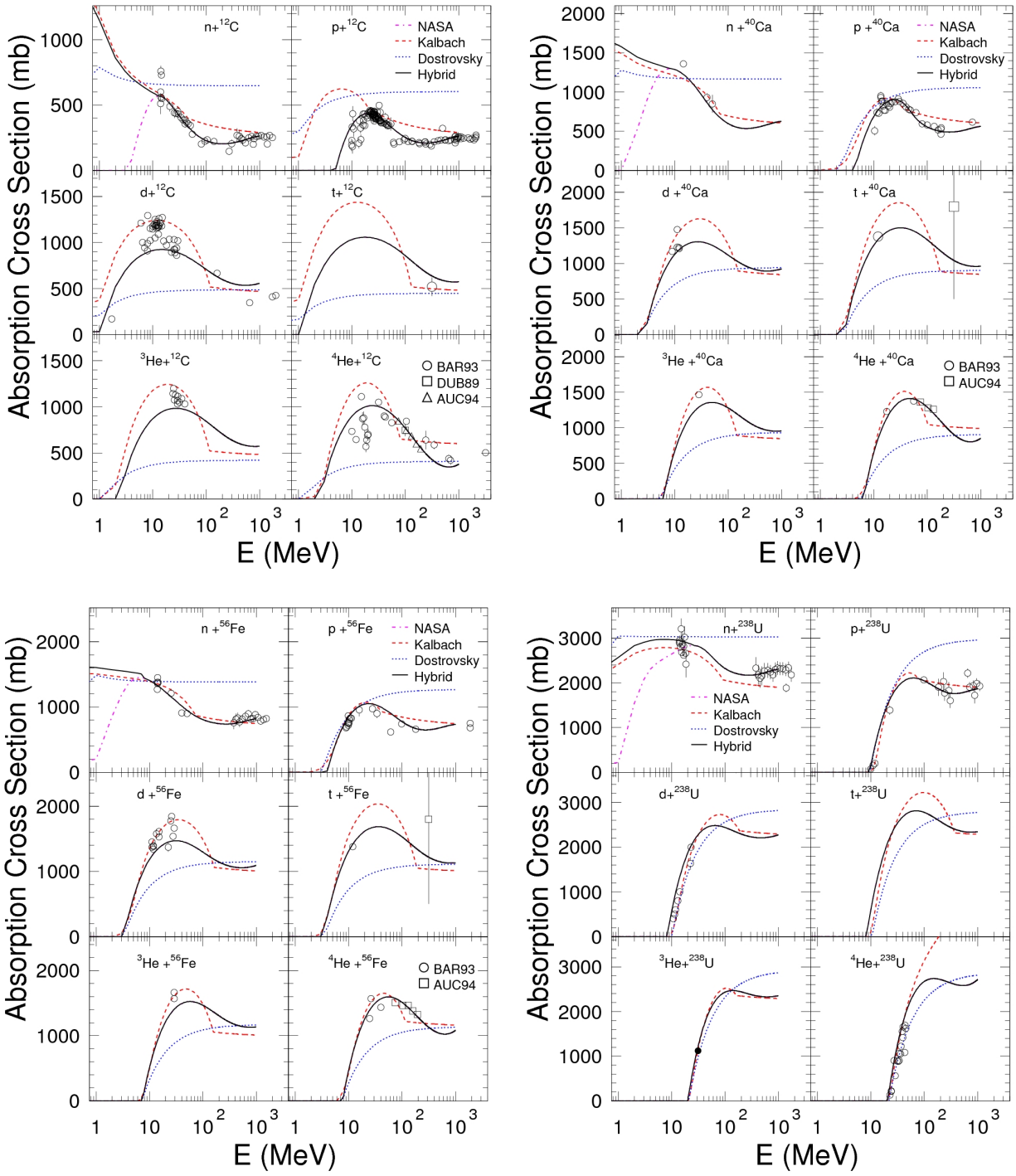

FIGURE 5.3: Absorption (inverse) cross section by energy for various reactions, as calculated in Ref. [137] by the NASA [114, 115, 116], Kalbach [124], and Dostrovsky *et al.* [113] systematics, as well as with a "Hybrid approach" suggested in [137] to account for both NASA [115] and Kalbach [124] systematics, in the case of neutron-induced reactions. "BAR93" shows experimental data from Ref. [65]; "DUB89" shows data from Ref. [140]; and "AUC94" shows data from Ref. [141].

5.2 COMPARISON OF TOTAL REACTION CROSS SECTION MODELS

We built in CEM03.03F the NASA model [114, 115, 116] and the models used in the preequilibrium (labeled as "Dostrovsky" in our figures below) and the evaporation (described with the code GEM2 by Furihata [31], therefore labeled in our figures below as "GEM2") stages of CEM03.03, and also compared reactions to calculations from the Barashenkov and Polanski (B&P) systematics [125], and, for comparison, to two neutron- and proton-induced reaction cross sections calculations by MCNP6 [4]. Note that MCNP6 uses currently an updated and improved version of the initial Barashenkov and Polanski (B&P) systematics [125], as outlined briefly in Refs. [126, 127], to simulate the mean-free path length of nucleons in matter.

5.2.1 *Neutron-Induced Reactions*

Fig. 5.4 displays the total reaction cross section for n + ^{208}Pb, as calculated by the NASA, Dostrovsky *et al.*, GEM2, and B&P models, and compared to calculations by MCNP6 and experimental data. There are several things to notice: 1) the Dostrovsky and GEM2 (also a Dostrovsky-based model) both approach asymptotic values very quickly–thus they are not as useful at their constant values, and 2) the NASA model, while much better at predicting the total reaction cross section throughout the energy region of projectiles, falls to zero at low energies in the case of neutrons, where we do not have Coulomb barriers. For this reason, we cannot use the NASA model as an approximation for inverse cross sections in the case of low-energy neutrons: neutrons are emitted with low energies, too. In the case of low energy neutrons, we use the Kalbach systematics [124], which proved to be a very good approximation for the inverse cross section of low-energy neutrons, as discussed in Ref. [137] and in subsection 5.3.1 below. Note that this problem of neutron cross sections was addressed first for the code CEM2k in Ref. [137], by combining the NASA systematics by Tripathi, Cucinota, and Wilson [114, 115, 116] and the Kalbach parameterization [124] into a FORTRAN routine called hybrid. We address this problem here, for our current CEM03.03F code, in a very similar way (see Ref. [97]).

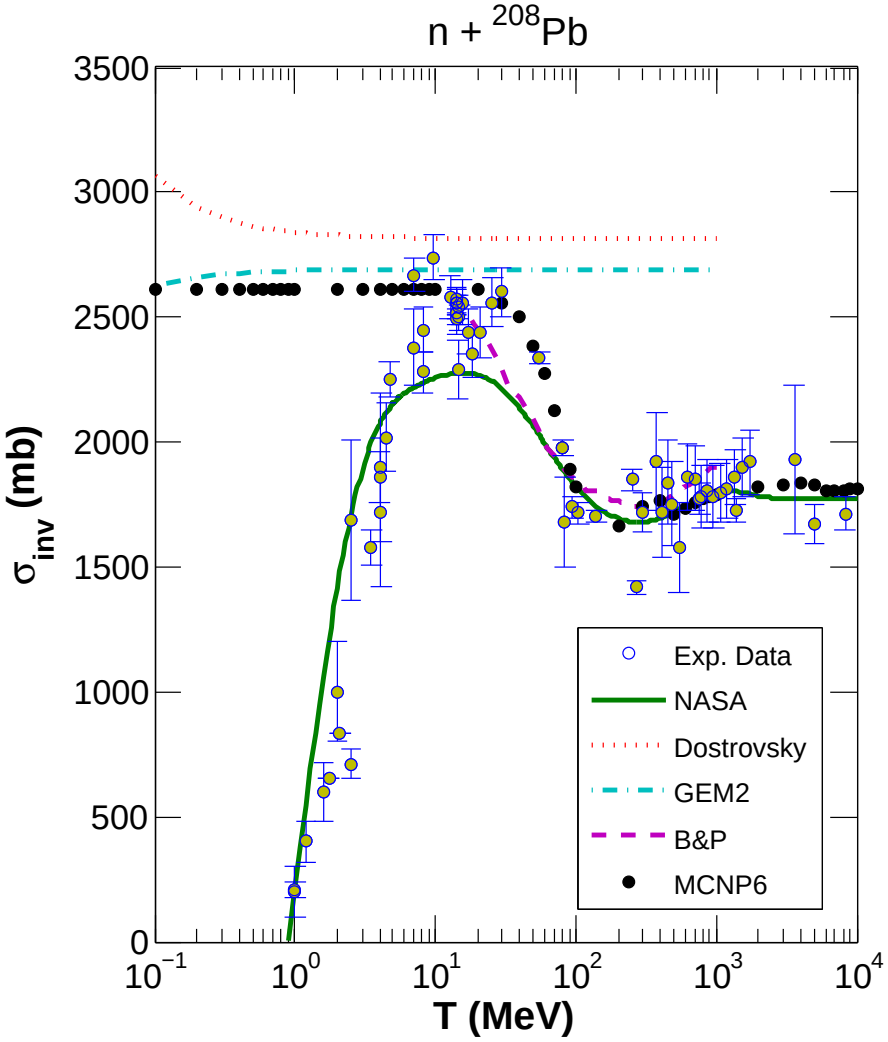

FIGURE 5.4: Reaction cross section for n + ^{208}Pb, as calculated by the NASA, Dostrovsky *et al.*, GEM2, and B&P models. The black dots are cross section calculations of MCNP6, and the yellow circles are experimental data [142, 143, 144, 145, 146, 147, 148, 149, 150, 151, 152].

See Ref. [97] for results of other neutron-induced reactions.

5.2.2 *Proton-Induced Reactions*

Fig. 5.5 illustrates calculated total reaction cross sections by the NASA, Dostrovsky *et al.*, GEM2, and B&P models, compared to calculations by MCNP6 and experimental data. The NASA model appears to be superior to the Dostrovsky-based models.

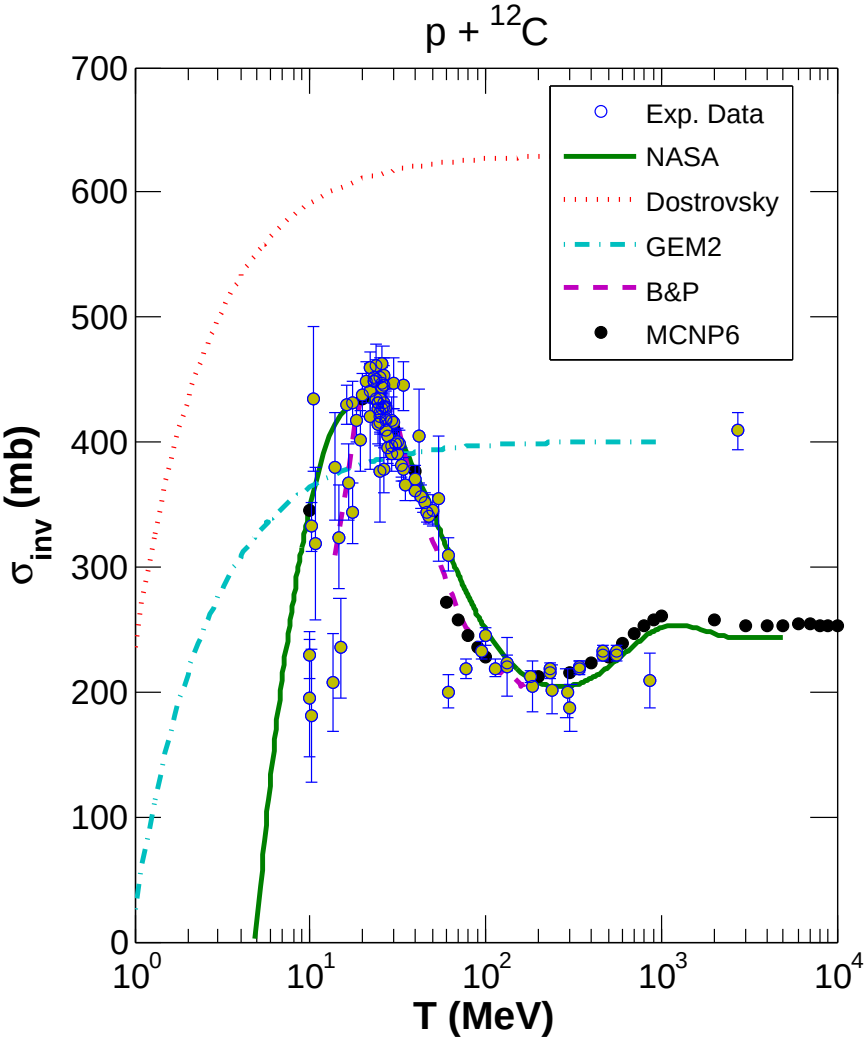

FIGURE 5.5: Reaction cross section for p + ^{12}C, as calculated by the NASA, Dostrovsky *et al.*, GEM2, and B&P models. The black dots are cross section calculations of MCNP6, and the yellow circles are experimental data [153].

As we can see from Figs. 5.4 and 5.5 on nucleons, as well as from examples on complex-particles and fragments heavier than ^{4}He presented below in Figs. 5.6 and 5.7, and in numerous figures published in Refs. [127, 137, 138, 139], the Barashenkov and Polanski approximations also agree very well with available data. For this reason, the B&P parametrization was chosen to be used for the calculation the total reaction cross sections in the transport code MCNP6 [4], and in several other transport codes, too, as far as we know. However, our numerous current comparisons for various reactions, as well as the voluminous results published in Refs. [127, 137, 138, 139],

show that, on the whole, the NASA approximation agree a little better with most of the available experimental data than the B&P systematics does.

See Ref. [97] for results of other proton-induced reactions.

5.2.3 *Heavy-Ion Induced Reactions*

We never tested before how CEM03.03 calculates inverse cross sections for light fragments (LF) heavier than ^{4}He. We address this question below.

Fig. 5.6 illustrates calculated total reaction cross sections by the NASA, Dostrovsky *et al.*, GEM2, and B&P models for the reactions α + ^{28}Si and ^{6}Li + ^{208}Pb, compared to experimental data.

Fig. 5.7 displays the total reaction cross section for ^{12}C + ^{12}C, as calculated by the NASA, Dostrovsky *et al.*, GEM2, and B&P models and compared to experimental data and to measured total charge-changing (TCC) cross sections. TCC cross sections should be $5\% - 10\%$ less than total reaction cross sections, as TCC cross sections do not include the neutron removal cross section.

See Ref. [97] for results of other heavy-ion-induced reactions.

We determined that the NASA cross section model fits the experimentally measured data, in general, better than the other models tested.

5.3 IMPLEMENTATION OF NASA CROSS SECTION MODEL INTO CEM03.03F

The implementation of the NASA cross section model into CEM involved adding Kalbach systematics for low-energy neutrons, updating the emission width calculation, and upgrading the emitted fragment kinetic energy simulation.

5.3.1 *Kalbach Systematics*

We added in CEM03.03F the Kalbach systematics [124] to replace the NASA inverse cross sections [114, 115, 116] for low-energy neutrons, similar to what was suggested and done in Ref. [137] for the code CEM2k. Fig. 5.8 displays the Kalbach systematics implementation for the cross section n + ^{208}Pb. At around 24 MeV and below, the

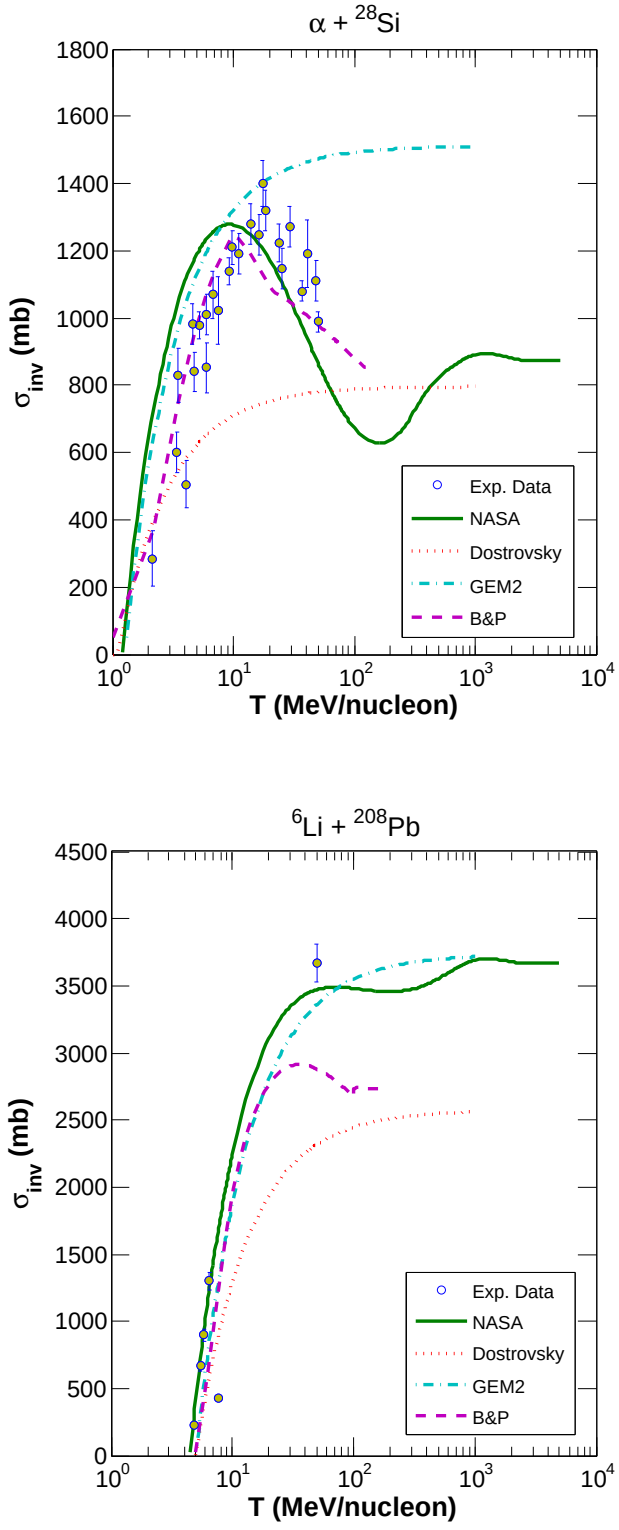

FIGURE 5.6: Reaction cross section for α + ^{28}Si and ^{6}Li + ^{208}Pb, as calculated by the NASA, Dostrovsky *et al.*, GEM2, and B&P models. The yellow circles are experimental data [154, 155, 156, 157, 158].

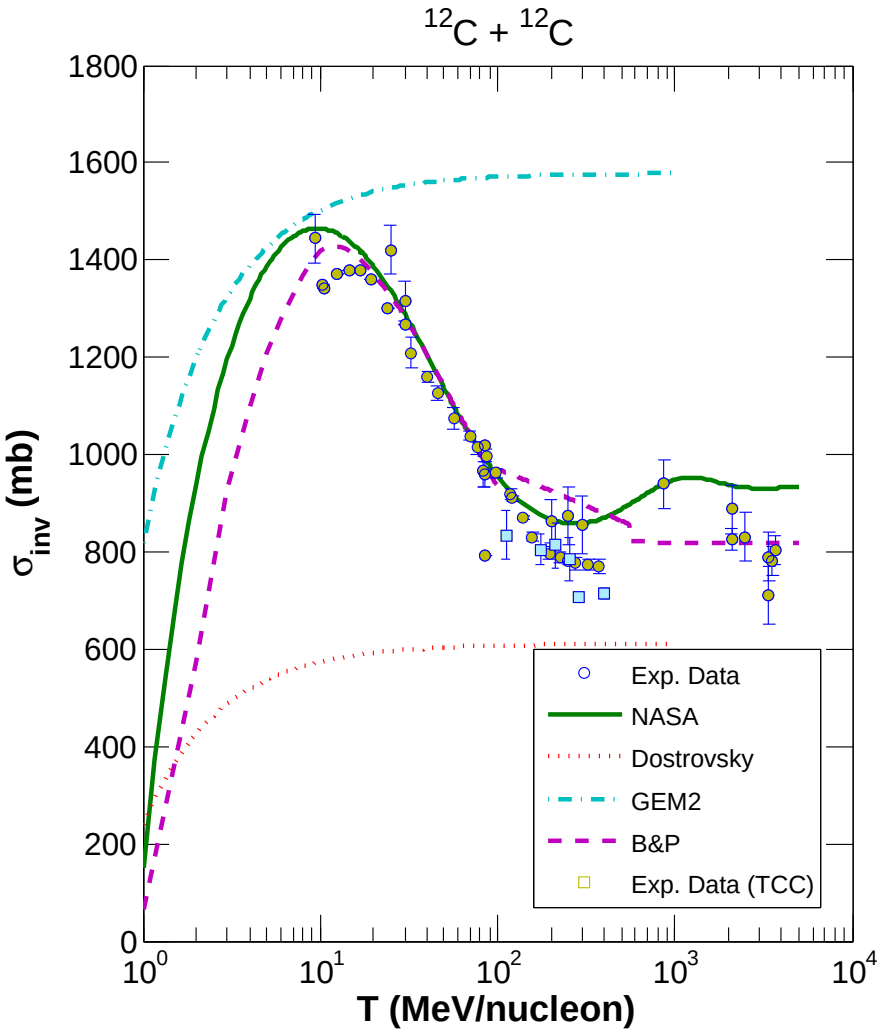

FIGURE 5.7: Reaction cross section for ^{12}C + ^{12}C, as calculated by the NASA, Dostrovsky *et al.*, GEM2, and B&P models. The yellow circles are experimental data [65, 159, 118] and the blue squares are total charge-changing cross section (TCC) measurements [160, 161].

calculation switches to Kalbach systematics, and uses the NASA model throughout the rest of the neutron-energy range. The Kalbach systematics is scaled to match the NASA model results at the switchpoint so as not to have a large jump.

As part of the Kalbach systematics implementation in CEM03.03F, switchpoints and scaling factors must be obtained for all possible residual nuclei, by mass number. Ref. [97] provides tables of these.

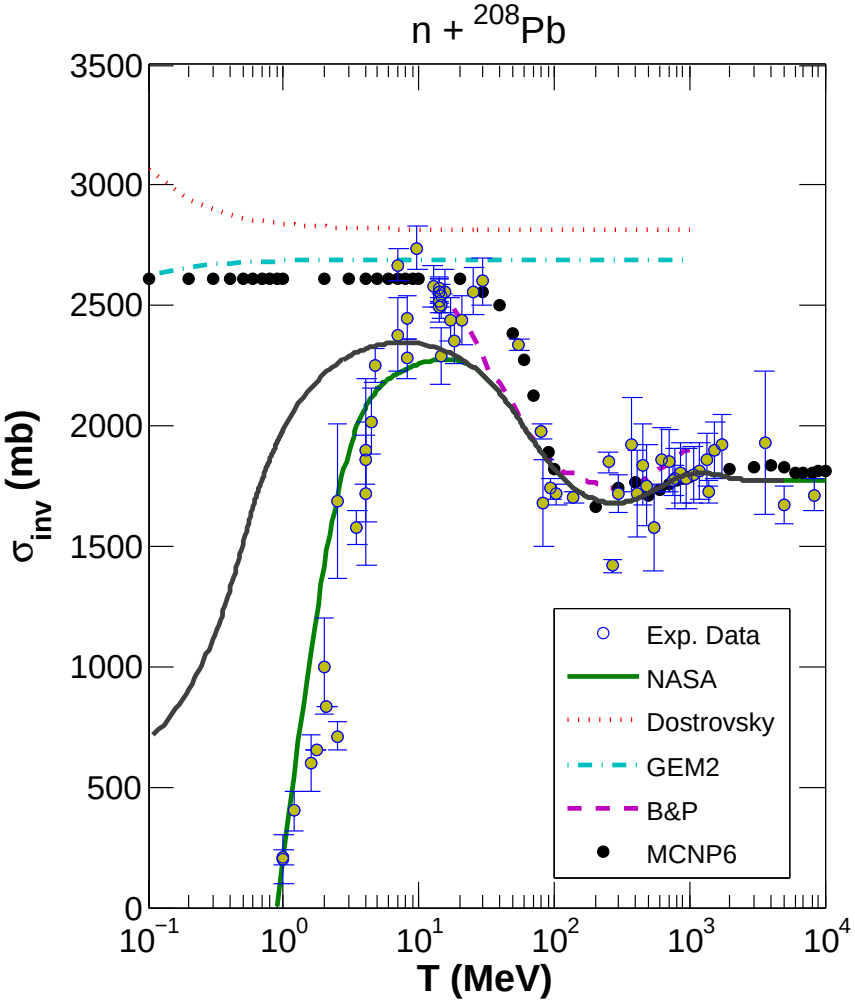

FIGURE 5.8: Reaction cross section for n + ^{208}Pb, as calculated by the NASA, NASA-Kalbach hybrid (black line), Dostrovsky *et al.*, GEM2, and B&P models, as indicated. The black dots are cross section calculations by MCNP6, and the yellow circles are experimental data from Refs. [142, 143, 144, 145, 146, 147, 148, 149, 150, 151, 152].

5.3.2 *Emission Width, Γ_j, Calculation*

CEM uses the inverse cross section, σ_j^{inv}, in determining what particles and/or fragments are emitted from the excited nucleus. We use the total reaction cross section as the best approximation for this inverse cross section. The emission width Γ_j, or

the probability of emitting fragment type j, is calculated according to Eq. (5.3). It is dependent upon σ_j^{inv} (see more details in Refs. [1, 2, 19]).

$$\Gamma_j(p,h,E) = \int_{V_j^c}^{E-B_j} \frac{2s_j+1}{\pi^2\hbar^3}\mu_j \Re(p,h)\frac{\omega(p-1,h,E-B_j-T)}{\omega(p,h,E)} T\sigma_j^{inv}(T)dT \ , \qquad (5.3)$$

where

p is number of particle excitons;
h is number of hole excitons;
E is internal energy of the excited nucleus (sometimes referred to as U);
s_j is the spin of the emitted particle j;
μ_j is the reduced mass of the emitted particle j;
ω is the level density of the n-exciton state;
B_j is the binding energy;
V_j^c is the Coulomb barrier;
T is the kinetic energy of the emitted particle j;
σ_j^{inv} is the inverse cross section; and
$\Re$ creates zero probability of emission if the number of particle excitons is less than the number of nucleons of particle j.

Eq. (5.3) is written in its simplest form, as is valid for neutrons and protons only. An extension of Eq. (5.3) for the case of complex particles and light fragments (LF) is described later on and in detail in Ref. [1].

In the "standard" (i.e., "old," for this study) calculation by CEM03.03, performed with a FORTRAN routine called gamagu2, therefore referred to below as "gamagu2," the Dostrovsky *et al.* form of the inverse cross section is simple enough so that for neutrons and protons this integral can be done analytically. However, for complex particles, the level density, ω, becomes too complicated (see details in Refs. [1, 2, 19]), therefore the integral is evaluated numerically. In this case, a 6-point Gaussian quadrature is used when the exciton number is 15 or less, and a 6-point Gauss-Laguerre quadrature is used when the number of excitons is over 15. We will soon see why the two different integration methods are needed.

In our current calculations we adopt here for CEM03.03F (performed with a FORTRAN routine called gamagu3, hereafter referred to as "gamagu3"), the NASA form of the cross section is too complicated and the integral is always calculated numerically. We use an 8-point Gaussian quadrature when the number of excitons is 15 or less, and an 8-point Gauss-Laguerre quadrature when the number of excitons is greater than 15.

The partial transmission probability λ_j, or the probability that a particle or a fragment of the type j will be emitted with kinetic energy T, is equal to the integrand of Eq. (5.3). For the emission of LF this is equal to

$$\begin{aligned}\lambda_j(p,h,E,T) =& \gamma_j \frac{2s_j+1}{\pi^2\hbar^3}\mu_j \Re(p,h)\frac{\omega(p-p_j,h,E-B_j-T)}{\omega(p,h,E)} \\ & \times \frac{\omega(p_j,0,T+B_j)}{g_j} T\sigma_j^{inv}(T)\ ,\end{aligned} \tag{5.4}$$

where

$$g_j = \frac{V(2\mu_j)^{3/2}}{4\pi^2\hbar^3}(2s_j+1)(T+B_j)^{1/2}\ . \tag{5.5}$$

See Ref. [162] for details on Eq. (5.5). For completeness sake, we write Eq. (5.4) (and also Eq. (5.6) below in the text) in their "complete form," as they should look in the case of complex particles and LF, but not in their "simplest" version needed only for nucleons as exemplified by Eq. (5.3). γ_j is the probability that the proper number of particle excitons will coalesce to form a type j fragment (also called γ_β in a number of early publications; see, *e.g.*, Refs. [163, 162, 164]). It is the subject of Chapter 6.

As an example, Fig. 5.9 shows λ_j for the emission of neutrons from a ^{198}Au excited nucleus, with an internal nucleus energy U of 200 MeV, using either the Dostrovsky *et al.* or NASA cross section. The top plot is for 55 excitons and the bottom plot is for 10 excitons. Notice that for high exciton number, λ_j becomes more concentrated in the low-energy region. Table 5.1 displays the abscissas for an 8-point Gaussian and an 8-point Gauss-Laguerre quadrature. For a small number of excitons (≤ 15) the Gaussian quadrature performs adequately. However, we see that in the 55-exciton case the λ_j becomes negligible by about 30 MeV, requiring a different integration method. For

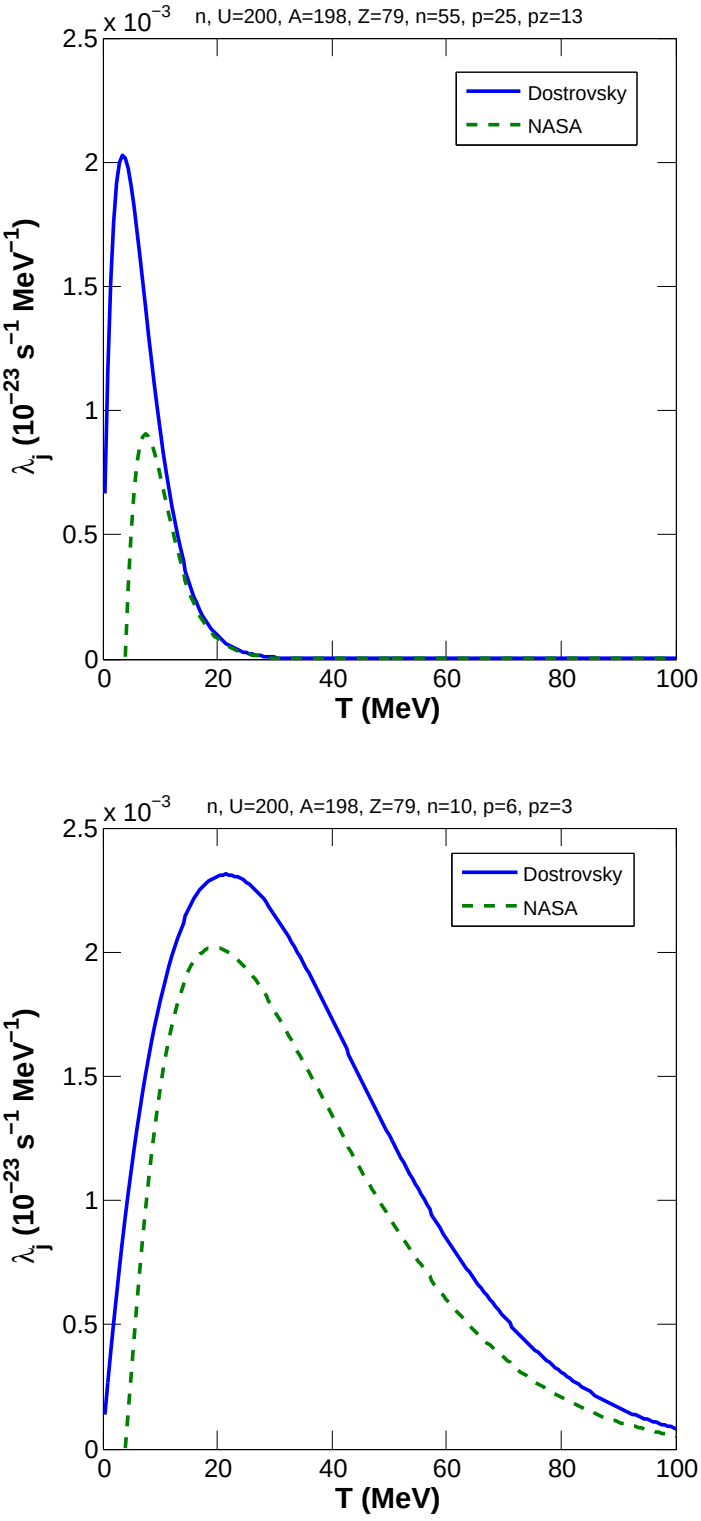

FIGURE 5.9: λ_j as a function of the kinetic energy of the emitted neutron, from an excited ^{198}Au nucleus with U = 200 MeV and 55 excitons, 25 particle excitons, and 13 charged particle excitons (top plot) and 10 excitons, 6 particle excitons, and 3 charged particle excitons (bottom plot).

high-exciton number the Gauss-Laguerre integration method is a much better choice than the simple Gaussian.

TABLE 5.1: 8-point Gaussian and Gauss-Laguerre sampling points

8-pt Gaussian	8-pt Gauss-Laguerre
3.84 MeV	0.428 MeV
19.7 MeV	2.27 MeV
45.9 MeV	5.66 MeV
79.0 MeV	10.7 MeV
114. MeV	17.7 MeV
148. MeV	27.1 MeV
174. MeV	39.6 MeV
190. MeV	57.5 MeV

Fig. 5.10 shows a comparison of the simple Gaussian and Gauss-Laguerre quadratures for 55 excitons. This figure also displays λ_j for the NASA-Kalbach cross section. Notice that the NASA-Kalbach has much higher values of λ_n at the low end of the spectrum than the pure NASA. The purple dots are the 8-pt Gaussian quadrature and the black dots are the 8-pt Gauss-Laguerre quadrature. The Gaussian was exceptionally fortunate in that it struck the peak with its one low-end point. However, this leads to significant overestimation of λ_j down the tail. The Gauss-Laguerre underestimates the peak but then overestimates slightly along the tail. Even though it is clear this is not a very close fitting of λ_j, changing to a 10-pt Gauss-Laguerre only yielded a 0.2% difference. A future project could include investigating the behavior of λ_j across the variable landscape, and implementing an adaptive quadrature scheme. However, whatever numerical integration method we use, it must be fast as this integral is calculated hundreds of times for every event, and therefore billions of times for a typical simulation.

Fig. 5.11 shows the plots of Γ_j as a function of the internal energy of the excited nucleus for emitted neutrons, protons, and ^{4}He from an excited ^{198}Au nucleus with 55 excitons, 25 particle excitons, and 13 charged particle excitons. "Gamagu2" shows the old CEM03.03 Γ_j calculation results. "Gamagu3" shows the results of our new calculations, using either the Dostrovsky *et al.* or NASA inverse cross sections. Note that "Gamagu2" should be very similar to "Gamagu3-Dostrovsky" because the

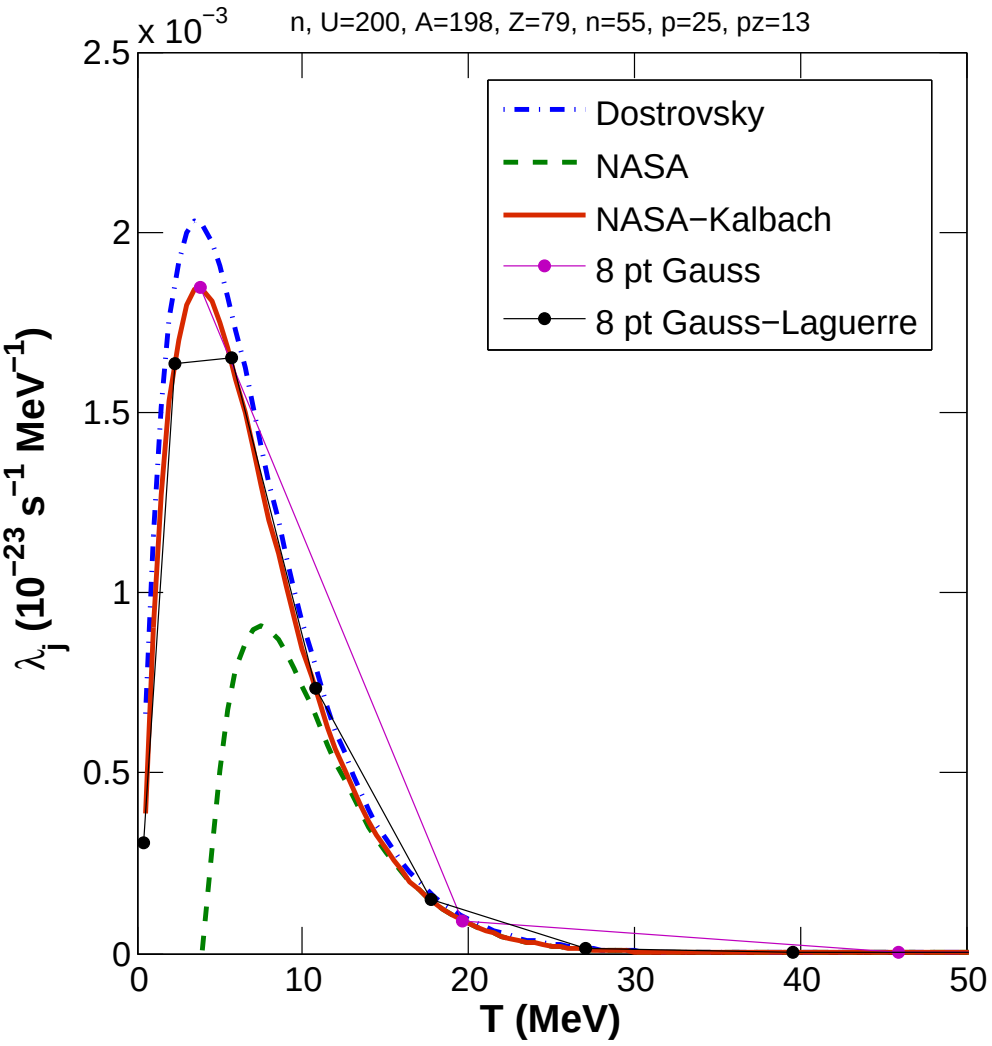

FIGURE 5.10: λ_j as a function of the kinetic energy of the emitted neutron, from an excited ^{198}Au nucleus with U = 200 MeV and 55 excitons, 25 particle excitons, and 13 charged particle excitons.

only significant difference is the method of integration. The proton and neutron Γ_j differences between "Gamagu2" and "Gamagu3-Dostrovsky" arise from numerical integration used in our new FORTRAN routine gamagu3 of CEM03.03F versus an analytical calculation used in the CEM03.03 FORTRAN routine gamagu2.

Better integration methods could be investigated at a later time. However, current integration methods are sufficient because individual Γ_j precision is not extremely important for choosing what type of particle/LF j will be emitted. In contrast to analytical preequilibrium models, the Monte Carlo method employed by our CEM

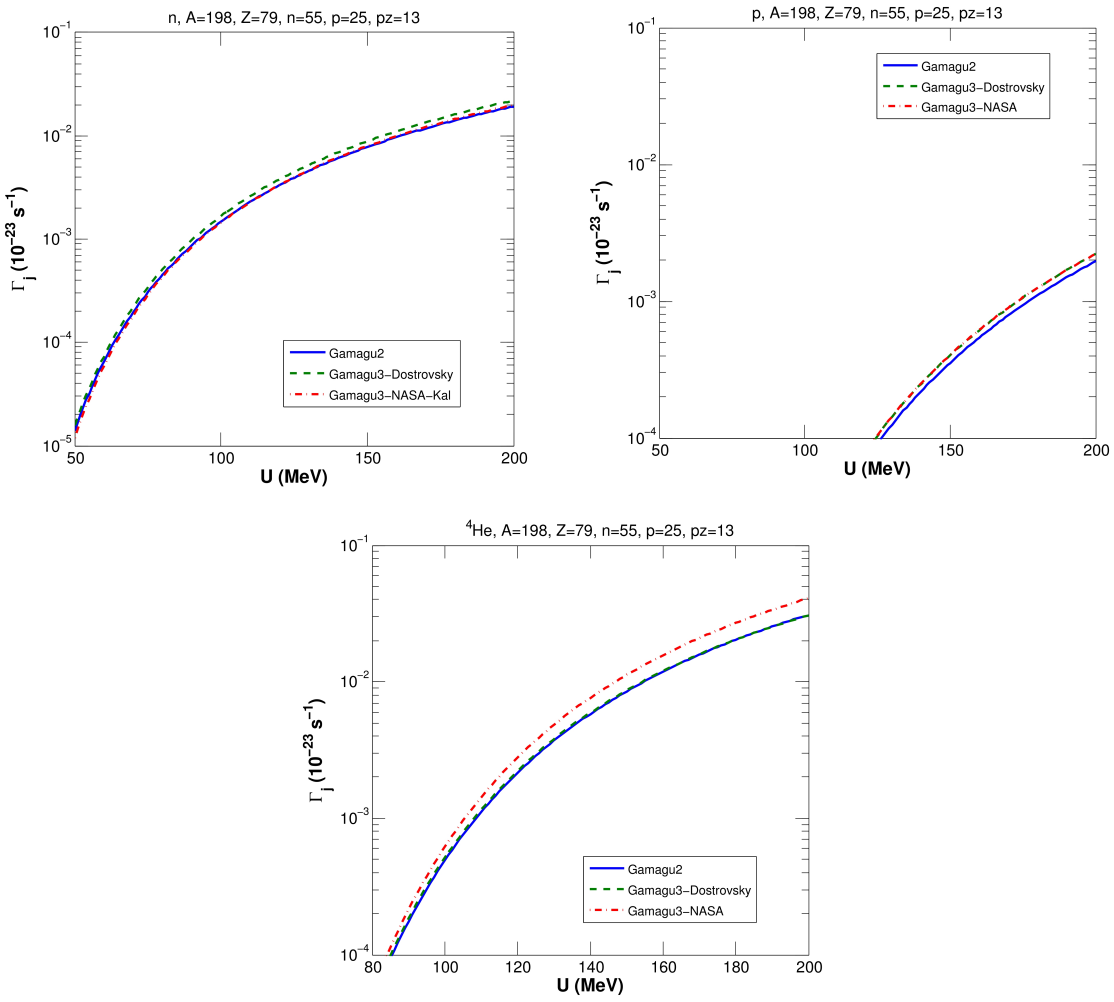

FIGURE 5.11: Γ_j as a function of the internal energy of the excited nucleus for emitted neutrons, protons, and ^{4}He from an excited ^{198}Au nucleus with 55 excitons, 25 particle excitons, and 13 charged particle excitons.

uses the ratios of Γ_j to the sum of Γ_j over all j. That is, if we estimate all Γ_j with the same percentage error, the final choice of the type j of particle/LF to be emitted as simulated by CEM would be the same as if we would calculate all Γ_j exactly. We think that this is the main reason why CEM provided quite reasonable results using the old Dostrovsky *et al.* approximation for inverse cross sections, in spite of the fact that, as we see from Figs. 5.3–5.8, individual inverse cross sections calculated with the Dostrovsky *et al.* method are not good enough in a large range of energies. The ratios $\Gamma_j / \sum_j(\Gamma_j)$ were probably estimated well enough, providing a reasonable Monte Carlo sampling of j.

5.3.3 *Kinetic Energy Simulation*

Once a fragment type j has been chosen for emission, the kinetic energy of this fragment needs to be determined. This is done by sampling the kinetic energy from the λ_j distribution. Our new λ_j, with the NASA cross section, is:

$$\begin{aligned}\lambda_j(p,h,E,T) =& \gamma_j \frac{2s_j+1}{\pi^2\hbar^3}\mu_j \Re(p,h)\frac{\omega(p-p_j,h,E-B_j-T)}{\omega(p,h,E)} \\ &\times \frac{\omega(p_j,0,T+B_j)}{g_j} T\pi r_0^2 \\ &\times (A_P^{1/3}+A_T^{1/3}+\delta_T)^2(1-R_c\frac{B_T}{T_{cm}})X_m(T).\end{aligned} \tag{5.6}$$

where g_j is defined by Eq. (5.5) and

$$\begin{aligned}\delta_T = 1.85S + \frac{0.16S}{T_{cm}^{1/3}} - D[1-e^{-T/T_1}] - 0.292e^{-T/792} + \frac{0.91(A_T-2Z_T)Z_P}{A_T A_P}, \\ X_m = 1 - X_1 exp\left(\frac{-T}{X_1(1.2+1.6[1-exp(T/15)])}\right), \\ B_T = 1.44 Z_P Z_T / \left(r_P + r_T + \frac{1.2(A_P^{1/3}+A_T^{1/3})}{T_{cm}^{1/3}}\right).\end{aligned} \tag{5.7}$$

The details of r_0, R_c, S, D, T_1, r_P, and r_T can be found in [116]. Note that the NASA inverse cross sections contain dependences on both the lab-reference-frame kinetic energy (T) and the center-of-momentum-reference-frame kinetic energy (T_{cm}). The relativistic transformation between the two is not trivial. In addition, T is in units of MeV/nucleon in the NASA inverse cross sections, while T_{cm} is in units of MeV. The level density, ω, also contains T-dependences, also in units of MeV. Finally, as noted above, for neutrons we use a NASA-Kalbach ("hybrid") inverse cross section in place of the pure NASA approximation. To conclude, the energy-dependence of λ_j for our new NASA-Kalbach inverse cross section approximation is very complicated, which affects the method we chose to sample T_j, as discussed below.

To sample T_j uniformly from the λ_j distribution using the Monte Carlo method, we must first find the maximum of λ_j. In CEM03.03, this is done analytically using the

derivative of λ_j with respect to T_j, due to the simple nature of the energy-dependence in the systematics by Dostrovsky *et al.*. As previously explained, however, the NASA cross section energy-dependence is extremely complicated and therefore we find the maximum of λ_j numerically using the Golden Section method. This also provides us flexibility in the future to modify λ_j without consequence to our kinetic energy module.

After finding the maximum value of λ_j, the kinetic energy of the emitted fragment j is uniformly sampled from the λ_j distribution using a Gamma distribution (shape parameter $\alpha = 2$) as the comparison function. Fig. 5.12 illustrates results for the probability of emitting ^{6}Li with a given kinetic energy T_{Li}. Probabilities from the λ_j distributions with the NASA inverse cross sections differ slightly from those with the Dostrovsky *et al.* inverse cross sections primarily because the NASA coulomb barriers are based on T_{cm}, as opposed to T.

5.4 RESULTS

Our preliminary results are promising. Fig. 5.13 shows the double differential cross section for the production of ^{6}Li and ^{7}Be from the reaction 200 MeV p + ^{59}Co. Notice the improved agreement with data in the high-energy tails. This reaction also highlights the importance of eventually upgrading the inverse cross sections used in the evaporation stage of CEM as well. The evaporation stage produces the peak of the spectra, which for this reaction is too low, especially for ^{7}Be. With the implementation of the NASA inverse cross sections in the preequilibrium stage we see improved agreement with data in the high-energy tails, but in order to achieve improved agreement in the peak we would need to also implement the NASA inverse cross sections in the evaporation stage. We plan to do this in the future.

For another example of our results, Fig. 5.14 displays the double differential cross section for the production of ^{6}He and ^{7}Li from the reaction 1200 MeV p + ^{197}Au. The blue dashed lines are the expanded-MEM (i.e., CEM03.03F) results with the Dostrovsky *et al.* inverse cross sections, and the red solid lines are results by CEM03.03F with the upgraded NASA-Kalbach (i.e., "hybrid") inverse cross sections. The green circles

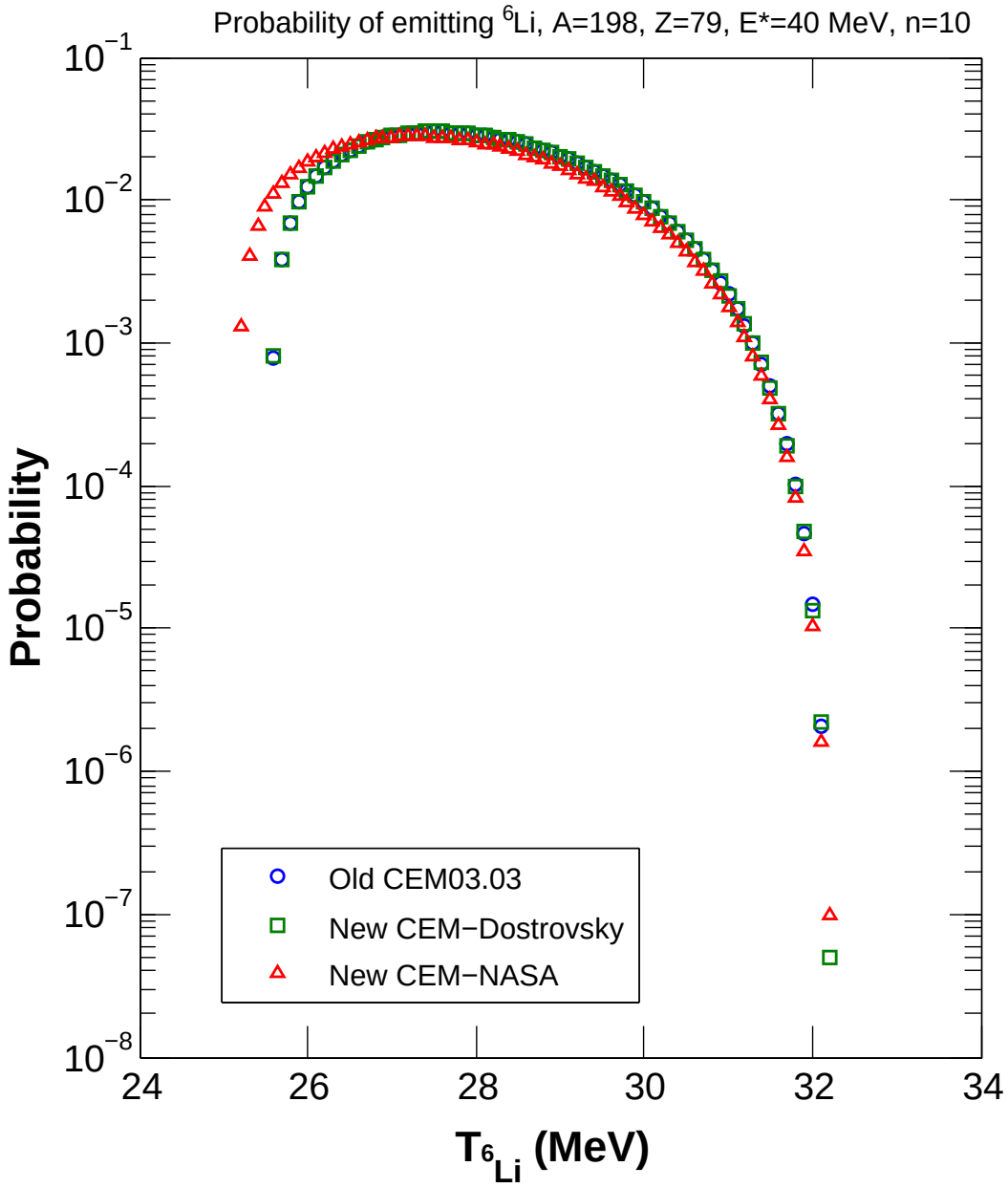

FIGURE 5.12: The normalized probability of emitting ^{6}Li with a given kinetic energy T_{Li}, simulated using the Monte Carlo method according to Eq. 5.6 in the preequilibrium stage. The circles are results from the old kinetic energy subroutine; the squares are results from the new kinetic energy subroutine using the Dostrovsky *et al.* inverse cross section; the triangles are from the new kinetic energy subroutine using the NASA inverse cross section.

are experimental data from Ref. [49]. We see an improved accuracy in the high-energy tails of spectra calculated with the NASA inverse cross sections, although some of the results are too hard and there is a dip in the spectra at 50–75 MeV. We would like

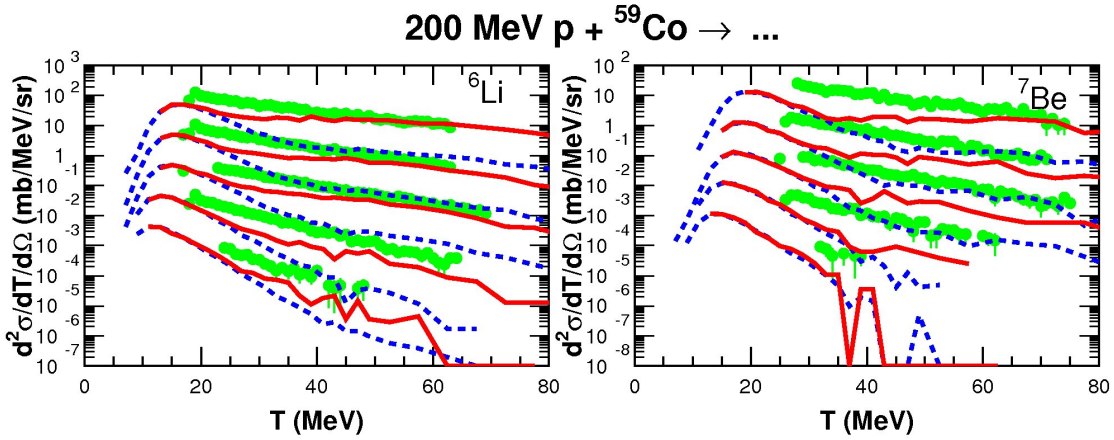

FIGURE 5.13: Double differential cross section for the production of ^{6}Li and ^{7}Be from the reaction 200 MeV p + ^{59}Co, for the angles of 20°, 45°, 60°, 90°, and 110°. The 110° spectra (the lower sets) are shown unscaled, while the 90°, 60°, 45°, and 20° spectra are scaled up by successive factors of 10, respectively. The blue dashed lines are the expanded-MEM (i.e., CEM03.03F) results with the Dostrovsky *et al.* inverse cross sections, and the red solid lines are results by CEM03.03F with the upgraded NASA-Kalbach (i.e., "hybrid") inverse cross sections. The green circles are experimental data by Machner, *et al* [11].

to note a recent paper by A. Boudard *et al.* [41], which obtained very similar results for ^{7}Li using INCL4.6 + ABLA07, and similar results for ^{6}He but with a little lower evaporation peak.

5.5 CONCLUSION

The inverse cross section approximation in the preequilibrium and evaporation stages of CEM03.03 is based on the Dostrovsky *et al.* inverse cross section model. Better cross section systematics are available at present. We performed a comparison of several inverse cross section models and determined that the NASA (Tripathi, *et al.*) approximation is, in general, the most accurate when compared with experimental data.

We implemented the NASA inverse cross section model into the preequilibrium stage of CEM03.03F. This included writing FORTRAN modules containing the NASA total reaction cross section and coulomb barrier approximations, adding Kalbach systematics for low-energy neutron inverse cross sections, re-writing the Γ_j routines (in-

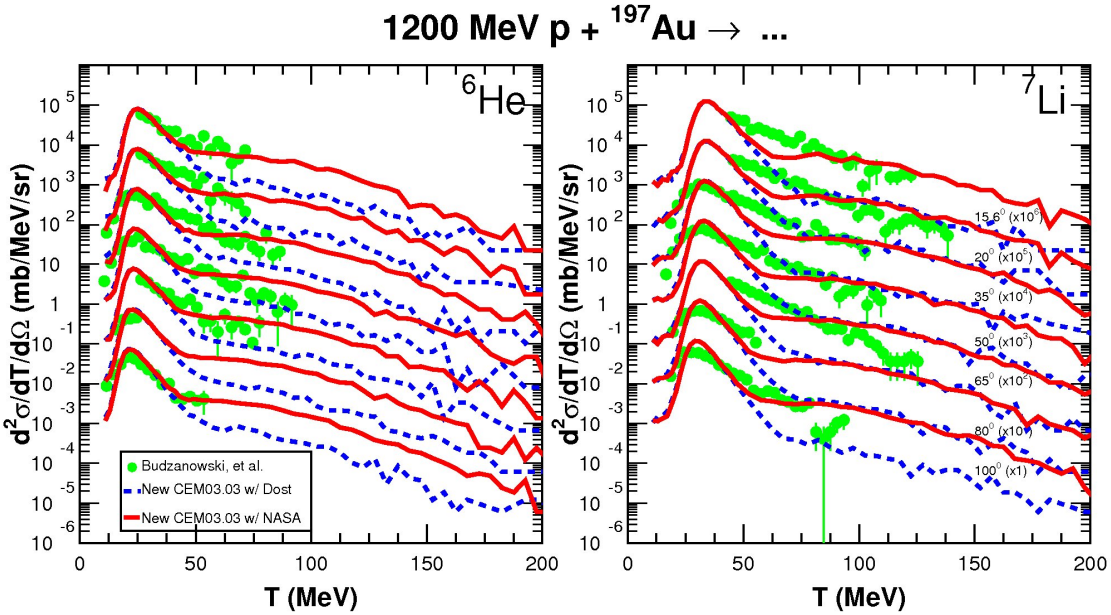

FIGURE 5.14: Double differential cross section for the production of ^{6}He and ^{7}Li from the reaction 1200 MeV p + ^{197}Au, for the angles of 15.6°, 20°, 35°, 50°, 65°, 80°, and 100°. The 100° spectra (the lower sets) are shown unscaled, while the 80°, 65°, etc., down to 15.6° spectra are scaled up by successive factors of 10, respectively. The blue dashed lines are the expanded-MEM (i.e., CEM03.03F) results with the Dostrovsky *et al.* inverse cross sections, and the red solid lines are results by CEM03.03F with the upgraded NASA-Kalbach (i.e., "hybrid") inverse cross sections. The green circles are experimental data from Ref. [49].

cluding transforming them into modular FORTRAN), adding Gauss-Laguerre quadrature for cases of high exciton number, and re-modeling the selection of particle or light fragment kinetic energy. These technical improvements lead to greater flexibility and robustness, and future upgrades can be made easily.

Our preliminary results are promising and indicate improved agreement with experimental data using the NASA inverse cross section model versus the Dostrovsky *et al.* approximation.

There are several implications of this work on MCNP6. CEM03.03 is the default event-generator in MCNP6 for high-energy collisions induced by nucleons, pions, and gammas at energies up to several GeVs. Improvements to the CEM inverse cross sections should, therefore, result in improved predictions of particle spectra and total

production cross sections, especially above ∼100 MeV and for fragments heavier than ^{4}He, among other results.

MCNP6 uses the updated Barashenkov and Polanski total reaction cross section systematics to simulate the mean-free path of neutrons, protons, and light fragments up to ^{4}He. It uses a parameterization based on a geometric cross section for fragments heavier than ^{4}He. Possible direct improvement of MCNP6 may be obtained by replacing the Barashenkov and Polanski model with NASA systematics and by replacing the geometric cross section approach with the better NASA model. We hope to do this in the future.

Future recommendations include investigating adaptive quadrature and upgrading the inverse cross section model used in the evaporation stage to the NASA-Kalbach (hybrid) cross sections.

CHAPTER 6

PREEQUILIBRIUM —γ_j MODEL

Below are relevant publications that result from the author's work pertaining to this chapter.

- L.M. Kerby and S.G. Mashnik, A New Model for the Condensation Probability, γ_j, in CEM, LANL Report, LA-UR-15-22370 (April 2015).

With the expansion of the preequilibrium model to allow emission of light fragments up to ^{28}Mg complete, the implementation of the NASA-Kalbach total reaction cross section into the preequilibrium stage inverse cross section, and the expansion of the Coalescence Model, we turned our attention to recalibrating γ_j. This process is long and involves the re-fitting of all available reliable experimental data. We concluded this process for most available proton-induced and neutron-induced reactions. Our results are encouraging.

The "condensation" probability, γ_j, is an important variable in the preequilibrium stage of nuclear spallation reactions. It represents the probability that p_j excited nucleons (excitons) will "condense" to form complex particle type j in the excited residual nucleus. It has a significant impact on the emission width, or probability of emitting fragment type j from the residual nucleus [163, 165, 110]. This paper explores the formulation of a new model for γ_j, one which is energy-dependent, and which provides improved fits compared to experimental fragment spectra.

6.1 BACKGROUND

This γ_j Model is part of a larger project [166, 102, 96, 97, 64, 94, 95] aimed at producing high-energy light fragments (LF) in nuclear spallation reactions simulated with CEM03.03 and LAQGSM03.03 [3, 2], which are the default event generators within MCNP6 [4] for high-energy nuclear reactions ($>$ 150 MeV).

The preequilibrium interaction stage of nuclear reactions is considered by our current CEM and LAQGSM in the framework of the latest version of the Modified

Exciton Model (MEM) [15, 16] as described in Ref. [20]. At the preequilibrium stage of a reaction, we take into account all possible nuclear transitions changing the number of excitons n with $\Delta = +2$, -2, and 0, as well as all possible multiple subsequent emissions of n, p, d, t, ^{3}He, and ^{4}He, for the current version CEM03.03. Our latest upgrades, called version CEM03.03F, include an expansion of the preequilibrium stage to allow for emission of heavy clusters up to ^{28}Mg. The corresponding system of master equations describing the behavior of a nucleus at the preequilibrium stage is solved by the Monte-Carlo technique [1].

Our new CEM03.03F considers the possibility of fast heavy cluster emission at the preequilibrium stage of a reaction in addition to the emission of nucleons and light fragments up to ^{4}He. We assume that in the course of a reaction p_j excited nucleons (excitons) are able to condense with probability γ_j forming a complex particle which can be emitted during the preequilibrium state. The "condensation" probability γ_j can be calculated from first principles, but such a calculation is not feasible given our Monte Carlo computation time limitations. γ_j is, therefore, estimated as the overlap integral of the wave function of independent nucleons with that of the complex particle (see details in [1]):

$$\gamma_j \simeq p_j^3 (p_j/A)^{p_j - 1} \ . \tag{6.1}$$

This is a rather crude estimate. As is frequently done (see e.g., Refs. [162, 164]), the values of γ_j are taken from fitting the theoretical preequilibrium spectra to the experimental ones. In CEM, to improve the description of preequilibrium complex-particle emission, we estimate γ_j by multiplying the estimate provided by Eq. 6.1 by an empirical coefficient $F_j(A, Z, T_0)$ whose values are fitted to available nucleon-induced experimental complex-particle spectra. Therefore, our new equation for γ_j with this coefficient is shown in Eq. 6.2:

$$\gamma_j = F_j p_j^3 \left(\frac{p_j}{A} \right)^{p_j - 1} \ . \tag{6.2}$$

Values of F_j for d, t, ^{3}He, and ^{4}He needed to be re-fit after our upgrades to the inverse cross section and coalescence models; and new values of F_j needed to be obtained

for heavy clusters, up to ^{28}Mg, after we expanded preequilibrium emission to include these heavy clusters.

Previously, γ_j had been formulated with no energy dependence [163, 165, 167]. We accordingly expect energy to be the largest factor in our model for F_j. Lastly, the importance of γ_j can be seen in the calculation of the emission width, Γ_j, for complex fragments, represented by Eq. 6.3:

$$\Gamma_j(p,h,E) = \int_{V_j^c}^{E-B_j} \gamma_j \frac{2s_j+1}{\pi^2\hbar^3}\mu_j \Re(p,h)\frac{\omega(p-p_j,h,E-B_j-T)}{\omega(p,h,E)} \times \frac{\omega(p_j,0,T+B_j)}{g_j} T\sigma_j^{inv}(T)dT \ , \tag{6.3}$$

where:

p is number of particle excitons;

h is number of hole excitons;

E is internal energy of the excited nucleus (sometimes referred to as U);

B_j is the binding energy of particle j;

V_j^c is Coulomb barrier of particle j;

γ_j is probability that the proper number of particle excitons will coalesce to form a type j fragment (also called γ_β in a number of early publications; see, *e.g.*, Refs. [163, 162, 164]);

s_j is the spin of the emitted particle j;

μ_j is the reduced mass of the emitted particle j;

$\Re$ creates zero probability of emission if the number of particle excitons is less than the number of nucleons in particle j;

ω is the level density of the n-exciton state;

T is the kinetic energy of the emitted particle j;

σ_{inv} is the inverse cross section.

The values for γ_j directly impact the emission width, which in turn determines the amount of fragment production.

6.2 STATISTICAL ANALYSIS

An increase or decrease in F_j generally leads to an increase or decrease in the emission of fragment type j, especially in the high-energy tails. We fit these values of F_j so that our CEM03.03F results matched experimental data as closely as possible. The F_j values we obtained, for several hundred reactions, are available in Appendix A. The results for predicted fragment spectra using these F_j fitted values were plotted against experimental data and predicted results from the original CEM03.03, for the several hundred reactions we fit, and are available in [168]. We do not show them here to conserve space.

With our data set complete, we can analyze it with the statistical programming language *R* [169]. We first look at F_j values for proton-induced reactions. Fig. 6.1 displays values of F_j according to incident proton energy. Two effects become apparent in this graph. First, F_j appears to have an exponentially decreasing energy dependence. This energy dependence makes sense considering the physics of nuclear reactions. We consider in this F_j Model the incident energy of the incoming proton, not the excitation energy of the residual nucleus at the time of preequilibrium, and after a certain incident energy we expect the residual nucleus energy to not change significantly as the incident energy continues to increase: *i.e.*, the amount of energy deposited in the target nucleus reaches a saturating limit and increasing the incident proton energy further does not lead to significantly greater residual nucleus energy. This idea is analogous to "limiting fragmentation" [82, 170]. In addition, CEM accounts for the IntraNuclear Cascade, preequilibrium, evaporation/fission, Fermi break-up, and coalescence mechanisms of nuclear reactions, but does not account for pick-up and knock-out reactions. Pick-up and knock-out mechanisms are especially important at low energies, and therefore, the increase in F_j at lower incident energies can be attributed to "compensating" for these missing physics in CEM. Furthermore, CEM does not account for some nuclear structure effects important at low energies, and for some reactions, also at high energies. Lastly, CEM, just as any other model, is "only a model," and probably misses some other aspects of the physics. For these reasons, we need to look at our "model" for γ_j in CEM philosophically, understanding that in some energy/target-size regions, it does not have exactly the right meaning of the

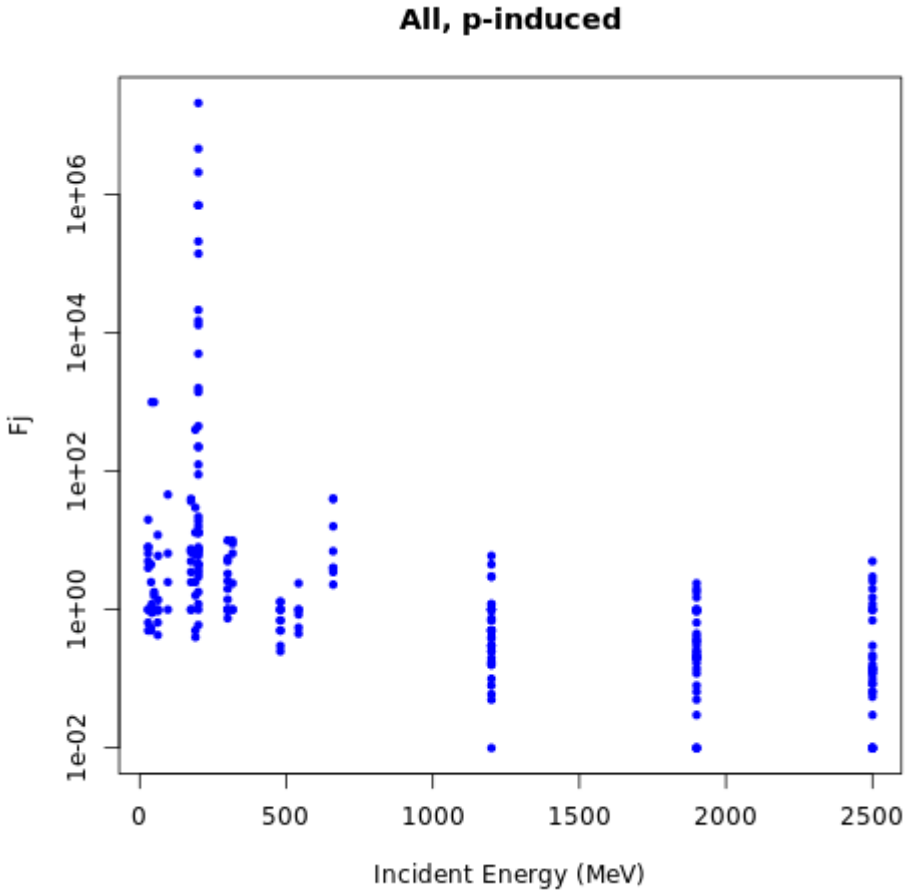

FIGURE 6.1: Values of F_j according to incident proton energy (MeV).

condensation probability, but also contains a component to counterbalance physics not accounted for in CEM.

The second effect we see from Fig. 6.1 are the "stacks" of F_j values at each energy; we will see that these correspond to different emitted fragment sizes, and therefore F_j is also dependent on the emitted fragment. Fig. 6.2 displays the incident-energy dependence of F_j for select emitted fragments individually. The "stacks" which occur in Fig. 6.2 are largely attributable to varying target sizes.

Fig. 6.3 displays the F_j values according to target atomic size. From this graph there is no clear dependence on target mass number. However, we suspected that if we separated out the energy dependence and fragment-size dependence, that we could uncover a dependence on target mass number. We first plotted F_j values by

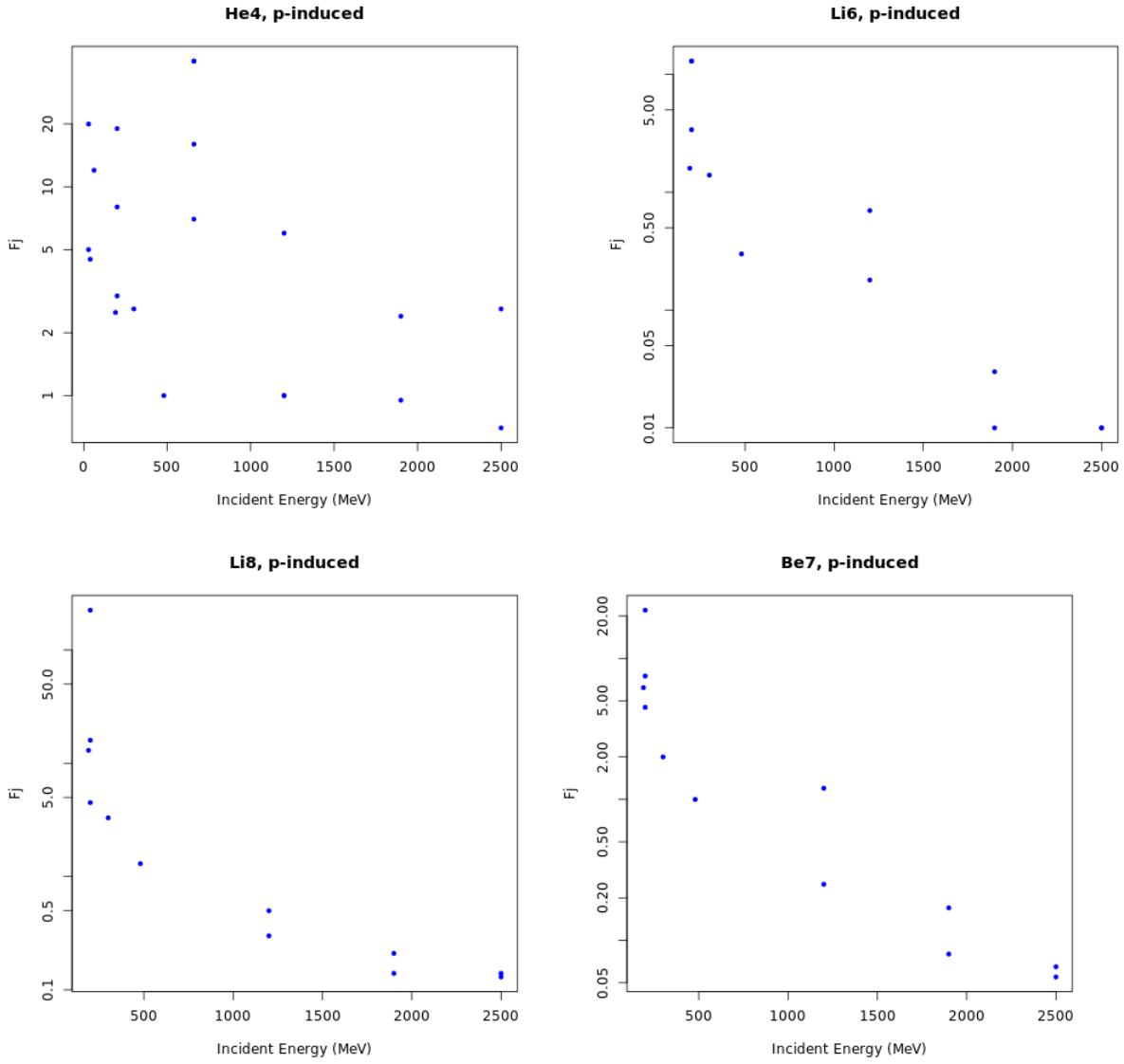

FIGURE 6.2: Values of F_j according to incident proton energy (MeV), for emitted fragments ^{4}He, ^{6}Li, ^{8}Li, and ^{7}Be.

both energy and target mass number (see Fig. 6.4). We zoomed in on F_j values < 1000, as there were some very large values for F_j which made it difficult to see any pattern. In Fig. 6.4 we can begin to see a target-size dependence, but it is still somewhat obscured by including all different emitted fragment sizes. We also plotted F_j by target size for each emitted fragment type (see Fig. 6.5 for a few examples). Interestingly, in these plots F_j appears to decrease as target size increases, but we must be careful because these results are largely obscured by including all different

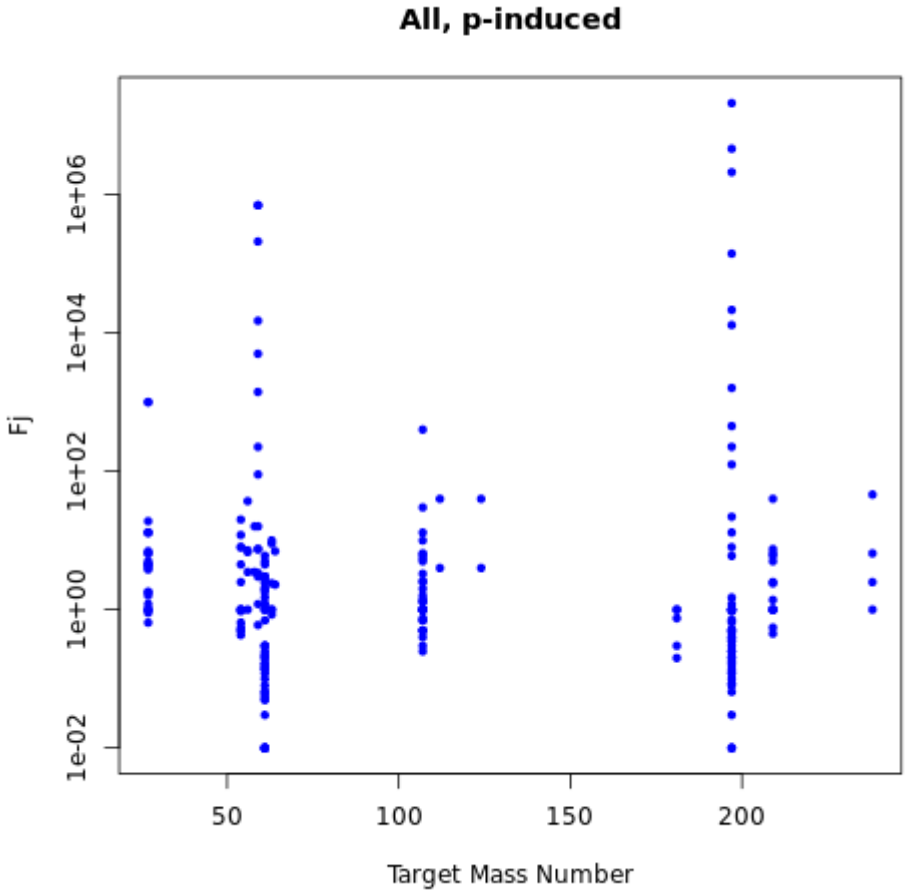

FIGURE 6.3: Values of F_j according to the mass number of the target.

incident energies. We will see that incident energy is the dominate variable in F_j, and therefore by including all incident energies we cannot draw any conclusions about variables of secondary importance. When we plot F_j by both incident energy and target size for each individual emitted fragment, we see a different pattern emerge: namely that F_j increases as target size increases (see Figs. 6.8–6.10).

We therefore have established that F_j is dependent upon incident energy, target size, and fragment size. We assume for mathematical simplicity that the dependencies on incident energy and target size are separable, and that the target-size dependence is not dependent upon fragment size.

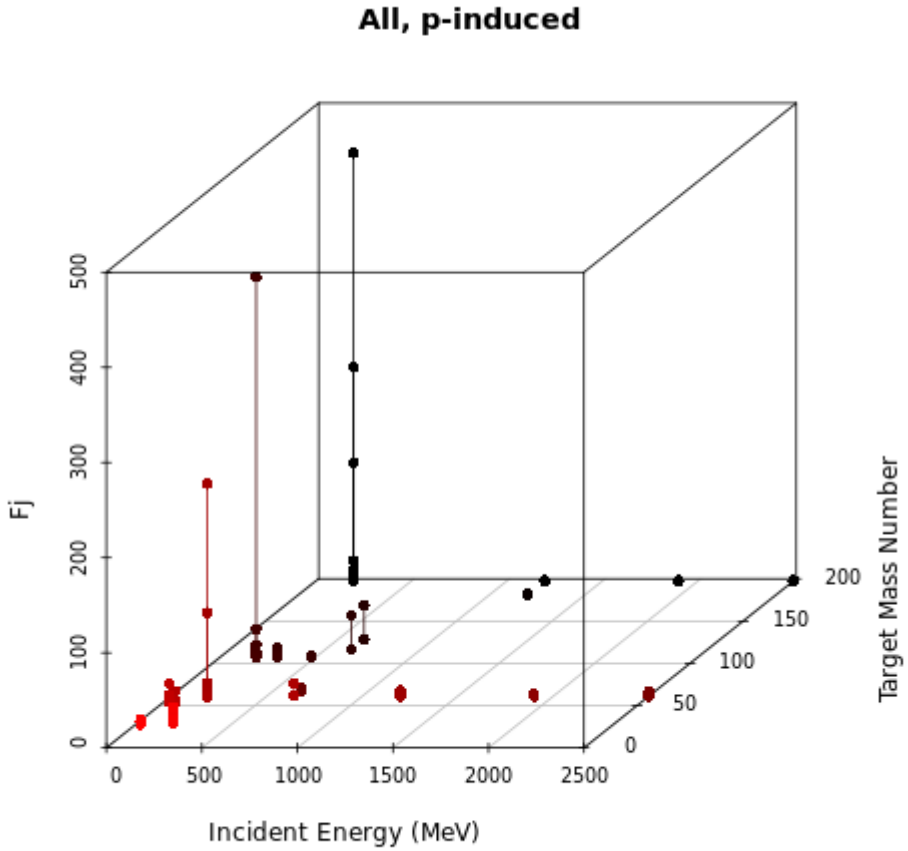

FIGURE 6.4: Values of F_j according to the incident proton energy (MeV) and mass number of the target.

6.2.1 *Fragment-Specific F_j*

As discussed in the previous section, we assume an F_j Model can be obtained which has the form of Eq 6.4.

$$F_j(T_0, A_j, Z_j, A_t) = f(T_0, A_j, Z_j)g(A_t) \tag{6.4}$$

T_0: Incident energy of projectile (MeV)

A_j: Mass number of emitted fragment type j

Z_j: Atomic number of emitted fragment type j

A_t: Mass number of target nucleus

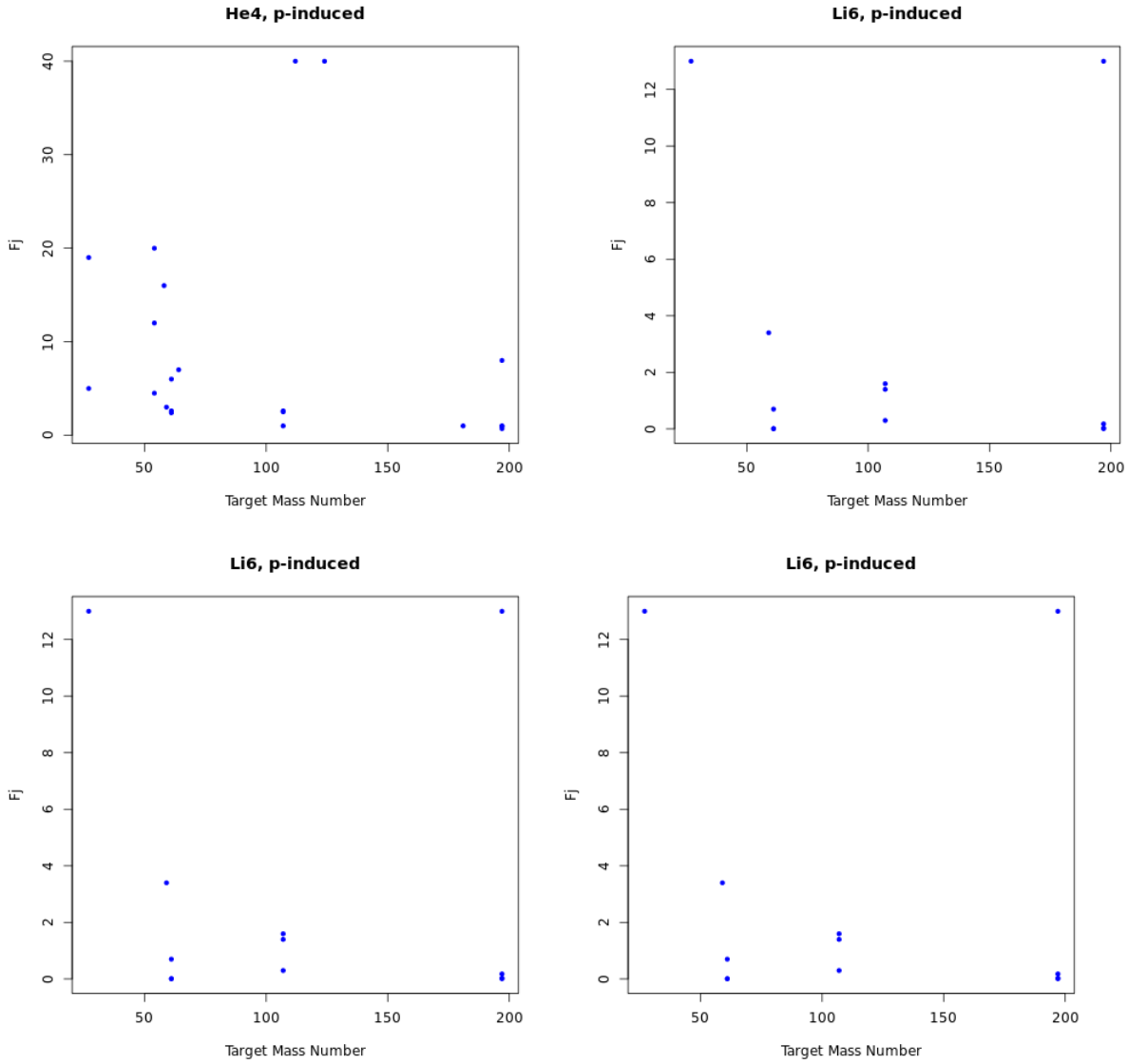

FIGURE 6.5: Values of F_j according to target mass number, for emitted fragments ^{4}He, ^{6}Li, ^{8}Li, and ^{7}Be.

A simple exponential decay described $g(A_t)$ quite well. We developed it such that it is valid for all $A_t < 300$. A suitable model for $f(T_0, A_j, Z_j)$ proved more difficult to obtain. All common distributions were tested and none of them were able to describe both the low-energy and high-energy dependencies of F_j. We therefore used one function (an exponential decay) to describe the low-energy dependence and a second function (a $1/T_0$ term) to describe the high-energy dependence. For the $1/T_0$ term, we added 100 to the denominator to ensure no singularities (code crashes) in our

range of conceivable energies. These two different energy dependencies make sense considering our previous discussion about CEM lacking some important physics in the low-energy region, and therefore our F_j Model is "compensating" for missing physics in that region, but in the higher-energy region CEM is reliable enough. We also found that for light LF (^{4}He and lighter), dependence on target size disappeared.

Equations for specific fragment types are shown in Eq. 6.5:

$$
\begin{aligned}
F_d &= -3e^{-T_0/20} + \frac{125}{T_0^{0.2} + 100}; \\
F_t &= 20e^{-T_0/20} + \frac{175}{T_0^{0.4} + 100}; \\
F_{^3He} &= 20e^{-T_0/20} + \frac{250}{T_0^{0.6} + 100}; \\
F_{^4He} &= 100e^{-T_0/20} + \frac{1000}{T_0^{0.8} + 100}; \\
F_{^6He} &= \left[1.4e5e^{-T_0/20} + \frac{1400}{T_0^{1.2} + 100}\right] e^{-\frac{300-A_t}{100}}; \\
F_{^6Li} &= \left[4.0e5e^{-T_0/20} + \frac{5000}{T_0^{1.2} + 100}\right] e^{-\frac{300-A_t}{100}}; \\
F_{^7Li} &= \left[1.0e6e^{-T_0/20} + \frac{2.5e4}{T_0^{1.4} + 100}\right] e^{-\frac{300-A_t}{100}}; \\
F_{^8Li} &= \left[2.5e6e^{-T_0/20} + \frac{1.0e5}{T_0^{1.6} + 100}\right] e^{-\frac{300-A_t}{100}}; \\
F_{^9Li} &= \left[6.25e6e^{-T_0/20} + \frac{4.0e5}{T_0^{1.8} + 100}\right] e^{-\frac{300-A_t}{100}}; \\
F_{^7Be} &= \left[1.0e6e^{-T_0/20} + \frac{5000}{T_0^{1.2} + 100}\right] e^{-\frac{300-A_t}{100}}; \\
F_{^9Be} &= \left[6.25e6e^{-T_0/20} + \frac{1.0e5}{T_0^{1.6} + 100}\right] e^{-\frac{300-A_t}{100}}; \\
F_{^{10}Be} &= \left[1.56e7e^{-T_0/20} + \frac{4.0e5}{T_0^{1.8} + 100}\right] e^{-\frac{300-A_t}{100}}; \\
F_{^{10}B} &= \left[1.56e7e^{-T_0/20} + \frac{1.5e5}{T_0^{1.6} + 100}\right] e^{-\frac{300-A_t}{100}}; \\
F_{^{11}B} &= \left[3.9e7e^{-T_0/20} + \frac{6.0e5}{T_0^{1.8} + 100}\right] e^{-\frac{300-A_t}{100}}; \\
F_{^{12}B} &= \left[9.75e7e^{-T_0/20} + \frac{2.4e6}{T_0^{2.0} + 100}\right] e^{-\frac{300-A_t}{100}}; \\
F_{^{12}C} &= \left[9.75e7e^{-T_0/20} + \frac{6.0e5}{T_0^{1.8} + 100}\right] e^{-\frac{300-A_t}{100}}; \\
F_{^{13}C} &= \left[2.44e8e^{-T_0/20} + \frac{2.4e6}{T_0^{2.0} + 100}\right] e^{-\frac{300-A_t}{100}}.
\end{aligned}
\tag{6.5}
$$

Examples of several fits are shown in Figs. 6.6–6.10. More results are available in [168].

6.2.2 *Neutron-Induced Reactions*

Having obtained a fragment-specific F_j Model for proton-induced reactions, we turned our attention to neutron-induced reactions. There is less experimental data available for neutron-induced reactions, due to the difficulty of conducting these experiments. There is also no experimental data on the emission of light fragments heavier than ^{4}He, in an energy range of interest to us in this paper. Therefore, for light fragments heavier than ^{4}He we use the fragment-specific F_j Model we obtained for proton-induced reactions as a "first guess." Our F_j equations for d, t, ^{3}He, and ^{4}He for neutron-induced reactions are presented in Eq. 6.6, and are similar to the respective F_j equations obtained for these emitted fragments for proton-induced reactions.

$$\begin{aligned} F_d &= -4.5e^{-T_0/20} + \frac{187.5}{T_0^{0.2}+100}; \\ F_t &= -6.75e^{-T_0/20} + \frac{281}{T_0^{0.2}+100}; \\ F_{^3He} &= 30e^{-T_0/20} + \frac{375}{T_0^{0.6}+100}; \\ F_{^4He} &= 500e^{-T_0/20} + \frac{5000}{T_0^{0.8}+100}. \end{aligned} \tag{6.6}$$

Examples of two fits are shown in Figs. 6.11 and 6.12.

6.2.3 *General F_j Model*

In studying the fragment-specific equations for F_j in Eq. 6.5, a pattern quickly emerges. Heavy clusters can be nicely generalized as approximately Eq. 6.7:

$$\begin{aligned} F_j(T_0, A_j, Z_j, A_t) = \left[7800(2.5)^{A_j}e^{-T_0/20} + \frac{2(4)^\tau}{T_0^{0.2\tau}+100}\right]e^{-\frac{300-A_t}{100}}, \\ \tau = A_j - (Z_j - 3). \end{aligned} \tag{6.7}$$

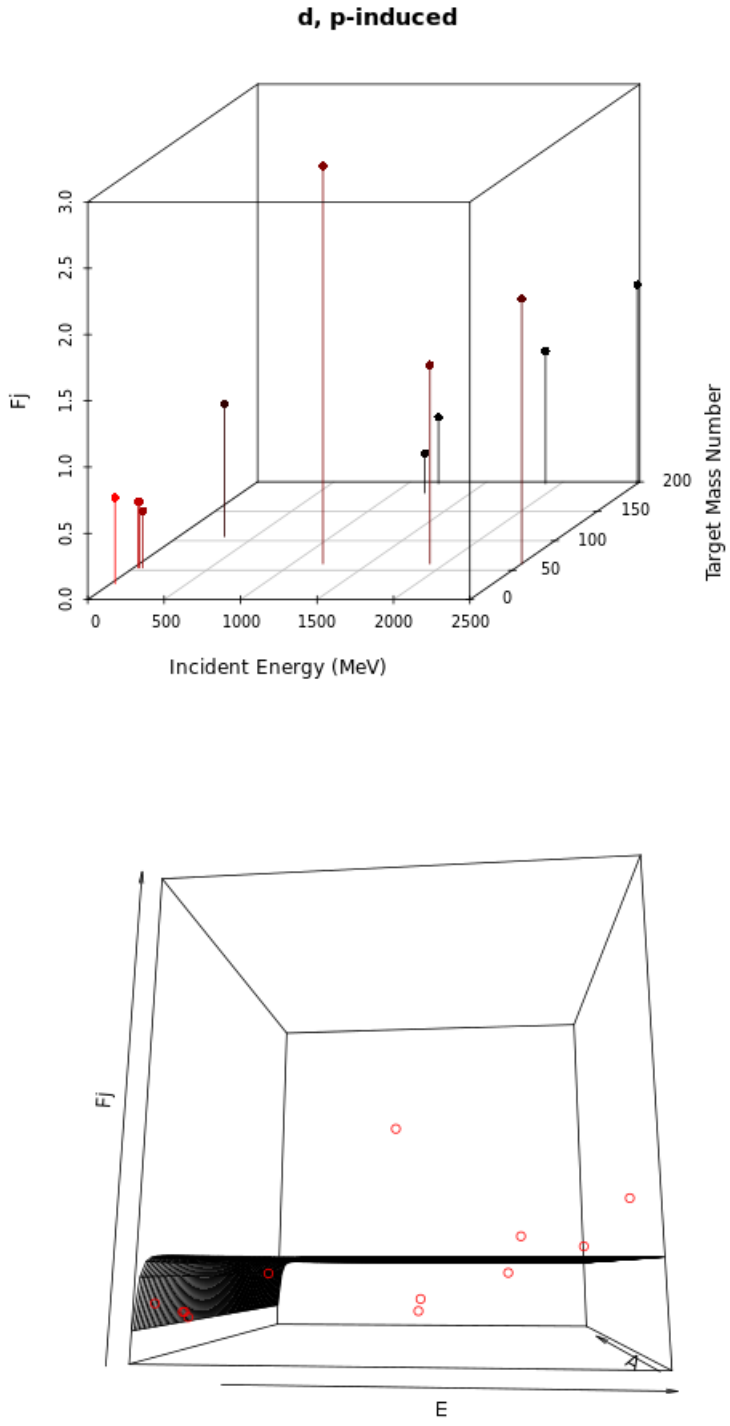

FIGURE 6.6: Values of F_j according to incident proton energy (MeV) and target mass number (top plot), shown with a corresponding surface mesh of the F_j Model, for deuterium.

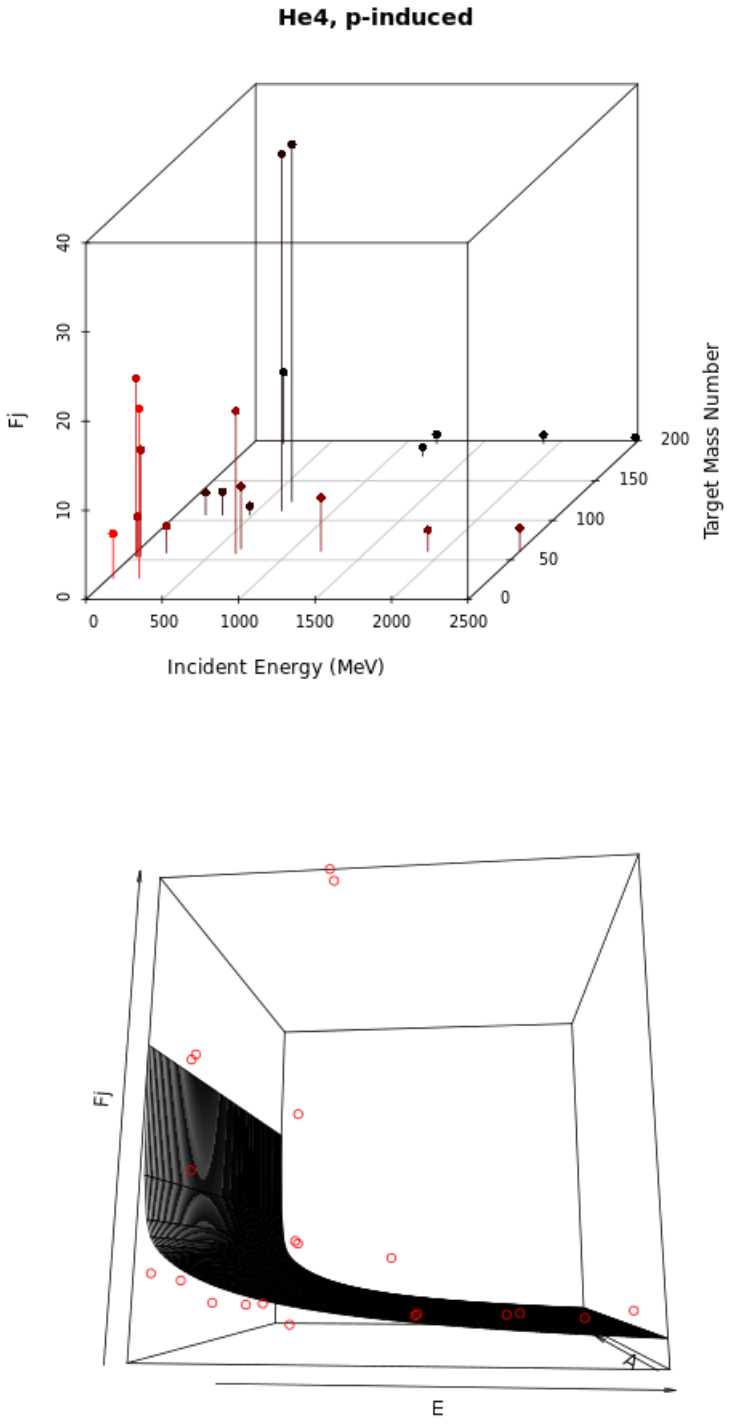

FIGURE 6.7: Values of F_j according to incident proton energy (MeV) and target mass number (top plot), shown with a corresponding surface mesh of the F_j Model, for ^{4}He.

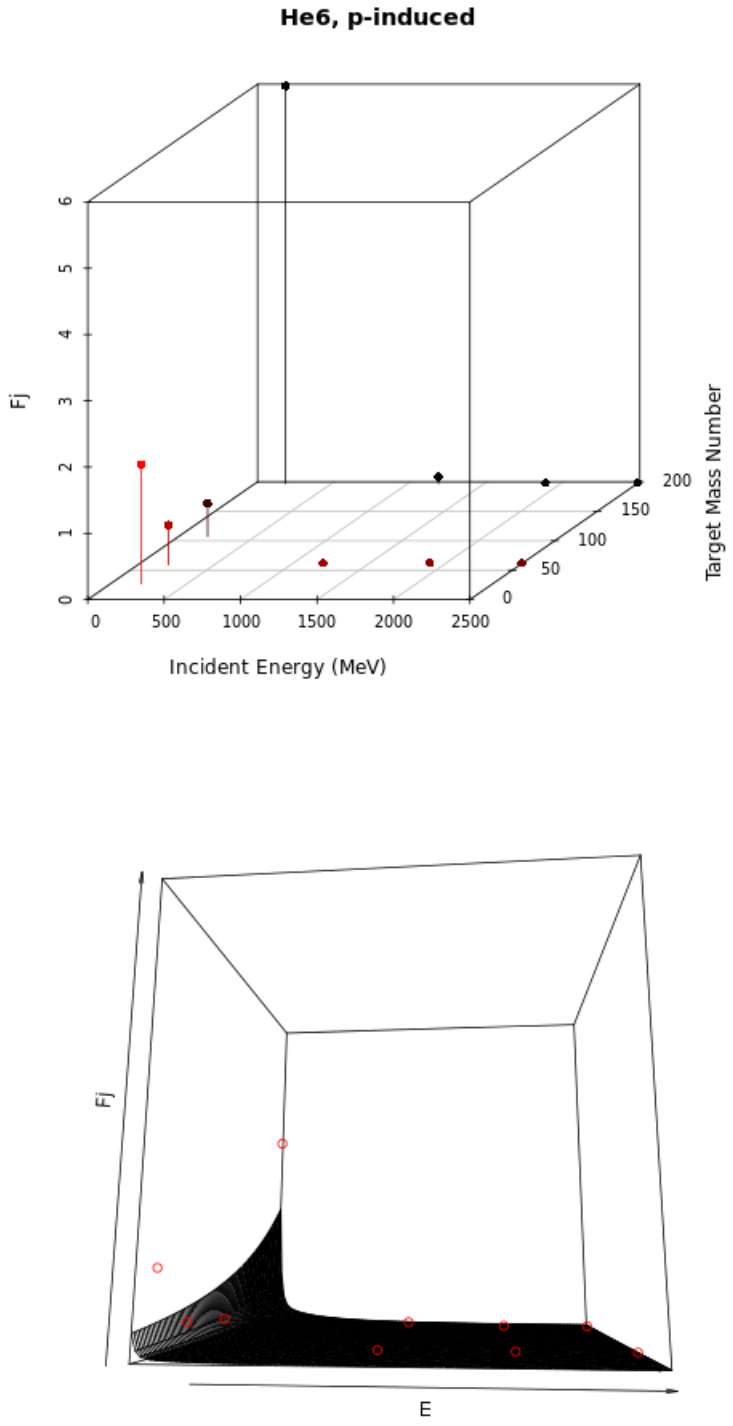

FIGURE 6.8: Values of F_j according to incident proton energy (MeV) and target mass number (top plot), shown with a corresponding surface mesh of the F_j Model, for ^{6}He.

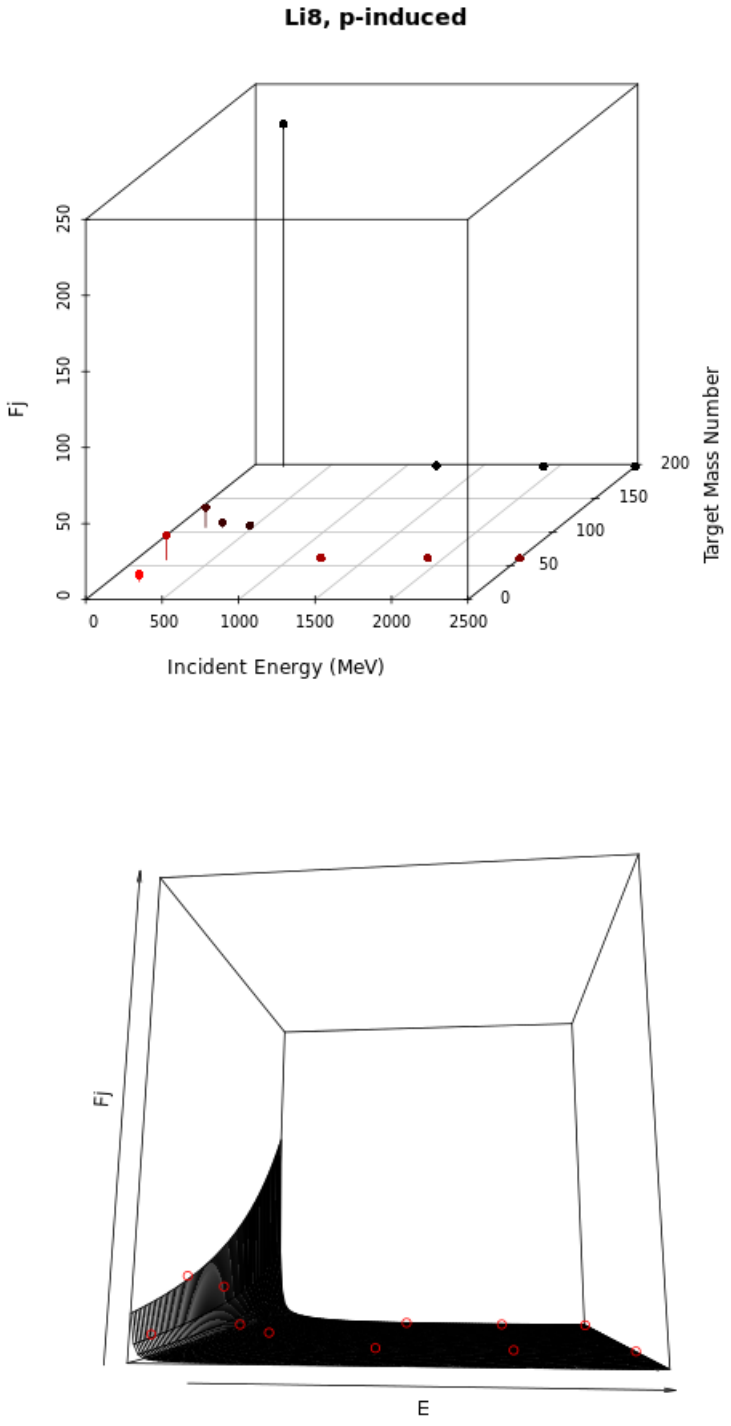

FIGURE 6.9: Values of F_j according to incident proton energy (MeV) and target mass number (top plot), shown with a corresponding surface mesh of the F_j Model, for ^{8}Li.

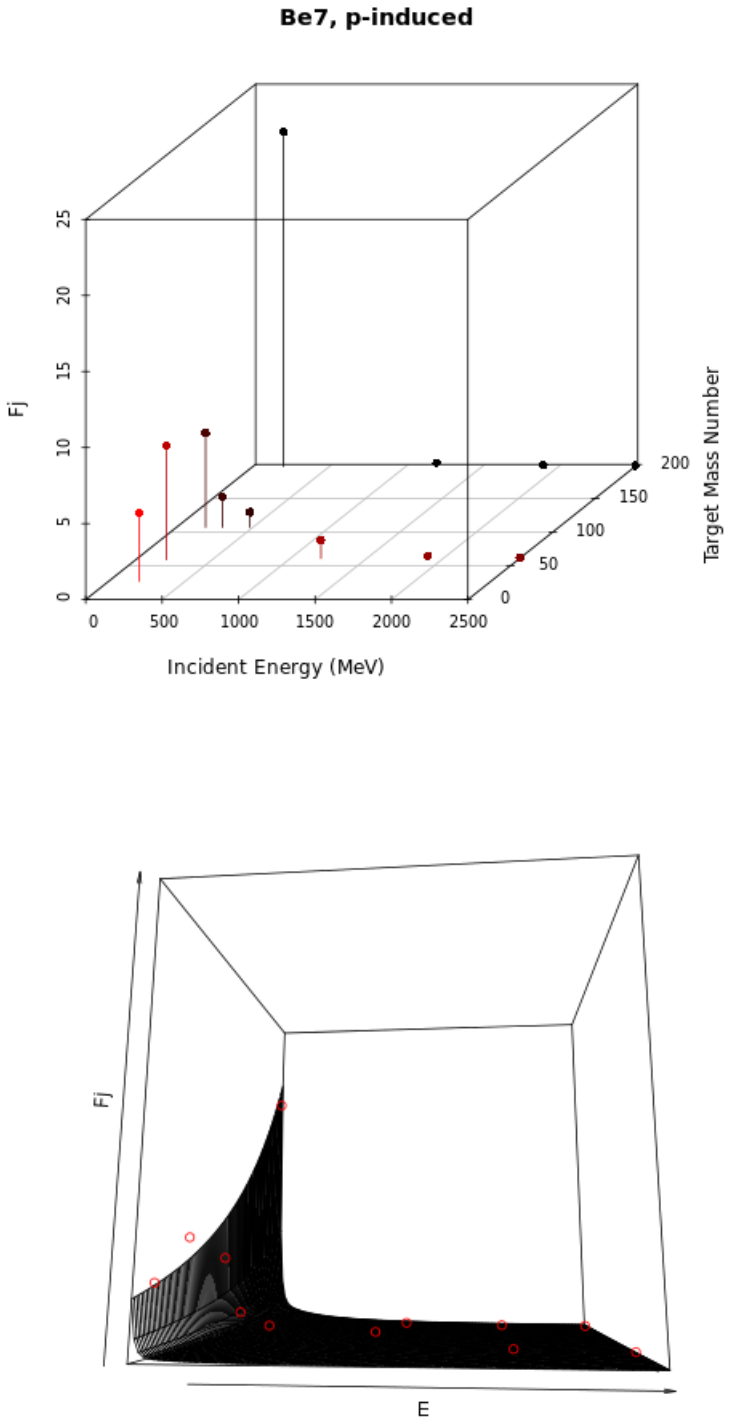

FIGURE 6.10: Values of F_j according to incident proton energy (MeV) and target mass number (top plot), shown with a corresponding surface mesh of the F_j Model, for ^{7}Be.

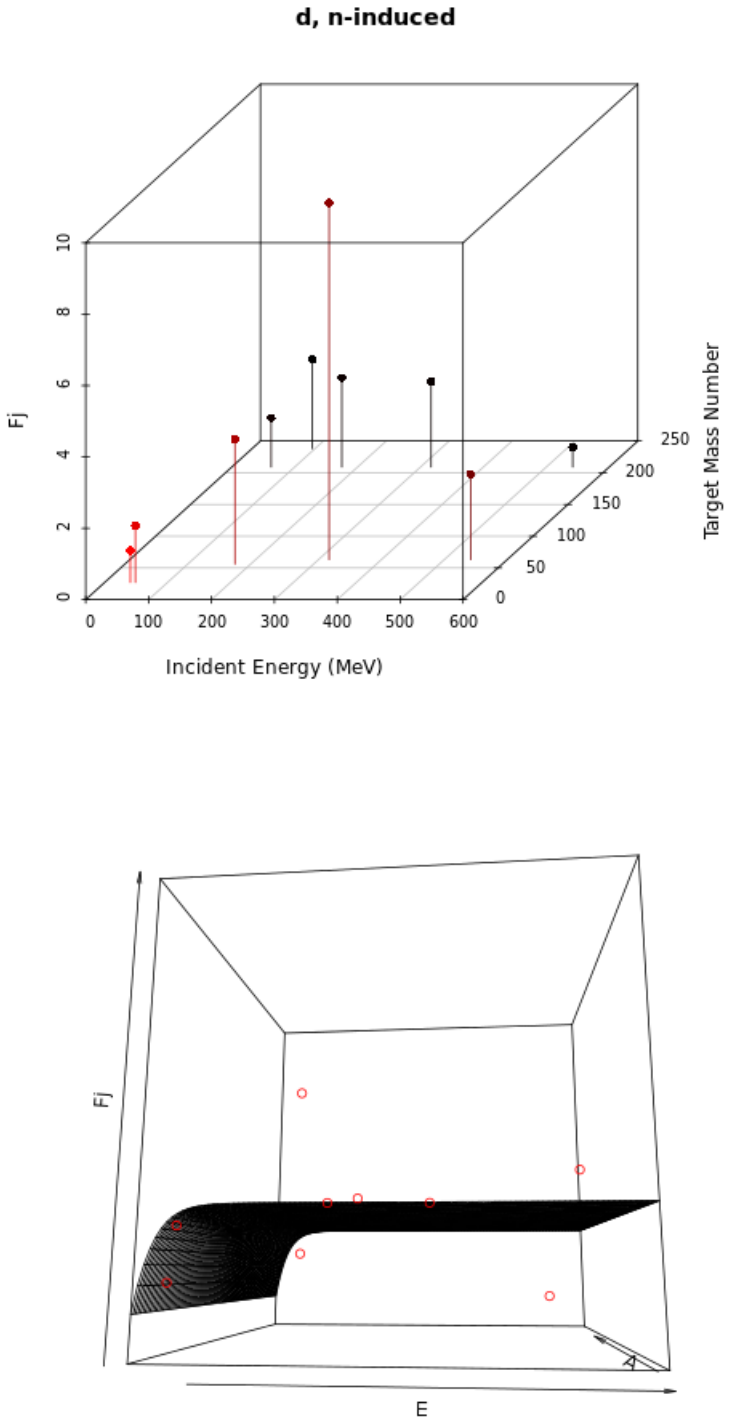

FIGURE 6.11: Values of F_j according to incident neutron energy (MeV) and target mass number (top plot), shown with a corresponding surface mesh of the F_j Model, for deuterium.

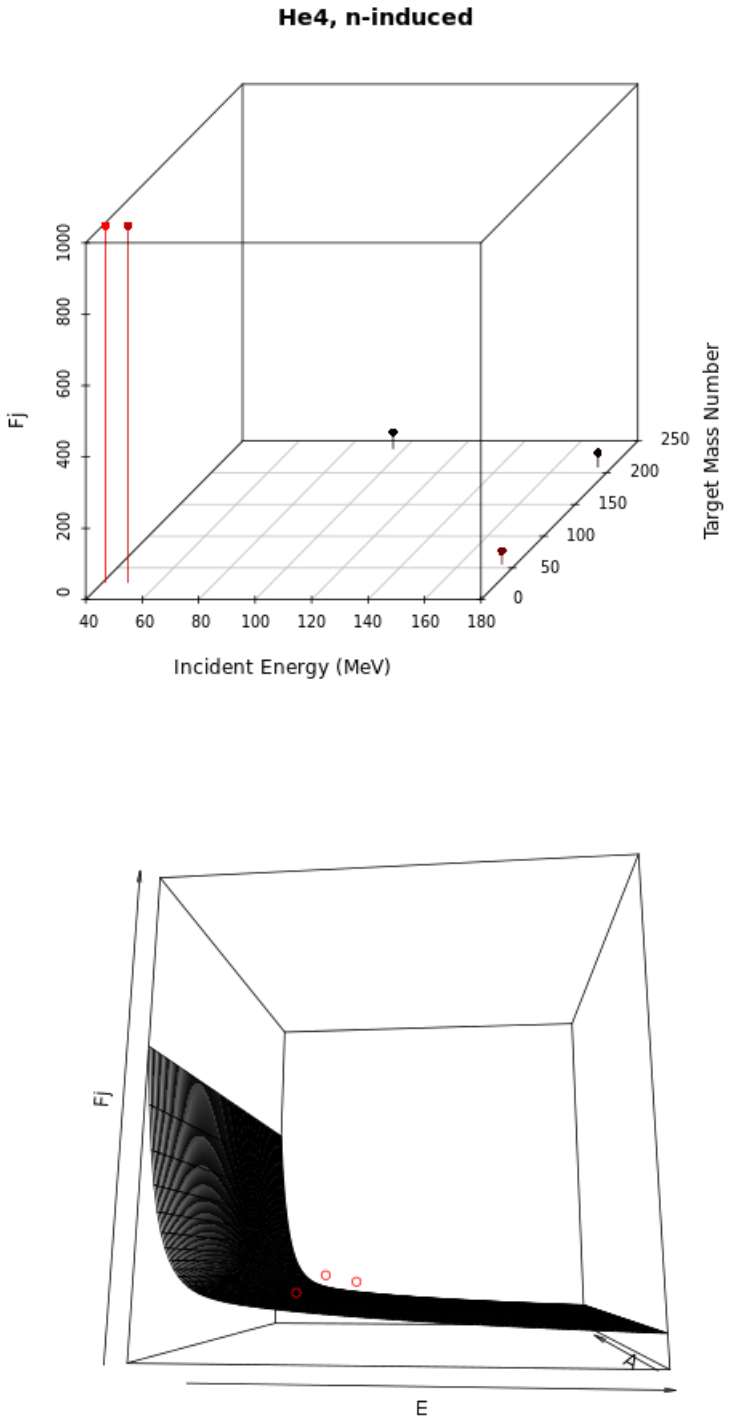

FIGURE 6.12: Values of F_j according to incident neutron energy (MeV) and target mass number (top plot), shown with a corresponding surface mesh of the F_j Model, for ^{4}He.

This general form is used for heavy clusters for which we do not have sufficient data: ^{8}He, ^{11,12}Be, ^{8,13}B, ^{10,11,14,15,16}C, and all fragments with $Z \geq 7$ (up to ^{28}Mg).

Recall that γ_j can theoretically be calculated from first principles, but that this is too computationally time-consuming. We therefore wish to obtain a γ_j Model that is both accurate and computationally fast. Our F_j Model (and therefore, γ_j Model) accomplishes both of these: it is computationally simple and very fast, and it provides reasonably accurate fragment spectra compared to experimental results.

For γ- and π-induced reactions, CEM03.03 uses $F_j = 1$ for emitted d, t, ^{3}He, and ^{4}He. We have followed this pattern in our model and use $F_j = 1$ for all emitted complex fragments, from deuterium to ^{28}Mg, in γ– and π–induced reactions.

6.3 COMPARISON OF SPECTRA WITH FITTED F_j VS. SPECTRA WITH F_j MODEL

For the large majority of reactions tested here, the predicted fragment spectra using the F_j Model was very similar to the predicted fragment spectra using fitted F_j values. See Figs. 6.13–6.15 for plots comparing results from the F_j Model with fitted F_j values. Many more comparisons can be found in [168]. Oftentimes the F_j Model resulted in slightly "softer" spectra (*i.e.*, ^{6}Li spectra from 200 MeV p + ^{197}Au, in Fig. 6.14), which was usually an improved match to experimental data than the F_j fitted values.

There were a handful of reactions for which the predicted spectra of a few particular fragment types varied significantly: for the emission of heavier clusters ($A \geq 8$) from reactions with low incident energies and heavy targets. For an example of this, see the spectra of ^{8}Li in Fig. 6.14. While the discrepancy is significant, it is not always negative, as sometimes the fitted values were "overfit." We believe this difference is due to several factors. First, our expanded Coalescence Model emits heavy clusters up to $A = 7$; this leads to a "jump" in fitted F_j values for emitted heavy clusters with $A > 7$ as it is "compensating" for the lack of coalescence emission, compared to those with $A \leq 7$. However, as our F_j Model is a "smooth" model it cannot completely account for this jump. We expect that expanding our Coalescence Model further will ease this effect. In addition, while we assumed for simplicity that

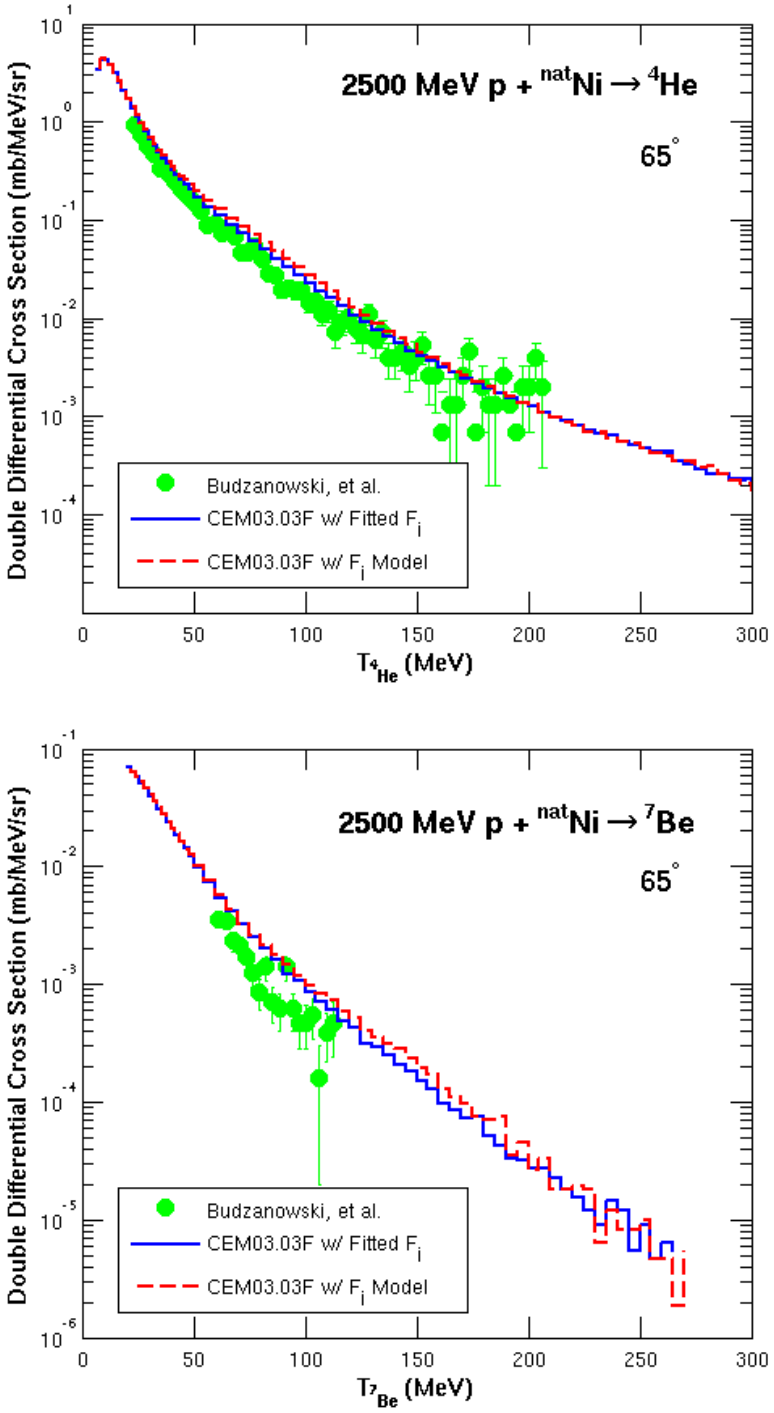

FIGURE 6.13: Comparison of experimental data by Budzanowski, *et al.* [50] (green circles) with results by the CEM03.03F with fitted F_j (blue solid lines) and CEM03.03F with F_j Model (red dashed lines) for 2500 MeV p + ^{nat}Ni → ^{4}He,^{7}Be.

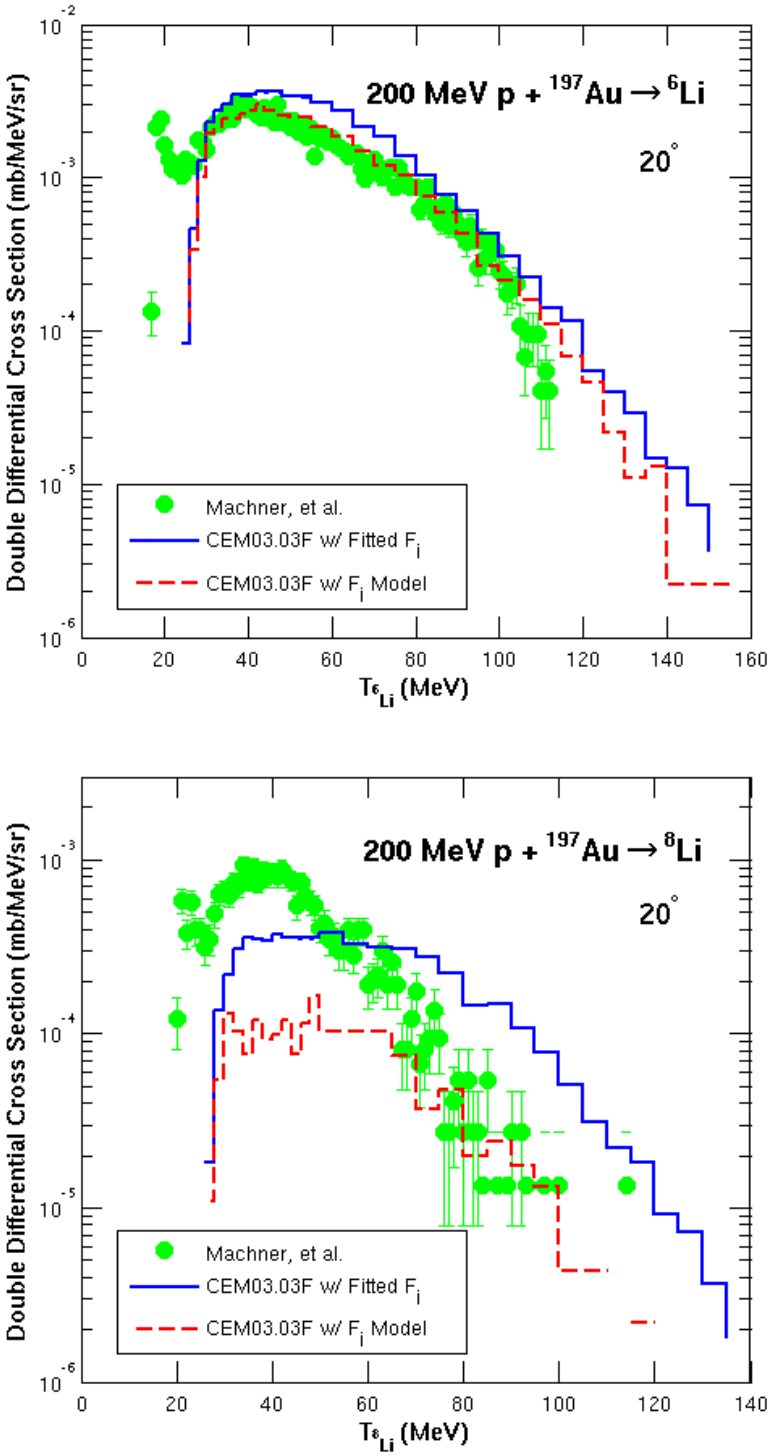

FIGURE 6.14: Comparison of experimental data by Machner, *et al.* [11] (green circles) with results by the CEM03.03F with fitted F_j (blue solid lines) and CEM03.03F with F_j Model (red dashed lines) for 200 MeV p + ^{197}Au → ^{6}Li, ^{8}Li

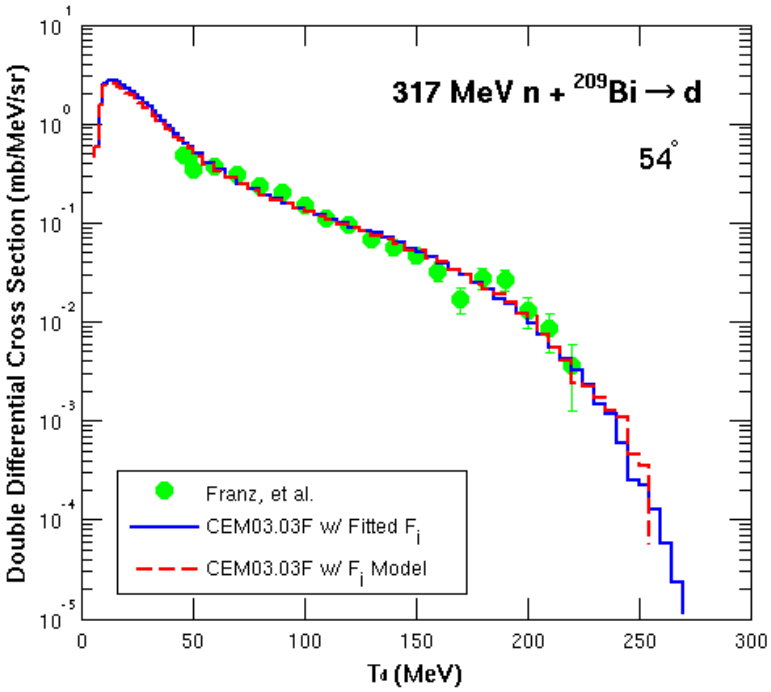

FIGURE 6.15: Comparison of experimental data by Franz, *et al.* [171] (green circles) with results by the CEM03.03F with fitted F_j (blue solid lines) and CEM03.03F with F_j Model (red dashed lines) for 317 MeV n + ^{209}Bi → d

the target-size dependence was independent of the fragment size and the incident energy, this is not strictly the case. The target-size dependence did, in fact, become more pronounced with increasing fragment size. We excluded target-size dependence from emitted ^{4}He and lighter, and included this term for heavier clusters, to partially account for this. However, the greater our fragment size the less valid this "constant" target-size dependence becomes. Lastly, we found that the target-size dependence also varied across the incident energy (also contrary to our assumption), becoming sharper at lower incident energies and flatter at higher incident energies. Thus, at low incident energies on heavy targets and looking at the emission of heavier clusters, we expect a "perfect storm" of factors to create significant discrepancy between our F_j Model and fitted values. However, as noted previously, this discrepancy is not always negative as sometimes it leads to either improved fit with experimental data or a more natural spectra. Furthermore, the ^{8}Li spectra of Fig. 6.14 demonstrate the

need to also upgrade our evaporation model, as it primarily produces the peak of the spectra, which is too low for this reaction. We hope to do this in the future.

6.4 CONCLUSION

While γ_j can theoretically be calculated from first principles, this is too computationally time-consuming. We therefore wish to obtain a γ_j Model that is both accurate and computationally fast. Our F_j Model (and therefore, γ_j Model) accomplishes both of these: it is computationally simple and very fast, and it provides reasonably accurate fragment spectra compared to experimental results.

Our γ_j Model is dependent upon incident projectile energy, target nucleus size, and emitted fragment size. We found two different energy dependencies: one for the low-energy region and a second for the higher-energy region. These energy dependencies make sense considering the physics of nuclear reactions. We consider in this F_j Model the incident energy of the incoming proton, not the excitation energy of the residual nucleus at the time of preequilibrium, and after a certain incident energy we expect the residual nucleus energy to not change significantly as the incident energy continues to increase: *i.e.*, the amount of energy deposited in the target nucleus reaches a saturating limit and increasing the incident proton energy further does not lead to significantly greater residual nucleus energy. This idea is analogous to "limiting fragmentation" [82, 170]. In addition, CEM accounts for the IntraNuclear Cascade, preequilibrium, evaporation/fission, Fermi break-up, and coalescence mechanisms of nuclear reactions, but does not account for pick-up and knock-out reactions. Pick-up and knock-out mechanisms are especially important at low energies, and therefore, the increase in F_j at lower incident energies can be attributed to "compensating" for these missing physics in CEM. Furthermore, CEM does not account for some nuclear structure effects important at low energies, and for some reactions, also at high energies. Lastly, CEM, just as any other model, is "only a model," and probably misses some other aspects of the physics. For these reasons, we need to look at our "model" for γ_j in CEM philosophically, understanding that in some energy/target-size regions, it does not have exactly the right meaning of the

condensation probability, but also contains a component to counterbalance physics not accounted for in CEM.

This γ_j Model is specifically designed for use in CEM, taking into account the reaction mechanisms used (or not used) in CEM. However, this model could be useful in other nuclear spallation codes and models, especially for heavy cluster production.

In conclusion, our new γ_j Model provides better agreement with experimental data than the old interpolation fits used in CEM03.03, especially for heavy-cluster spectra. We plan to apply this to LAQGSM as well, and implement the new model within MCNP6.

CHAPTER 7

Testing the Predictive Power of CEM03.03F

Below are relevant publications that result from the author's work pertaining to this chapter.

- L.M. Kerby and S.G. Mashnik, A New Model for the Condensation Probability, γ_j, in CEM, LANL Report, LA-UR-15-22370 (April 2015);
- S. G. Mashnik and L. M. Kerby, MCNP6 Simulation of Light and Medium Nuclei Fragmentation at Intermediate Energies, LA-UR-15-22811, Los Alamos (2015), talk presented at the 12th International Conference on Nucleus-Nucleus Collisions (NN2015), 2015-06-21/2015-06-26 (Catania, Italy);
- S. G. Mashnik, L. M. Kerby, and K. K. Gudima, Fragmentation of Light Nuclei at Intermediate Energies Simulated with MCNP6, LA-UR-15-20953, Los Alamos (2015), Invited Talk to be presented at the Fifth International Conference on Nuclear Fragmentation "From Basic Research to Applications" (NUFRA2015), 2015-10-04/2015-10-11 (Antalya (Kemer), Turkey).

Results of our "F" version of CEM03.03, called CEM03.03F, are shown in this chapter, and are compared to the original CEM03.03 and experimental results. The most important test of CEM03.03F are of its predictions for reactions we did not use in our fitting or previously consider in our upgrades. These results are shown in Sections 7.3 and 7.4. We see that CEM03.03F performs well. To be clear, CEM03.03F as referred to in this chapter includes our expanded Modified Exciton Model, upgraded NASA-Kalbach inverse cross sections within the preequilibrium stage, the expanded Coalesence Model, and the new γ_j Model. (We left the cut-off for Fermi breakup at $A_{Fermi} = 12$.) For more details on these upgrades, see Refs [168, 166, 102, 96, 97, 64, 94, 95].

7.1 FRAGMENT SPECTRA FOR PROTON-INDUCED REACTIONS

Double differential cross section spectra for several reactions are plotted in this section. Figs. 7.1–7.17 compare experimental data with results by the unmodified CEM03.03 (blue solid lines) and CEM03.03F with the expanded Modified Exciton Model, upgraded NASA-Kalbach inverse cross section (in the preequilibrium stage), expanded Coalescence Model, and new F_j Model (red dashed lines) for proton-induced reactions. We see that our new CEM03.03F, in general, has improved results over the unmodified CEM03.03, especially for heavy cluster spectra.

Fig. 7.1 displays our results for 190 MeV p + ^{nat}Ag $\rightarrow$ ^{6}Li,^{7}Be at 90° with experimental data by Green, *et al.* [79]. This figure exemplifies the many dramatically improved results achieved with CEM03.03F, particularly for heavy clusters. This figure also highlights the need to improve our evaporation model, as we see the peak of the spectra is too low, and this peak is largely produced by evaporation. We hope to do this work in the future.

Fig. 7.2 shows our results for 200 MeV p + ^{27}Al $\rightarrow$ ^{4,6}He at 60° with experimental data by Machner, *et al.* [11]. The figure for ^{4}He spectra demonstrates that CEM03.03F achieves increased production of heavy clusters without "destroying" the established spectra of nucleons and light fragments up to ^{4}He (in this particular case ^{4}He), but in some cases it even achieves improved results for nucleons and light fragments up to ^{4}He. For the spectra of ^{6}He, we again see significant improvement with CEM03.03F.

Fig. 7.3 illustrates our results for 200 MeV p + ^{59}Co $\rightarrow$ ^{8,9}Li at 60° with experimental data by Machner, *et al.* [11]. This figure demonstrates results for the rare, neutron-rich lithium isotopes ^{8,9}Li. We see dramatic improvement in the production of high-energy ^{8,9}Li with CEM03.03F. These results again highlight the need to improve our evaporation model, as the low-energy peak (produced largely by evaporation) is too low (see also Fig. 7.1).

Figs. 7.4 and 7.5 display our results for 200 MeV p + ^{197}Au $\rightarrow$ ^{6}Li,^{7}Be at 45° with experimental data by Machner, *et al.* [11]. These figures show not only dramatically improved heavy cluster production at high energies, but also improved production at relatively low energies around the peak. We believe this is due to the heavy target

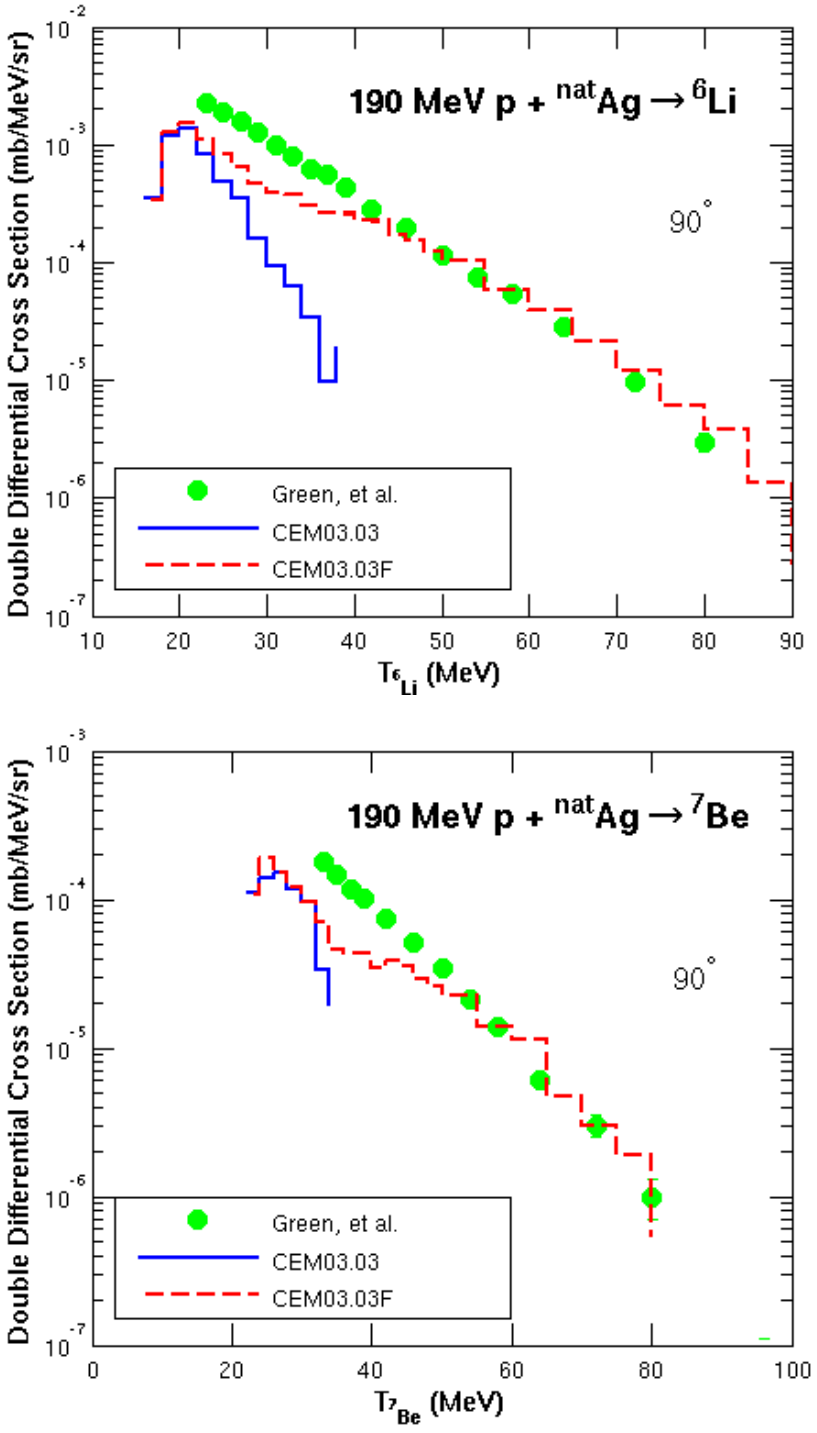

FIGURE 7.1: Comparison of experimental data by Green, *et al.* [79] (green circles) with results by the unmodified CEM03.03 (blue solid lines) and new CEM03.03F (red dashed lines) for 190 MeV p + ^{nat}Ag → ^{6}Li,^{7}Be at 90°.

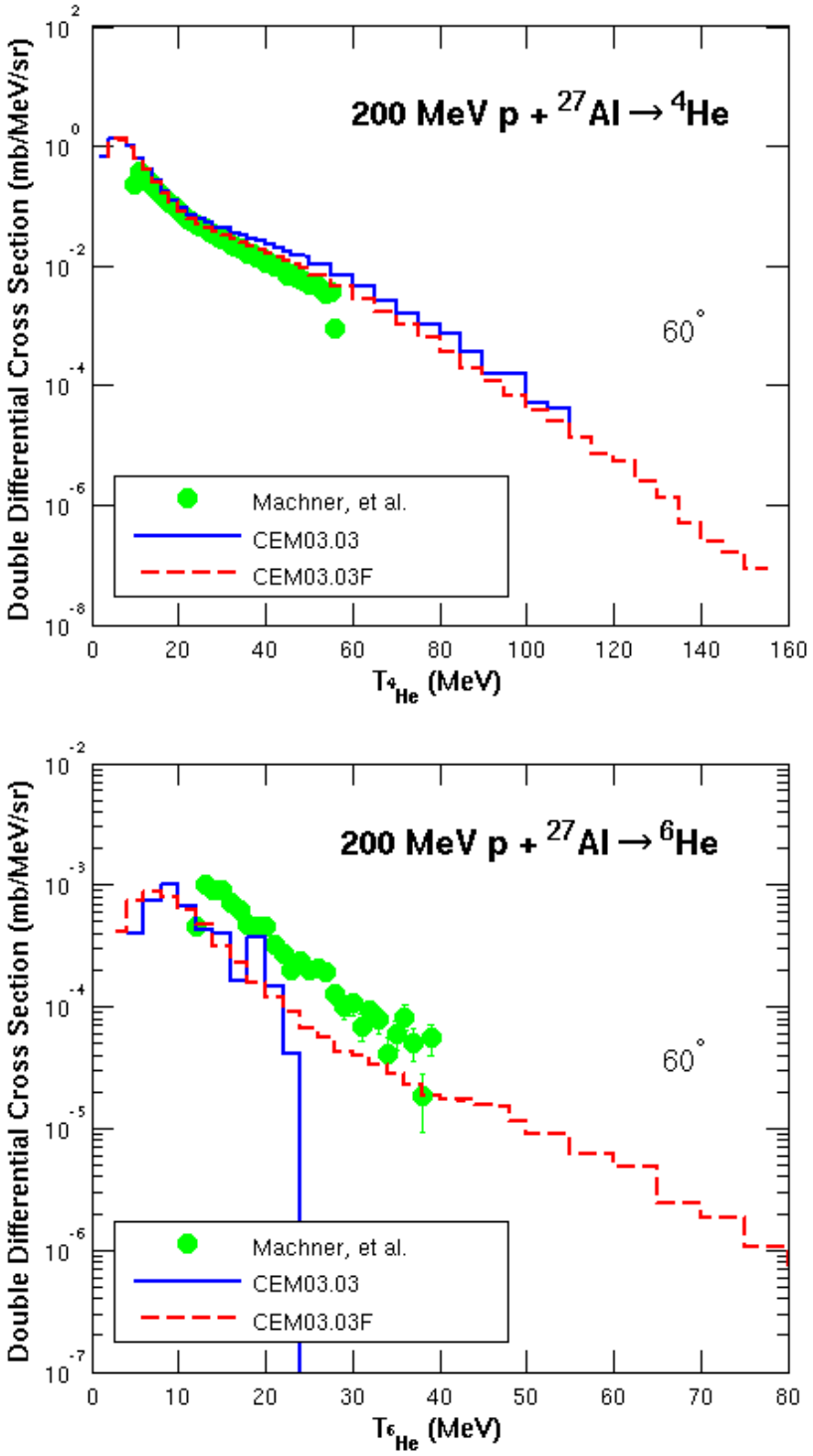

FIGURE 7.2: Comparison of experimental data by Machner, *et al.* [11] (green circles) with results by the unmodified CEM03.03 (blue solid lines) and new CEM03.03F (red dashed lines) for 200 MeV p + ^{27}Al → ^{4,6}He at 60°.

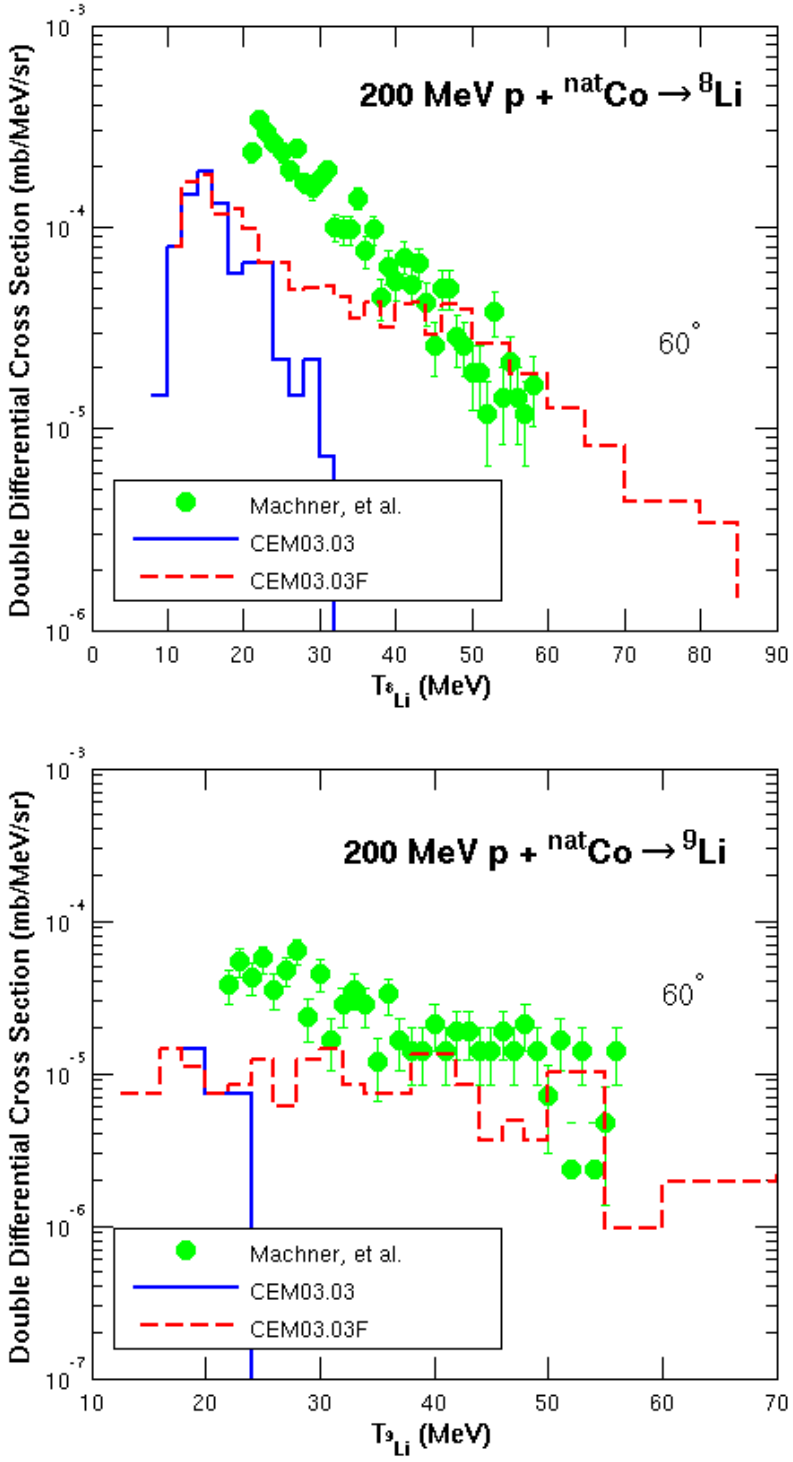

FIGURE 7.3: Comparison of experimental data by Machner, *et al.* [11] (green circles) with results by the unmodified CEM03.03 (blue solid lines) and new CEM03.03F (red dashed lines) for 200 MeV p + ^{59}Co → ^{8,9}Li at 60°.

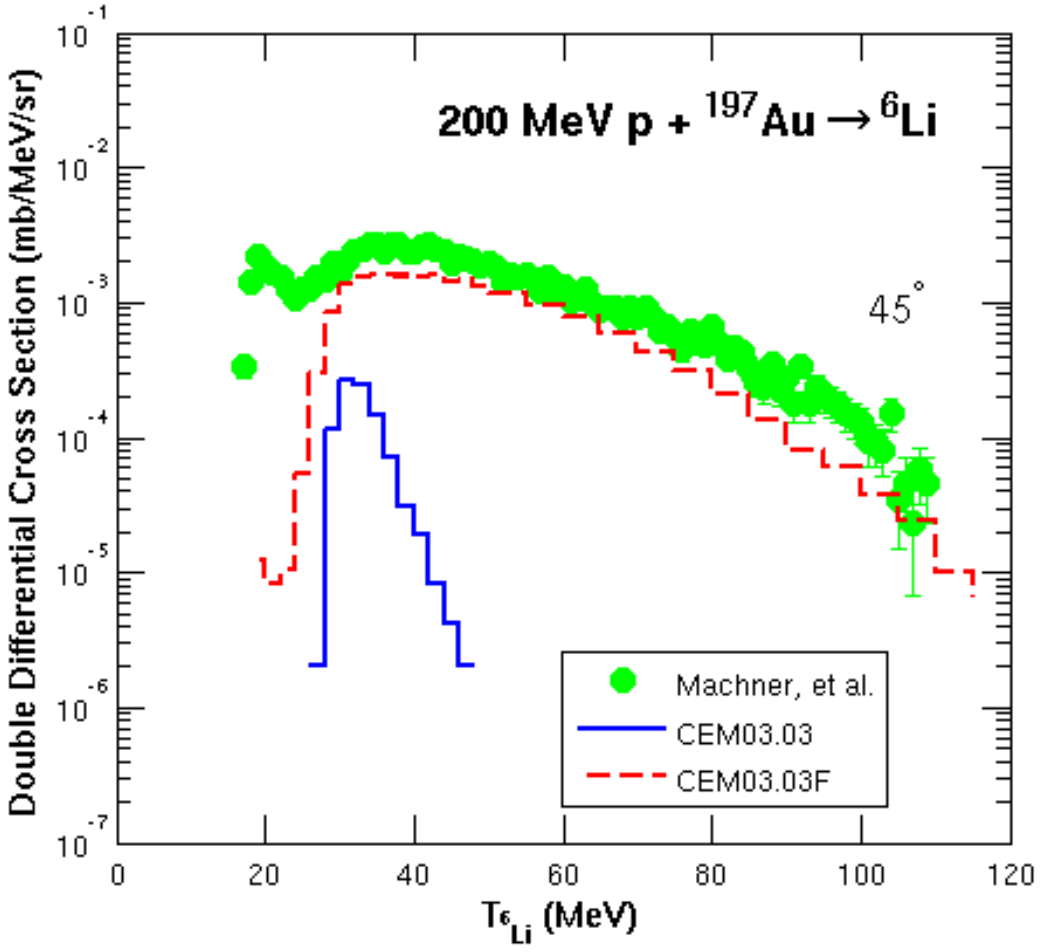

FIGURE 7.4: Comparison of experimental data by Machner, *et al.* [11] (green circles) with results by the unmodified CEM03.03 (blue solid lines) and new CEM03.03F (red dashed lines) for 200 MeV p + ^{197}Au → ^{6}Li at 45°.

(gold) and therefore an increased ability to produce these low-energy heavy clusters from both our expanded Coalescence model and expanded MEM.

Fig. 7.6 shows our results for 480 MeV p + ^{nat}Ag → ^{7}Li,^{7}Be at 40° with experimental data by Green, *et al.* [103]. We see that CEM03.03F produces significantly improved results and matches the data reasonably well. Fig. 7.7 plots spectra of ^{6}Li and includes a version of CEM03.03F without the Coalescence expansion (green dash-dotted lines). This reaction illustrates how the coalescence can produce heavy clusters not just of high-energy, but also of low- and moderate-energy, thus improving agreement with experimental data in these energy regions as well.

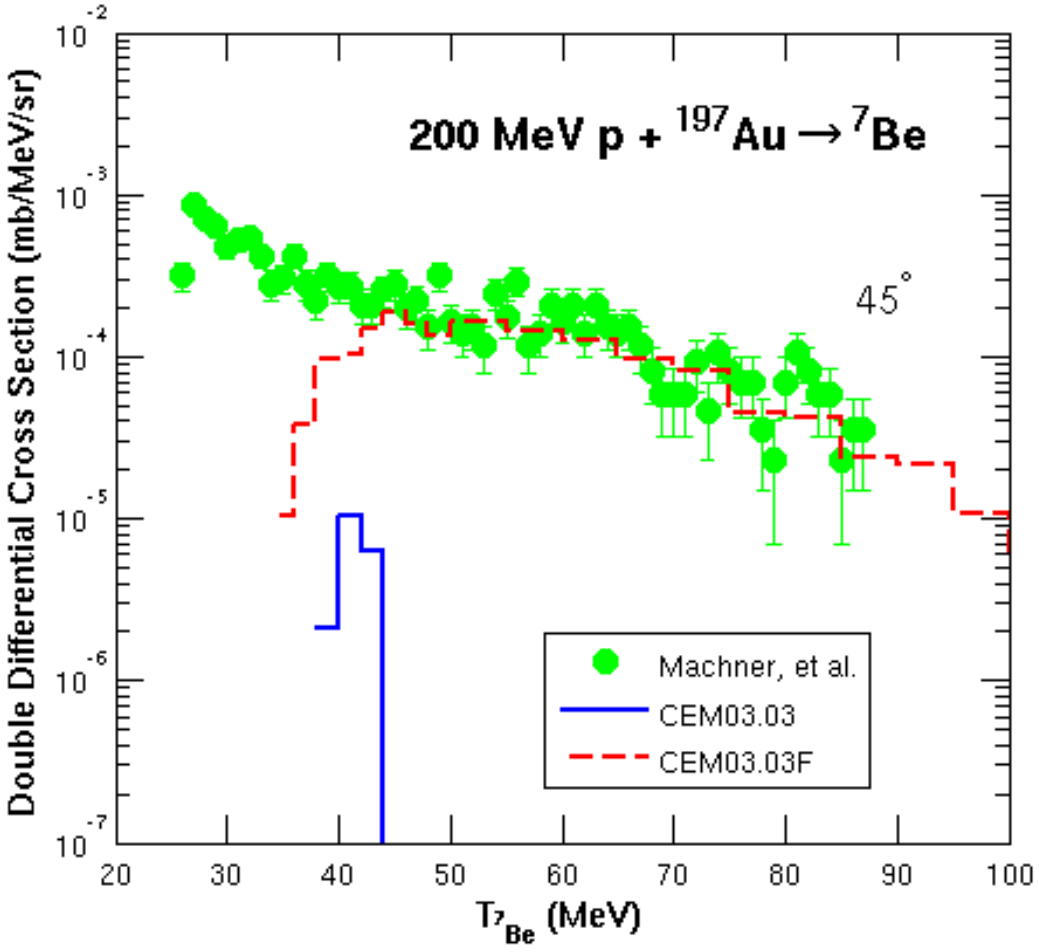

FIGURE 7.5: Comparison of experimental data by Machner, *et al.* [11] (green circles) with results by the unmodified CEM03.03 (blue solid lines) and new CEM03.03F (red dashed lines) for 200 MeV p + ^{197}Au → ^{7}Be at 45°.

Fig. 7.8 displays our results for 500 MeV p + ^{58}Ni → p with experimental data by Roy, *et al.* [173]. This figure further illustrates that CEM03.03F achieves increased production of heavy clusters without "destroying" the established spectra of nucleons and light fragments up to ^{4}He (in this particular case protons).

Fig. 7.9 displays our results for 660 MeV p + ^{58}Ni → ^{4}He at 90° with experimental data by Bogatin, *et al.* [174]. This figure again demonstrates that CEM03.03F achieves increased production of heavy clusters without "destroying" the established spectra of nucleons and light fragments up to ^{4}He (in this particular case ^{4}He), but in some cases it even achieves improved results for nucleons and light fragments up to ^{4}He.

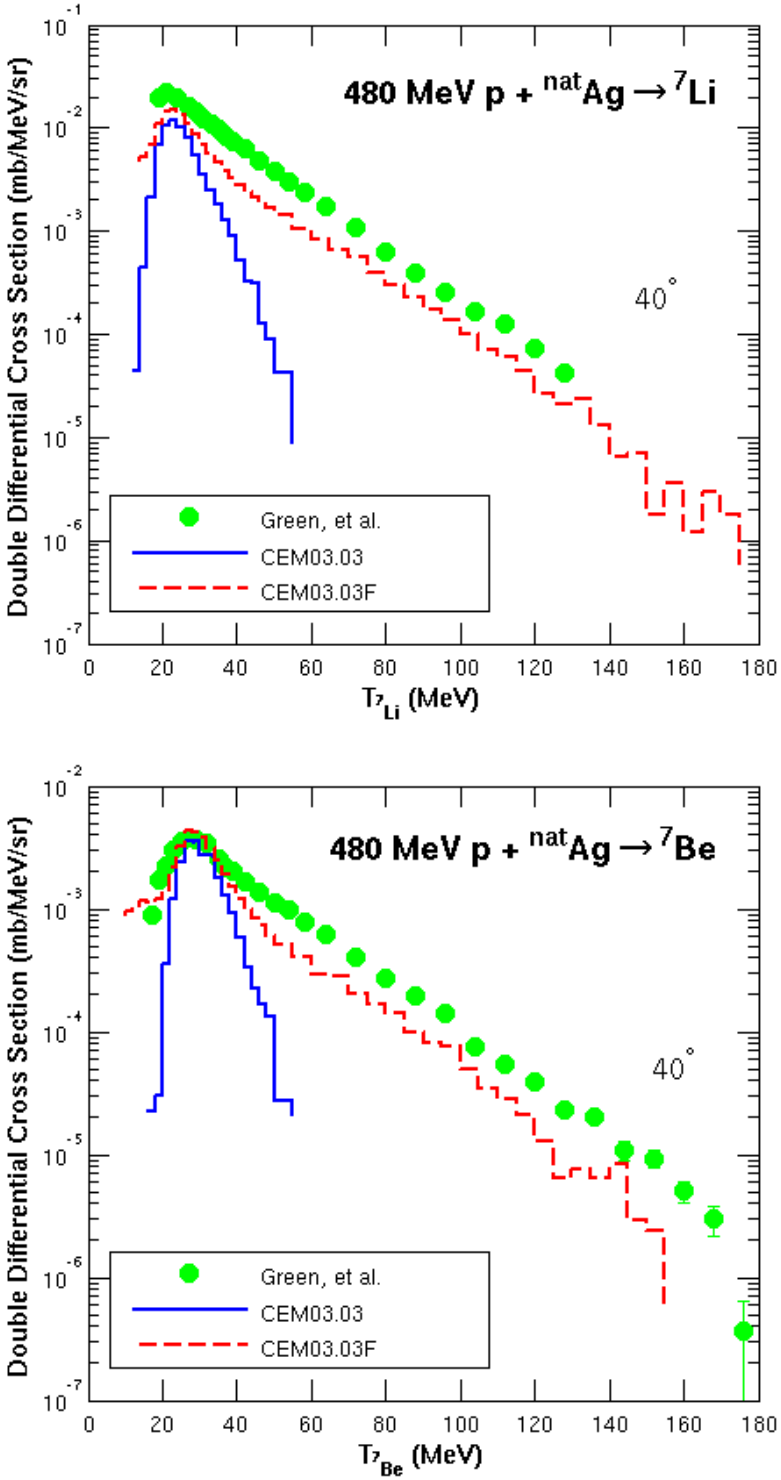

FIGURE 7.6: Comparison of experimental data by Green, *et al.* [103] (green circles) with results by the unmodified CEM03.03 (blue solid lines) and new CEM03.03F (red dashed lines) for 480 MeV p + ^{nat}Ag → ^{7}Li,^{7}Be at 40°.

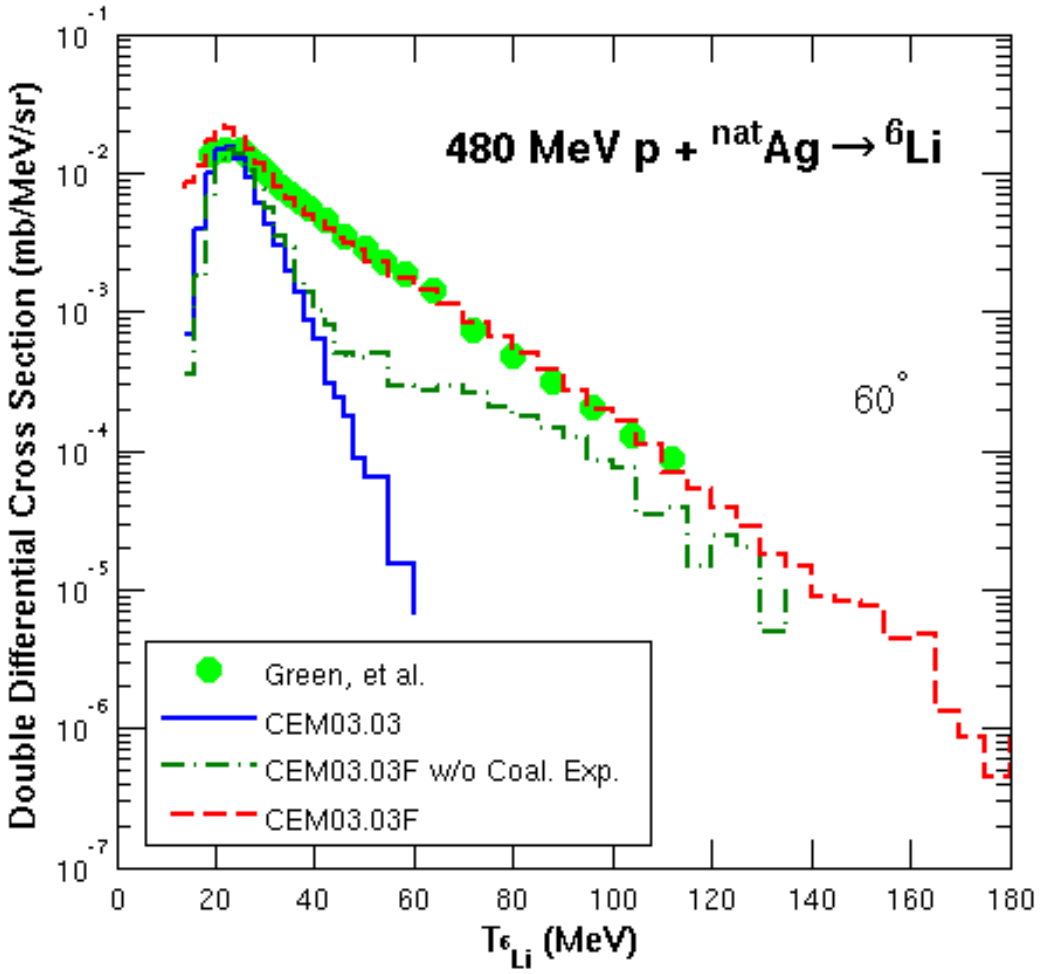

FIGURE 7.7: Comparison of experimental data by Green, *et al.* [103] (green circles) with results by the unmodified CEM03.03 (blue solid lines) and new CEM03.03F (red dashed lines) for 480 MeV p + ^{nat}Ag → ^{6}Li at 60°.

Fig. 7.10 demonstrates our results for 1200 MeV p + ^{nat}Ni → p,^{6}Li at 65° with experimental data by Budzanowski, *et al.* [50]. The proton spectra again illustrate that CEM03.03F achieves increased production of heavy clusters without "destroying" the established spectra of nucleons and light fragments up to ^{4}He (in this particular case protons). The spectra of ^{6}Li again show markedly improved production of heavy clusters at mid and high energies.

Fig. 7.11 shows our results for 1200 MeV p + ^{nat}Ni → ^{7}Li at 15.6° with experimental data by Budzanowski, *et al.* [50]. We again see that CEM03.03F matches the experimental data significantly better than the original CEM03.03.

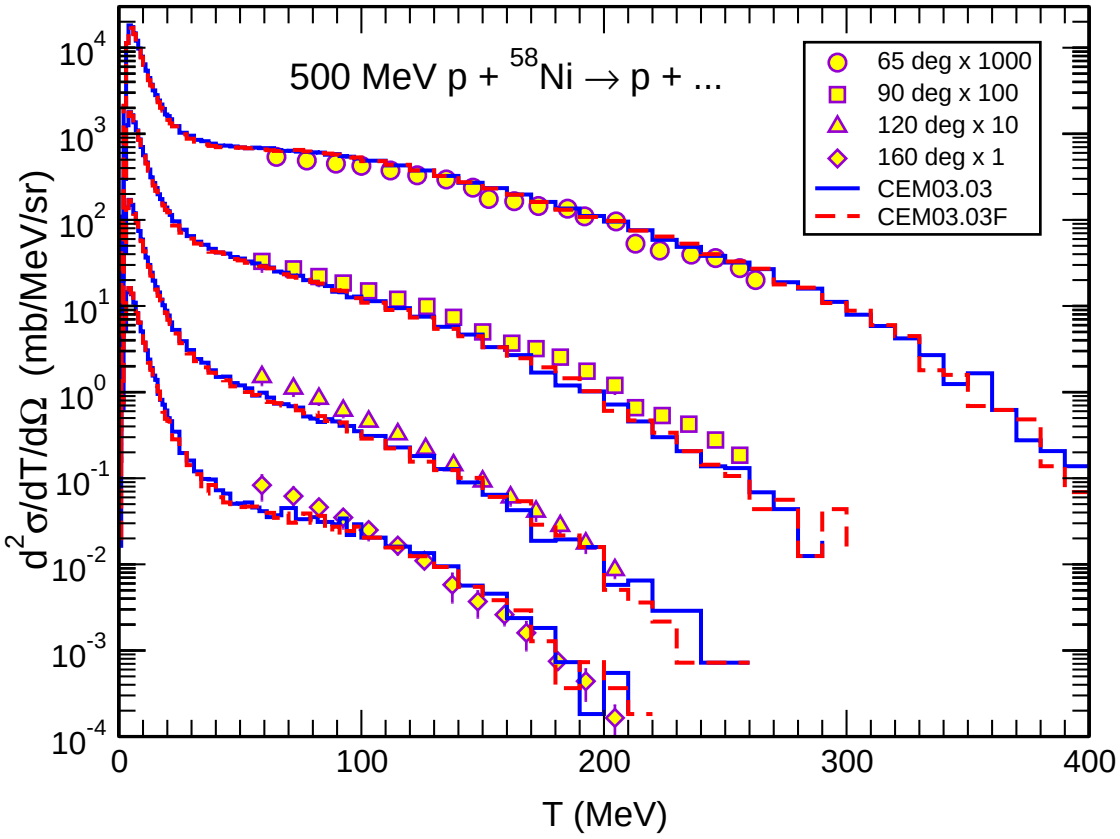

FIGURE 7.8: Comparison of experimental data by Roy, *et al.* [173] (symbols) with results by the unmodified CEM03.03 (blue solid lines) and new CEM03.03F (red dashed lines) for 500 MeV p + ^{58}Ni → p.

Fig. 7.12 displays our results for 1200 MeV p + ^{197}Au → ^{6}Li,^{7}Be at 20° with experimental data by Budzanowski, *et al.* [49]. Again CEM03.03F demonstrates dramatically increased production of heavy clusters in the mid- and high-energy regions compared to the original CEM03.03.

Fig. 7.13 illustrates our results for 1200 MeV p + ^{197}Au → ^{6}He at 35° with experimental data by Budzanowski, *et al.* [49]. This figure provides an example of our improved results for ^{6}He spectra.

Fig. 7.14 demonstrates our results for 2500 MeV p + ^{nat}Ni → t,^{7}Be at 100° and 65°, respectively, with experimental data by Budzanowski, *et al.* [50]. The triton spectra again illustrate that CEM03.03F achieves increased production of heavy clusters without "destroying" the established spectra of nucleons and light fragments up to

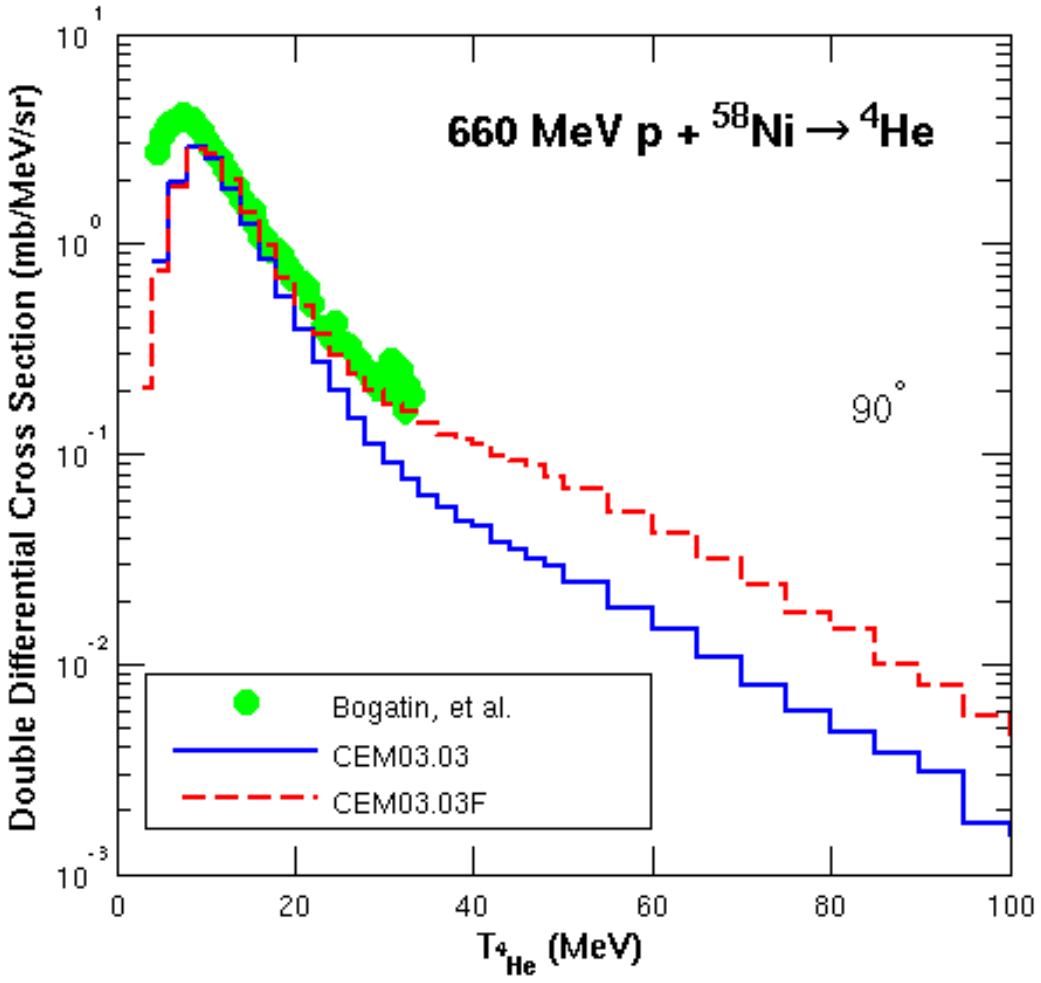

FIGURE 7.9: Comparison of experimental data by Bogatin, *et al.* [174] (green circles) with results by the unmodified CEM03.03 (blue solid lines) and new CEM03.03F (red dashed lines) for 660 MeV p + ^{58}Ni → ^{4}He at 90°.

^{4}He (in this particular case tritons). The ^{7}Be spectra show increased production of heavy clusters, and sometimes in the case of high incident energy, a little too much production from our Coalescence model. We hope to remedy this in the future in creating both a more expanded Coalescence model (which can coalesce fragments heavier than $A = 7$ which we expanded to in this work) and a model which is smoothly dependent upon incident energy.

Fig. 7.15 displays our results for 2500 MeV p + ^{nat}Ni → ^{7}Li at 100° with experimental data by Budzanowski, *et al.* [50]. We see again dramatically improved results for energetic heavy cluster production with our CEM03.03F.

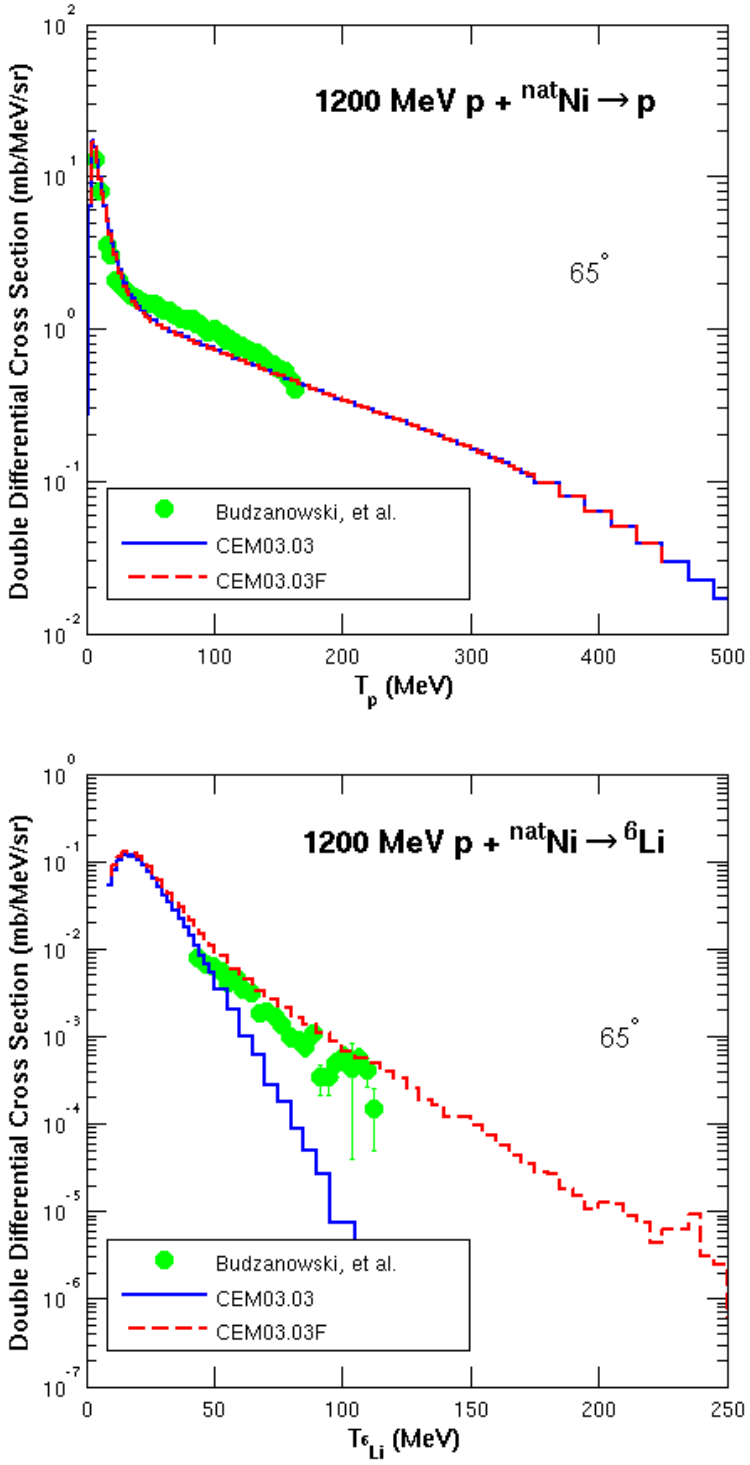

FIGURE 7.10: Comparison of experimental data by Budzanowski, *et al.* [50] (green circles) with results by the unmodified CEM03.03 (blue solid lines) and new CEM03.03F (red dashed lines) for 1200 MeV p + ^{nat}Ni → p,^{6}Li at 65°.

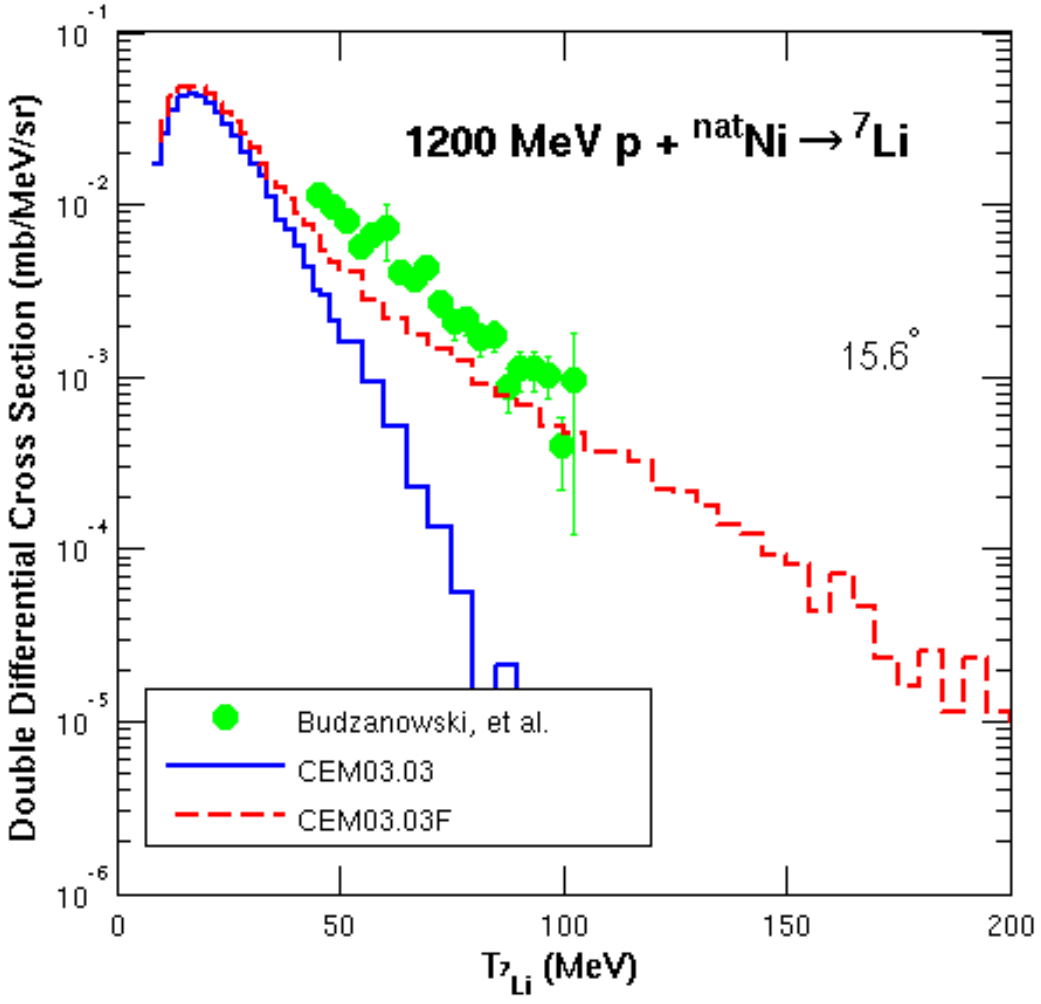

FIGURE 7.11: Comparison of experimental data by Budzanowski, *et al.* [50] (green circles) with results by the unmodified CEM03.03 (blue solid lines) and new CEM03.03F (red dashed lines) for 1200 MeV p + ^{nat}Ni → ^{7}Li at 15.6°.

Fig. 7.16 shows our results for 2500 MeV p + ^{197}Au → ^{7}Li, ^{9}Be at 50° and 15.6°, respectively, with experimental data by Bubak, *et al.* [51]. This figure, combined with Fig. 7.17, provide examples of our results from CEM03.03F for rare, neutron-rich, isotopes of lithium and berrylium. CEM03.03F produces improved results compared to the unmodified CEM03.03.

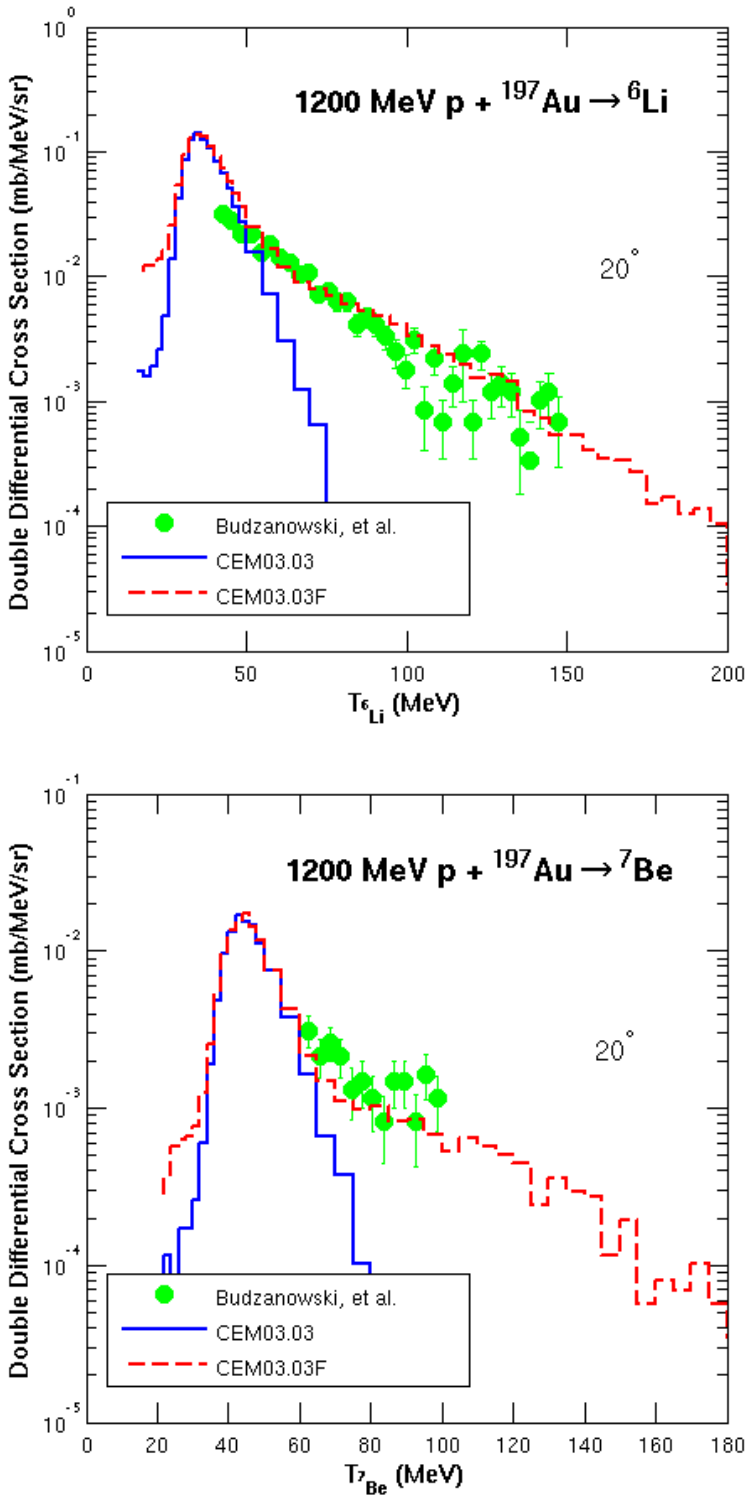

FIGURE 7.12: Comparison of experimental data by Budzanowski, *et al.* [49] (green circles) with results by the unmodified CEM03.03 (blue solid lines) and new CEM03.03F (red dashed lines) for 1200 MeV p + ^{197}Au → ^{6}Li,^{7}Be at 20°.

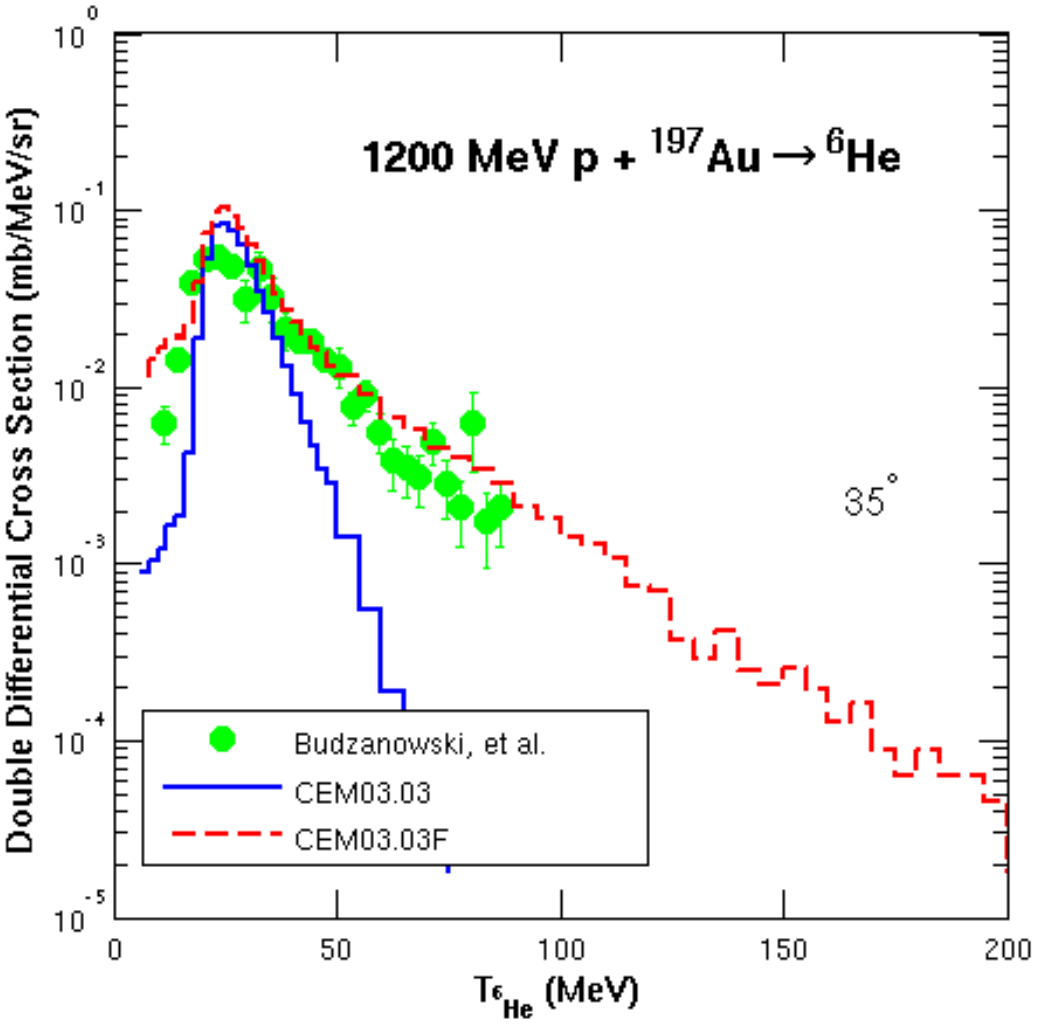

FIGURE 7.13: Comparison of experimental data by Budzanowski, *et al.* [49] (green circles) with results by the unmodified CEM03.03 (blue solid lines) and new CEM03.03F (red dashed lines) for 1200 MeV p + ^{197}Au → ^{6}He at 35°.

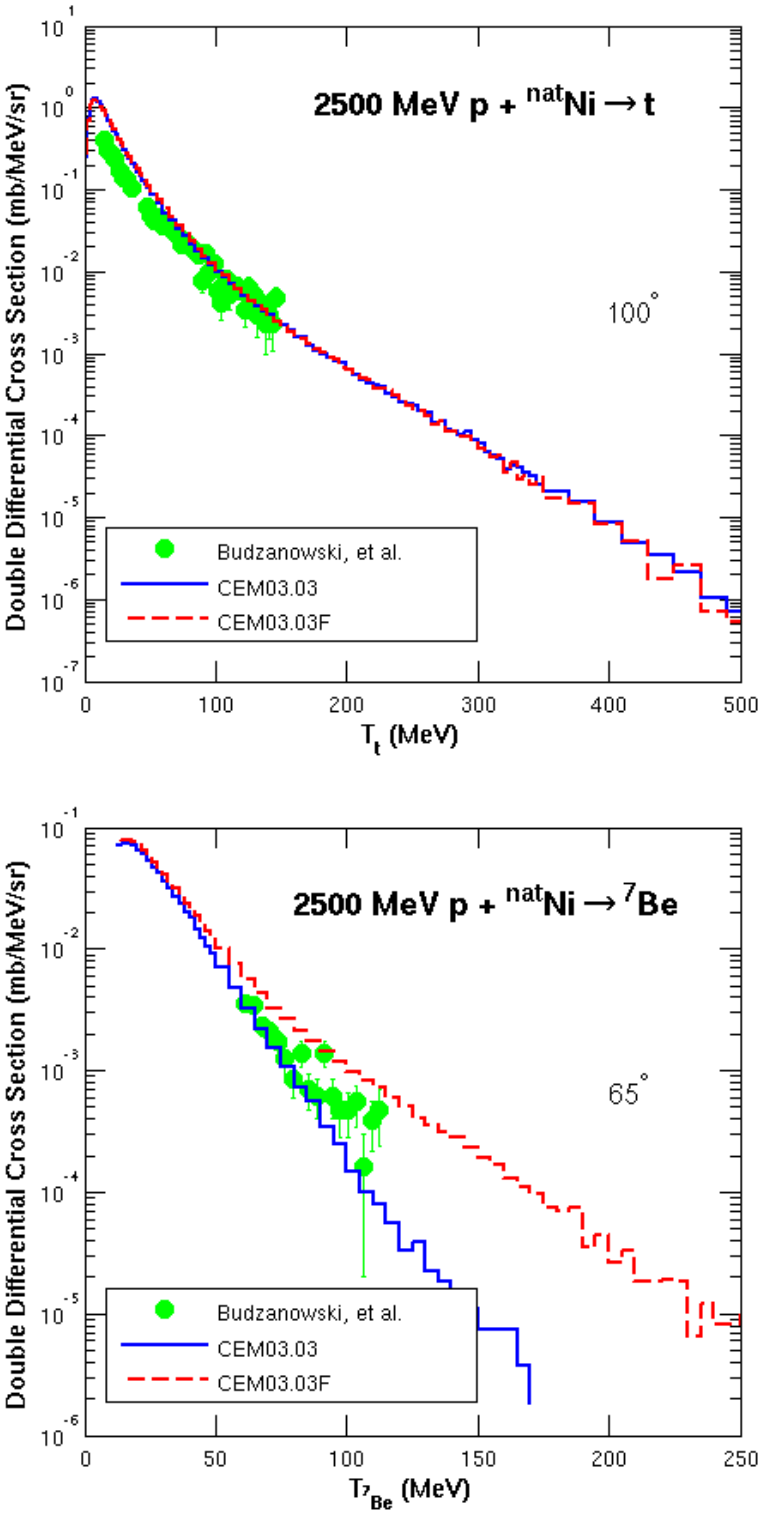

FIGURE 7.14: Comparison of experimental data by Budzanowski, *et al.* [50] (green circles) with results by the unmodified CEM03.03 (blue solid lines) and new CEM03.03F (red dashed lines) for 2500 MeV p + ^{nat}Ni → t,^{7}Be at 100°and 65°, respectively.

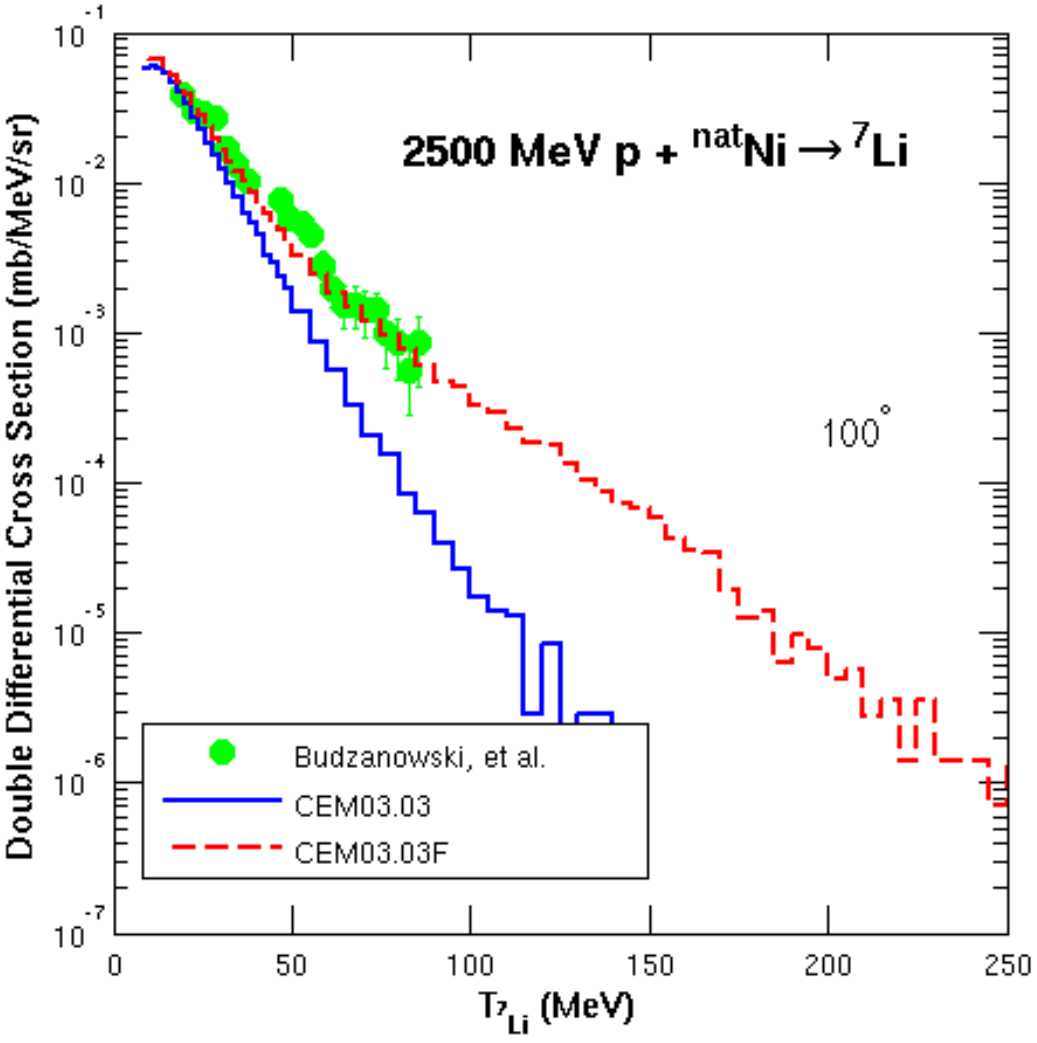

FIGURE 7.15: Comparison of experimental data by Budzanowski, *et al.* [50] (green circles) with results by the unmodified CEM03.03 (blue solid lines) and new CEM03.03F (red dashed lines) for 2500 MeV p + ^{nat}Ni → ^{7}Li at 100°.

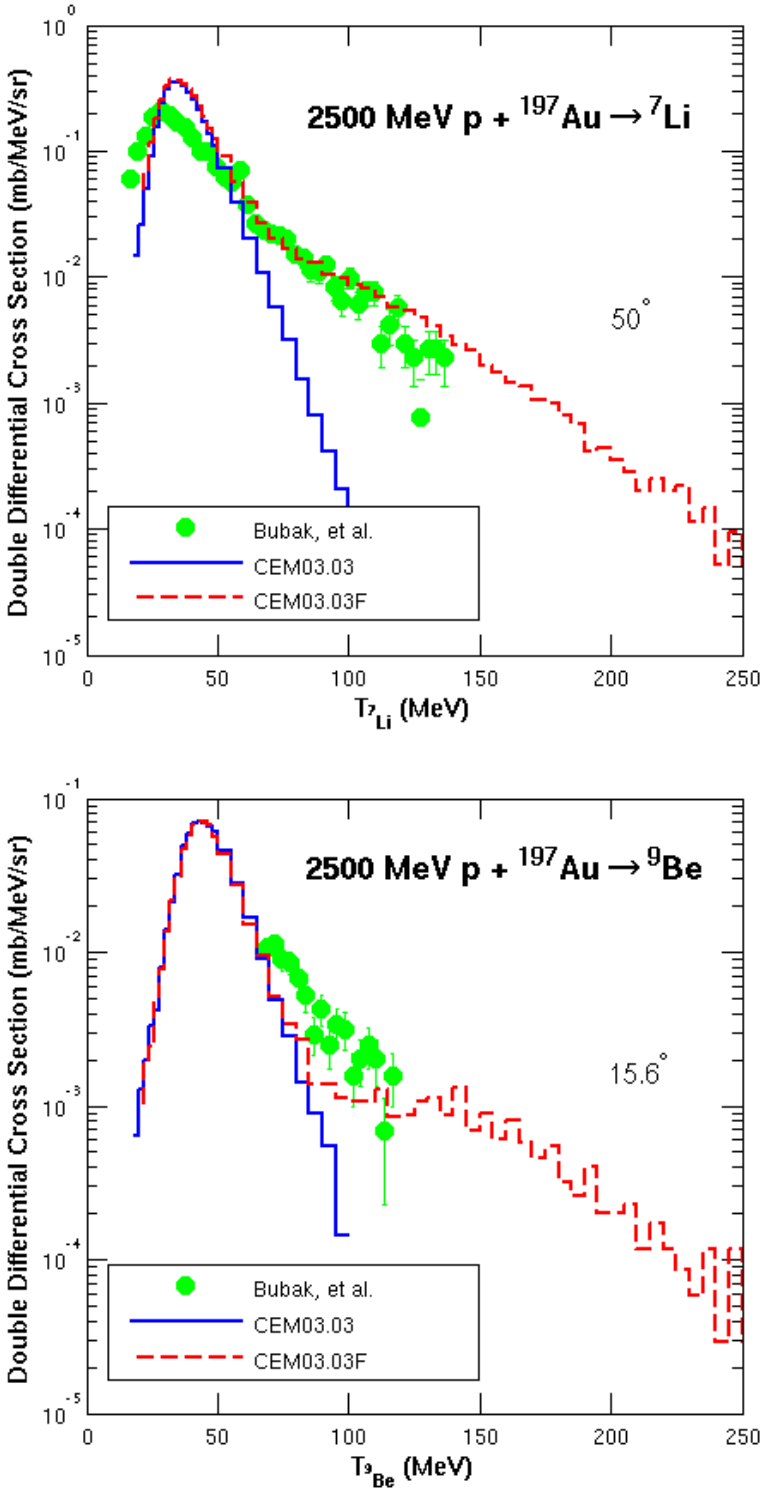

FIGURE 7.16: Comparison of experimental data by Bubak, *et al.* [51] (green circles) with results by the unmodified CEM03.03 (blue solid lines) and new CEM03.03F (red dashed lines) for 2500 MeV p + ^{197}Au → ^{7}Li, ^{9}Be at 50°and 15.6°, respectively.

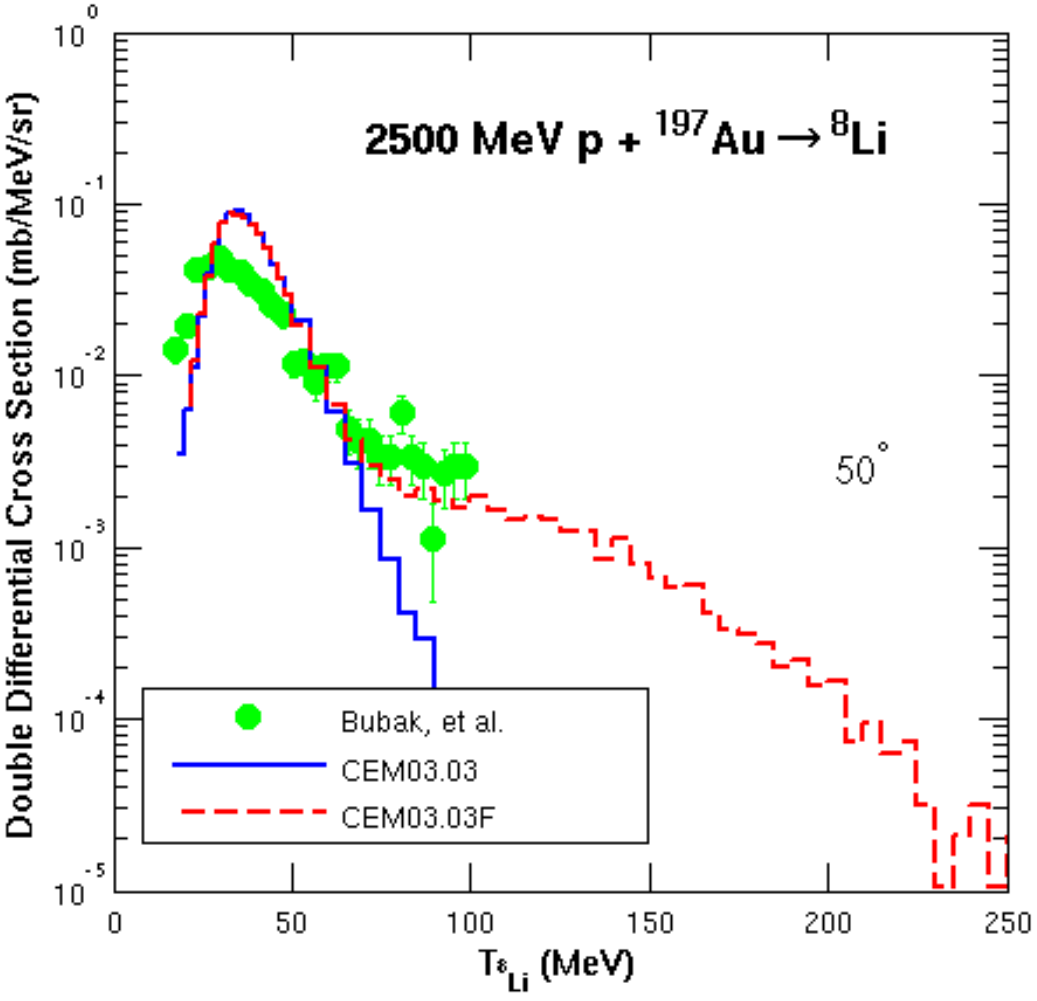

FIGURE 7.17: Comparison of experimental data by Bubak, *et al.* [51] (green circles) with results by the unmodified CEM03.03 (blue solid lines) and new CEM03.03F (red dashed lines) for 2500 MeV p + ^{197}Au → ^{8}Li at 50°.

7.2 FRAGMENT SPECTRA FOR NEUTRON-INDUCED REACTIONS

Figs. 7.18–7.20 compare examples of experimental data with results by the unmodified CEM03.03 (blue solid lines) and CEM03.03F with the expanded Modified Exciton Model, upgraded NASA-Kalbach inverse cross section (in the preequilibrium stage), expanded Coalescence Model, and new F_j Model (red dashed lines) for neutron-induced reactions. We see here that our new CEM03.03F generally has little effect upon the spectra of emitted fragments up to ^{4}He, and as there is no experimental data for emitted heavy clusters heavier than ^{4}He, we cannot compare our improved models. However, we see that our upgraded CEM03.03F gives results that are "no worse" than the current CEM03.03.

Fig. 7.18 displays our results for 96 MeV n + ^{nat}U $\rightarrow$ p,^{4}He at 20° with experimental data by Blideanu, *et al.* [164]. This figure provides examples of the consistency between results from CEM03.03F and CEM03.03 for nucleons and light fragments equal to ^{4}He and lighter.

Fig. 7.19 shows our results for 317 MeV n + ^{209}Bi $\rightarrow$ d,t at 54° with experimental data by Franz, *et al.* [171]. This figure again illustrates that our improved production of heavy clusters in CEM03.03F does not "destroy" the spectra of complex particles and light fragments equal to ^{4}He and lighter.

Fig. 7.20 shows our results for 542 MeV n + ^{nat}Cu $\rightarrow$ t,^{6}Li at 68° with experimental data by Franz, *et al.* [171]. This figure again demonstrates that our new CEM03.03F produces more energetic heavy clusters while remaining consistent in the production of nucleons and light fragments equal to ^{4}He and lighter. The ^{6}Li spectra provide a "first guess" for the production of heavy clusters from neutron-induced reactions. We hope to be able to compare our predictions to experimental data of heavy-cluster spectra from neutron-induced reactions in the future.

Fig. 7.21 shows our results for 562.5 MeV n + ^{nat}Cu $\rightarrow \pi^+$ with experimental data by Brooks, *et al.* [179]. This figure shows that our improved production of heavy clusters in CEM03.03F does not "destroy" the spectra of pions.

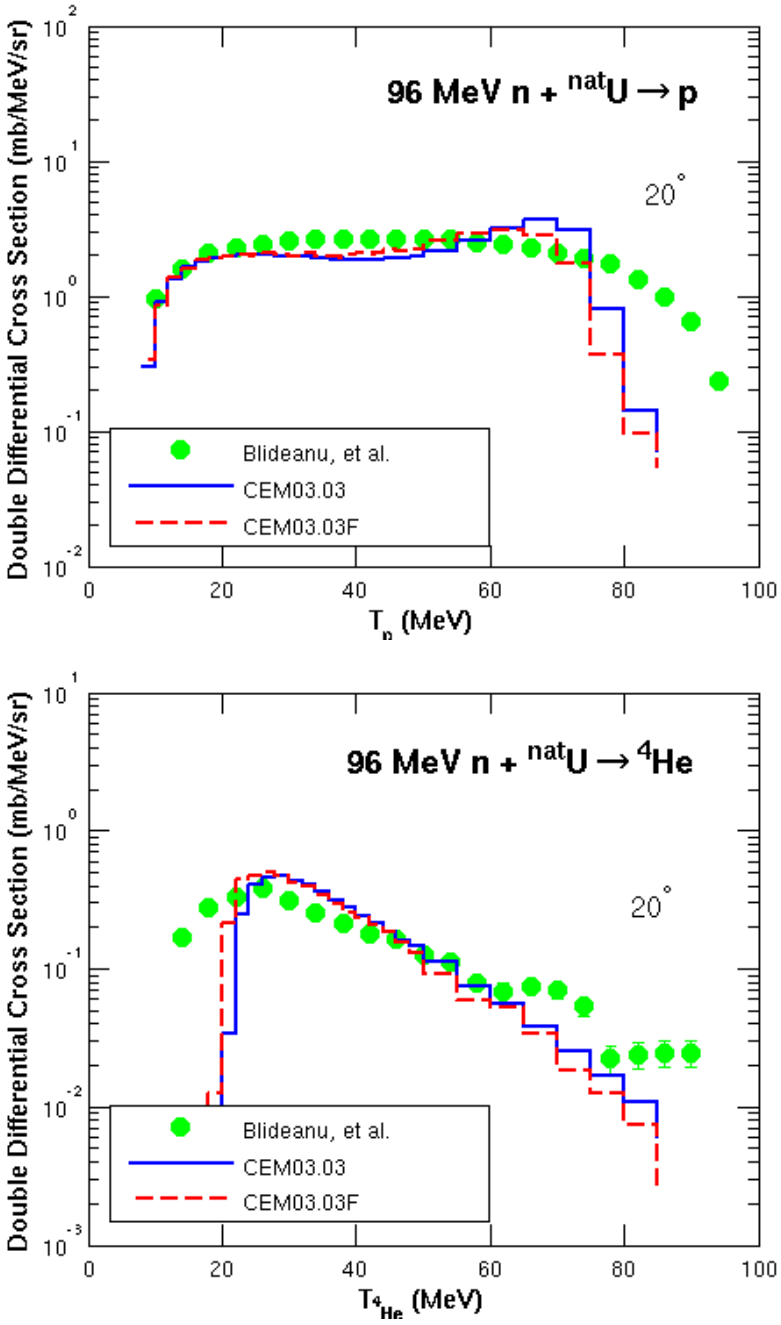

FIGURE 7.18: Comparison of experimental data by Blideanu, *et al.* [164] (green circles) with results by the unmodified CEM03.03 (blue solid lines) and new CEM03.03F (red dashed lines) for 96 MeV n + ^{nat}U → p,^{4}He at 20°.

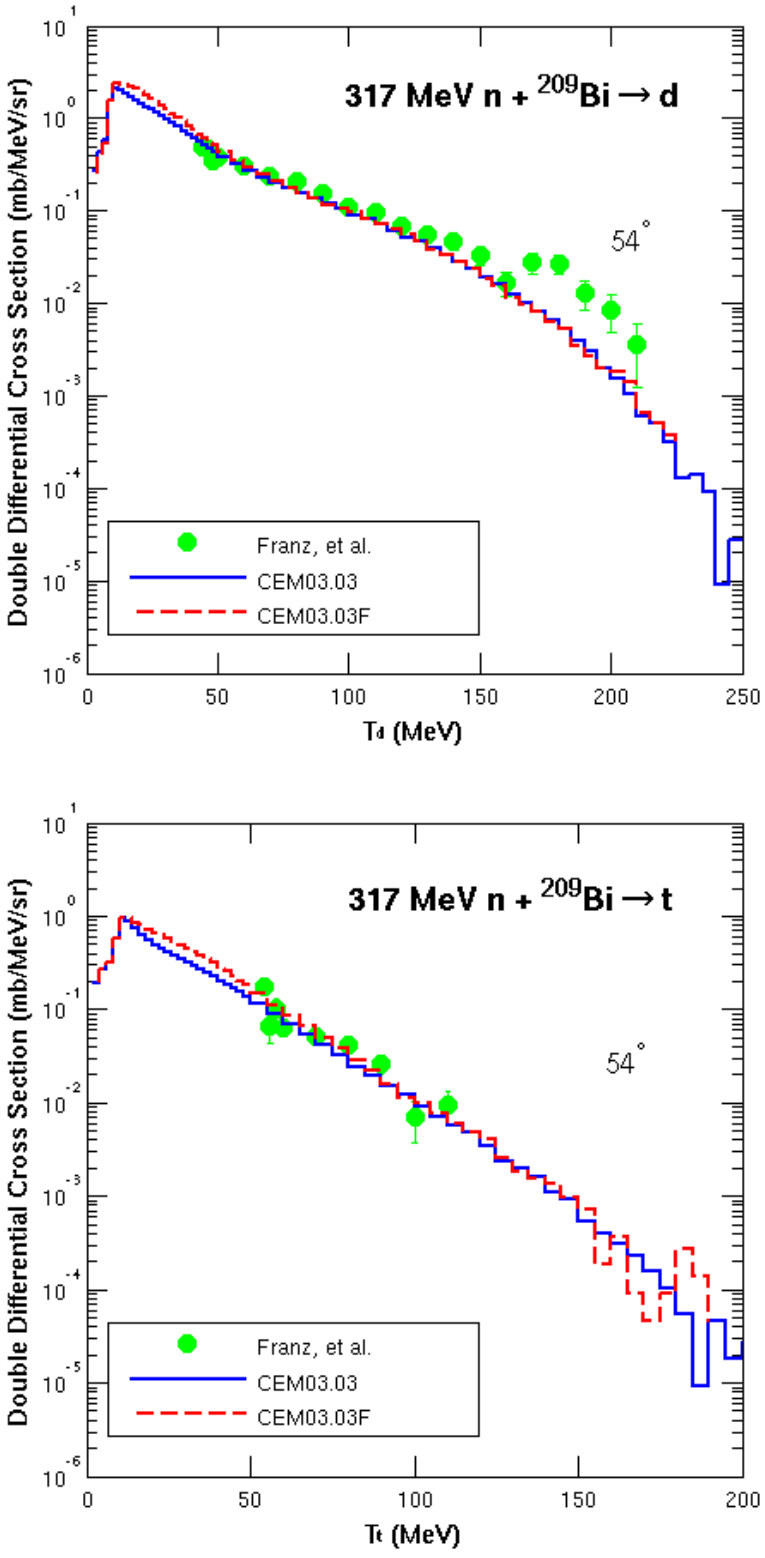

FIGURE 7.19: Comparison of experimental data by Franz, *et al.* [171] (green circles) with results by the unmodified CEM03.03 (blue solid lines) and new CEM03.03F (red dashed lines) for 317 MeV n + ^{209}Bi → d,t at 54°.

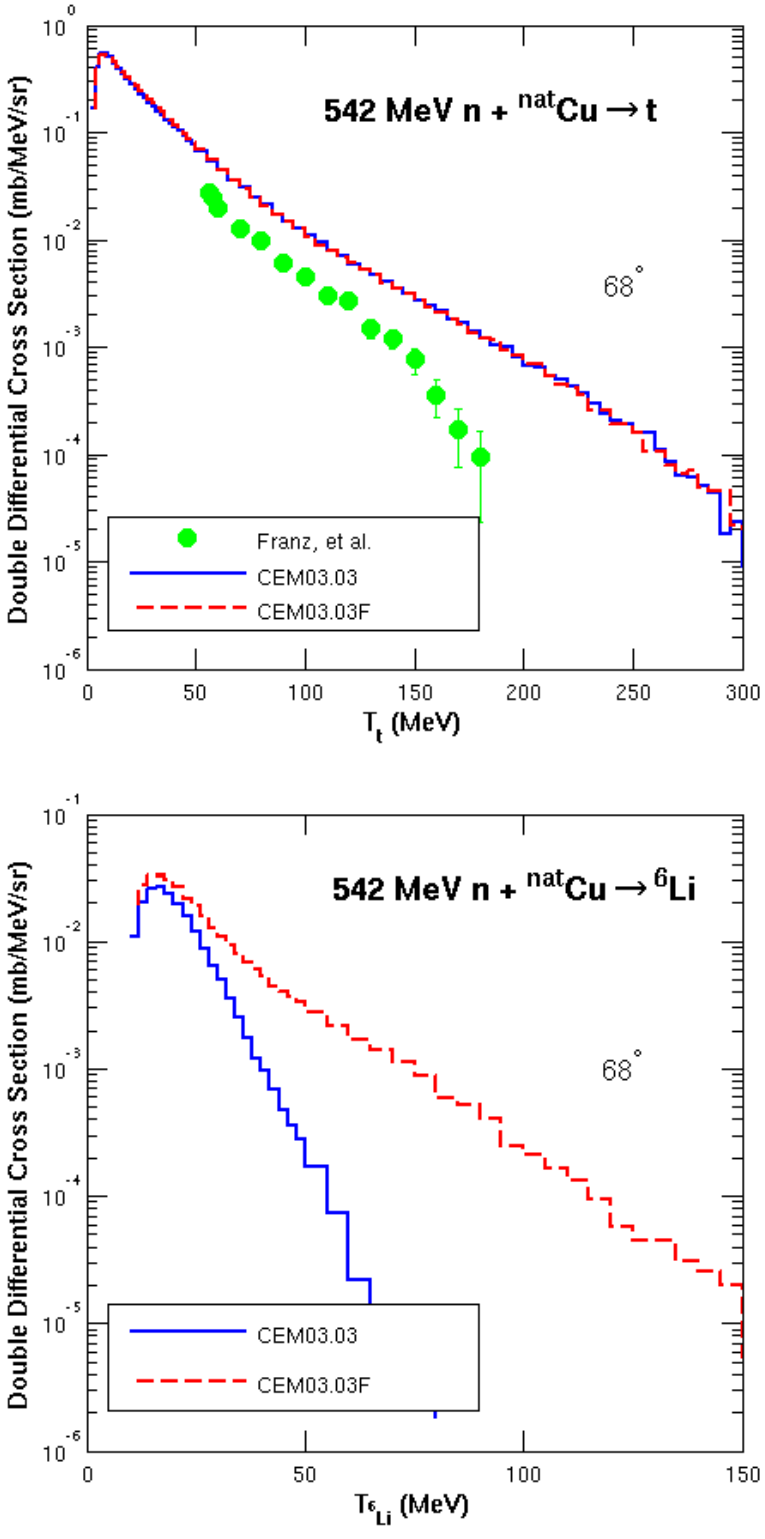

FIGURE 7.20: Comparison of experimental data by Franz, *et al.* [171] (green circles) with results by the unmodified CEM03.03 (blue solid lines) and new CEM03.03F (red dashed lines) for 542 MeV n + ^{nat}Cu → t,^{6}Li at 68°.

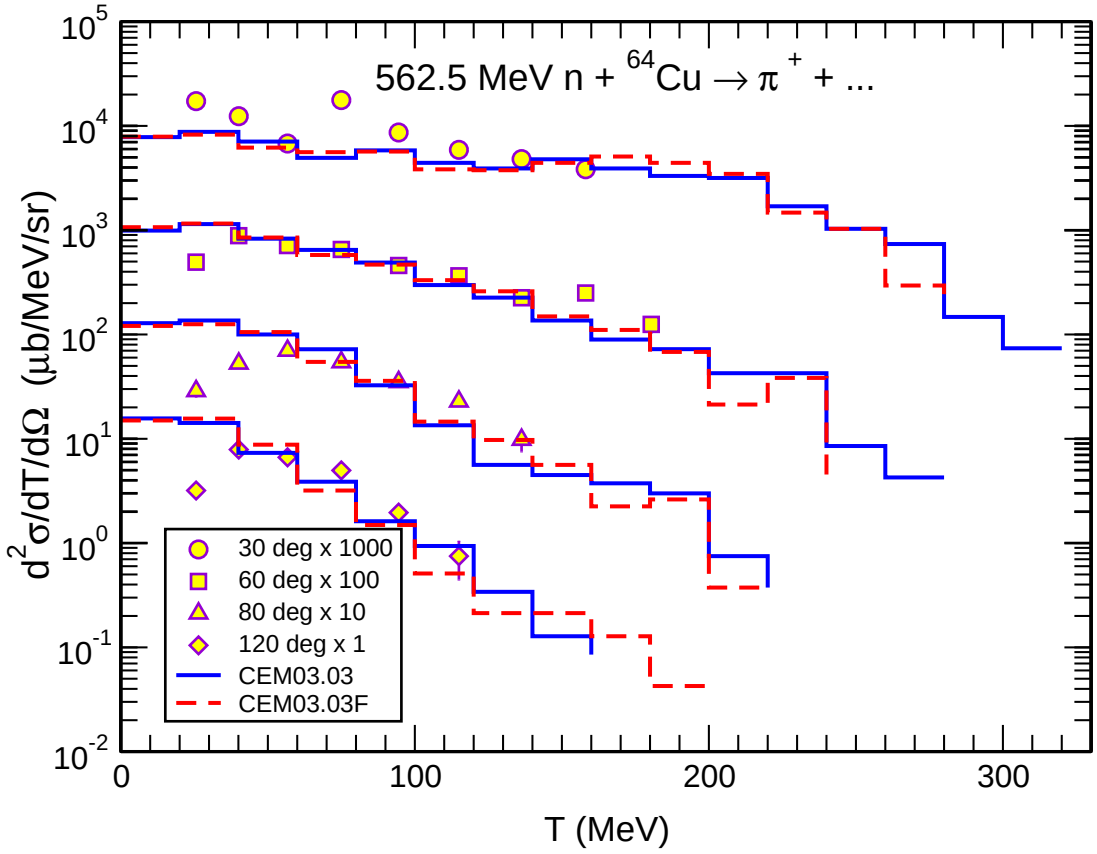

FIGURE 7.21: Comparison of experimental data by Brooks, *et al.* [179] (symbols) with results by the unmodified CEM03.03 (blue solid lines) and new CEM03.03F (red dashed lines) for 562.5 MeV n + ^{nat}Cu $\rightarrow \pi^+$.

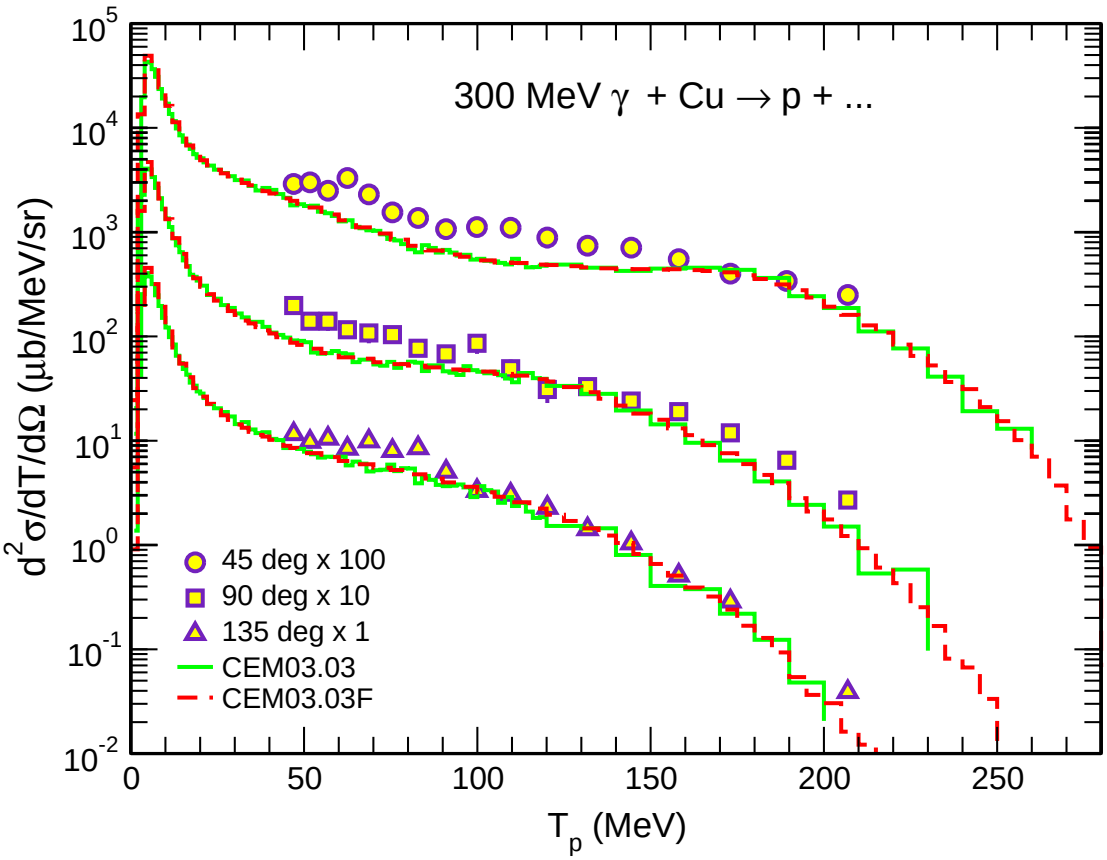

FIGURE 7.22: Comparison of experimental data by Schumacher, *et al.* [180] (filled symbols) with results by the unmodified CEM03.03 (green solid lines) and new CEM03.03F (red dashed lines) for 300 MeV γ + ^{nat}Cu $\rightarrow$ p at 45°, 90°, and 135°.

7.3 FRAGMENT SPECTRA FROM γ- AND π-INDUCED REACTIONS

Figs. 7.22–7.23 compare examples of experimental data with results by the unmodified CEM03.03 (blue solid lines) and CEM03.03F with the expanded Modified Exciton Model, upgraded NASA-Kalbach inverse cross section (in the preequilibrium stage), expanded Coalescence Model, and new F_j Model (red dashed lines) for γ- and π-induced reaction. We see here that our new CEM03.03F generally has little effect upon the spectra of emitted fragments up to ^{4}He, and as there is no appropriate experimental data for emitted heavy clusters heavier than ^{4}He, we cannot compare our improved models. However, we see that our upgraded CEM03.03F gives results that are "no worse" than the current CEM03.03, while also producing mid- and high-energy heavy clusters.

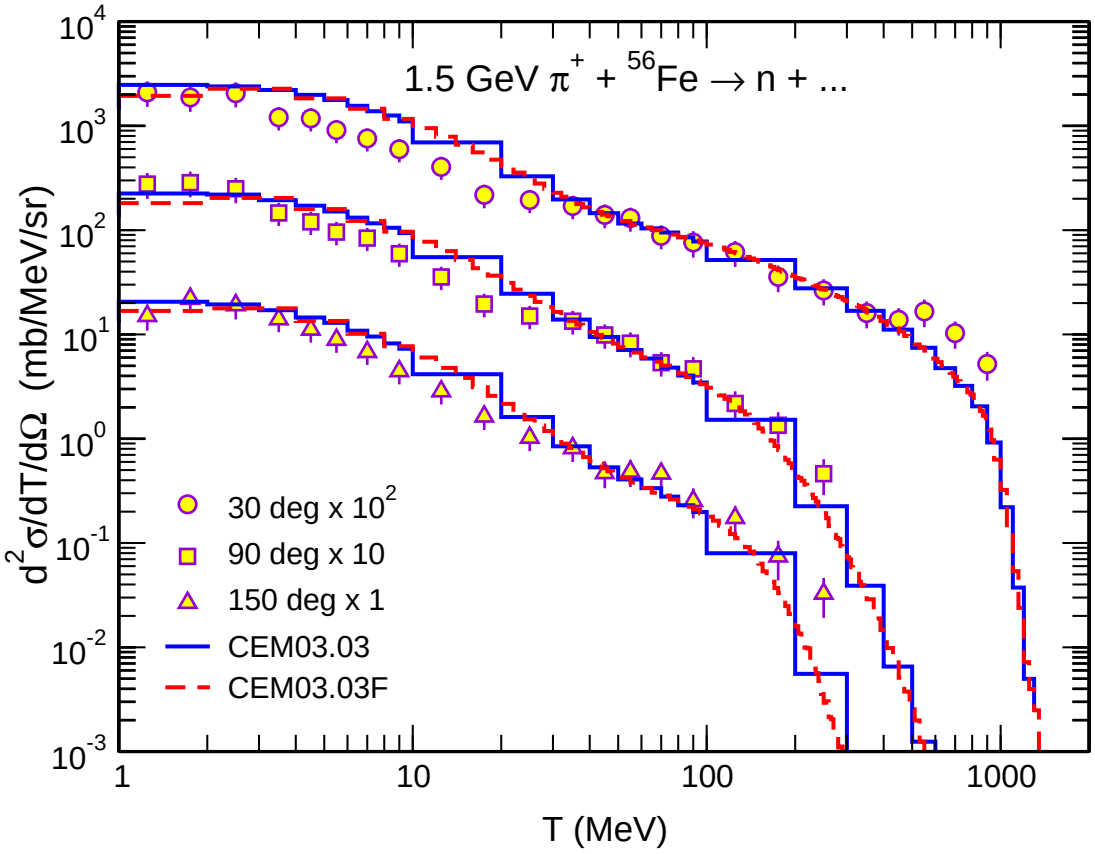

FIGURE 7.23: Comparison of experimental data by Nakamoto, *et al.* [181] (filled symbols) with results by the unmodified CEM03.03 (blue solid lines) and new CEM03.03F (red dashed lines) for 1500 MeV $\pi^+ + {}^{nat}\mathrm{Fe} \rightarrow$ n at 30°, 90°, and 150°.

Fig. 7.22 shows our results for 300 MeV $\gamma + {}^{nat}\mathrm{Cu} \rightarrow$ p at 45°, 90°, and 135° with experimental data by Schumacher, *et al.* [180]. This figure provides another example of the consistency between CEM03.03F and CEM03.03 for spectra of ^{4}He and lighter for γ-induced reactions.

Fig. 7.23 shows our results for 1500 MeV $\pi^+ + {}^{nat}\mathrm{Fe} \rightarrow$ n at 30°, 90°, and 150° with experimental data by Nakamoto, *et al.* [181]. This figure provides an example of the consistency between CEM03.03F and CEM03.03 for spectra of ^{4}He and lighter for π-induced reactions.

Fig. 7.24 shows our results for 500 MeV $\pi^- + {}^{64}\mathrm{Cu} \rightarrow \pi^0$ at 30°, 50°, and 70° with experimental data [182, 183]. This figure provides another example of the consistency

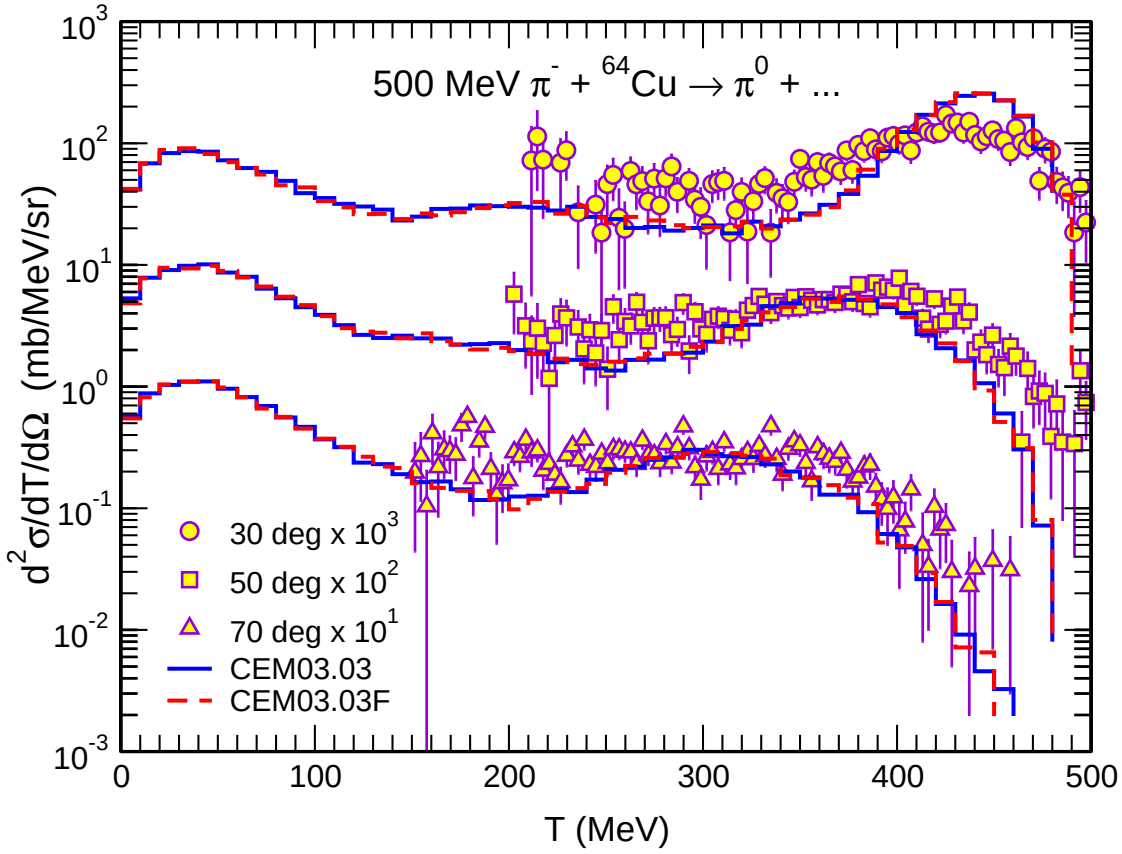

FIGURE 7.24: Comparison of experimental data [182, 183] (filled symbols) with results by the unmodified CEM03.03 (blue solid lines) and new CEM03.03F (red dashed lines) for 500 MeV π^- + ^{64}Cu $\rightarrow$ π^0 at 30°, 50°, and 70°.

between CEM03.03F and CEM03.03 for spectra of ^{4}He and lighter for π-induced reactions.

7.4 PRODUCT YIELDS

Fig. 7.25 shows the measured [184] mass and charge distributions of the product yields from the reaction 800 MeV p + ^{197}Au, and of the mean kinetic energy of these products, and the mass distributions of the cross sections for the production of thirteen elements with the charge Z from 20 to 80 (open symbols), compared with predicted results from the original CEM03.03 (solid lines) and the new CEM03.03F (dashed lines). We see that our new CEM03.03F has maintained consistency with CEM03.03 on these measures.

Fig. 7.26 displays experimental mass distributions of the yields of eight isotopes from Na to Mn [185] and of all light fragments from Li to O [186] from the reaction 1 GeV p + ^{56}Fe and the mass number- and charge-distributions of the product yield compared with results from both CEM03.03 and CEM03.03F. Predictions of CEM03.03/F for the mean kinetic energy, mean production angle Θ, mean parallel velocity v_z, and of the F/B ratio of the forward product cross sections to the backward ones of all isotopes in the laboratory system are given as well. We see that for the mass and charge distributions of product yields, CEM03.03 and CEM03.03F are very similar, but there is a significant difference between CEM03.03 and CEM.03F in the mean angle, v_z, and F/B distributions by charge number. This can be understood by the increase in coalescence of lithium and berrylium–we expect a more forward-peaked production of these fragments with the expansion of coalescence to include them. However, we would like to investigate and test this further.

Fig. 7.27 shows the measured [187] mass and charge distributions of the product yields from the reaction 1000 MeV p + ^{nat}U, and of the mean kinetic energy of these products, with results by the unmodified CEM03.03 and new CEM03.03F. This figure illustrates that the CEM03.03F version of CEM describes these types of reactions not worse, and often better, than the standard CEM03.03.

Fig. 7.28 shows the measured [188, 189] fission cross sections for n + Bi, with results by the unmodified CEM03.03 and new CEM03.03F. CEM03.03F agrees reasonably well with these new data on n + Bi fission cross sections, and even shows an improvement around energies of 100 MeV. But, because "F" considers emission of LF at the preequilibrium stage, the mean values of A, Z, and E of the fissioning nuclei differ a little from

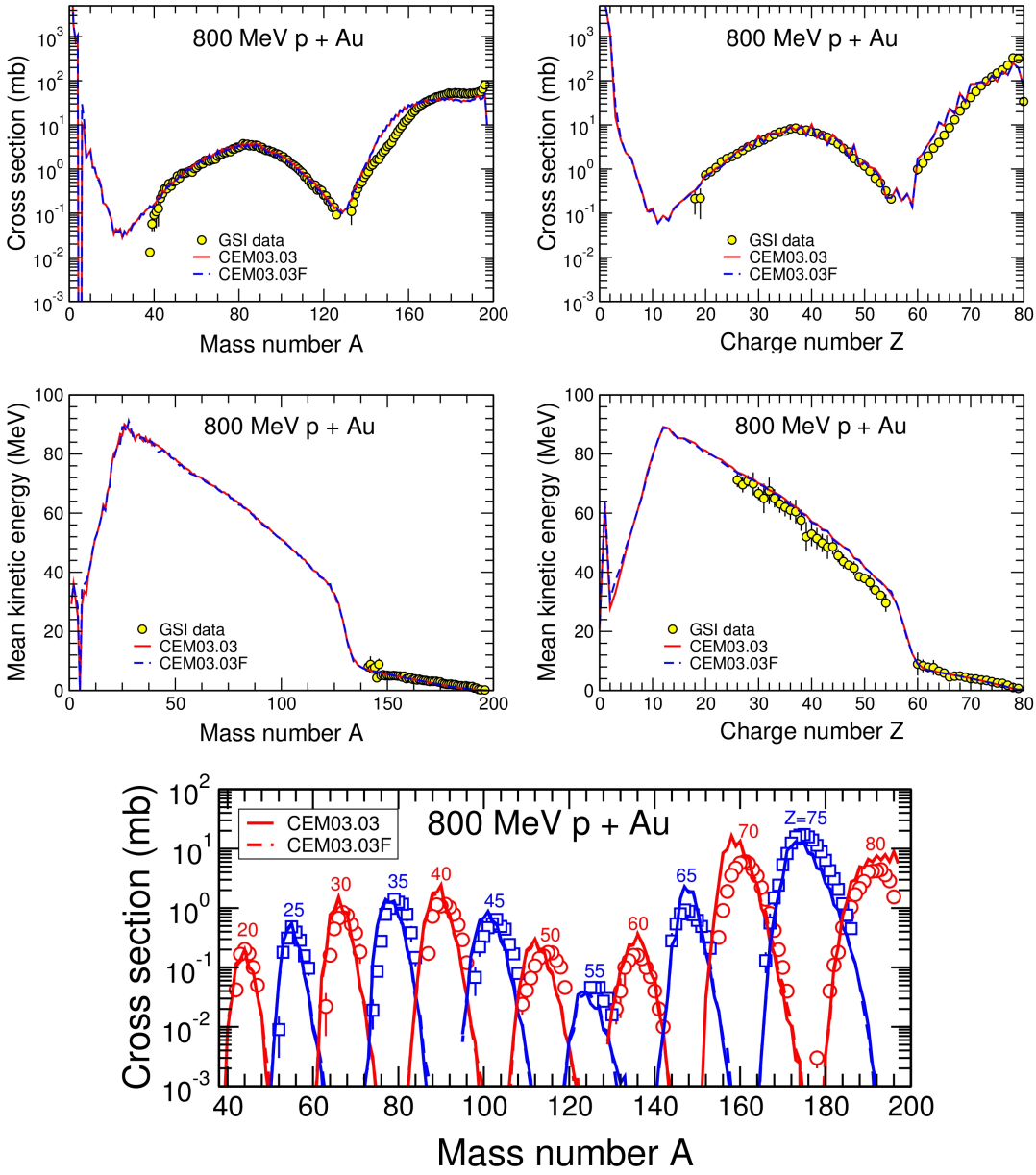

FIGURE 7.25: Comparison of measured [184] mass and charge distributions of the product yields from the reaction 800 MeV p + ^{197}Au, and of the mean kinetic energy of these products, and the mass distributions of the cross sections for the production of thirteen elements with the charge Z from 20 to 80 (open symbols), with predicted results from the original CEM03.03 (solid lines) and the new CEM03.03F (dashed lines).

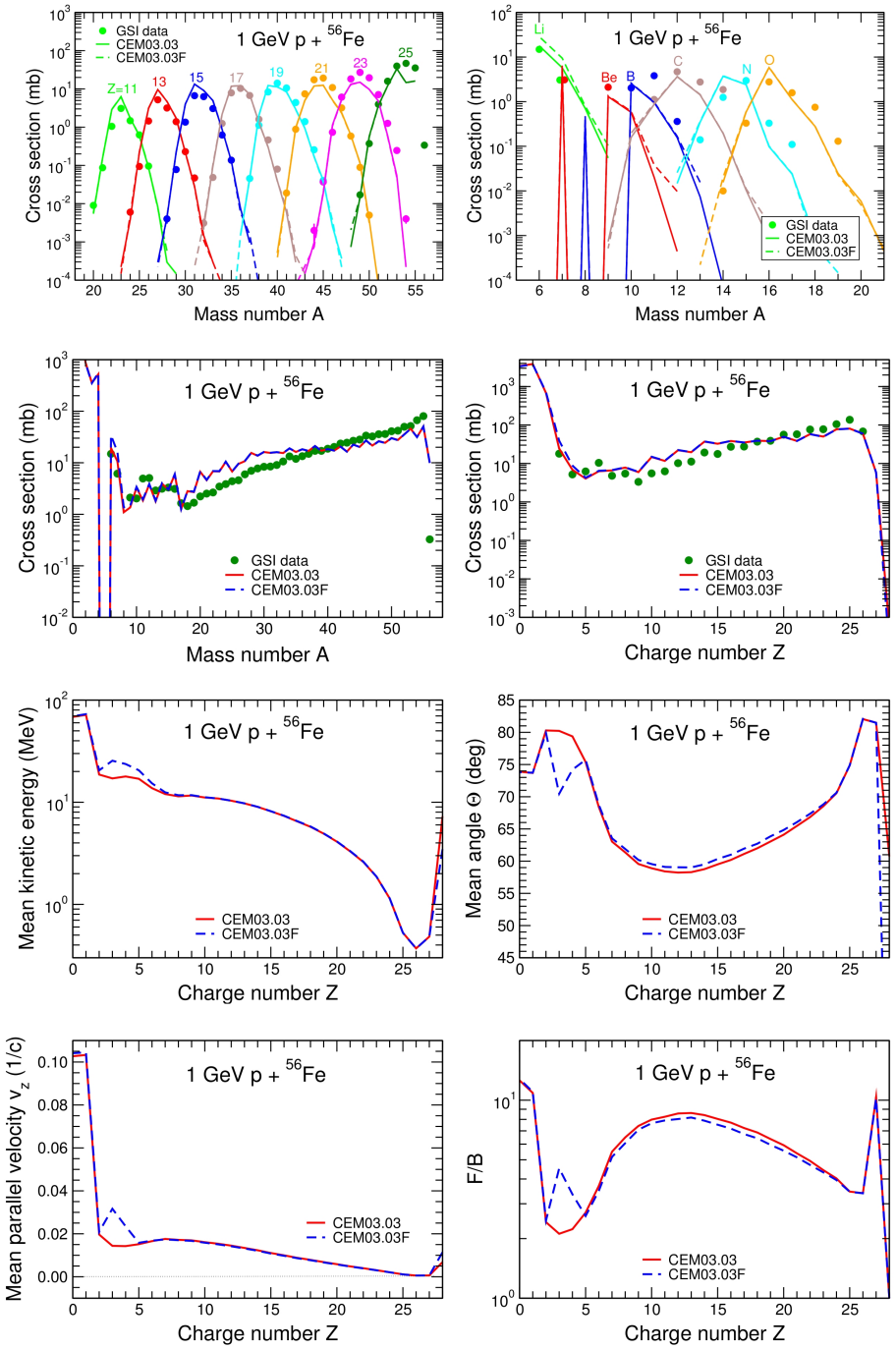

FIGURE 7.26: Experimental mass distributions of the yields of eight isotopes from Na to Mn [185] and of all light fragments from Li to O [186] from the reaction 1 GeV p + ^{56}Fe and the mass number- and charge-distributions of the product yield (color circles), compared with results from both CEM03.03 and CEM03.03F. Predictions of CEM03.03/F for the mean kinetic energy, mean production angle Θ, mean parallel velocity v_z, and of the F/B ratio of the forward product cross sections to the backward ones of all isotopes in the laboratory system are given as well.

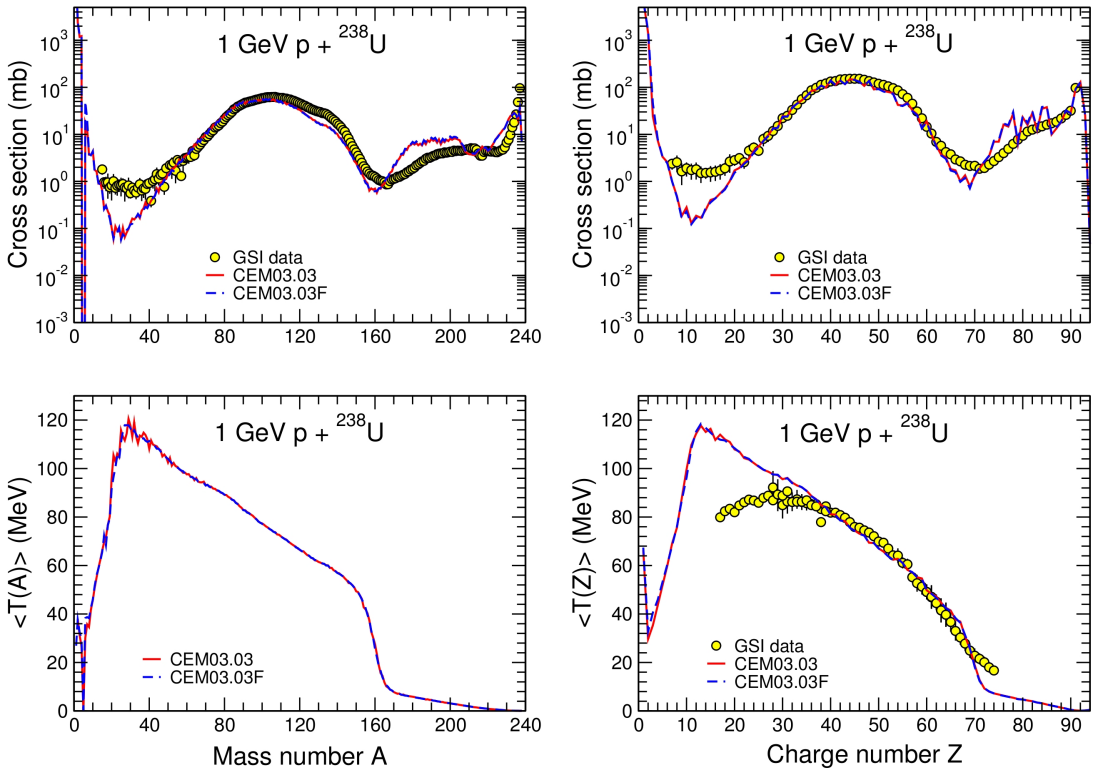

FIGURE 7.27: Comparison of measured [187] mass and charge distributions of the product yields from the reaction 1000 MeV p + ^{nat}U, and of the mean kinetic energy of these products (color circles), with results by the unmodified CEM03.03 (red solid lines) and new CEM03.03F (blue dashed lines).

such values by CEM03.03, therefore, to improve the description of fission cross section, and of the yield of fission fragments, a refitting of the a_f/a_n parameter in CEM03.03F would be desirable. All details on the RAL and GEM2 codes and all formulas used by them to calculate σ_f can be found in Refs. [190, 191]. Let us mention here only that in the case of subactinide nuclei, the main parameter that determines the fission cross sections calculated by GEM2 is the level-density parameter in the fission channel, a_f (or more exactly, the ratio a_f/a_n, where a_n is the level-density parameter for neutron evaporation). Such a work on improving the fission model of CEM03.03F is outside the aim of the present thesis, but we plan to perform such a work at a later time, as a separate project on improving further CEM03.03F.

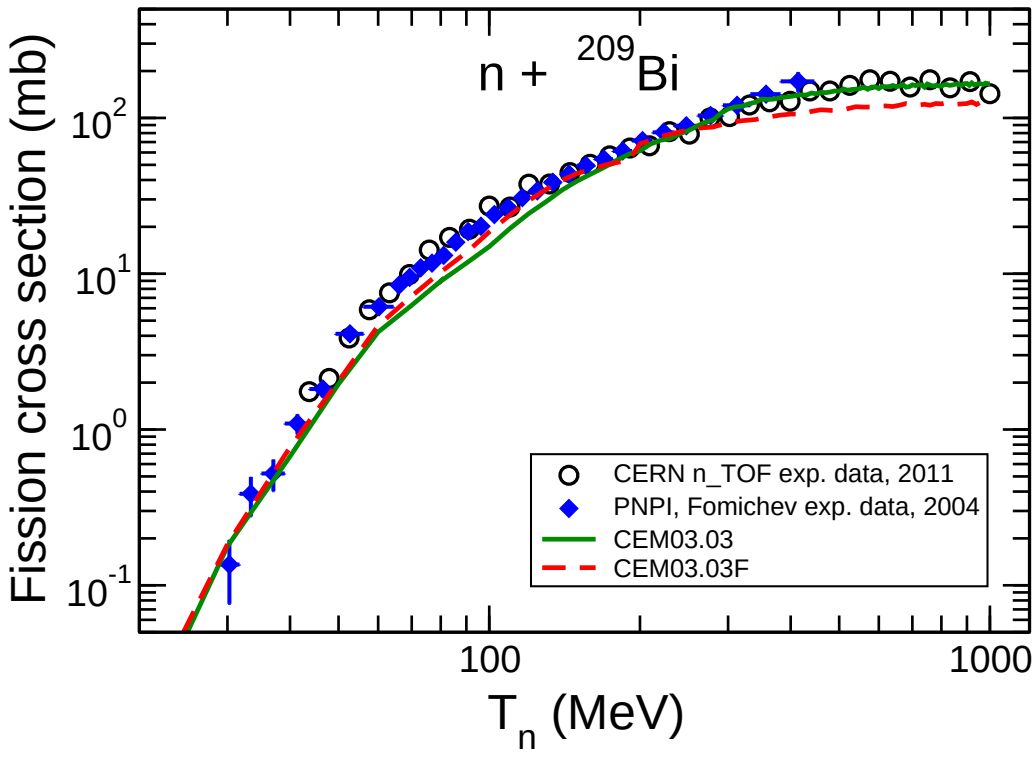

FIGURE 7.28: Comparison of measured [188, 189] fission cross sections for n + Bi (symbols), with results by the unmodified CEM03.03 (red solid lines) and new CEM03.03F (blue dashed lines).

7.5 COMPUTATION TIME CONSIDERATIONS

As CEM03.03 is the default event generator within MCNP6, we care about its ability to run simulations quickly. We tested the impact of our upgrades on computation time with each incremental upgrade, and found either no significant increase or a small increase in computation time. We wish to test the cumulative effect of all of our upgrades on computation time, and address these concerns in this section.

TABLE 7.1: Computation Times for CEM03.03 and CEM03.03F

Reaction	# Events	CEM03.03	CEM03.03F	% Increase
61 MeV p + ^{nat}Fe	10 Million	27.92 min	48.15 min	+72.5%
190 MeV p + ^{nat}Ag	10 Million	41.93 min	75.82 min	+80.8%
200 MeV p + ^{27}Al	10 Million	21.01 min	28.62 min	+36.2%
480 MeV p + ^{nat}Ag	10 Million	85.75 min	123.6 min	+44.1%
1200 MeV p + ^{197}Au	10 Million	349.1 min	458.9 min	+31.5%
2500 MeV p + ^{nat}Ni	10 Million	176.2 min	216.4 min	+22.8%
	Total:	701.9 min	951.5 min	+35.6%

Adding all of our upgrades increases the computation time by approximately one-third, depending upon the incident energy and target nucleus. Considering the comprehensive nature of our upgrades, and the dramatic improvements made to the production of heavy clusters, this is a small increase.

If the production of energetic heavy clusters is not needed, the variable `npreqtyp` in the input file can be set to 6 (only up to ^{4}He) instead of 66 (up to ^{28}Mg). A similar flag could be created to use or not use the expanded Coalescence model. Such features would eliminate most of the computational increase of CEM03.03F. The upgraded NASA-Kalbach inverse cross section model and the new γ_j model would remain implemented, but these require little extra computational effort.

7.6 CONCLUSIONS

Our goal of producing energetic light fragments with a new version of CEM03.03, called "CEM03.03F," has been successfully accomplished with our expansions to the Modified Exciton Model (MEM) and the Coalescence Model. We further improved our results by upgrading our inverse cross section model in the preequilibrium stage

to the NASA-Kalbach hybrid model. We also created a model for γ_j which affords us greater flexibility and predictability, as well as being physically "smoother."

We have tested CEM03.03F on many proton-, neutron-, gamma-, and pion-induced reactions and have found, in general, better or "no worse" results compared to the standard CEM03.03. In the case of heavy cluster production the results of CEM03.03F generally far outperform CEM03.03. The increase in computation time for CEM03.03F is reasonable (about one-third longer).

Our recommendations for future work include upgrading the evaporation model used in CEM, including implementing the NASA-Kalbach inverse cross section into the evaporation stage. We also recommend expanding the Coalescence model further to include fragments with $A \geq 8$.

CHAPTER 8

Implementation within MCNP6

Below is a relevant publication that results from the author's work pertaining to this chapter.

- L. M. Kerby, S. G. Mashnik, and J. S. Bull, GENXS Expansion to Include Fragment Spectra of Heavy Ions, LANL Report, LA-UR-15-24006 (May 2015).

MCNP6 (Monte Carlo N-Particle transport code, version 6) [4] is a general-purpose, continuous-energy, generalized-geometry, time-dependent, Monte Carlo radiation-transport code designed to track many particle types over broad ranges of energies. Application areas include, but are not limited to:

- Radiation protection and dosimetry;
- Radiation shielding;
- Radiography;
- Nuclear criticality safety;
- Detector design and analysis;
- Nuclear oil well logging;
- Fission and fusion reactor design;
- Decontamination and decommissioning;
- Design of accelerator spallation targets, particularly for neutron scattering facilities;
- Investigations for accelerator isotope production and destruction programs, including the transmutation of nuclear waste;
- Research into accelerator-driven energy sources;

- Activation of accelerator components and surrounding groundwater and air;
- High-energy dosimetry and neutron detection;
- Medical physics, especially proton and neutron therapy;
- Investigations of cosmic-ray radiation backgrounds and shielding for high altitude aircraft and spacecraft;
- Single-event upset in semiconductors from cosmic rays in spacecraft or from the neutron component on the earth's surface;
- Analysis of cosmo-chemistry experiments, such as Mars Odyssey;
- Charged-particle propulsion concepts for spaceflight;
- Investigation of fully coupled neutron and charged-particle transport for lower-energy applications;
- Transmutation, activation, and burnup in reactor and other systems;
- Nuclear safeguards;
- Nuclear material detection;
- Design of neutrino experiments.

The culmination of our work is the implementation of our heavy-ion upgrades in CEM into the MCNP6 transport code.

8.1 EXPANDED GENXS OPTION

The GENXS option allows for various cross sections to be tallied in MCNP6 (see Ref. [192] for details). Previously, double differential cross sections (cross section per emitted fragment energy and angle) were only available for fragments up to ^{4}He. Thus, a necessary first step in implementing our improvements from CEM into MCNP6 included expanding the ability of MCNP6 to output production cross sections of heavy clusters. This GENXS upgrade accomplishes this and includes the ability

to tally and output double differential cross sections for any heavy ion (with valid ZAID). It also includes the ability to tally and output angle-integrated cross sections per emitted fragment energy and energy-integrated cross sections per emitted angle, for any ZAID.

8.1.1 *MCNP6 and GENXS Example Input Files*

A sample MCNP6 input using GENXS is displayed below:

```
MCNP6 test: Spectra from 200 MeV p + Al27 by CEM03.03
1 1 1.0 -1 2 -3
2 0 -4(1:-2:3)
3 0 4

c ————————————————————————
1 cz 4.0
2 pz -1.0
3 pz 1.0
4 so 50.0

c ————————————————————————
m1 13027 1.0
sdef erg=200 par=H dir=1 pos=0 0 0 vec 0 0 1
imp:h 1 1 0
phys:h 300
mode h n a #
LCA 8j 1 $ use CEM03.03
tropt genxs inxcp200al nreact on nescat off
c ————————————————————————
print 40 110 95
nps 10000000
prdmp 2j -1
```

This example simulates the nuclear spallation reaction of 200 MeV protons striking ^{27}Al. Note that in order to tally double differential cross sections of heavy ions, heavy ions (#) must be added to the MODE card. As explained in [192], the GENXS card requires a second input file. The line

tropt genxs inxcp200al nreact on nescat off

specifies the use of GENXS and the name of the second, auxiliary MCNP6 input file required by GENXS (called inxcp200al in this example). The file inxcp200al appears below:

```
MCNP6 test: p, d, t, LF spectra from 200 MeV p + Al27 by CEM03.03
1 1 1 /
Cross Section Edit
72 -11 15 /
5. 10. 15. 20. 25. 30. 35. 40. 45. 50. 55. 60. 65. 70. 75. 80.
85. 90. 95. 100. 120. /
155. 145. 115. 105. 95. 85. 55. 45. 25. 15. 0. /
1 5 21 22 23 24 2006 3006 3007 3008 3009 4007 4009 4010 5010 /
```

See Ref. [192] for a full explanation of the GENXS input file. Note that the last line,

1 5 21 22 23 24 2006 3006 3007 3008 3009 4007 4009 4010 5010 /

contains the particle types to be tallied and output. Numbers $1-24$ refer to the MCNP6 particle types, as used in the previous GENXS version. With this expansion, heavy ions may now be tallied, according to their ZAID $(Z*1000+A)$. Therefore, numbers >1000 refer to the ZAID of a particular heavy ion. As an example, this GENXS input instructs MCNP6 to tally

1 5 21 22 23 24 2006 3006 3007 3008 3009 4007 4009 4010 5010

n p d t ^{3}He ^{4}He ^{6}He ^{6}Li ^{7}Li ^{8}Li ^{9}Li ^{7}Be ^{9}Be ^{10}Be ^{10}B.

Fig. 8.1 displays an excerpt of the double differential cross section portion of the MCNP6 output file for ^{6}Li (ZAID=3006). Note that instead of showing "mu max" for the emission direction, GENXS now outputs the angles in "degrees+/-spread". We

File: Unsaved Document 1 Page 1 of 1

3006 production cross section

E(MeV)	167.5deg+/-12.5	150.0deg+/- 5.0	130.0deg+/-15.0	110.0deg+/- 5.0	100.0deg+/- 5.0	90.0deg+/- 5.0	70.0deg+/-15.0
5.000000E+00	0.000E+00 0.000	0.000E+00 0.000	0.000E+00 0.000	0.000E+00 0.000	0.000E+00 0.000	0.000E+00 0.000	0.000E+00 0.000
1.000000E+01	8.301E-06 0.040	9.325E-06 0.039	1.165E-05 0.016	1.442E-05 0.023	1.529E-05 0.022	1.614E-05 0.021	1.803E-05 0.012
1.500000E+01	2.598E-06 0.072	2.822E-06 0.071	3.920E-06 0.028	6.006E-06 0.036	7.040E-06 0.032	8.988E-06 0.028	1.277E-05 0.014
2.000000E+01	6.929E-07 0.139	6.303E-07 0.151	1.011E-06 0.056	1.791E-06 0.065	2.538E-06 0.054	3.180E-06 0.047	5.867E-06 0.021
2.500000E+01	1.999E-07 0.258	1.146E-07 0.354	2.865E-07 0.105	5.259E-07 0.120	6.763E-07 0.104	1.110E-06 0.080	2.287E-06 0.034
3.000000E+01	9.327E-08 0.378	2.865E-08 0.707	1.039E-07 0.174	1.601E-07 0.218	3.200E-07 0.151	3.724E-07 0.139	7.161E-07 0.060
3.500000E+01	0.000E+00 0.000	1.432E-08 1.000	3.463E-08 0.302	3.049E-08 0.500	6.545E-08 0.333	1.003E-07 0.267	2.490E-07 0.102
4.000000E+01	1.332E-08 1.000	0.000E+00 0.000	9.445E-09 0.577	7.622E-09 1.000	1.454E-08 0.707	2.865E-08 0.500	6.673E-08 0.196
4.500000E+01	0.000E+00 0.000	0.000E+00 0.000	0.000E+00 0.000	0.000E+00 0.000	0.000E+00 0.000	7.162E-09 1.000	2.823E-08 0.302
5.000000E+01	0.000E+00 0.000	0.000E+00 0.000	6.297E-09 0.707	0.000E+00 0.000	0.000E+00 0.000	7.162E-09 1.000	1.283E-08 0.447
5.500000E+01	0.000E+00 0.000	0.000E+00 0.000	0.000E+00 0.000	0.000E+00 0.000	0.000E+00 0.000	0.000E+00 0.000	2.567E-09 1.000
6.000000E+01	0.000E+00 0.000	0.000E+00 0.000	0.000E+00 0.000	0.000E+00 0.000	0.000E+00 0.000	0.000E+00 0.000	2.567E-09 1.000
6.500000E+01	0.000E+00 0.000	0.000E+00 0.000	0.000E+00 0.000	0.000E+00 0.000	0.000E+00 0.000	0.000E+00 0.000	2.567E-09 1.000

E(MeV)	50.0deg+/- 5.0	35.0deg+/-10.0	20.0deg+/- 5.0	7.5deg+/- 7.5
5.000000E+00	0.000E+00 0.000	0.000E+00 0.000	0.000E+00 0.000	0.000E+00 0.000
1.000000E+01	1.901E-05 0.022	1.826E-05 0.019	1.853E-05 0.034	1.825E-05 0.045
1.500000E+01	1.709E-05 0.023	1.932E-05 0.018	2.134E-05 0.031	2.213E-05 0.041
2.000000E+01	8.508E-06 0.033	1.070E-05 0.024	1.315E-05 0.040	1.392E-05 0.051
2.500000E+01	3.852E-06 0.049	4.644E-06 0.037	6.638E-06 0.056	6.778E-06 0.074
3.000000E+01	1.683E-06 0.075	2.125E-06 0.054	2.680E-06 0.088	2.528E-06 0.120
3.500000E+01	4.862E-07 0.139	8.711E-07 0.085	1.026E-06 0.143	1.429E-06 0.160
4.000000E+01	2.618E-07 0.189	2.632E-07 0.154	5.863E-07 0.189	5.862E-07 0.250
4.500000E+01	6.544E-08 0.378	1.128E-07 0.236	6.282E-08 0.577	2.198E-07 0.408
5.000000E+01	2.805E-08 0.577	3.134E-08 0.447	6.282E-08 0.577	1.099E-07 0.577
5.500000E+01	0.000E+00 0.000	2.507E-08 0.500	0.000E+00 0.000	0.000E+00 0.000
6.000000E+01	0.000E+00 0.000	0.000E+00 0.000	0.000E+00 0.000	0.000E+00 0.000
6.500000E+01	0.000E+00 0.000	6.267E-09 1.000	0.000E+00 0.000	3.664E-08 1.000

E(MeV)	angle integrated	mu max	deg min	energy integrated
5.000000E+00	0.000E+00 0.000	-0.906307787037	155.0000000	5.949E-05 0.033
1.000000E+01	1.928E-04 0.006	-0.819152044289	145.0000000	6.467E-05 0.033
1.500000E+01	1.267E-04 0.008	-0.422618261741	115.0000000	8.510E-05 0.014
2.000000E+01	5.770E-05 0.012	-0.258819045103	105.0000000	1.147E-04 0.018
2.500000E+01	2.335E-05 0.018	-0.087155742748	95.0000000	1.297E-04 0.017
3.000000E+01	9.052E-06 0.029	0.087155742748	85.0000000	1.496E-04 0.015
3.500000E+01	3.255E-06 0.049	0.573576436351	55.0000000	2.002E-04 0.008
4.000000E+01	1.184E-06 0.081	0.707106781187	45.0000000	2.549E-04 0.014
4.500000E+01	3.608E-07 0.147	0.906307787037	25.0000000	2.818E-04 0.011
5.000000E+01	1.726E-07 0.213	0.965925826289	15.0000000	3.204E-04 0.018
5.500000E+01	3.922E-08 0.447	1.000000000000	0.0000000	3.299E-04 0.024
6.000000E+01	7.844E-09 1.000			
6.500000E+01	2.353E-08 0.577			

total 3006 production cross section = 2.073E-03 0.0045 yield = 5.28630E-03

FIGURE 8.1: Double differential cross section output from MCNP6 using GENXS for the reaction 200 MeV p + ^{27}Al, with angle- and/or energy-integrated cross sections also calculated.

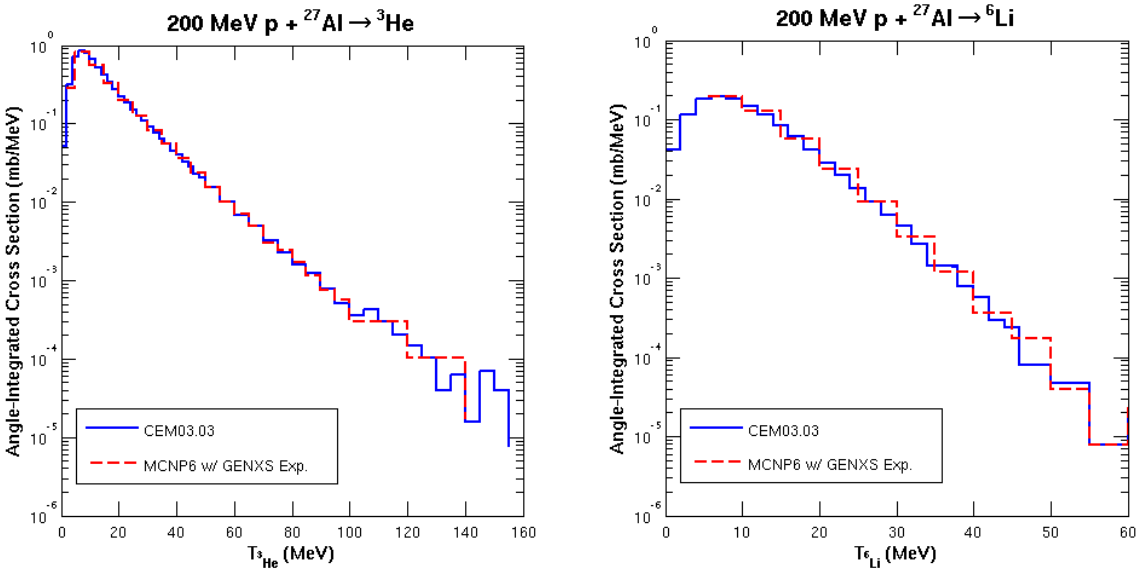

FIGURE 8.2: Comparison of emitted ^{3}He and ^{6}Li angle-integrated fragment spectra for the reaction 200 MeV p + ^{27}Al, calculated by MCNP6 (red dashed lines) and CEM03.03 (blue solid lines).

believe this will be easier and more intuitive for users, and help avoid user error and misinterpretation. Angle-integrated spectra and energy-integrated spectra are also calculated, as well as the total angle- and energy-integrated production cross section.

Figs 8.2 and 8.3 show plots of the example spectra from MCNP6 compared to results by CEM03.03, for the reaction 200 MeV p + ^{27}Al. The results between MCNP6 and CEM03.03 are consistent. In addition, other "test" reactions studied revealed the expected consistency between MCNP6 and CEM03.03.

The MCTAL tallies have also been updated so that angle-integrated cross section spectra of specified heavy ions may be viewed from within `mcplot`, similar to how specified nucleons and light fragments were viewed in the previous version of GENXS (see Fig. 8.4).

Lastly, up to 50 heavy ions can be tallied. This limit is according to the parameter, `heavymax`, in `xs_mod.F90`, and can be easily altered in subsequent versions.

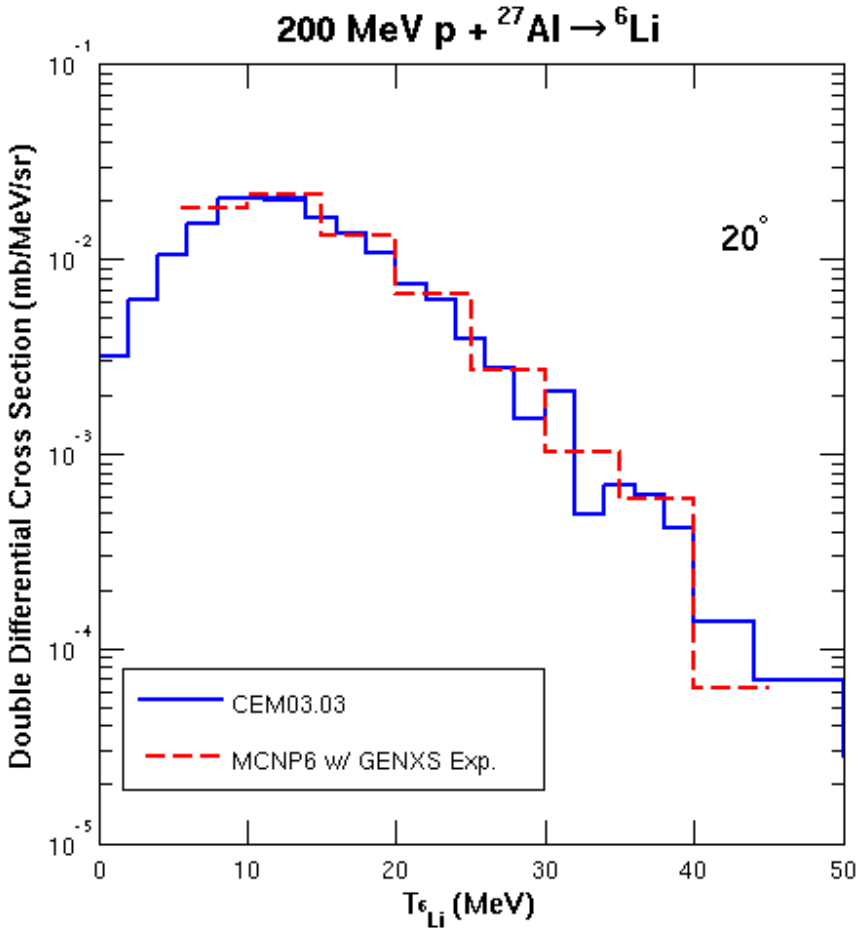

FIGURE 8.3: Comparison of emitted ^{6}Li double differential spectra for the reaction 200 MeV p + ^{27}Al, at an emission angle of 20°, calculated by MCNP6 (red dashed lines) and CEM03.03 (blue solid lines).

8.1.2 *Further Tests*

We additionally tested this GENXS heavy-ion expansion with several different event generators (CEM03.03, Bertini+Dresner+RAL, INCL+ABLA, and LAQGSM03.03). Results of this test appear in Fig. 8.5. Results are as we expect.

Furthermore, we tested MCNP6 with the GENXS heavy-ion expansion on a nucleus-induced reaction using the LAQGSM03.03 event generator. Results of this simulation compared with experimental data are seen in Fig. 8.6. Similar results were found in Example 6.5 of the MPI Testing Primer [63].

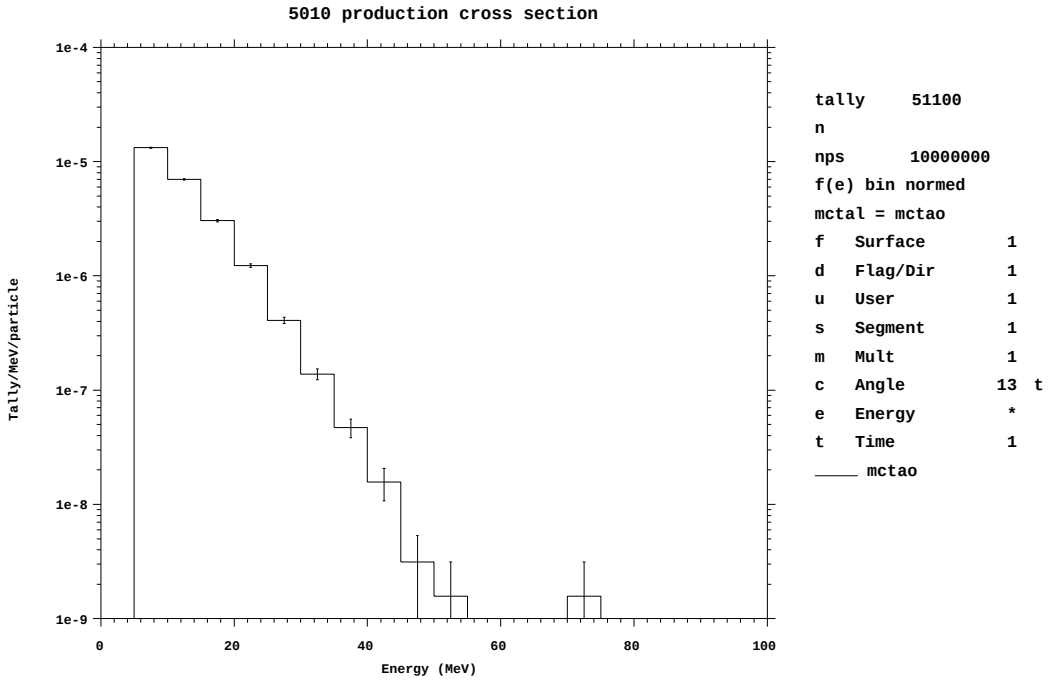

FIGURE 8.4: Example of MCTAL production cross section plot for ^{10}B for the reaction 200 MeV p + ^{27}Al.

We also tested our GENXS expansion running MPI, as well as with the 1400+ test suite. We conclude that this expansion works as expected across several different event generators and for both nucleon- and nucleus-induced reactions.

8.2 MCNP6 IMPLEMENTATION

The CEM03.03F heavy-ion upgrades discussed in this work were implemented into a working version of MCNP6, which we call "MCNP6-F". Two of our upgrades are always implemented in our MCNP6-F model: the upgraded, NASA-Kalbach, inverse cross sections in the preequilibruim stage, and the new energy-dependent γ_j Model. The other two upgrades (expansion of preequilibrium emission to ^{28}Mg, and the expansion of the Coalescence Model to ^{7}Be), both of which increase computation

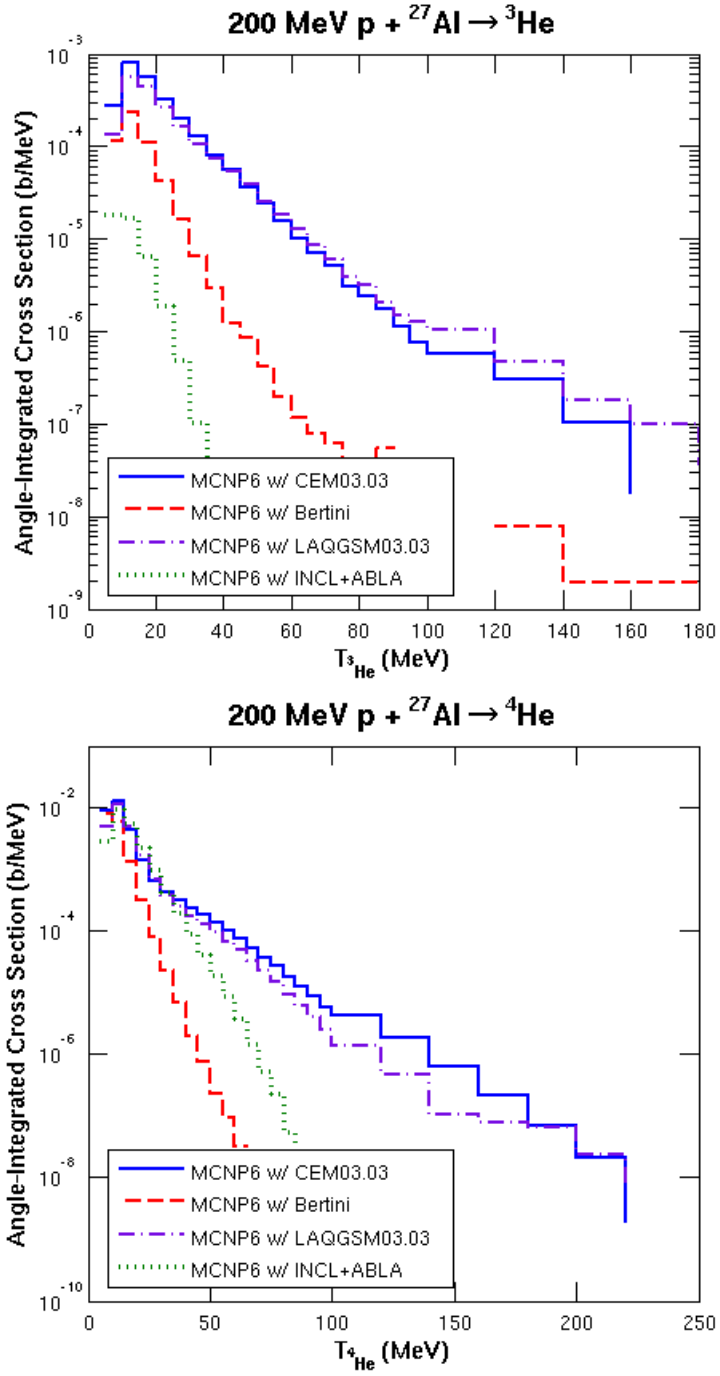

FIGURE 8.5: Comparison of emitted ^{3}He and ^{4}He angle-integrated fragment spectra for the reaction 200 MeV p + ^{27}Al, calculated by MCNP6 with CEM03.03 (blue solid lines), with Bertini (red dashed lines), with LAQGSM03.03 (purple dash-dotted lines), and with INCL-ABLA (green dotted lines), all run with the GENXS expansion for heavy ions discussed in this paper.

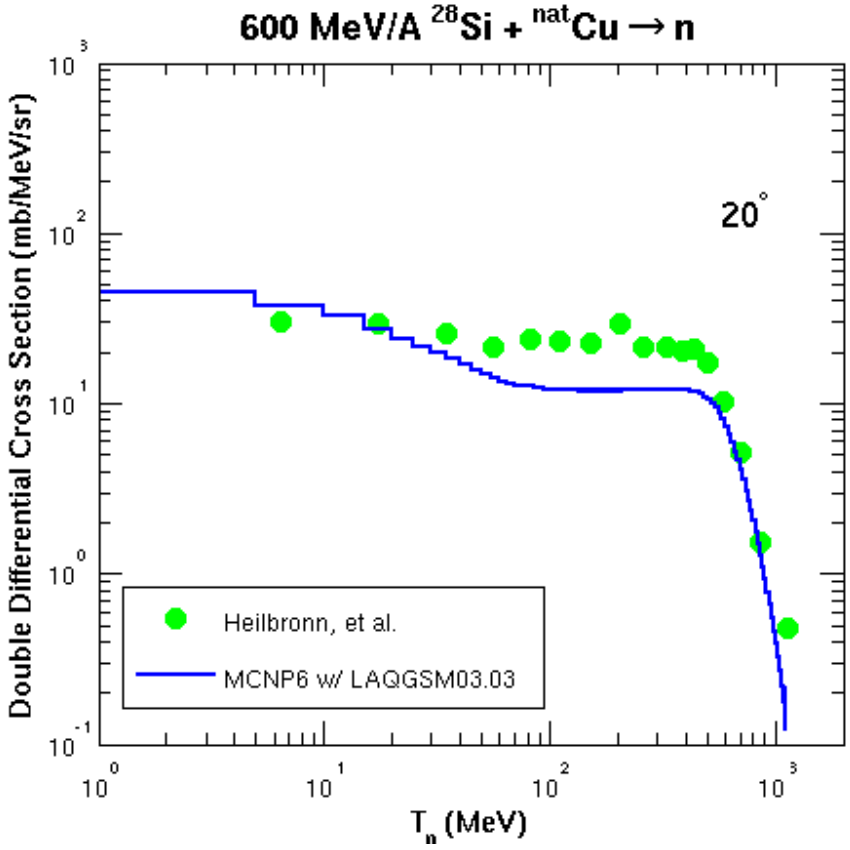

FIGURE 8.6: Comparison of emitted neutron double differential spectra for the reaction 600 MeV/A ^{28}Si + ^{nat}Cu, at an emission angle of 20°, calculated by MCNP6 with LAQGSM03.03 with this GENXS heavy-ion expansion (blue solid line), compared to results by Heilbronn, et al (green points).

time, may be turned "off" if desired. A variable, called npreqtyp, was created to specify the number of preequilibrium particles considered for emission. It is now the twelfth option on the LCA Card. It's maximum (and default) value is 66, similar to the nevtype variable used for the evaporation stage. See Table 4.1 for a list of the 66 particles considered in the preequilibrium stage. In the old model, 6 preequilibrium particles were considered, and therefore a value of npreqtyp=6 "turns off" the preequilibrium expansion (and the coalescence expansion). The expanded Coalescence Model is implemented for values of npreqtyp>6. MCNP6-F also includes the GENXS expansion.

Basic testing and verification of MCNP6-F has been completed and results are presented in the following section. In addition, MPI testing has been completed. Upon

further testing, we anticipate these upgrades being included in the next release of MCNP6.

8.2.1 *Results*

Double differential cross section spectra for several reactions are plotted in this section. Figs. 8.7–8.15 compare experimental data with results by CEM03.03F (blue solid lines), MCNP6-F with npreqtyp=66 (red dashed lines), and MCNP6 with the GENXS expansion only (purple dash-dotted lines). MCNP6 with the GENXS expansion only does not contain any of the four heavy-ion upgrades discussed in this work (but contains the GENXS expansion so that we can output double differential cross sections for light fragments). We see that our new MCNP6-F with the heavy-ion upgrades, in general, has improved results over the unmodified MCNP6, with GENXS expansion only, especially for heavy cluster spectra.

Fig. 8.7 shows our results for 200 MeV p + ^{27}Al $\rightarrow$ ^{4,6}He at 60°with experimental data by Machner, *et al.* [11]. The figure for ^{4}He spectra demonstrates that MCNP6-F not only achieves increased production of heavy clusters without "destroying" the established spectra of nucleons and light fragments up to ^{4}He (in this particular case ^{4}He), but in some cases it even achieves improved results for nucleons and light fragments up to ^{4}He. For the spectra of ^{6}He, we again see significant improvement with MCNP6-F. The ^{6}He spectra also highlight the need to improve our evaporation model, as we see the peak of the spectra is too low, and this peak is largely produced by evaporation. We hope to do this work in the future.

Figs. 8.8 and 8.9 display our results for 200 MeV p + ^{197}Au $\rightarrow$ ^{6}Li,^{7}Be at 45°with experimental data by Machner, *et al.* [11]. We expect our results from MCNP6-F with npreqtyp=6 to be similar to MCNP6 with the GENXS expansion only, as the only difference between the two is that MCNP6-F contains the improved inverse cross sections and the γ_j Model. These two figures show not only dramatically improved heavy cluster production at high energies, but also improved production at relatively low energies around the peak. We believe this is due to the heavy target (gold) and therefore an increased ability to produce these low-energy heavy clusters from both our expanded Coalescence model and expanded preequilibrium.

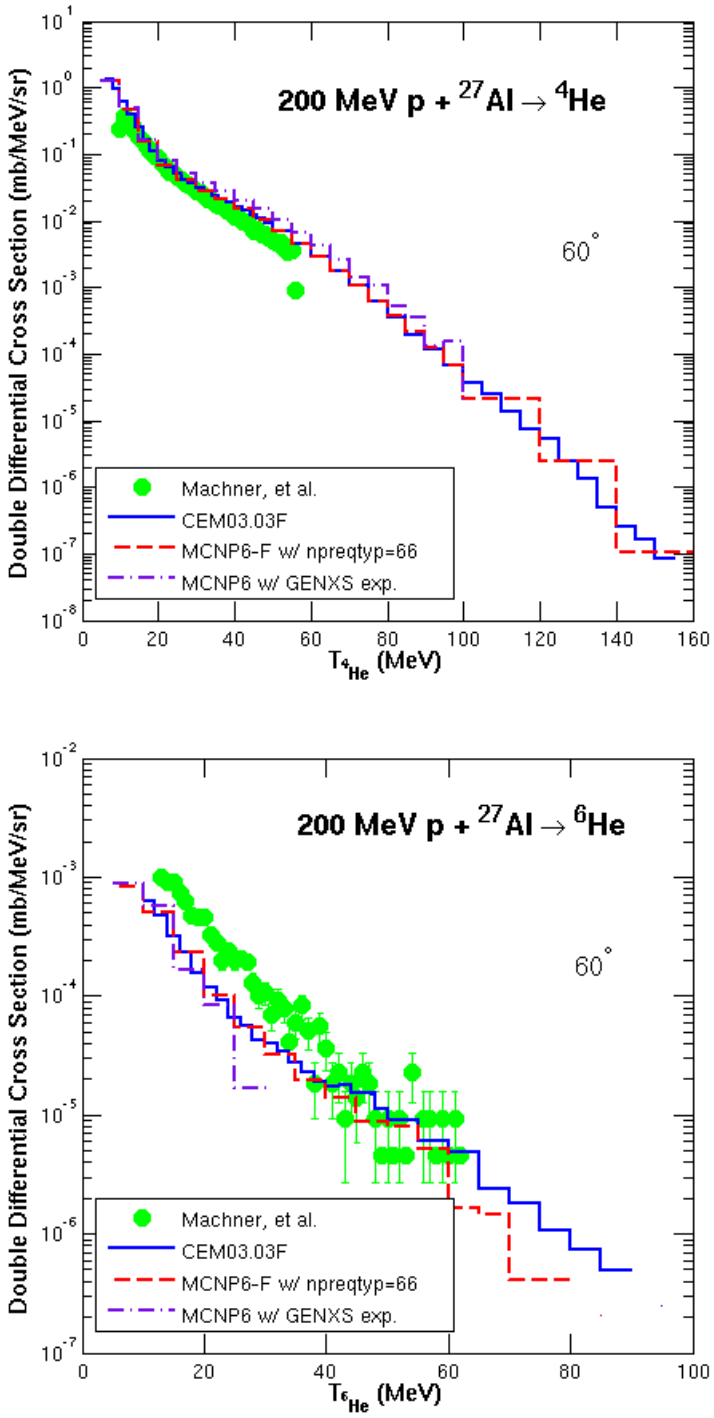

FIGURE 8.7: Comparison of experimental data by Machner, *et al.* [11] (green circles) with results by CEM03.03F (blue solid lines), MCNP6-F with npreqtyp=66 (red dashed lines), and MCNP6 with the GENXS expansion only (purple dash-dotted lines) for 200 MeV p + ^{27}Al → ^{4,6}He at 60°.

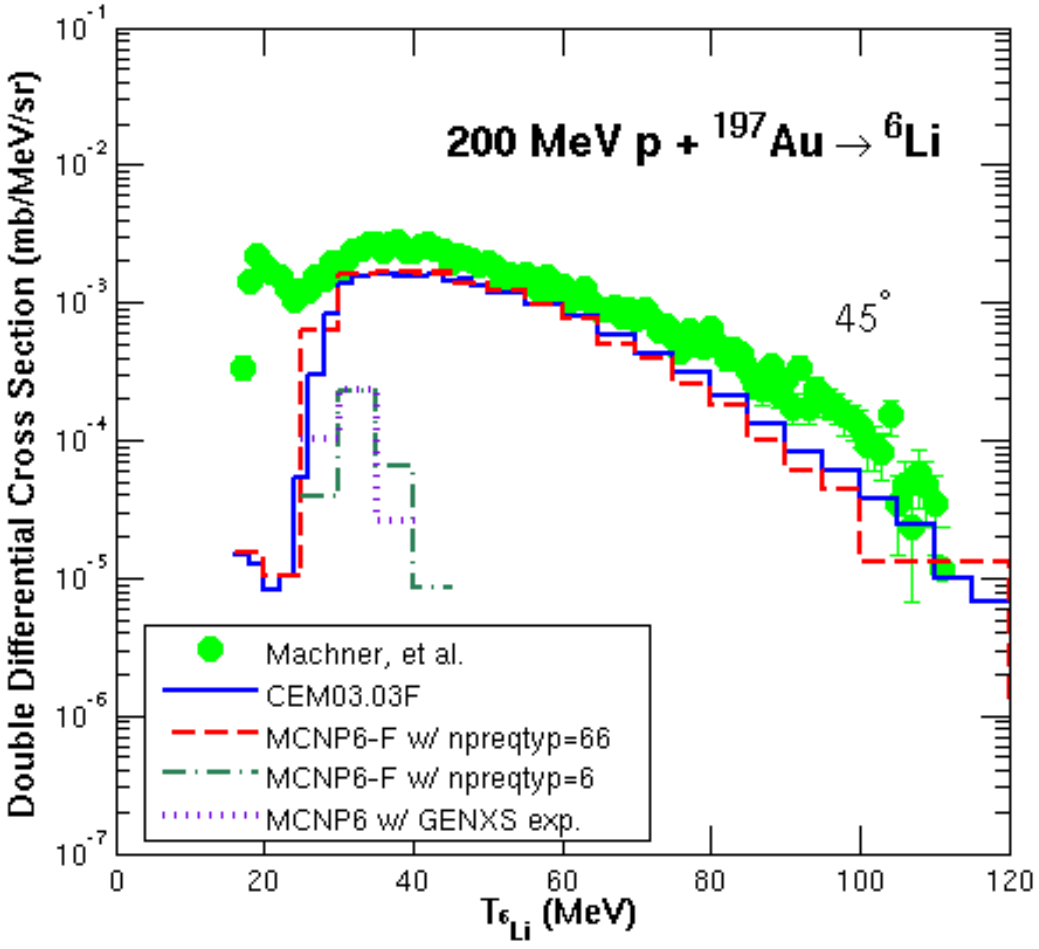

FIGURE 8.8: Comparison of experimental data by Machner, *et al.* [11] (green circles) with results by CEM03.03F (blue solid lines), MCNP6-F with npreqtyp=66 (red dashed lines), MCNP6-F with npreqtyp=6 (green dash-dotted lines), and MCNP6 with the GENXS expansion only (purple dotted lines) for 200 MeV p + ^{197}Au → ^{6}Li at 45°.

Fig. 8.10 shows our results for 480 MeV p + ^{nat}Ag → ^{6}Li at 60°with experimental data by Green, *et al.* [103]. We see that MCNP6-F produces significantly improved results and matches the data reasonably well.

Fig. 8.11 displays our results for 1200 MeV p + ^{197}Au → p,^{6}He at 20°with experimental data by Budzanowski, *et al.* [49]. The proton spectra again illustrate that CEM03.03F achieves increased production of heavy clusters without "destroying" the established spectra of nucleons and light fragments up to ^{4}He (in this particular case protons). The ^{6}He spectra additionally evidence that MCNP6-F demonstrates

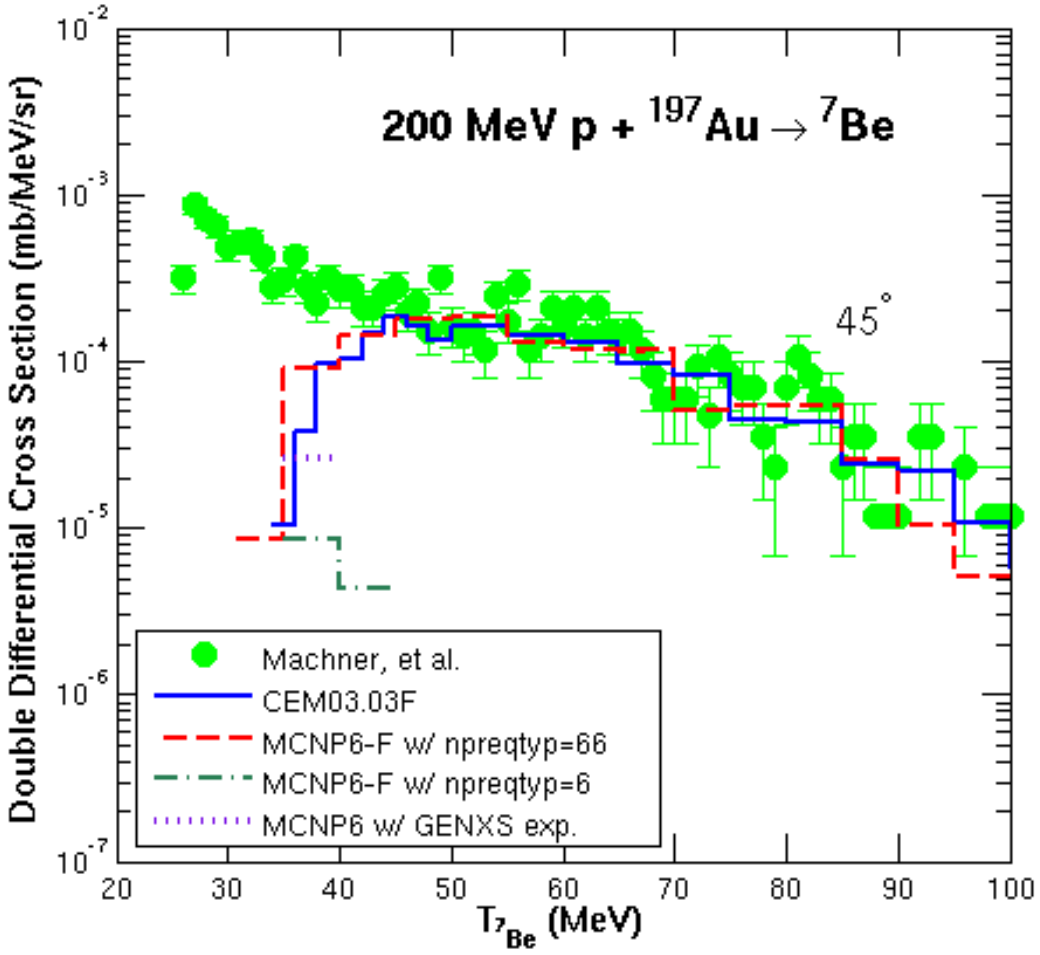

FIGURE 8.9: Comparison of experimental data by Machner, *et al.* [11] (green circles) with results by CEM03.03F (blue solid lines), MCNP6-F with npreqtyp=66 (red dashed lines), MCNP6-F with npreqtyp=6 (green dash-dotted lines), and MCNP6 with the GENXS expansion only (purple dotted lines) for 200 MeV p + ^{197}Au → ^{7}Be at 45°.

increased production of heavy clusters in the mid- and high-energy regions compared to the original MCNP6.

Figs. 8.12 and 8.13 illustrate our results for 1200 MeV p + ^{197}Au → ^{6}Li,^{7}Be at 20°with experimental data by Budzanowski, *et al.* [49]. These figures provides examples of our improved results for ^{6}Li and ^{7}Be spectra.

Figs. 8.14 and 8.15 demonstrate our results for 2500 MeV p + ^{nat}Ni → t, ^{7}Li at 100°, with experimental data by Budzanowski, *et al.* [50]. The triton spectra again illustrate that MCNP6-F achieves increased production of heavy clusters without "destroying"

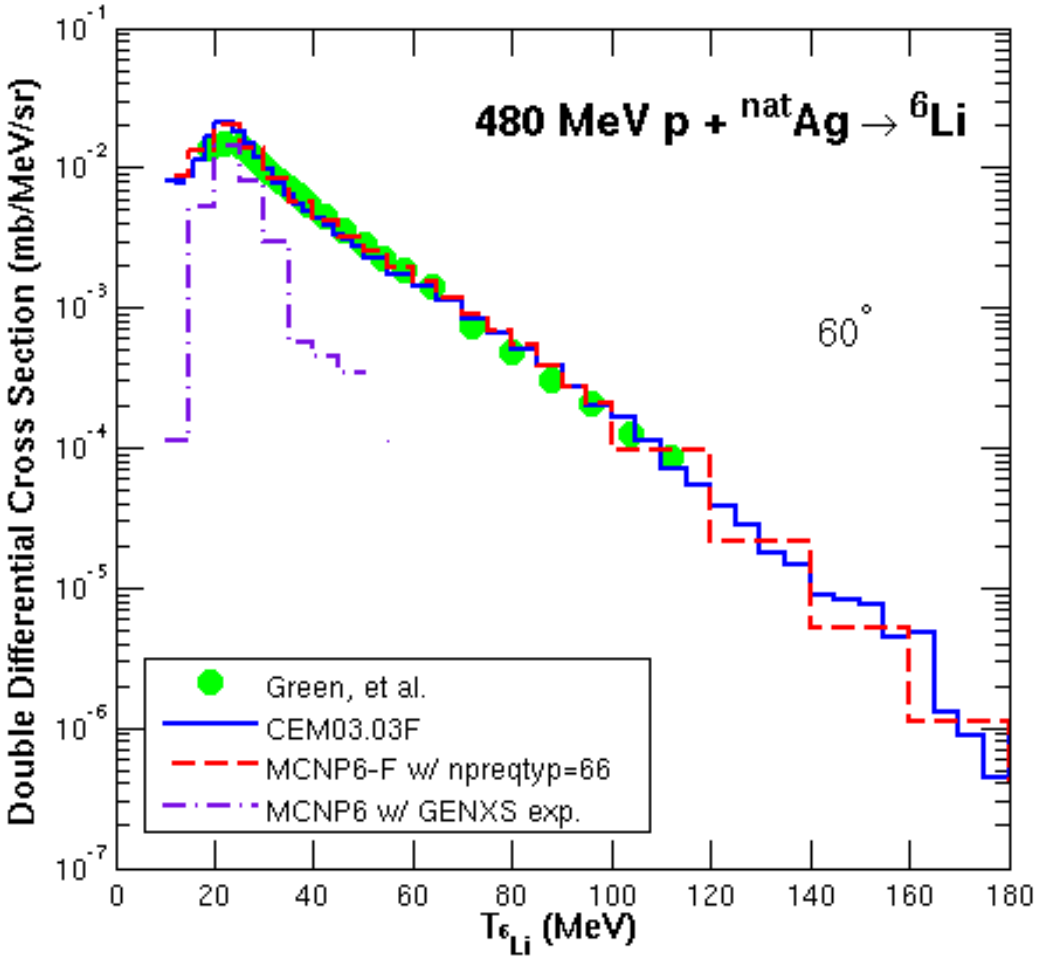

FIGURE 8.10: Comparison of experimental data by Green, *et al.* [103] (green circles) with results by CEM03.03F (blue solid lines), MCNP6-F with npreqtyp=66 (red dashed lines), and MCNP6 with the GENXS expansion only (purple dash-dotted lines) for 480 MeV p + ^{nat}Ag → ^{6}Li at 60°.

the established spectra of nucleons and light fragments up to ^{4}He (in this particular case tritons). The ^{7}Li spectra show improved results with MCNP6-F.

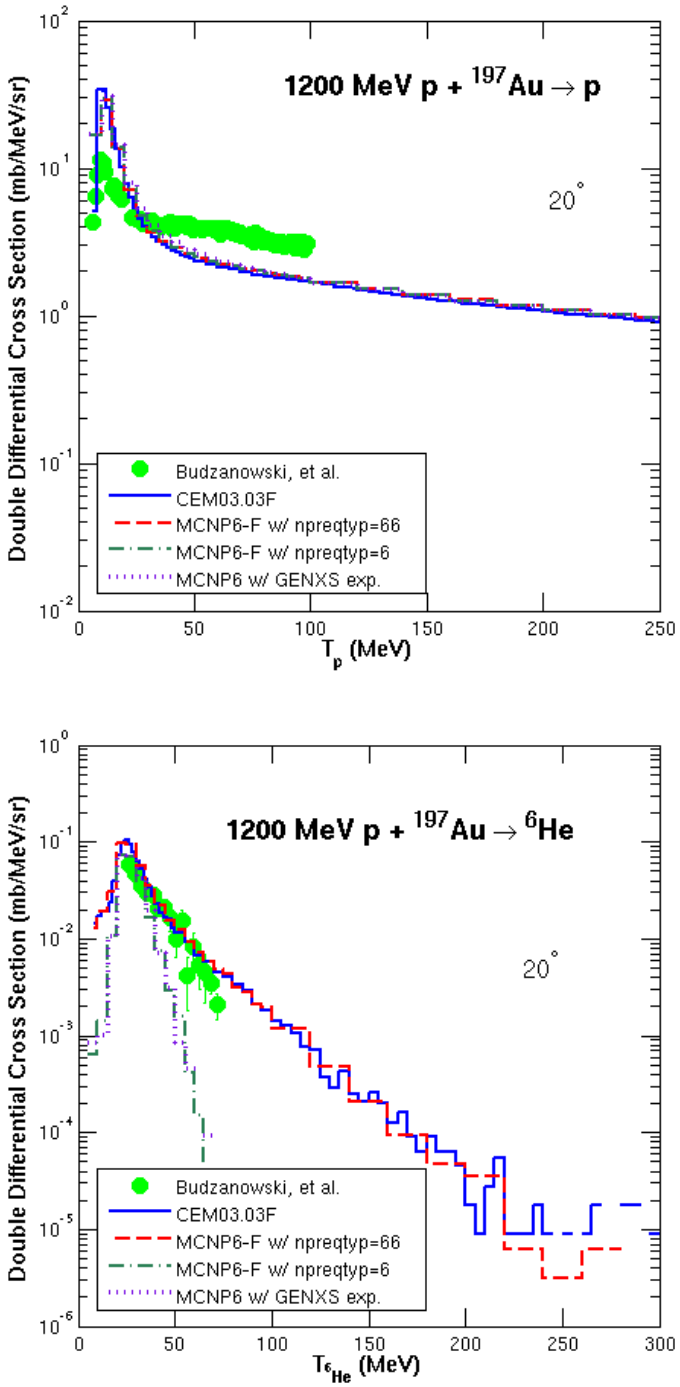

FIGURE 8.11: Comparison of experimental data by Budzanowski, *et al.* [49] (green circles) with results by CEM03.03F (blue solid lines), MCNP6-F with npreqtyp=66 (red dashed lines), MCNP6-F with npreqtyp=6 (green dash-dotted lines), and MCNP6 with the GENXS expansion only (purple dotted lines) for 1200 MeV p + ^{197}Au → p,^{6}He at 20°.

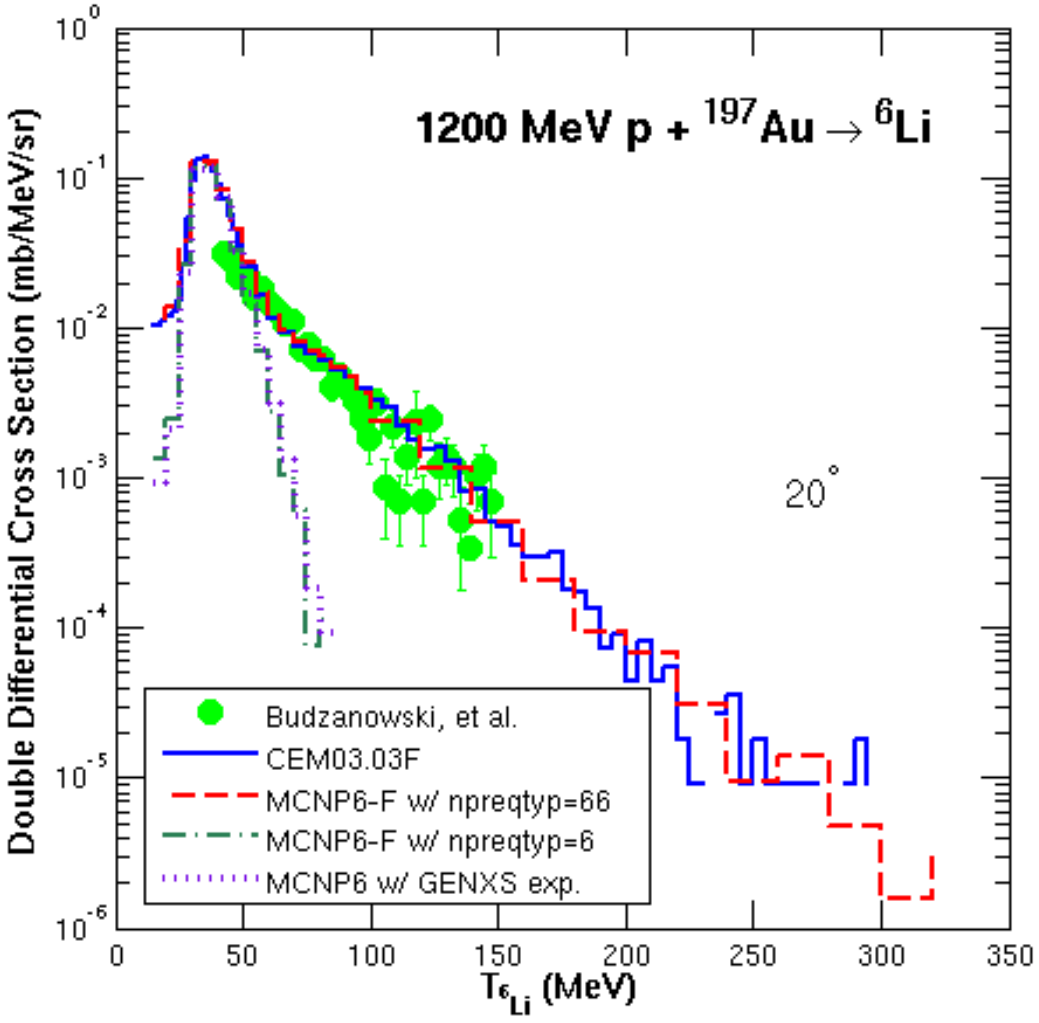

FIGURE 8.12: Comparison of experimental data by Budzanowski, *et al.* [49] (green circles) with results by CEM03.03F (blue solid lines), MCNP6-F with npreqtyp=66 (red dashed lines), MCNP6-F with npreqtyp=6 (green dash-dotted lines), and MCNP6 with the GENXS expansion only (purple dotted lines) for 1200 MeV p + ^{197}Au → ^{6}Li at 20°.

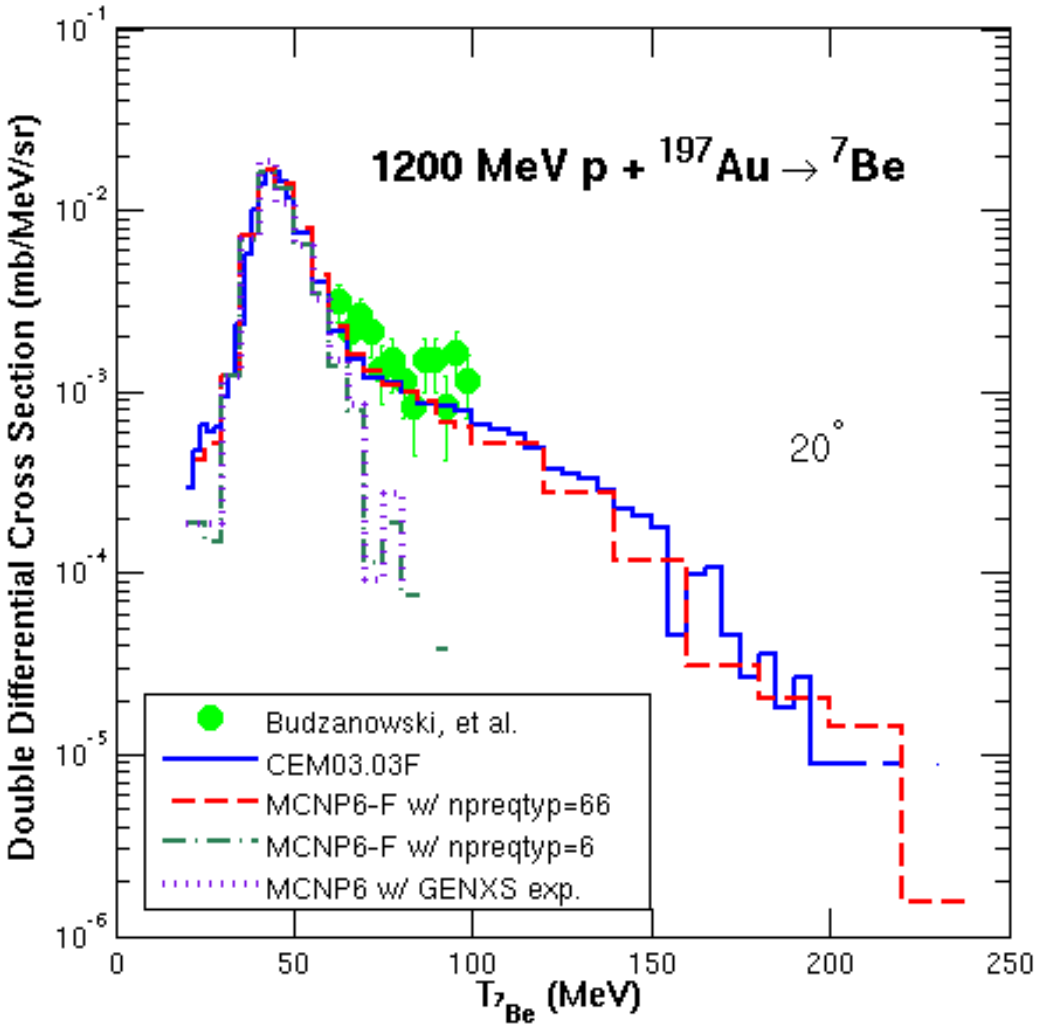

FIGURE 8.13: Comparison of experimental data by Budzanowski, *et al.* [49] (green circles) with results by CEM03.03F (blue solid lines), MCNP6-F with npreqtyp=66 (red dashed lines), MCNP6-F with npreqtyp=6 (green dash-dotted lines), and MCNP6 with the GENXS expansion only (purple dotted lines) for 1200 MeV p + ^{197}Au → ^{7}Be at 20°.

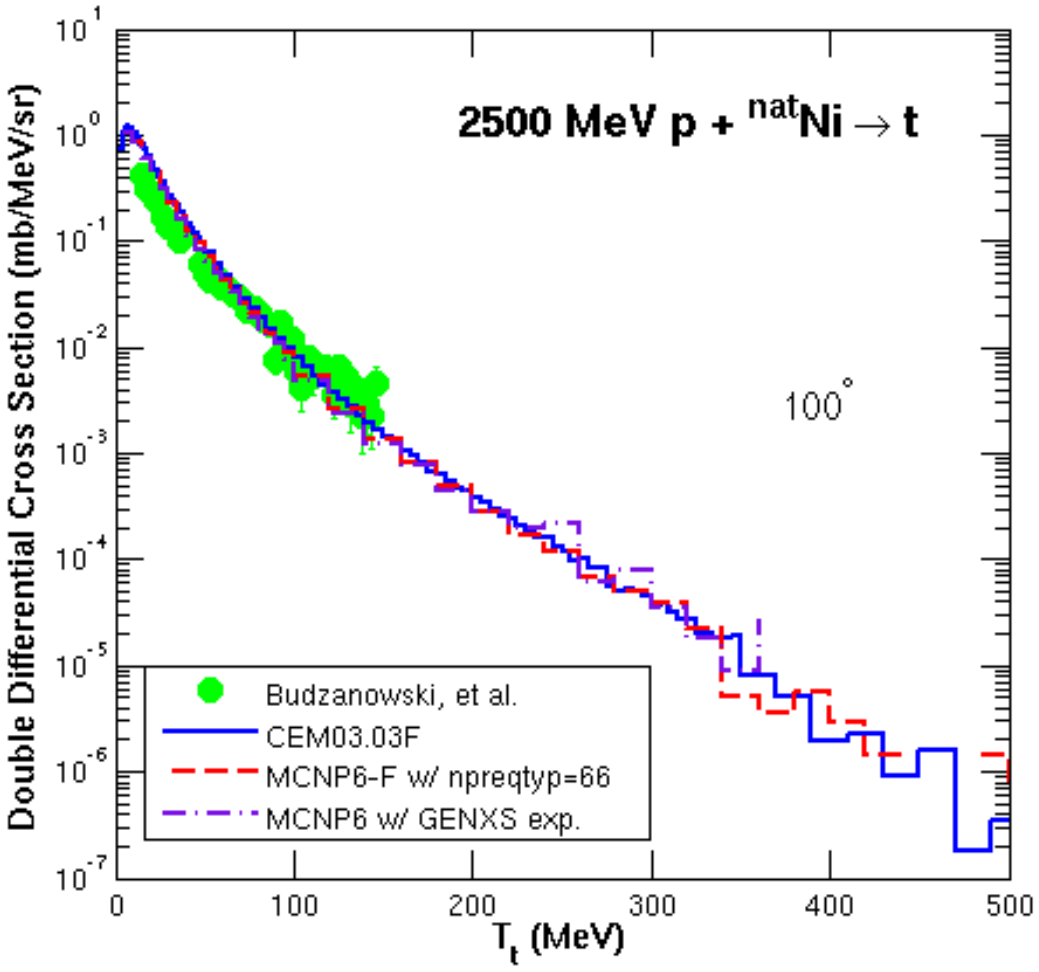

FIGURE 8.14: Comparison of experimental data by Budzanowski, *et al.* [50] (green circles) with results by CEM03.03F (blue solid lines), MCNP6-F with npreqtyp=66 (red dashed lines), and MCNP6 with the GENXS expansion only (purple dash-dotted lines) for 2500 MeV p + ^{nat}Ni → t at 100°.

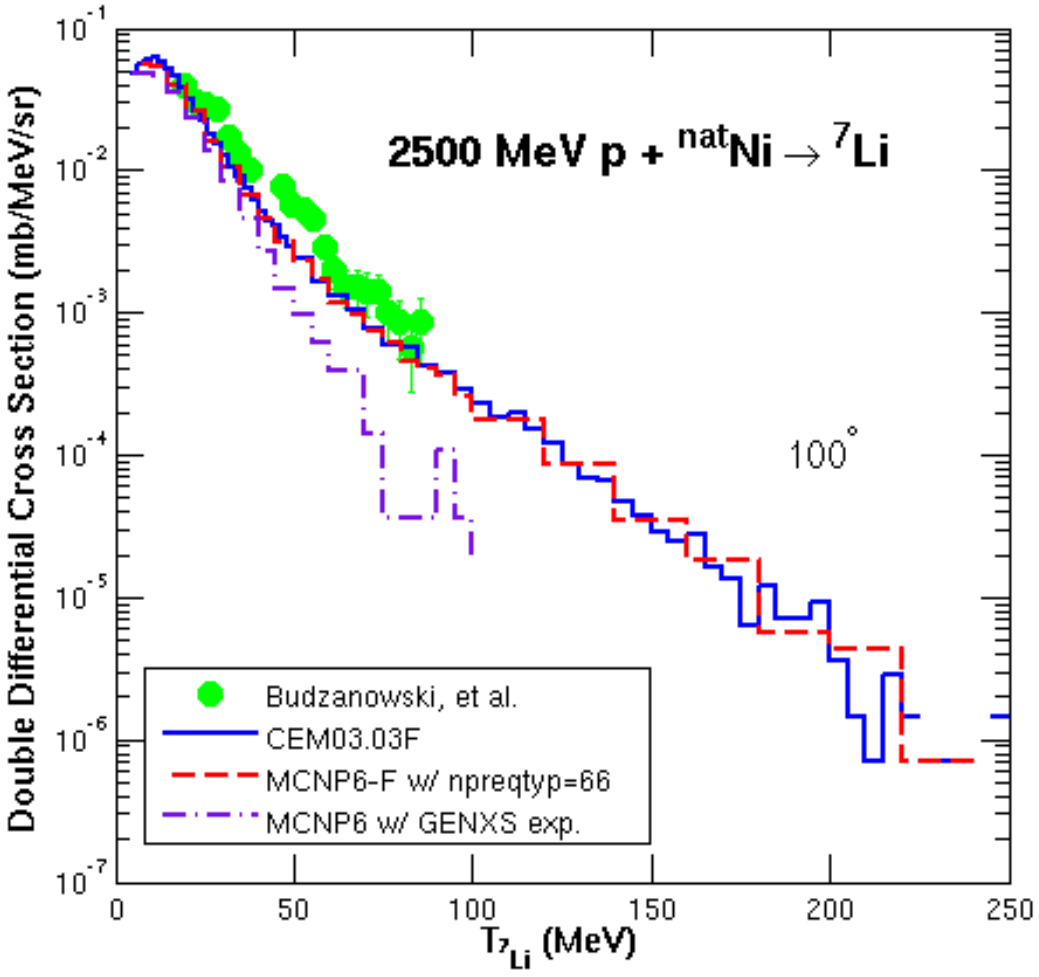

FIGURE 8.15: Comparison of experimental data by Budzanowski, *et al.* [50] (green circles) with results by CEM03.03F (blue solid lines), MCNP6-F with npreqtyp=66 (red dashed lines), and MCNP6 with the GENXS expansion only (purple dash-dotted lines) for 2500 MeV p + ^{nat}Ni → ^{7}Li at 100°.

8.3 CONCLUSION

We have accomplished our goal of improving predictions of MCNP6 for the production of energetic heavy clusters. We have successfully implemented the following heavy-ion upgrades from CEM03.03F into a working version of MCNP6:

- Expanded preequilibrium emission to ^{28}Mg;
- Upgraded preequilibrium inverse cross sections to NASA-Kalbach model;
- Expanded Coalescence Model to ^{7}Be;
- Developed new, energy-dependent, γ_j Model.

In addition, we expanded the GENXS option in MCNP6 to include production cross sections for all isotopes. Preliminary results of our working MCNP6-F version are promising. Upon further testing of MCNP6-F, we anticipate our upgrades to be included in the next release of MCNP6.

CHAPTER 9

Summary

The accomplishments of this work include the following:

- *Analysis of the Fermi Breakup Model used by CEM and LAQGSM.* We altered the A_{Fermi} cut-off and observed the results across numerous reactions. We determined that a higher cut-off was better for some reactions, but for other reactions a lower cut-off yielded better results. **(Chapter 2)**

- *Extended the Coalescence Model to account for coalescence of light fragments (LF) up to $A = 7$.* The previous version of the Coalescence Model only "coalesced" neutrons and protons emitted during the INC into fragments up to ^{4}He. This extension proved to play an important role in attaining smooth predicted spectra that matched well with experimental data. **(Chapter 3)**

- *Expanded the Modified Exciton Model (MEM) of the Preequilibrium stage to allow for production of LF up to ^{28}Mg.* Previously, the MEM allowed for emission of up to ^{4}He only. This expansion resulted in dramatically improved prediction of the emission of energetic LF. **(Chapter 4)**

- *Upgraded the inverse cross section approximation in CEM to a NASA-Kalbach "hybrid" model.* We analyzed several prominent cross section models and chose the NASA (Tripathi, *et al.*) model for incorporation into CEM. We also added Kalbach systematics for low-energy neutron production. We obtained improved results compared to experimental data. **(Chapter 5)**

- *Created an energy-dependent model for the condensation probability, γ_j, in CEM.* We analyzed our γ_j fits for hundreds of different reactions and created a mathematical model from our data. This model has the benefit of being physically smooth across a broad range of possible reactions, as well as being computationally flexible and fast. **(Chapter 6)**

- *Validation and verification of CEM03.03F.* We compared CEM03.03 and CEM03.03F across a broad range of reactions (including those that were not used to fit, or create, our CEM03.03F models) to prove that CEM03.03F is significantly better at producing heavy clusters while retaining good results for nucleons and fragments up to ^{4}He. CEM03.03F, with the heavy cluster options turned on, requires an acceptable increase in computation time (about 35%). **(Chapter 7)**

- *Implementation within MCNP6.* We expanded the GENXS option in MCNP6 to include the tally and output of production cross sections for all isotopes (previously limited to ^{4}He). We created a working version of MCNP6, called "MCNP6-F", which contains the upgrades of CEM03.03F. Preliminary testing has been completed. **(Chapter 8)**

This work has contributed to the following publications:

- L. M. Kerby and S. G. Mashnik, Total Reaction Cross Sections in CEM and MCNP6 at Intermediate Energies, Nuclear Instruments and Methods in Physics Research B **356-357** (2015) 135, arXiv:1505.00842;

- L. M. Kerby and S. G. Mashnik, Production of Heavy Clusters with an Expanded Coalescence Model in CEM, Transactions of the American Nuclear Society **112** (2015) 577;

- S. G. Mashnik and L. M. Kerby, MCNP6 Simulation of Light and Medium Nuclei Fragmentation at Intermediate Energies, LA-UR-15-22811, Los Alamos (2015), talk presented at the 12th International Conference on Nucleus-Nucleus Collisions (NN2015), 2015-06-21/2015-06-26 (Catania, Italy);

- S. G. Mashnik, L. M. Kerby, and K. K. Gudima, Fragmentation of Light Nuclei at Intermediate Energies Simulated with MCNP6, LA-UR-15-20953, Los Alamos (2015), Invited Talk to be presented at the Fifth International Conference on Nuclear Fragmentation "From Basic Research to Applications" (NUFRA2015), 2015-10-04/2015-10-11 (Antalya (Kemer), Turkey);

- L. M. Kerby and S. G. Mashnik, A New Model for the Condensation Probability, γ_j, in CEM, LANL Report, LA-UR-15-22370 (April 2015);

- L. M. Kerby and S. G. Mashnik, An Expanded Coalescence Model within the IntraNuclear Cascade of CEM, LANL Report, LA-UR-15-20322 (January 2015);
- S. G. Mashnik and L. M. Kerby, MCNP6 Fragmentation of Light Nuclei at Intermediate Energies, Nuclear Instruments and Methods in Physics Research A **764** (2014) 59; arXiv:1404.7820;
- L. M. Kerby, S. G. Mashnik, and A. T. Tokuhiro, Production of Energetic Light Fragments with Expanded Cascade Exciton Model (CEM), Transactions of the American Nuclear Society **110** (2014) 465;
- S. G. Mashnik, L. M. Kerby, K.K. Gudima, and A.J. Sierk, Extension of the CEM and LAQGSM Models to Describe Production of Energetic Light Fragments in Spallation Reactions, European Physical Journal Web of Conferences **66** (2014) 03059; arXiV:1306.6547;
- L. M. Kerby, S. G. Mashnik, and A. J. Sierk, Preequilibrium Emission of Light Fragments in Spallation Reactions, Nuclear Data Sheets **118** (2014) 316;
- L. M. Kerby and S. G. Mashnik, Fiscal Year 2014 Report, LANL Report, LA-UR-14-27533 (November 2014);
- L. M. Kerby and S. G. Mashnik, Total Reaction Cross Section Models in CEM and MCNP6 in the Intermediate-Energy Range (>1 MeV), LANL Summer 2014 Internship Report, LANL Resport, LA-UR-14-26657 (August 2014);
- L. M. Kerby, S. G. Mashnik, and A. J. Sierk, Comparison of Expanded Preequilibrium CEM Model with CEM03.03 and Experimental Data, FY2013, LANL Report, LA-UR-13-21828 (November 2013);
- L. M. Kerby, S. G. Mashnik, and A. J. Sierk, Preliminary Results of Investigating Precompound Emission of Light Fragments in Spallation Reactions, Summer 2012, LANL Report, LA-UR-12-24190 (August 2012).

Papers in preparation:

- L. M. Kerby, S. G. Mashnik, K. K. Gudima, A. J. Sierk, J. S. Bull, and M. R. James, Production of Energetic Heavy Clusters in CEM and MCNP6, to be submitted to Reviews of Modern Physics;

- S. G. Mashnik, L. M. Kerby, K. K. Gudima, and A. J. Sierk, Current Status of the Cascade-Exciton Model and Los Alamos Version of the Quark-Gluon String Model Event-Generators used by the MCNP6 Transport Code, to be submitted to Physical Review C;

- L. M. Kerby and S. G. Mashnik, An Energy-Dependent Model for the Condensation Probability, γ_β, in CEM and MCNP6, to be submitted to Computer Physics Communications;

- K. K. Gudima, S. G. Mashnik, and L. M. Kerby, Extension of the Coalescence Model in LAQGSM to Describe Emission of Energetic Fragments up to $A = 12$, to be submitted to Physical Review C.

Awards and honors that this work (or author, related to this work) has received:

- American Physical Society (APS) M. Hildred Blewett Fellowship, 2013-2014, 2014-2015;

- American Nuclear Society (ANS) "Best Paper" Award, Radiation Protection and Shielding division, ANS Annual Meeting, Reno, NV, June 2014;

- National Organization of Gay and Lesbian Scientists and Technical Professionals (NOGLSTP) Motorola Out-to-Innovate Graduate Scholar, 2014;

- American Nuclear Society (ANS) John and Muriel Landis Scholar, 2014;

- Roy G. Post Foundation Scholar, 2013.

References

[1] K. K. Gudima, S. G. Mashnik, and V. D. Toneev, Cascade-Exciton Model of Nuclear Reactions, Nuclear Physics **A401** (1983) 329.

[2] S. G. Mashnik, K. K. Gudima, R. E. Prael, A. J. Sierk, M. I. Baznat, and N. V. Mokhov, CEM03.03 and LAQGSM03.03 Event Generators for the MCNP6, MCNPX, and MARS15 Transport Codes, Joint ICTP-IAEA Advanced Workshop on Model Codes for Spallation Reactions. Trieste, Italy, February 2008, LANL Report, LA-UR-08-2931. arXiv:0805.0751.

[3] K. K. Gudima, S. G. Mashnik, and A. J. Sierk, User Manual for the Code LAQGSM, LANL Report LA-UR-01-6804; http://lib-www.lanl.gov/lapubs/00818645.pdf.

[4] T. Goorley, M. James, T. Booth, F. Brown, J. Bull, L. J. Cox, J. Durkee, J. Elson, M. Fensin, R. A. Forster, J. Hendricks, H. G. Hughes, R. Johns, B. Kiedrowski, R. Martz, S. Mashnik, G. McKinney, D. Pelowitz, R. Prael, J. Sweezy, L. Waters, T. Wilcox, and T. Zukaitis, Initial MCNP6 Release Overview, MCNP6 version 0.1, Nuclear Technology **180** (2012) 298.

[5] N. Cooper, The Invisible Neutron Threat, National Security Science (February 2012) 12.

[6] R. Singleterry, Space Travel and the Long Tent Pole, presentation at LANL, San Ildefonso Auditory, August 2012, and private communication from Dr. Singleterry, 2012.

[7] A. Borning, Computer System Reliability and Nuclear War, Foundation for Global Community (1987).

[8] N. MacReady, The Promise of Protons in Cancer Therapy, Journal of the National Cancer Institute **104**(9) (2012).

[9] S. G. Mashnik, A. J. Sierk, K. K. Gudima, and M. I. Baznat, The MCNP6 Event Generator CEM03.03: Lessons Learned from the Intercomparison, LANL Report LA-UR-10-00510, viewgraphs of the invited talk presented at the Second Advanced Workshop on Model Codes for Spallation Reactions, 8-11 February 2010, CEA-Saclay, France; http://nds121.iaea.org/alberto/mediawiki-1.6.10/index.php/Benchmark:2ndWorkProg.

[10] S. Leray, J. C. David, M. Khandaker, G. Mank, A. Mengoni, N. Otsuka, D. Filges, F. Gallmeier, A. Konobeyev, and R. Michel, Results from the IAEA Benchmark of Spallation Models, Journal of the Korean Physical Society **59**(2) (August 2011) 791.

[11] H. Machner, D. G. Aschman, K. Baruth-Ram, J. Carter, A. A. Cowley, F. Goldenbaum, B. M. Nangu, J. V. Pilcher, E. Sideras-Haddad, J. P. F. Sellschop, F. D. Smit, B. Spoelstra, and D. Steyn, Isotopic Production Cross Sections in Proton-Nucleus Collisions at 200 MeV, Physical Review C **73** (2006) 044606.

[12] S. Furihata, Statistical Analysis of Light Fragment Production from Medium Energy Proton–Induced Reactions, Nuclear Instruments and Methods in Physics Research B **171** (2000) 251; S. Furihata, K. Nita, S. Meigo, Y. Ikeda, and F. Maekawa, GEM Code - a Simulation Program for the Evaporation and the Fission Process of an Excited Nucleus, Japan Atomic Energy Research Institute (2001).

[13] V. S. Barashenkov and V. D. Toneev, Interaction of High Energy Particle and Nuclei with Atomic Nuclei, Atomizdat, Moscow, 1972 (in Russian).

[14] V. S. Barashenkov, A. S. Il'inov, N. M. Sobolevskii, and V. D. Toneev, Uspekhi Fiziches-kikh Nauk **109** (1073) 91 [Soviet Physics Uspekhi 16 (1973) 31].

[15] K. K. Gudima, G. A. Ososkov, and V. D. Toneev, Model for Pre-Equilibrium Decay of Excited Nuclei, Yadernaya Fizika **21** (1975) 260, [Soviet Journal of Nuclear Physics 21 (1975) 139].

[16] S. G. Mashnik and V. D. Toneev, MODEX–the Program for Calculation of the Energy Spectra of Particles Emitted in the Reactions of Pre-Equilibrium and Equilibrium Statstical Decays, JINR Communication **P4-8417** (1974).

[17] S. G. Mashnik, K. K. Gudima, N. V. Mokhov, and R. E. Prael, LAQGSM03.03 Upgrade and Its Validation, LANL Report LA-UR-07-6198, Los Alamos 2007; arXiv:0709.1736.

[18] N. S. Amelin, K. K. Gudima, and V. D. Toneev, Soviet Journal of Nuclear Physics **51** (1990) 327.

[19] S. G. Mashnik and A. J. Sierk, CEM03.03 User Manual, LANL Report LA-UR-12-01364, Los Alamos (2012); https://mcnp.lanl.gov/.

[20] S. G. Mashnik, K. K. Gudima, A. J. Sierk, M. I. Baznat, and N. V. Mokhov, CEM03.01 User Manual, LANL Report LA-UR-05-7321, Los Alamos 2005; https://mcnp.lanl.gov/.

[21] S. G. Mashnik, K. K. Gudima, M. I. Baznat, A. J. Sierk, R. E. Prael, and N. V. Mokhov, CEM03.01 and LAQGSM03.01 Versions of the Improved Cascade-Exciton Model (CEM) and Los Alamos Quark-Gluon String Model (LAQGSM) Codes, LANL Report LA-UR-05-2686, Los Alamos 2005; https://mcnp.lanl.gov/.

[22] V. S. Barashenkov, K. K. Gudima, and V. D. Toneev, JINR Communications P2-4065 and P2-4066, Dubna, 1968.

[23] K. K. Gudima and S. G. Mashnik, Extension of the LAQGSM03 Code to Describe Photo-Nuclear Reactions up to Tens of GeV, in: *Proc. 11th Int. Conf. on Nuclear Reaction Mechanisms, Varenna, Italy, 2006*, edited by E. Gadioli (University of Milan, 2006), pp. 525-534; arXiv:nucl-th/0607007.

[24] V. D. Toneev and K. K. Gudima, Particle Emission in Light and Heavy Ion Reactions, Nuclear Physics **A400** (1983) 173c.

[25] N. S. Amelin, K. K. Gudima, and V. D. Toneev, Sov. J. Nucl. Phys. **51** (1990) 1093 [Yad. Fiz. **51** (1990) 1730]; ibid, **52** (1990) 172 [Yad. Fiz. **52** (1990) 272]; A. B.

Kaidalov, Soviet Journal of Nuclear Physics **45** (1987) 902 [Yadernaya Fizika **45** (1987) 1452]; N. S. Amelin, Simulation of Nuclear Collisions at High Energy in the Framework of the Quark-Gluon String Model, JINR Communication 86-802, Dubna (1986); N. S. Amelin, V. S. Barashenkov, N. V. Slavin, Soviet Journal of Nuclear Physics **40** (1984) 991 [Yad. Fiz. **40** (1984) 1560].

[26] A. S. Iljinov, I. A. Pshenichnov, N. Bianchi, E. De Sanctis, V. Muccifora, M. Mirazita, and P. Rossi, Extension of the Intranuclear Cascade Model for Photonuclear Reactions at Energies up to 10 GeV, Nuclear Physics **A616** (1997) 575.

[27] S. G. Mashnik, M. I. Baznat, K. K. Gudima, A. J. Sierk, and R. E. Prael, Extension of the CEM2k and LAQGSM Codes to Describe Photo-Nuclear Reactions, Journal of Nuclear and Radiochemical Sciences **6** (2005) A1; arXix:nucl-th/0503061.

[28] C. Kalbach, Systematics of Continuum Angular Distributions: Extensions to Higher Energies Physical Review C **37** (1988) 2350.

[29] S. G. Mashnik and A. J. Sierk, CEM2k - Recent Developments in CEM, in: *Proc. AccAppoo, 2000, Washington, DC*, USA, ANS, La Grange Park, IL, USA, 2001, p. 328; arXiv:nucl-th/0011064.

[30] M. Veselsky, Production Mechanism of Hot Nuclei in Violent Collisions in the Fermi Energy Domain, Nucl. Phys. **A705** (2002) 193.

[31] S. Furihata, Development of a Generalized Evaporation Model and Study of Residual Nuclei Prodution, Ph.D. thesis, Tohoku University, March 2003, and references therein.

[32] F. Atchison, Spallation and Fission in Heavy Metal Nuclei under Medium Energy Proton Bombardment, in: *Proc. Meeting on Targets for Neutron Beam Spallation Source, Julich, June 11-12, 1979*, edited by G. S. Bauer, (Jul-Conf-34, Julich GmbH, Germany, 1980) p. 17; Nuclear Instruments and Methods in Physics Research B **259** (2007) 909.

[33] M. Baznat, K. Gudima, and S. Mashnik, Proton-Induced Fission Cross Section Calculation with the LANL Codes CEM2k+GEM2 and LAQGSM+GEM2, in: *Proc. AccAppo3, San Diego, California, June 1-5, 2003*, (ANS, La Grange Park, IL 60526, USA, 2004), p. 976; arXiv:nucl-th/0307014.

[34] S. G. Mashnik, A. J. Sierk, and R. E. Prael, MCNP6 Fission Cross Section Calculation at Intermediate and High Energies, in: *Proc. 2013 Int. Conf. on Nuclear Data for Sci. & Technol. (ND2013)*, March 4-8, 2013, New York, USA, Nuclear Data Sheets, 2014; arXiv:1303.4308.

[35] E. Fermi, High Energy Nuclear Events, Progress of Theoretical Physics **5** (1950) 570.

[36] N. Amelin, Physics and Algorithms of the Hadronic Monte-Carlo Event Generators. Notes for a developer, CERN/IT/ASD Report CERN/IT/99/6, Geneva, Switzerland and JINR LHE, Dubna, Russia (1998); http://www.infocern.ch/asd/geant/geant4_public/

G4UsersDocuments/Overview/html/index.html/.

[37] J.-C. David, A. Boudard, J. Cugnon, S. Leray, and D. Mancusi, Report on the Predicting Capabilities of the Standard Simulation Tools in the $150 - 600$ MeV Energy Range, Rapport interne IRFU-11-249, ANDES (Accurate Nuclear Data for nuclear Energy Sustainability) EURATOM FP7 grant agreement No. 249671, Task T4.1 - Deliverable D4.1, FP7-ANDES - WP 4 , http://www-ist.cea.fr/publicea/exl-php/cadcgp.php.

[38] D. Mancusi, A. Boudard, J. Cugnon, J.-C. David, P. Kaitaniemi, and S. Leray Extension of the Liège Intranuclear-Cascade Model to Reactions Induced by Light Nuclei, Physical Review C **90** (2014) 054602; arXiv:1407.7755v2.

[39] J. Cugnon, A. Boudard, J.-C. David, A. Kelić-Heil, S. Leray, D. Mancusi, and M. V. Ricciardi, Production of Heavy Clusters (up to A $= 10$) by Coalescence during the Intranuclear Cascade Phase of Spallation Reactions, Journal of Physics: Conference Series **312** (2011) 082019.

[40] J. Cugnon, A. Boudard, J.-C. David, A. Kelić-Heil, D. Mancusi, M. V. Ricciardi, and S. Leray, Production of Clusters (up to $A = 10$) during the Intranuclear Cascade Phase of Spallation Reactions, Proc. of the Tenth Int. Topical Meeting on Nuclear Applications of Accelerators (accApp), April 3-7, 2011, Knoxville, USA, 978-0-89448-706-4, 2012 .

[41] A. Boudard, J. Cugnon, J.-C. David, S. Leray, and D. Mancusi, New Potentialities of the Liège Intranuclear Cascade (INCL) Model for Reactions Induced by Nucleons and Light Charged Particles, Phys. Rev. C **87** (2013) 014606.

[42] A. Y. Konobeyev and Y. A. Korovin, Emission of ^{7}Be from Nuclei with Atomic Numbers $Z \leq 13$ Induced by Intermediate Energy Photons, Kerntechnik **60** (1995) 147.

[43] Y. Uozumi, P. Evtoukhovitch, H. Fukuda, M. Imamura, H. Iwamoto, V. Kalinikov, W. Kallies, N. Khumutov, T. Kin, N. Koba, Y. Koba, N. Kuchinski, A. Moisenko, D. Mzavia, M. Nakano, V. Samoilov, Z. Tsamalaidze, G. Wakabayashia, and Y. Yamashita, Magnitude Factor Systematics of Kalbach Phenomenology for Reactions Emitting Helium and Lithium Ions, Nuclear Instruments and Methods in Physics Research **A 571** (2007) 743.

[44] S. G. Mashnik, A. J. Sierk, and K. K. Gudima, Complex Particle and Light Fragment Emission in the Cascade-Exciton Model of Nuclear Reactions, LANL Report, LA-UR-02-5185, and private communication with Dr. K. K. Gudima, 2006.

[45] J. P. Bondorf, A. S. Botvina, A. S. Iljinov, I. N. Mishustin, and K. Sneppen, Statistical Multifragmentation of Nuclei, Physics Reports **257** (1995) 133.

[46] S. R. Souza, B. V. Carlson, R. Donangelo, W. G. Lynch, and M. B. Tsang, Statistical Multifragmentation Model with Discretized Energy and the Generalized Fermi Breakup: Formulation of the Model, Physical Review C **88** (2013) 014607.

[47] R. J. Charity, L. G. Sobotka, J. Cibor, K. Hagel, M. Murray, J. B. Natowitz, R. Wada, Y. El Masri, D. Fabris, G. Nebbia, G. Viesti, M. Cinausero, E. Fioretto, G. Prete, A. Wagner, and H. Xu, Emission of Unstable Clusters from Yb Compound Nuclei, Physical Review C **63** (2001) 024611; http://www.chemistry.wustl.edu/ rc/gemini/.

[48] Y. Ronen, On the Light Particles in Ternary Fission, Physica Scripta **86** (2012) 065203.

[49] A. Budzanowski, M. Fidelus, D. Filges, F. Goldenbaum, H. Hodde, L. Jarczyk, B. Kamys, M. Kistryn, S. Kistryn, S. Kliczewski, A. Kowalczyk, E. Kozik, P. Kulessa, H. Machner, A. Magiera, B. Piskor-Ignatowicz, K. Pysz, Z. Rudy, R. Siudak, and M. Wojciechowski, Competition of Coalescence and "Fireball" Processes in Nonequilibrium Emission of Light Charged Particles from p+Au Collisions, Phys. Rev. C **78** (2008) 024603.

[50] A. Budzanowski, M. Fidelus, D. Filges, F. Goldenbaum, H. Hodde, L. Jarczyk, B. Kamys, M. Kistryn, S. Kistryn, S. Kliczewski, A. Kowalczyk, E. Kozik, P. Kulessa, H. Machner, A. Magiera, B. Piskor-Ignatowicz, K. Pysz, Z. Rudy, R. Siudak, and M. Wojciechowski, Comparison of Nonequilibrium Processes in p+Ni and p+Au Collisions at GeV Energies, Physical Review C **82** (2010) 034605.

[51] A. Bubak, A. Budzanowski, D. Filges, F. Goldenbaum, A. Heczko, H. Hodde, L. Jarczyk, B. Kamys, M. Kistryn, S. Kistryn, S. Kliczewski, A. Kowalczyk, E. Kozik, P. Kulessa, H. Machner, A. Magiera, W. Migdal, N. Paul, B. Piskor-Ignatowicz, M. Puchala, K. Pysz, Z. Rudy, R. Siudak, M. Wojciechowski, and P. Wüstner, Non-equilibrium Emission of Complex Fragments From p+Au Collisions at 2.5 GeV Proton Beam Energy, Physical Review C **76** (2007) 014618.

[52] D. Filges and F. Goldenbaum, Handbook of Spallation Research: Theory, Experiments and Applications, WILEY-VCH Verlag GmbH & Co., 2009, ISBN: 978-3-527-40714-9.

[53] J.-C. David, Spallation Reactions: A Successful Interplay Between Modeling and Applications, arXiv:1505.0382; Eur. Phys. J. A **51** (2015) 157.

[54] I. Pshenichnov, A. Botvina, I. Mishustin, and W. Grainer, Nuclear Fragmentation Reactions in Extended Media Studied with GEANT4 Toolkit, Nuclear Instruments and Methods in Physics Research B **268** (2010) 604.

[55] M. Hultqvist, M. Lazzeroni, A. Botvina, I. Gudowska, N. Sobolevsky, and A. Brahme, Evaluation of Nuclear Reaction Cross-Sections and Fragment Yields in Carbon Beams Using the SHIELD-HIT Monte Carlo Code. Comparison with Experiments, Physics in Medicine & Biology **57** (2012) 4369.

[56] D.C. Hansen, A. Lühr, N. Sobolevsky, and N. Bassler, Optimizing SHIELD-HIT for Carbon Ion Treatment, Physics in Medicine & Biology **57** (2012) 2393.

[57] A. Lühr, D.C. Hansen, R. Teiwes, N. Sobolevsky, O. Jäkel, and N. Bassler, The Impact of Modeling Nuclear Fragmentation on Delivered Dose and Radiobiology in Ion Therapy, Physics in Medicine & Biology **57** (2012) 5169.

[58] T. Ogawa, T. Sato, S. Hashimoto, and K. Niita, Analysis of Multi-Fragmentation Reactions Induced by Relativistic Heavy Ions Using the Statistical Multi-Fragmentation Model, Nuclear Instruments and Methods in Physics Research A **723** (2013) 36.

[59] T. Sato, K. Niita, N. Matsuda, S. Hashimoto, Y. Iwamoto, S. Noda, T. Ogawa, H. Iwase, H. Nakashima, T. Fukahori, K. Okumura, T. Kai, S. Chiba, T. Furuta, and L. Sihver, Particle and Heavy Ion Transport code System, PHITS, version 2.52, Journal of Nuclear Science and Technology **50** (2013) 913.

[60] S. G. Mashnik, Validation and Verification of MCNP6 Against Intermediate and High-Energy Experimental Data and Results by Other Codes, European Physical Journal - Plus **126** (2011) 49; arXiv:1011.4978.

[61] S. G. Mashnik, Validation and Verification of MCNP6 Against High-Energy Experimental Data and Calculations by Other Codes. I. The CEM Testing Primer, LANL Report LA-UR-11-05129, Los Alamos 2011; https://mcnp.lanl.gov/.

[62] S. G. Mashnik, Validation and Verification of MCNP6 Against High-Energy Experimental Data and Calculations by other Codes. II. The LAQGSM Testing Primer, LANL Report LA-UR-11-05627, Los Alamos 2011; https://mcnp.lanl.gov/.

[63] S. G. Mashnik, Validation and Verification of MCNP6 Against High-Energy Experimental Data and Calculations by other Codes. III. The MPI Testing Primer, LANL Report LA-UR-13-26944, Los Alamos 2013; https://mcnp.lanl.gov/.

[64] S. G. Mashnik and L. M. Kerby, MCNP6 Fragmentation of Light Nuclei at Intermediate Energies, Nuclear Instruments and Methods in Physics Research A **764** (2014) 59; arXiv:1404.7820.

[65] V. S. Barashenkov, Cross Sections of Interaction of Particles and Nuclei with Nuclei (in Russian), JINR, Dubna, Russia (1993); tabulated data available at: http://www.nea.fr/html/dbdata/bara.html.

[66] R. F. Carlson, A. J. Cox, T. N. Nasr, M. S. De Jong, D. L. Ginther, D. K. Hasell, A. M. Sourkes, W. T. H. Van Oers, and D. J. Margaziotis, Measurements of Proton Total Reaction Cross Sections for ^{6}Li, ^{7}Li, ^{14}N, ^{20}Ne and ^{40}Ar between 23 and 49 MeV, Nuclear Physics A **445** (1985) 57.

[67] A. E. Taylor, and E. Wood, Proton Scattering from Light Elements at 142 MeV, Nuclear Physics **25** (1961) 642.

[68] S. G. Mashnik, A. J. Sierk, K. A. Van Riper, and W. B. Wilson, Production and Validation of Isotope Production Cross Section Libraries for Neutrons and Protons to 1.7 GeV, LANL Report LA-UR-98-6000 1998; in: Proc. SARE-4, Knoxville, TN, September 13-16, 1998 (ORNL, 1999, pp. 151-162); arXiv:nucl-th/9812071; our T-16 Library "T-16 Lib" is updated permanently when new experimental data became available to us.

[69] A. Ingemarsson, Nyberg, P. U. Renberg, O. Sundberg, R. F. Carlson, A. Auce, R. Johansson, G. Tibell, B. C. Clark, L. Kurth Kerr, and S. Hama, Reaction Cross Sections for 65 MeV Protons on Targets from ^{9}Be to ^{208}Pb, Nuclear Physics A

653 (1999) 341.

[70] R. F. Carlson, A. J. Cox, J. R. Nimmo, N. E. Davison, S. A. Elbakr, J. L. Horton, A. Houdayer, A. M. Sourkes, W. T. H. van Oers, and D. J. Margaziotis, Proton Total Reaction Cross Sections for the Doubly Magic Nuclei ^{16}O, ^{40}Ca, and ^{208}Pb in the Energy Range 20-50 MeV, Physics Review C **12** (1975) 1167.

[71] N. Okumura, Y. Aoki, T. Joh, Y. Honkyu, K. Hirota, and K. S. Itoh, Measuring System of Proton Total Reaction Cross-Sections at Tandem Energy Region, Nuclear Instruments and Methods in Physics Research A **487** (2002) 565.

[72] F. S. Dietrich, E. P. Hartouni, S. C. Johnson, G. J. Schmid, R. Soltz, W. P. Abfalterer, R. C. Haight, L. S. Waters, A. L. Hanson, R. W. Finlay, and G. S. Blanpied, Proton Reaction Cross Sections Measured in the BNL/AGS E943 Experiment, Journal of Nuclear Science and Technology Suppl. **2** (2002) 269.

[73] W. R. Webber, J. C. Kish, and D. A. Schrier, Individual Isotopic Fragmentation Cross Sections of Relativistic Nuclei in Hydrogen, Helium, and Carbon Targets, Physical Review C **41** (1990) 547.

[74] C. Zeitlin, J. Miller, S. Guetersloh, L. Heilbronn, A. Fukumura, Y. Iwata, T. Murakami, S. Blattnig, R. Norman, and S. Mashnik, Fragmentation of ^{14}N, ^{16}O, ^{20}Ne, and ^{24}Mg Nuclei at 290 to 1000 MeV/nucleon, Physical Review C **83** (2011) 034909.

[75] C. Zeitlin, A. Fukumura, L. Heilbronn, Y. Iwata, J. Miller, and T. Murakami, Fragmentation Cross Sections of 600 MeV/nucleon ^{20}Ne on Elemental Targets Physical Review C **64** (2001) 024902.

[76] J. W. Wilson, J. L. Shinn, L. W. Townsend, R. K. Tripathi, F. F. Badavi, and S. Y. Chun, NUCFRG2: A Semiempirical Nuclear Fragmentation Model, Nuclear Instruments and Methods in Physics Research B **94** (1994) 95.

[77] B. S. Nilsen, C. J. Waddington, J. R. Cummings, T. L. Garrard, and J. Klarmann, Fragmentation Cross Sections of Relativistic $^{84}_{36}$Kr and $^{109}_{47}$Ag Nuclei in Targets from Hydrogen to Lead, Physical Review C **52** (1995) 3277.

[78] F. A. Cucinotta, J. W. Wilson, R. K. Tripathi, and L. W. Townsend, Microscopic Fragmentation Model for Galactic Cosmic Ray Studies, Advances in Space Research **22** (1998) 533.

[79] R. E. L. Green, R. G. Korteling, J. M. D'Auria, K. P. Jackson, and R. L. Helmer, Light Fragment Spectra to Upper Kinematic Limits for 300 MeV Proton Reactions with Be and Ag, Physical Review C **35** (1987) 1341.

[80] M. Hagiwara, T. Sanami, T. Oishi, M. Baba, and M. Takada, Differential Cross Sections on Fragments ($2 \leq Z \leq 9$) Production for Carbon, Aluminum, Silicon Induced by Tens-of-MeV Protons, Journal of Nuclear Science and Technology **49** (2012) 571.

[81] T. Sanami, M. Hagiwara, H. Iwase, M. Takada, D. Satoh, Y. Iwamoto, S. Kunieda, H. Yashima, A. Tamii, and M. Baba, Fragment DDX Measurement of Proton

Induced Reactions on Light-Medium Nuclei for Energy Range from Reaction Threshold to a Few Hundred MeV, Journal of the Korean Physical Society **59** (2011) 1805.

[82] J. Benecke, T. T. Chou, C. N. Yang, and E. Yen, Hypothesis of Limiting Fragmentation in High-Energy Collisions, Physical Review **188** (1969) 2159.

[83] M. Fidelus, Model Description of Proton Induced Fragmentation of Atomic Nuclei, Ph.D. Thesis, Cracow, 2010.

[84] S. G. Mashnik, A. J. Sierk, O. Bersillon, and T. Gabriel, Cascade-Exciton Model Detailed Analysis of Proton Spallation at Energies from 10 MeV to 5 GeV, LANL Report LA-UR-97-97-2905, Los Alamos 1997; https://mcnp.lanl.gov/; S.G. Mashnik, A.J. Sierk, O. Bersillon, T. Gabriel, Nuclear Instruments and Methods in Physics Research A **414** (1998) 68.

[85] A. Yu. Konobeyev and U. Fischer, Status of Evaluation of ^{9}Be DPA and Gas Production Cross-sections at Neutron Incident Energies up to 200 MeV, presentation at the Fall 2014 Nuclear Data Week, 24-28 November 2014, NEA, Issy-le-Moulineaux, France; http://www.oecd-nea.org/dbdata/meetings/nov2014/; https://www.researchgate.net/profile/AYu_Konobeyev/publication/275517905_Status_of_evaluation_of_9Be_dpa_and_gas_production_cross-sections_at_neutron_incident_energies_up_to_200_MeV/links/553e0316ocf29b5ee4bcf5fo.pdf.

[86] H. W. Bertini, Low-Energy Intranuclear Cascade Calculation, Phys. Rev. **131** (1963) 1801; Intranuclear Cascade Calculation of the Secondary Nucleon Spectra from Nucleon-Nucleus Interactions in the Energy Range 340 to 2900 MeV and Comparison with Experiment, Physical Review **188** (1969) 1711.

[87] Y. Yariv and Z. Frankel, Intranuclear Cascade Calculation of High-Energy Heavy-Ion Interactions, Physical Review C **20** (1979) 2227; Y. Yariv and Z. Frankel, Inclusive Cascade Calculation of High Energy Heavy Ion Collisions: Effect of Interactions between Cascade Particles, Physical Review C **24** (1981) 488; Y. Yariv, ISABEL — INC Model for High-Energy Hadron-Nucleus Reactions, Proc. Joint ICTP-IAEA Advanced Workshop on Model Codes for Spallation Reactions, ICTP Trieste, Italy, 4-8 February 2008, INDC(NDS)-0530 Distr. SC, IAEA, Vienna, August 2008, pp. 15–28.

[88] J. Cugnon, C. Volant, and S. Vuillier, Improved Intranuclear Cascade Model for Nucleon-Nucleus Interactions, Nuclear Physics A **620** (1997) 475; A. Boudard, J. Cugnon, S. Leray, and C. Volant, Intranuclear Cascade Model for a Comprehensive Description of Spallation Reaction Data, Physical Review C **66** (2002) 044615.

[89] A. R. Junghans, M. de Jong, H.-G. Clerc, A. V. Ignatyuk, G. A. Kudyaev, and K.-H. Schmidt, Projectile-Fragment Yields as a Probe for the Collective Enhancement in the Nuclear Level Density, Nuclear Physics A **629** (1998) 635; J.-J. Gaimard, and K.-H. Schmidt, A Reexamination of the Abrasion-ablation Model for the Description of the Nuclear Fragmentation Reaction, Nuclear

Physics A **531** (1991) 709.

[90] A. J. Koning, S. Hilaire, and M. C. Duijvestijn, TALYS: Comprehensive Nuclear Reaction Modeling, Proc. Int. Conf. on Nuclear Data for Sci. & Techn. (ND2004), September 26 - October 1, 2004, Santa Fe, NM, USA, edited by R. C. Haight, M. B. Chadwick, T. Kawano, and P. Talou, (AIP Conference Proceedings, Volume 769, Melville, New York, 2005), pp. 1154–1159.

[91] M. M. Meier, D. A. Clark, C. A. Goulding, J. B. McClelland, G. L. Morgan, C. E. Moss, and W. B. Amian, Differential Neutron Production Cross Sections and Neutron Yields from Stopping-Length Targets for 113-MeV Protons, Nuclear Science and Engineering **102** (1989) 310.

[92] M. M. Meier, W. B. Amian, C. A. Goulding, G. L. Morgan, and C. E. Moss, Differential Neutron Production Cross Sections for 256-MeV Protons, Nuclear Science and Engineering **110** (1992) 289.

[93] S. G. Mashnik, L. M. Kerby, K. K. Gudima, and A. J. Sierk, Extension of the CEM and LAQGSM Models to Describe Production of Energetic Light Fragments in Spallation Reactions, European Physical Journal Web of Conferences **66** (2014) 03059; arXiV:1306.6547.

[94] L. M. Kerby, S. G. Mashnik, and A. T. Tokuhiro, Production of Energetic Light Fragments with Expanded Cascade Exciton Model(CEM), Transactions of the American Nuclear Society **110** (2014) 465.

[95] L. M. Kerby, S. G. Mashnik, and A. J. Sierk, Preequilibrium Emission of Light Fragments in Spallation Reactions, Nuclear Data Sheets **118** (2014) 316; arXiv:1303.4311.

[96] L. M. Kerby and S. G. Mashnik, Total Reaction Cross Sections in CEM and MCNP6 at Intermediate Energies, Nuclear Instruments and Methods B **356-357** (2015) 135; LANL Report, LA-UR-14-29371; arXiv:1505.00842.

[97] L. M. Kerby and S. G. Mashnik, LANL Fiscal Year 2014 Report, LANL Report LA-UR-14-27533, Los Alamos (2014); http://www.osti.gov/scitech/biblio/1162152.

[98] H. Schulz, G. Röpke, K. Gudima, and V. Toneev, "The Coalescence Phenomenon and the Pauli Quenching in High-Energy Heavy Ion Collisions," Physics Letters, **134B** (1983) 458.

[99] S. Leray, A. Boudard, B. Braunn, J. Cugnon, J.-C. David, A. Leprince, and D. Mancusi, Recent Developments of the Liège Intranuclear Cascade Model in View of its Use into High-energy Transport Codes, *Nuclear Data Sheets*, **118** (2014) 312.

[100] M.-C. Lemaire, S. Nagamiya, O. Chamberlain, G. Shapiro, S. Schnetzer, H. Steiner, and I. Tanihata, Tables of Light-Fragment Inclusive Cross Sections in Relativistic Heavy Ion Collisions. Part I, Lawrence Berkeley Laboratory Report LBL-8463 1978.

[101] S. Nagamiya, M.-C. Lemaire, E. Moeller, S. Schnetzer, G. Shapiro, H. Steiner, and I. Tanihata, Production of Pions and Light Fragments at Large Angles in High-Energy Nuclear Collisions, Physical Review C **24** (1981) 971.

[102] L. M. Kerby and S. G. Mashnik, An Expanded Coalescence Model within the IntraNuclear Cascade of CEM, LANL Report, LA-UR-15-20322.

[103] R. E. L. Green, R. G. Korteling, and K. P. Jackson, Inclusive Production of Isotopically Resolved Li Through Mg Fragments by 480 MeV p+Ag Reactions, Physical Review C **29** (1984) 1806.

[104] S. G. Mashnik, L. M. Kerby, and K. K. Gudima, Fragmentation of Light Nuclei at Intermediate Energies Simulated with MCNP6, LANL Report LA-UR-15-20953, to be presented at the Fifth International Conference on Nuclear Fragmentation From Basic Research to Applications (NUFRA2015), 4 – 11 October 2015, Kemer (Antalya), Turkey.

[105] S. G. Mashnik and L. M. Kerby, MCNP6 Simulation of Light and Medium Nuclei Fragmentation at Intermediate Energies, LANL Report LA-UR-15-22811, Los Alamos (2015), presented at the 12th International Conference on Nucleus-Nucleus Collisions, June 21-26, 2015, Catania, Italy.

[106] S.G. Mashnik and S.A. Smolyansky, The Cascade-Exciton Approach to Nuclear Reactions (Foundation and Achievements), Joint Institute for Nuclear Research (JINR) Preprint E2-94-353, Dubna, 1994, 24 p.; Proc. Int. Study Centre in Nonliniar Science *Dynamic of Transport in Fluids, Plasmas and Charged Beams*, Villa Gualino, Torino, Italy, June-September, 1994, Eds. G. Maino and M. Ottaviani, Singapore: World Scientific, 1996, pp. 137-159.

[107] T. Ericson, The Statistical Model and Nuclear Level Densities, Adv. in Physics **9** (1960) 425.

[108] F. C. Williams Jr., Intermediate State Transition Rates in the Griffin Model, Phys. Lett. B **31** (1970) 184.

[109] F. C. Williams Jr., Particle-Hole State Density in the Uniform Spacing Model, Nucl. Phys. **A161** (1971) 231.

[110] I. Ribansky, P. Oblozinsky, and E. Betak, Pre-Equilibrium Decay and the Exciton Model, Nucl. Phys. **A205** (1973) 545.

[111] G. Mantzouranis, H. A. Weidenmüller, and D. Agassi, Generalized Exciton Model for the Description of Preequilibrium Angular Distributions, Z. Phys. A **276** (1976) 145.

[112] L.M. Kerby and S.G. Mashnik, Total Reaction Cross Section Models in CEM and MCNP6 in the Intermediate-Energy Range (>1 MeV), LANL Summer 2014 Internship Report, LANL Report, LA-UR-14-26657 (August 2014).

[113] I. Dostrovsky, Z. Fraenkel, and G. Friedlander, Monte Carlo Calculations of Nuclear Evaporation Processes. III. Applications to Low-Energy Reactions, Physical Review **116** (1959) 683.

[114] R. K. Tripathi, F. A. Cucinotta, and J. W. Wilson, Accurate Universal Parameterization of Absorption Cross Sections, Nuclear Instruments and Methods in Physics Research B **117** (1996) 347.

[115] R. K. Tripathi, F. A. Cucinotta, and J. W. Wilson, Accurate Universal Parameterization of Absorption Cross Sections II–Neutron Absorption Cross Sections, Nuclear Instruments and Methods in Physics Research B **129** (1997) 11.

[116] R. K. Tripathi, F. A. Cucinotta, and J. W. Wilson, Universal Parameterization of Absorption Cross Sections III–Light Systems, Nuclear Instruments and Methods in Physics Research B **155** (1999) 349.

[117] W. Shen, B. Wang, J. Feng, W. Zhan, Y. Zhu, and E. Feng, Total Reaction Cross Section for Heavy-Ion Collisions and Its Relation to the Neutron Excess Degree of Freedom, Nuclear Physics A **491** (1989) 130.

[118] M. Takechi, M. Fukuda, M. Mihara, K. Tanaka, T. Chinda, T. Matsumasa, M. Nishimoto, R. Matsumiya, Y. Nakashima, H. Matsubara, K. Matsuta, T. Minamisono, T. Ohtsubo, T. Izumikawa, S. Momota, T. Suzuki, T. Yamaguchi, R. Koyama, W. Shinozaki, M. Takahashi, A. Takizawa, T. Matsuyama, S. Nakajima, K. Kobayashi, M. Hosoi, T. Suda, M. Sasaki, S. Sato, M. Kanazawa, and A. Kitagawa, Reaction Cross Sections at Intermediate Energies and Fermi-Motion Effect, Physical Review C **79** (2009) 061601.

[119] S. Kox, A. Gamp, C. Perrin, J. Arvieux, R. Bertholet, J. F. Bruandet, M. Buenerd, R. Cherkaoui, A. J. Cole, Y. El-Masri, N. Longequeue, J. Menet, F. Merchez, and J. B. Viano, Trends of Total Reaction Cross Sections for Heavy Ion Collisions in the Intermediate Energy Range, Physical Review C **35** (1987) 1678.

[120] L. W. Townsend and J. W. Wilson, Comment on "Trends of Total Reaction Cross Sections for Heavy Ion Collisions in the Intermediate Energy Range," Physical Review C **37** (1988) 892.

[121] K. Iida, A. Kohama, and K. Oyamatsu, Formula for Proton-Nucleus Reaction Cross Section at Intermediate Energies and Its Application, Journal of the Physical Society of Japan **76** (2007) 044201; arXiv:nucl-th/0601039.

[122] A. Ingemarsson and M. Lantz, Geometrical Aspects of Reaction Cross Sections for ^{3}He, ^{4}He, and ^{12}C Projectiles, Physical Review C **67** (2003) 064605.

[123] H. H. K. Tang, G. R. Srinivasan, and N. Azziz, Cascade Statistical Model for Nucleon-Induced Reactions on Light Nuclei in the Energy Range 50 MeV–1 GeV, Physical Review C **42** (1990) 1598.

[124] C. Kalbach, Toward a Global Exciton Model; Lessons at 14 MeV, Journal of Physics G: Nuclear and Particle Physics **24** (1998) 847.

[125] V. S. Barashenkov and A. Polanski, Electronic Guide for Nuclear Cross-Sections, Joint Institute for Nuclear Research Communication E2-94-417, JINR, Dubna, Russia (1994).

[126] V. S. Barashenkov, W. Gudowski, and A. Polanski, Integral High-Energy Nucleon-Nucleus Cross Sections for Mathematical Experiments with Electronuclear Facilities, JINR Communication E2-99-207, JINR, Dubna, Russia (1990); private communications from Drs. Alexander Polanski and Dick Prael to Stepan Mashnik.

[127] R. E. Prael, A. Ferrari, R. K. Tripathi, and A. Polanski, Comparison of Nucleon Cross Section Parametrization Methods for Medium and High Energies, LANL Report LA-UR-98-5813, Los Alamos (1998); Proc. Forth Int. Workshop on Simulating Accelerator Radiation Environments (SARE-4), Hyatt Regency, Knoxville, TN, September 13-16, 1998, edited by Tony A. Gabriel, Oak Ridge National Laboratory (1999) pp. 171.

[128] L. Sihver, M. Lantz, and A. Kohama, Improved Parametrization of the Transparency Parameter in Kox and Shen Models of Total Reaction Cross Sections, Physical Review C **89** (2014) 067602.

[129] L. Sihver, A. Kohama, K. Iida, S. Hashimoto, H. Iwase, and K. Niita, Current Status of the "Hybrid Kurotama model" for Total Reaction Cross Sections, Nuclear Instruments and Methods in Physics Research B **334** (2014) 34.

[130] L. Sihver, M. Lantz, M. Takechi, A. Kohama, A. Ferrari, F. Cerutti, and T. Sato, A Comparison of Total Reaction Cross Section Models Used in Particle and Heavy Ion Transport Codes, Advances in Space Research **49** (2012) 812.

[131] V. Andersen, F. Ballarini, G. Battistoni, M. Campanella, M. Carboni, F. Cerutti, A. Empl, A. Fassò, A. Ferrari, E. Gadioli, M. V. Garzelli, K. Lee, A. Ottolenghi, M. Pelliccioni, L. S. Pinsky, J. Ranft, S. Roesler, P. R. Sala, and T. L. Wilson, The FLUKA Code for Space Applications: Recent Developments, Advances in Space Research **34** (2004) 1302.

[132] L. Sihver, C. H. Tsao, R. Silberberg, T. Kanai, and A.F. Barghouty, Total Reaction and Partial Cross Section Calculations in Proton-Nucleus ($Z_t \leq 26$) and Nucleus-Nucleus Reactions (Z_p and $Z_t \leq 26$), Physical Review C **47** (1993) 1225.

[133] H. P. Wellisch and D. Axen, Total Reaction Cross Section Calculations in Proton-Nucleus Scattering, Physical Review C **54** (1996) 1329.

[134] L. Sihver, M. Lantz, T. T. Böhlen, A. Mairani, A. F. Cerutti, and A. Ferrari, A cCmparison of Total Reaction Cross Section Models Used in FLUKA, GEANT4, and PHITS, IEEE Aerospace Conf. pp 1-10 (2012); DOI: 10.1109/AERO.2012.6187014.

[135] GEANT4 Physics Reference Manual, Chapter 23: Total Reaction Cross Section in Nucleus-Nucleus Reactions, gentoo.osuosl.org/distfiles/PhysicsReferenceManual-4.10.0.pdf. (2013).

[136] A. Krylov, M. Paraipan, N. Sobolevsky, G. Timoshenko, and V. Tret'yakov, GEANT4, MCNPX, and SHIELD Code Comparison Concerning Relativistic Heavy Ion Interaction with Matter, Physics of Particles and Nuclei Letters **11** (2014) 549.

[137] S. G. Mashnik, A. J. Sierk, and K. K. Gudima, Complex Particle and Light Fragment Emission in the Cascade-Exciton Model of Nuclear Reactions, LANL Report LA-UR-02-5185, Los Alamos (2002), Invited talk presented at the 12th Biennial Topical Meeting of the Radiation Protection and Shielding Division (RPSD) of the American Nuclear Society, April 14-17, 2002, Santa Fe, NM; E-print: nucl-th/0208048.

[138] S. G. Mashnik, R. E. Prael, and K. K. Gudima, Implementation of CEM03.01 into MCNP6 and its Verification and Validation Running through MCNP6. CEM03.02 Upgrade, LANL Research Note X-3-RN(U)-07-03, LANL Report LA-UR-06-8652, Los Alamos (2007); https://mcnp.lanl.gov/.

[139] R. E. Prael, A. Ferrari, R. K. Tripathi, and A. Polanski, Plots Supplemental to: Comparison of Nucleon Cross Section Parametrization Methods for Medium and High Energies, LANL Report LA-UR-98-5843, Los Alamos (December 16, 1998).

[140] L. V. Dubar, D. Sh. Eleukenov, L. I. Slyusarenko, and N. P. Yurkuts, Parameterization of the Total Cross Sections of Reactions in the Intermediate Energy Region, Yadernaya Fizika **49** (1989) 1239 [Soviet Journal of Nuclear Physics **49** (1989) 771].

[141] A. Auce, R. F. Carlson, A. J. Cox, A. Ingemarsson, R. Johansson, P. U. Renberg, O. Sundberg, G. Tibell, and R. Zorro, Reaction Cross Section for 75–190 MeV Alpha Particles on Targets from ^{12}C to ^{208}Pb, Physical Review C **50** (1994) 871.

[142] T. W. Bonner and J. C. Slattery, Nonelastic Scattering Cross Sections for 8-20 MeV, Physical Review **113** (1959) 1088.

[143] J. R. Beyster, M. Walt, and E. W. Salmi, Interaction of 1.0-, 1.77-, 2.5-, 3.25-, and 7.0-MeV Neutrons with Nuclei, Physical Review **104** (1956) 1319.

[144] H. L. Taylor, O. Lönsjö, and T. W. Bonner, Nonelastic Scattering Cross Sections for Fast Neutrons, Physical Review **100** (1955) 174.

[145] M. V. Pasechnik, Nonelastic Scattering of the Fast Neutrons, 1st UN Conf. Peaceful Uses Atomic Energy, Geneva 1955, **2** (1955) 3.

[146] J. R. Beyster, R. L. Henkel, R. A. Nobles, and J. M. Kister, Inelastic Collision Cross Sections at 1.0-, 4.0-, and 4.5-MeV Neutron Energies, Physical Review **98** (1955) 1216.

[147] V. I. Strizhak, Inelastic Scattering Cross Sections of Nuclei for 2.5 MeV Neutrons, Soviet Physics - JETP **4** (1957) 769.

[148] L. E. Beghian, F. Hofman, and S. Wilensky, Measurement of Nonelastic Cross Section for Lead at 2.1 and 1.7 MeV, Neutron Cross-Section Techn. Conf., Washington 1966, **2** (1966) 726.

[149] G. C. Morrison, Inelastic Neutron Scattering, Physica (Utrecht) **22** (1956) 1135.

[150] Ju. G. Degtjarev, Nonelastic Cross Section for Neutrons with Nuclei by ^{7}Li, ^{12}C, ^{14}N, ^{26}Fe, Cu, Pb, ^{235}U, and ^{239}Pu, J. Nuclear Energy, Part A+B (Reactor Sci. Techn.) **20** (1966) 818.

[151] M. Walt and J. R. Beyster, Interaction of 4.1 MeV Neutrons with Nuclei, Physical Review **98** (1955) 677.

[152] K. R. Poze and N. P. Glazkov, Inelastic Scattering of 0.3, 0.77, and 1.0 MeV Photoneutrons, Soviet Physics - JETP **3** (1956) 745.

[153] R. F. Carlson, Proton-Nucleus Total Reaction Cross Sections and Total Cross Sections Up to 1 GeV Atomic Data and Nuclear Data Tables **63** (1996) 93.

[154] R. E. Warner, R. A. Patty, P. M. Voyles, A. Nadasen, F. D. Becchetti, J. A. Brown, H. Esbensen, A. Galonsky, J. J. Kolata, J. Kruse, M. Y. Lee, R. M. Ronningen, P. Schwandt, J. von Schwarzenberg, B. M. Sherrill, K. Subotic, J. Wang, and P. Zecher, Total Reaction and 2n-Removal Cross Sections of 20-60A MeV ^{4,6,8}He, $^{6-9,11}$Li, and ^{10}Be on Si, Physical Review C **54** (1996) 1700.

[155] V.Yu. Ugryumov, I. V . Kuznetsov, E. Bialkowski, A. Kugler, K. A. Kuterbekov, I. N. Kuhtina, V. F. Kushniruk, V. G. Lyapin, V. A. Maslov, Yu. E. Penionzhkevich, Yu. G. Sobolev, W. Trzaska, G. P. Tjurin, S. V. Khlebnikov, and S. Yamaletdinov, Energy Dependence of the Total Cross Section for the Reaction of ^{4}He Ions with Silicon Nuclei, Physics of Atomic Nuclei **68** (2005) 16 [Yad. Fiz. **68** (2005) 17].

[156] V. Yu Ugryumov, I. V Kuznetsov, K. B Basybekov, E. Bialkowski, A. Budzanowski, A. Duysebaev, B. A. Duysebaev, T. K. Zholdybaev, K. M. Ismailov, K. K. Kadyrzhanov, R. Kalpakchieva, A. Kugler, I. N. Kukhtina, V. F. Kushniruk, K. A. Kuterbekov, A. Mukhambetzhan, Yu. E. Penionzhkevich, B. M. Sadykov, I. Skwirczynska, and Yu. G. Sobolev, Total Reaction Cross Section for ^{4}He Collisions with Silicon in the Energy Range 3-10 MeV/u, Nuclear Physics A **734** (2004) E53.

[157] A. Ingemarsson, J. Nyberg, P. U. Renberg, O. Sundberg, R. F. Carlson, A. J. Cox, A. Auce, R. Johansson, G. Tibell, D. T. Khoa, and R. E. Warner, New Results for Reaction Cross Sections of Intermediate Energy α-Particles on Targets from ^{9}Be to ^{208}Pb, Nuclear Physics A **676** (2000) 3.

[158] M. K. Baktybaev, A.Duisebaev, B . A. Duisebaev, K. M. Ismailov, M. G. Itkis, K. K. Kadyrzhanov, R. Kalpakchieva, I. V. Kuznetsov, K. A. Kuterbekov, I. N. Kukhtina, S. M. Lukyanov, A. Mukhamedzhan, Yu. E. Penionzhkevich, B. M. Sadykov, Yu. G. Sobolev, and V. Yu. Ugryumov, Total Reaction Cross Section from the Interaction of ^{4}He Ions with ^{28}Si at 10-30 MeV, Physics of Atomic Nuclei **66** (2003) 1615 [Yad. Fiz. **66** (2003) 1662].

[159] M. G. Mazarakis and W. E. Stephens, Experimental Measurements of the ^{12}C + ^{12}C Nuclear Reactions at Low Energies, Physical Review C **7** (1973) 1280.

[160] C. Zeitlin, S. Guetersloh, L. Heilbronn, J. Miller, A. Fukumura, Y. Iwata, and T. Murakami, Fragmentation Cross Sections of 290 and 400 MeV/nucleon ^{12}C Beams on Elemental Targets, Physical Review C **76** (2007) 014911.

[161] A. N. Golovchenko, J. Skvarč, N. Yasuda, M. Giacomelli, S. P. Tretyakova, R. Ilić, R. Bimbot, M. Toulemonde, and T. Murakami, Total Charge-Changing and Partial Cross-Section Measurements in the Reactions of ∼110-250 MeV/nucleon ^{12}C in Carbon, Paraffin, and Water, Physical Review C **66** (2002) 014609.

[162] J. R. Wu and C. C. Chang, Complex-Particle Emission in the Pre-Equilibrium Exciton Model, Physical Review C **17** (1978) 1540.

[163] E. Betak, Complex Particle Emission in the Exciton Model of Nuclear Reactions, Acta Physica Slovaka **26** (1976) 21.

[164] V. Blideanu, F. R. Lecolley, J. F. Lecolley, T. Lefort, N. Marie, A. Ataç, G. Ban, B. Bergenwall, J. Blomgren, S. Dangtip, K. Elmgren, Ph. Eudes, Y. Foucher, A. Guertin, F. Haddad, A. Hildebrand, C. Johansson, O. Jonsson, M. Kerveno, T. Kirchner, J. Klug, Ch. Le Brun, C. Lebrun, M. Louvel, P. Nadel-Turonski, L. Nilsson, N. Olsson, S. Pomp, A. V. Prokofiev, P.-U. Renberg, G. Rivière, I. Slypen, L. Stuttgé, U. Tippawan, and M. Österlund, Nucleon-induced reactions at intermediate energies: New data at 96 MeV and theoretical status, Physical Review C **70** (2004) 014607.

[165] C. Cline, Extensions to the Pre-Equilibrium Statistical Model and a Study of Complex Particle Emission, Nuclear Physics A **193** (1972) 417.

[166] L. M. Kerby and S. G. Mashnik, Production of Heavy Clusters with an Expanded Coalescence Model in CEM, Transactions **112** (2015) 577.

[167] I. Ribansky and P. Oblozinsky, Emission of Complex Particles in the Exciton Model, Physics Letters **45B**(4) (1973).

[168] L.M. Kerby and S.G. Mashnik, A New Model for the Condensation Probability, γ_j, in CEM, LANL Report, LA-UR-15-22370 (April 2015).

[169] W. N. Venables, D. M. Smith, and the R Core Team, An Introduction to R. Notes on R: A Programming Environment for Data Analysis and Graphics Version 3.2.0 (2015-04-16), http://cran.r-project.org/doc/manuals/r-release/R-intro.pdf.

[170] M.S. El-Nagdy, A. Abdelsalam, Z. Abou-Moussa, and B.M. Badawy, Limiting fragmentation of target nucleus at high energy, Canadian Journal of Physics, **91** (2013) 737-743.

[171] J. Franz, P. Koncz, E. Roessle, C. Sauerwein, H. Schmitt, K. Schmoll, J. Eroe, Z. Fodor, J. Kecskemeti, Z. Kovacs, and Z. Seres, Neutron-Induced Production of Protons, Deuterons and Tritons on Copper and Bismuth, Nuclear Physics A **510** (1990) 774.

[172] F. E. Bertrand and R. W. Peelle, Complete Hydrogen and Helium Particle Spectra from 30 to 60 MeV Proton Bombardment of Nuclei With A=12 to 209 and Comparison with the Intranuclear Cascade Model, Physical Review C **8** (1973) 1045.

[173] G. Roy, L. Greeniaus, G. A. Moss, D. A. Hutcheon, R. Liljestrand, R. M. Woloshyn, D. H. Boal, A. W. Stetz, K. Aniol, A. Willis, N. Willis, and R. McCamis, Inclusive Scattering of Protons on Helium, Nickel, and Tantalum at 500 MeV, Physical Review C **23** (1981) 16711.

[174] V. I. Bogatin, V. F. Litvin, O. V. Lozhkin, N. A. Perfilov, and Yu. P. Yakovlev, Isotopic Effects in High-Energy Nuclear Reactions and Isospin Correlations of

Fragmentation Cross Sections, Nuclear Physics A **260** (1976) 446.

[175] C. M. Herbach, D. Hillscher, U. Jahnke, V. G. Tishchenko, J. Galin, A. Letourneau, A. Péghaire, D. Filges, F. Goldenbaum, L. Pienkowski, W. .U. Schröder, and J. Tõke, Charged-Particle Evaporation and Pre-Equilibrium Emission in 1.2 GeV Proton-Induced Spallation Reactions, Nuclear Physics A **765** (2006) 426.

[176] S. Benck, I. Slypen, J.P. Meulders, V. Corcalciuc, M.B. Chadwick, P.G. Young, and A.J. Koning, Light Charged Particle Production in Neutron-Induced Reactions on Aluminium at En= $28.5 - 62.7$ MeV Physical Review C, **58** (1998) 1558.

[177] E. Raeymackers, S. Benck, N. Nica, I. Slypen, J.P. Meulders, V. Corcalciuc, and A.J. Koning, Light Charged Particle Emission in fast neutron ($25 - 65$ MeV) induced reactions on Bi-209 Nuclear Physics A **726** (2003) 210.

[178] R.Bevilacqua, S.Pomp, V.D.Simutkin, U.Tippawan, P.Andersson, J.Blomgren, M.Oesterlund, M.Hayashi, S.Hirayama, Y.Naitou, Y.Watanabe, M.Tesinsky, F.R.LeColley, N.Marie, A.Hjalmarsson, A.V.Prokofiev, A.Kolozhvari, C.Gustavsson, E.Tengborn, G.Ban, and Q.Hamel, Neutron induced light-ion production from iron and bismuth at 175 MeV, EPJ Web of Conferences **2** (2010) 05005.

[179] M. L. Brooks, Neutron Induced Pion Production on C, Al, Cu, and W at Neutron Energies of $200 - 600$ MeV, Ph. D. Thesis, University of New Mexico (LA-12210-T, UC-910, Oct 1991, Los Alamos); M. L. Brooks, B. Bassalleck, B. D. Dierterle, R. A. Reeder, D. M. Lee, J. A. McGill, M. E. Schillaci, R. A. Ristinen, and W. R. Smythe, Neutron Induced Pion Production on C, Al, Cu, and W at $200 - 600$ MeV, Physical Review C **45** (1992) 2343.

[180] R.A. Schumacher, G.S. Adams, D.R. Ingham, J.L. Matthews, W.W. Sapp, R.S. Turley, R.O. Owens, and B.L. Roberts, Cu(γ, p)X Reaction at E_γ = 150 and 300 MeV, Physical Review C **25** (1982) 2269.

[181] T. Nakamoto, K. Ishibashi, N. Matsufuji, N. Shigyo, K. Maehata, H. Arima, S. Meigo, H. Takada, S. Chiba, and M. Numajiri, Experimental Neutron-Production Double-Differential Cross Section for the Nuclear reaction by 1.5 GeV π^+ Mesons Incident on Iron, Journal of Nuclear Science and Technology **34** (1997) 860.

[182] S. G. Mashnik, R. J. Peterson, A. J. Sierk, and M. R. Braunstein, Pion-Induced Transport of π Mesons in Nuclei, Physical Review C **61** (2000) 034601.

[183] J. Ouyang, Quasi-Free Pion Single Charge Exchange, Ph. D. Thesis, University of Colorado (LANL Report LA-12457-T, UC-413, 1992).

[184] F. Rejmund, B. Mustapha, P. Armbruster, J. Benlliure, M. Bernas, A. Boudard, J.P. Dufour, T. Enqvist, R. Legrain, S. Leray, K.-H. Schmidt, C. Stéphan, J. Taieb, L. Tassan-Got, and C. Volant, Measurement of Isotopic Cross Sections of Spallation Residues in 800 A MeV ^{197}Au + p Collisions, Nuclear Physics **A683** (2001) 540; J. Benlliure, P. Armbruster, M. Bernas, A. Boudard, J.P. Dufour, T. Enqvist, R. Legrain, S. Leray, B. Mustapha, F. Rejmund, K.-H. Schmidt, C.

Stéphan, L. Tasaan-Got, and C. Volant, Isotopic Production Cross Sections of Fission Residues in ^{197}Au-on-Proton Collisions at 800 *A* MeV, Nuclear Physics **A683** (2001) 513.

[185] C. Villagrasa-Canton, A. Boudard, J.-E. Ducret, B. Fernandez, S. Leray, C. Volant, P. Armbruster, T. Enqvist, F. Hammache, K. Helariutta, B. Jurado, M.-V. Ricciardi, K.-H. Schmidt, K. Summerer, F. Vives, O. Yordanov, L. Audouin, C.-O. Bacri, L. Ferrant, P. Napolitani, F. Rejmund, C. Stéphan, L. Tassan-Got, J. Benlliure, E. Casarejos, M. Fernandez-Ordonez, J. Pereira, S. Czajkowski, D. Karamanis, M. Pravikoff, J.S. George, R.A. Mewaldt, N. Yanasak, M. Wiedenbeck, J.J. Connell, T. Faestermann, A. Heinz, and A. Junghans, Spallation Residues in the Reaction ^{56}Fe + p at 0.3, 0.5, 0.75, 1.0 and 1.5 A GeV, E-print: nucl-ex/0612001, Physical Review C **75** (2007) 044603; C. Villagrasa-Canton, Etude de la production des noyaux résiduels dans la réaction de spallation Fe + p à 5 énergies ($300 - 1500$ MeV/A) et application au calcul de dommage sur une fenêtre de système hybride, Ph.D. Thesis, Universite de Paris XI Orsay, December 5, 2003, http://www-w2k.gsi.de/charms/theses.htm, and private communication from Dr. Villagrasa to S. Mashnik, March 11, 2004.

[186] P. Napolitani, New Findings on the Onset of Thermal Disassembly in Spallation Reactions, PhD Thesis, University Paris XI Orsay, IPNO-T-04-14, September 24, 2004; P. Napolitani, K.-H. Schmidt, A. S. Botvina, F. Rejmund, L. Tassan-Got, and C. Villagrasa, High-Resolution Velocity Measurements on Fully Identified Light Nuclides Produced in ^{56}Fe + Hydrogen and ^{56}Fe + Titanium Systems, Physical Review C **70** (2004) 054607.

[187] J. Taieb, K.-H. Schmidt, L. Tissan-Got, P. Armstrong, J. Benlliure, M. Bernas, A. Boudard, E. Casarejos, S. Czajkowski, T. Enqvist, R. Legrain, S. Leray, B. Mustapha, M. Pravikoff, F. Rejmund, C. Stéphan, C. Volant, and W. Wlazlo, Evaporation Residues Produced in the Spallation Reaction ^{238}U + p at 1 A GeV, Nuclear Physics A **724** (2003) 413; M. Bernas, P. Armstrong, J. Benlliure, A. Boudard, E. Casarejos, S. Czajkowski, T. Enqvist, R. Legrain, S. Leray, B. Mustapha, P. Napolitani, J. Pereira, F. Rejmund, M.-V. Ricciardi, K.-H. Schmidt, C. Stéphan, J. Taieb, L. Tissan-Got, and C. Volant, Fission-Residues Produced in the Spallation Reaction ^{238}U + p at 1 A GeV, nucl-ex/0304003, Nuclear Physics A **725** (2003) 213.

[188] D. Tarrío, L. Tassan-Got, L. Audouin, B. Berthier, I. Duran, L. Ferrant, S. Isaev, C. Le Naour, C. Paradela, C. Stephan, D. Trubert, U. Abbondanno, G. Aerts, F. Álvarez-Velarde, S. Andriamonje, J. Andrzejewski, P. Assimakopoulos, G. Badurek, P. Baumann, F. Bečvář, F. Belloni, E. Berthoumieux, F. Calviño, M. Calviani, D. Cano-Ott, R. Capote, C. Carrapiço, A. Carrillo de Albornoz, P. Cennini, V. Chepel, E. Chiaveri, N. Colonna, G. Cortes, A. Couture, J. Cox, M. Dahlfors, S. David, I. Dillmann, R. Dolfini, C. Domingo-Pardo, W. Dridi, C. Eleftheriadis, M. Embid-Segura, A. Ferrari, R. Ferreira-Marques, L. Fitzpatrick, H. Frais-Koelbl, K. Fujii, W. Furman, I. Goncalves, E. González-Romero, A. Goverdovski, F. Gramegna, E. Griesmayer, C. Guerrero, F. Gunsing, B. Haas,

R. Haight, M. Heil, A. Herrera-Martinez, M. Igashira, E. Jericha, Y. Kadi, F. Käppeler, D. Karadimos, D. Karamanis, M. Kerveno, V. Ketlerov, P. Koehler, V. Konovalov, E. Kossionides, M. Krtička, C. Lampoudis, H. Leeb, C. Lederer, A. Lindote, I. Lopes, R. Losito, M. Lozano, S. Lukic, J. Marganiec, L. Marques, S. Marrone, T. Martínez, C. Massimi, P. Mastinu, E. Mendoza, A. Mengoni, P. M. Milazzo, C. Moreau, M. Mosconi, F. Neves, H. Oberhummer, S. O'Brien, M. Oshima, J. Pancin, C. Papachristodoulou, C. Papadopoulos, N. Patronis, A. Pavlik, P. Pavlopoulos, L. Perrot, M. T. Pigni, R. Plag, A. Plompen, A. Plukis, A. Poch, J. Praena, C. Pretel, J. Quesada, T. Rauscher, R. Reifarth, M. Rosetti, C. Rubbia, G. Rudolf, P. Rullhusen, J. Salgado, C. Santos, L. Sarchiapone, R. Sarmento, I. Savvidis, G. Tagliente, J. L. Tain, L. Tavora, R. Terlizzi, G. Vannini, P. Vaz, A. Ventura, D. Villamarin, V. Vlachoudis, R. Vlastou, F. Voss, S. Walter, H. Wendler, M. Wiescher, and K. Wisshak, (n_TOF Collaboration), Neutron-induced Fission Cross Section of ^{nat}Pb and ^{209}Bi from threshold to 1 GeV: An Improved Parametrization, Physical Review C **83** (2011) 044620.

[189] A. V. Fomichev, V. N. Dushin, S. M. Soloviev, A. A. Fomichev, and S. Mashnik, Fission Cross Sections for ^{240}Pu, ^{243}Am, ^{209}Bi, ^{nat}W Induced by Neutrons up to 500 MeV Measured Relative to ^{235}U, LANL Report LA-UR-05-1533, Los Alamos, 2005; V. G. Khlopin Radium Institute Preprint RI-262, St. Petersburg, Russia, 2004.

[190] S. Furihata, Nuclear Instruments and Methods in Physics Research B **171** (2000) 252.

[191] F. Atchison, Nuclear Instruments and Methods in Physics Research B **259** (2007) 909.

[192] R. E. Prael, Tally Edits for the MCNP6 GENXS Option, LANL Report, LA-UR-11-02146 (2011).

APPENDIX A

Fitted F_j Values

Table A.1 displays the fitted F_j values for several hundred different reactions, by Z and A number of the projectile, incident energy (T_0) of the projectile, Z and A number of the target nucleus, and Z and A number of the emitted fragment.

Table A.1: F_j for various reactions.

Z_{proj}	A_{proj}	T_0 (MeV)	Z_{target}	A_{target}	Z_{frag}	A_{frag}	F_j
1	1	28.8	13	27	1	1	1
1	1	28.8	13	27	1	2	0.65
1	1	28.8	13	27	1	3	4
1	1	28.8	13	27	2	3	6.5
1	1	28.8	13	27	2	4	5
1	1	28.8	26	54	1	1	1
1	1	28.8	26	54	1	2	0.5
1	1	28.8	26	54	1	3	8
1	1	28.8	26	54	2	3	8
1	1	28.8	26	54	2	4	20
1	1	38.8	26	54	1	1	1
1	1	38.8	26	54	1	2	0.5
1	1	38.8	26	54	1	3	0.55
1	1	38.8	26	54	2	3	2.5
1	1	38.8	26	54	2	4	4.5
1	1	61.5	26	54	1	1	1
1	1	61.5	26	54	1	2	0.43
1	1	61.5	26	54	1	3	0.65
1	1	61.5	26	54	2	3	0.95
1	1	61.5	26	54	2	4	12

Continued on next page

Table A.1 – continued from previous page

Z_{proj}	A_{proj}	T_0 (MeV)	Z_{target}	A_{target}	Z_{frag}	A_{frag}	F_j
1	1	200	13	27	2	3	6.5
1	1	200	13	27	2	4	19
1	1	200	13	27	2	6	1.8
1	1	200	13	27	3	6	13
1	1	200	13	27	3	7	3.8
1	1	200	13	27	3	8	4.5
1	1	200	13	27	3	9	4.5
1	1	200	13	27	4	7	4.5
1	1	200	13	27	4	9	7
1	1	200	13	27	4	10	13
1	1	200	13	27	5	10	13
1	1	200	27	59	2	3	1.2
1	1	200	27	59	2	4	3
1	1	200	27	59	2	6	0.6
1	1	200	27	59	3	6	3.4
1	1	200	27	59	3	7	7.5
1	1	200	27	59	3	8	16
1	1	200	27	59	3	9	225
1	1	200	27	59	4	7	7.5
1	1	200	27	59	4	9	90
1	1	200	27	59	4	10	1400
1	1	200	27	59	5	10	5000
1	1	200	27	59	5	11	15000
1	1	200	27	59	5	12	210000
1	1	200	27	59	6	12	700000
1	1	200	27	59	6	13	700000
1	1	200	79	197	2	3	1
1	1	200	79	197	2	4	8

Continued on next page

Table A.1 – continued from previous page

Z_{proj}	A_{proj}	T_0 (MeV)	Z_{target}	A_{target}	Z_{frag}	A_{frag}	F_j
1	1	200	79	197	2	6	6
1	1	200	79	197	3	6	13
1	1	200	79	197	3	7	125
1	1	200	79	197	3	8	225
1	1	200	79	197	3	9	450
1	1	200	79	197	4	7	22
1	1	200	79	197	4	9	1600
1	1	200	79	197	4	10	13000
1	1	200	79	197	5	10	21500
1	1	200	79	197	5	11	140000
1	1	200	79	197	5	12	2100000
1	1	200	79	197	6	12	4600000
1	1	200	79	197	6	13	21000000
1	1	190	47	107	2	3	0.4
1	1	190	47	107	2	4	2.5
1	1	190	47	107	2	6	0.5
1	1	190	47	107	3	6	1.6
1	1	190	47	107	3	7	6.5
1	1	190	47	107	3	8	13
1	1	190	47	107	4	7	6.2
1	1	190	47	107	4	9	30
1	1	190	47	107	4	10	400
1	1	300	47	107	1	1	1
1	1	300	47	107	1	2	1
1	1	300	47	107	1	3	0.75
1	1	300	47	107	2	3	1
1	1	300	47	107	2	4	2.6
1	1	300	47	107	3	6	1.4

Continued on next page

Table A.1 – continued from previous page

Z_{proj}	A_{proj}	T_0 (MeV)	Z_{target}	A_{target}	Z_{frag}	A_{frag}	F_j
1	1	300	47	107	3	7	5
1	1	300	47	107	3	8	3.3
1	1	300	47	107	4	7	2
1	1	300	47	107	4	9	5.5
1	1	300	47	107	4	10	10
1	1	480	47	107	2	3	0.7
1	1	480	47	107	2	4	1
1	1	480	47	107	3	6	0.3
1	1	480	47	107	3	7	0.7
1	1	480	47	107	3	8	1.3
1	1	480	47	107	3	9	0.5
1	1	480	47	107	4	7	1
1	1	480	47	107	4	9	0.5
1	1	480	47	107	4	10	1.3
1	1	480	47	107	5	10	0.25
1	1	480	47	107	6	12	1
1	1	660	28	58	2	3	3.5
1	1	660	28	58	2	4	16
1	1	660	28	64	2	3	2.3
1	1	660	28	64	2	4	7
1	1	660	50	112	2	3	4
1	1	660	50	112	2	4	40
1	1	660	50	124	2	3	4
1	1	660	50	124	2	4	40
1	1	1200	28	61	1	1	1
1	1	1200	28	61	1	2	3
1	1	1200	28	61	1	3	3
1	1	1200	28	61	2	3	4.5

Continued on next page

Table A.1 – continued from previous page

Z_{proj}	A_{proj}	T_0 (MeV)	Z_{target}	A_{target}	Z_{frag}	A_{frag}	F_j
1	1	1200	28	61	2	4	6
1	1	1200	28	61	2	6	0.01
1	1	1200	28	61	3	6	0.7
1	1	1200	28	61	3	7	1.2
1	1	1200	28	61	3	8	0.3
1	1	1200	28	61	3	9	0.06
1	1	1200	28	61	4	7	1.2
1	1	1200	28	61	4	9	0.16
1	1	1200	28	61	4	10	0.16
1	1	1200	28	61	5	10	0.25
1	1	1200	28	61	5	11	0.08
1	1	1200	28	61	5	12	0.05
1	1	1900	28	61	1	1	1
1	1	1900	28	61	1	2	1.5
1	1	1900	28	61	1	3	2
1	1	1900	28	61	2	3	1.8
1	1	1900	28	61	2	4	2.4
1	1	1900	28	61	2	6	0.01
1	1	1900	28	61	3	6	0.01
1	1	1900	28	61	3	7	0.12
1	1	1900	28	61	3	8	0.14
1	1	1900	28	61	3	9	0.065
1	1	1900	28	61	4	7	0.17
1	1	1900	28	61	4	9	0.22
1	1	1900	28	61	4	10	0.2
1	1	1900	28	61	5	10	0.3
1	1	1900	28	61	5	11	0.2
1	1	1900	28	61	5	12	0.05

Continued on next page

Table A.1 – continued from previous page

Z_{proj}	A_{proj}	T_0 (MeV)	Z_{target}	A_{target}	Z_{frag}	A_{frag}	F_j
1	1	2500	28	61	1	1	1
1	1	2500	28	61	1	2	2
1	1	2500	28	61	1	3	3
1	1	2500	28	61	2	3	5
1	1	2500	28	61	2	4	2.6
1	1	2500	28	61	2	6	0.01
1	1	2500	28	61	3	6	0.01
1	1	2500	28	61	3	7	0.01
1	1	2500	28	61	3	8	0.14
1	1	2500	28	61	3	9	0.065
1	1	2500	28	61	4	7	0.055
1	1	2500	28	61	4	9	0.22
1	1	2500	28	61	4	10	0.14
1	1	2500	28	61	5	10	0.3
1	1	2500	28	61	5	11	0.1
1	1	2500	28	61	5	12	0.03
1	1	1200	73	181	1	1	1
1	1	1200	73	181	1	2	0.3
1	1	1200	73	181	1	3	0.75
1	1	1200	73	181	2	3	0.2
1	1	1200	73	181	2	4	1
1	1	1200	79	197	1	1	1
1	1	1200	79	197	1	2	0.5
1	1	1200	79	197	1	3	0.7
1	1	1200	79	197	2	3	0.4
1	1	1200	79	197	2	4	1
1	1	1200	79	197	2	6	0.1
1	1	1200	79	197	3	6	0.18

Continued on next page

Table A.1 – continued from previous page

Z_{proj}	A_{proj}	T_0 (MeV)	Z_{target}	A_{target}	Z_{frag}	A_{frag}	F_j
1	1	1200	79	197	3	7	0.38
1	1	1200	79	197	3	8	0.5
1	1	1200	79	197	3	9	0.17
1	1	1200	79	197	4	7	0.25
1	1	1200	79	197	4	9	0.3
1	1	1200	79	197	4	10	0.5
1	1	1200	79	197	5	10	0.5
1	1	1200	79	197	5	11	0.5
1	1	1200	79	197	5	12	1
1	1	1900	79	197	1	1	1
1	1	1900	79	197	1	2	1
1	1	1900	79	197	1	3	0.95
1	1	1900	79	197	2	3	0.65
1	1	1900	79	197	2	4	0.95
1	1	1900	79	197	2	6	0.01
1	1	1900	79	197	3	6	0.03
1	1	1900	79	197	3	7	0.25
1	1	1900	79	197	3	8	0.21
1	1	1900	79	197	3	9	0.2
1	1	1900	79	197	4	7	0.08
1	1	1900	79	197	4	9	0.25
1	1	1900	79	197	4	10	0.45
1	1	1900	79	197	5	10	0.4
1	1	1900	79	197	5	11	0.35
1	1	1900	79	197	5	12	0.35
1	1	2500	79	197	1	1	1
1	1	2500	79	197	1	2	1.5
1	1	2500	79	197	1	3	1.2

Continued on next page

Table A.1 – continued from previous page

Z_{proj}	A_{proj}	T_0 (MeV)	Z_{target}	A_{target}	Z_{frag}	A_{frag}	F_j
1	1	2500	79	197	2	3	1
1	1	2500	79	197	2	4	0.7
1	1	2500	79	197	2	6	0.01
1	1	2500	79	197	3	6	0.01
1	1	2500	79	197	3	7	0.12
1	1	2500	79	197	3	8	0.13
1	1	2500	79	197	3	9	0.12
1	1	2500	79	197	4	7	0.065
1	1	2500	79	197	4	9	0.085
1	1	2500	79	197	4	10	0.14
1	1	2500	79	197	5	10	0.16
1	1	2500	79	197	5	11	0.2
1	1	2500	79	197	5	12	0.085
0	1	41	13	27	1	1	1
0	1	41	13	27	1	2	0.9
0	1	41	13	27	1	3	1.2
0	1	41	13	27	2	4	1000
0	1	49	13	27	1	1	1
0	1	49	13	27	1	2	1.6
0	1	49	13	27	1	3	1.8
0	1	49	13	27	2	4	1000
0	1	62.7	83	209	1	1	1
0	1	62.7	83	209	1	2	1.38
0	1	62.7	83	209	1	3	6
0	1	96	92	238	1	1	1
0	1	96	92	238	1	2	2.5
0	1	96	92	238	1	3	6.5
0	1	96	92	238	2	4	46

Continued on next page

Table A.1 – continued from previous page

Z_{proj}	A_{proj}	T_0 (MeV)	Z_{target}	A_{target}	Z_{frag}	A_{frag}	F_j
0	1	175	26	56	1	1	1
0	1	175	26	56	1	2	3.5
0	1	175	26	56	1	3	7.2
0	1	175	26	56	2	3	6.8
0	1	175	26	56	2	4	37
0	1	175	83	209	1	1	1
0	1	175	83	209	1	2	2.5
0	1	175	83	209	1	3	7.5
0	1	175	83	209	2	3	5
0	1	175	83	209	2	4	40
0	1	317	29	63	1	1	1
0	1	317	29	63	1	2	10
0	1	317	29	63	1	3	9
0	1	317	83	209	1	1	1
0	1	317	83	209	1	2	2.4
0	1	317	83	209	1	3	6.5
0	1	542	29	63	1	1	1
0	1	542	29	63	1	2	2.4
0	1	542	29	63	1	3	0.85
0	1	542	83	209	1	1	1
0	1	542	83	209	1	2	0.55
0	1	542	83	209	1	3	0.45
1	1	50	13	27	2	All	7
1	1	50	13	27	3	All	1000
1	1	50	14	28	2	All	7
1	1	50	14	28	3	All	10000
1	1	70	13	27	2	All	7
1	1	70	13	27	3	All	1000

Continued on next page

Table A.1 – continued from previous page

Z_{proj}	A_{proj}	T_0 (MeV)	Z_{target}	A_{target}	Z_{frag}	A_{frag}	F_j
1	1	70	14	28	2	All	7
1	1	70	14	28	3	All	10000